Further Process Understanding and Prediction on Selective Laser Melting of Stainless Steel 316L

by

Bochuan Liu

A Doctoral Thesis Submitted in Partial Fulfilment of the Requirements for the Award of Doctor of Philosophy of Loughborough University

Wolfson School of Mechanical and Manufacturing Engineering

May 2013

Dedicated to my parents and my cat

Abstract

Additive Manufacturing (AM) is a group of manufacturing technologies which are capable to produce 3D solid parts by adding successive layers of material. Parts are fabricated in an additive manner, layer by layer; and the geometric data can be taken from a CAD model directly. The main revolutionary aspect of AM is the ability of quickly producing complex geometries without the need of tooling, allowing for greater design freedom. As one of AM methods, Selective Laser Melting (SLM) is a process for producing metal parts with minimal subtractive post-processing required. It relies on the generation and distribution of laser generated heat to raise the temperature of a region of a powder bed to above the melting point. Due to high energy input to enable full melting of the powder bed materials, SLM is able to build fully dense metal parts without post heat treatment and other processing.

Successful fabrications of parts by SLM require a comprehensive understanding of the main process controlling parameters such as energy input, powder bed properties and build conditions, as well as the microstructure formation procedure as it can strongly affect the final mechanical properties. It is valuable to control the parts' microstructure through controlling the process parameters to obtain acceptable mechanical properties for end-users. In the SLM process, microstructure characterisation strongly depends on the thermal history of the process. The temperature distribution in the building area can significantly influence the melting pool behaviour, solidification process and thermal mechanical properties of the parts. Therefore, it is important to have an accurate prediction of the temperature distribution history during the process.

The aim of this research is to gain a better understanding of process control parameters in SLM process, and to develop a modelling methodology for the

prediction of microstructure forming procedure. The research is comprised of an experiment and a finite element modelling part.

Experimentation was carried out to understand the effect of each processing control parameters on the final part quality, and characterise the model inputs. Laser energy input, build conditions and powder bed properties were investigated. Samples were built and tested to gain the knowledge of the relationship between samples' density and mechanical properties and each process control factor. Heat transfer model inputs characterisation, such as defining and measuring the material properties, input loads and boundary conditions were also carried out via experiment.

For the predictive modelling of microstructure, a methodology for predicting the temperature distribution history and temperature gradient history during the SLM process has been developed. Moving heat source and states variable material properties were studied and applied to the heat transfer model for reliable prediction. Multi-layers model were established to simulate the layer by layer process principles. Microstructure was predicted by simulated melting pool behaviour and the history of three dimensional temperature distribution and temperature gradient distribution. They were validated by relevant experiment examination and measurement.

Acknowledgement

I am deeply indebted to my supervisors Prof. Richard Hague, Dr. Christopher Tuck, Prof. Ian Ashcroft and Prof. Ricky Wildman for their guidance, kindness, suggestions, patience and supervision throughout the entire research. This work would not have been possible without their insight and awareness. Special thanks to Dr. Christopher Tuck for his suggestions on my thesis writing. His encouragement and understanding helped me sail through the hard times.

Sincere thanks to technician Andy Sandaver and Mark East for their guidance and help during the experimentation of this research, as well as being my best friends and supporting me all the time. Special thanks to IT technician Darren Smith who saved my research data from a broken hard drive. Thanks are also due to Dr. Yau Yau Tse for her help on metal phase characterisation experiment and Dr. Sozon Tsopanos for his help in the initial stage of the research.

I am grateful to all the staff of the Wolfson School of Mechanical and Manufacturing Engineering, Loughborough University for their support and help, especially Andy Price, Clive Turner, Alan Trahar, Jagpal Smith, Dave Britton, Chris Harris, Bob Temple, Keven Smith and Richard Price. Thanks to all the members of the Additive Manufacturing Research Group (AMRG). I am sincerely grateful to Mark Hardy, Dr. Candi Majewski, Dr. Helen Thomas and Jiaming Bai for all their help, encouragement, kindness and friendship.

Finally, I would like to thank Dr. Chris Sutcliffe and Dr. Yau Yau Tse for their efforts as external and internal examiners respectively.

Contents

List of Figures

List of Tables

List of Symbols

r	radial distance from the centre axis of the beam
z	axial distance from the beam's narrowest point (the "waist")
I_0	intensity at the centre of the beam at its waist
$w(z)$	radius at which the field amplitude and intensity drop to $1/e$ and $1/e^2$ of their axial values respectively
w_0	waist size
η	characteristic impedance of the medium in which the beam is propagating
z_R	distance along the propagation direction of the laser beam from the waist to the place where the area of the cross section is doubled, and is called the Rayleigh range
b	depth of focus of the beam
M^2	beam propagation factor
f_1	focal length of the lens
λ	laser wavelength
D_1	beam diameter at the lens
P	laser power
P_0	total power transmitted by the beam
E_ρ	laser energy density
u	laser scanning speed
δ	laser beam spot size on the powder bed
ΔH	energy required to melt material
ρ	density
V_p	volume
r_p	radius
C_p	specific heat capacity
ΔT	temperature difference between ambient and material melting temperature
L_f	latent heat of fusion
E	melt energy
q	heat flux
k	thermal conductivity

T	temperature
H	amount of the heat flow
r	radial distance from point source
T_0	environment temperature
α	thermal diffusivity
P	point source power
u	constant moving speed in the same direction of x
x	axis of movement
D	beam diameter
Q	total heat input
η	thermal efficiency
f_f	fraction of the heat deposited in the front quadrant
f_r	fraction of the heat deposited in the rear quadrant
α	contact radius
λ_e	effective contact thermal conductivity
R	radius of the sphere
H	Hausner ratio
ρ_T	tapped density of powder
ρ_A	apparent density of powder
m	mass of sample
Nu	Nusselt number
Pr	Prandtl number
Re	Reynolds number
h	heat transfer coefficient
D	characteristic length parameter
μ	viscosity of the fluid
V	velocity of the fluid
D_h	hatch distance
R_a	surface roughness

List of Acronyms

AM	Additive Manufacturing
CAD	Computer Aided Design
ASTM	American Society for Testing and Materials
3D	Three-Dimensional
2D	Two-Dimensional
SLM	Selective Laser Melting
SFF	Solid Freeform Fabrication
LM	Layered Manufacturing
SLA	Stereolithography
UV	Ultraviolet
FDM	Fused Deposition Modelling
ABS	Acrylonitrile Butadiene Styrene
UC	Ultrasonic Consolidation
3D LC	Three-Dimensional Laser Cladding
LENS	Laser Engineered Net Shaping
3DP	Three-Dimensional Printing
SLS	Selective Laser Sintering
EBM	Electron Beam Melting
SLM	Selective Laser Melting
DMLF	Direct Metal Laser Fabrication
Nd:YAG	Neodymium-doped Yttrium Aluminium Garnet
TEM	Transverse Electromagnetic Mode
LASER	Light Amplification Stimulated by Emission of Radiation
FCC	Face-centred Cubic
BCC	Body-centred Cubic
UTS	Ultimate Tensile Strength
SEM	Scanning Electron Microscope
EBSD	Electron backscatter diffraction
DSC	Differential Scanning Calorimetry
DFLUX	Defined Heat Flux
UMAT	User Defined Material Property

FEA	Finite Element Analysis
FWHM	Full Width at Half-maximum
EDX	Energy Dispersive X-ray Spectroscopy
1D	One-Dimensional

1 Introduction

1.1 Background

In the history of manufacturing, subtractive methods have usually come first, with many machining methods, such as turning, milling, drilling, grinding, etc. In fact, “subtractive manufacturing” is used more as a word to distinguish the traditional mechanical manufacturing methods to the more recent additive manufacturing (AM) method. Although some “additive” fabrication methods like welding and casting have been used in the industry for centuries, they are still considered as traditional manufacturing since they do not employ modern computer aided design (CAD) and manufacturing techniques.

Additive Manufacturing is defined by the ASTM F42 committee in their first standard ASTM F2792-10 as:

“The process of joining materials to make objects from 3D model data, usually layer upon layer, as opposed to subtractive manufacturing technologies.”

During the mechanical manufacturing development history, industry has strived for a more efficient fabrication method with less economic cost. Manufacturing time, raw material and equipment costs, manufacturing sustainability, social and environmental costs have been investigated to develop a revolutionary manufacturing method to benefit both manufacturers and end users.

Additive manufacturing’s early application, Rapid Prototyping, was developed to reduce the fabrication time and cost of developing prototypes of new parts, which was previously achieved by slow and expensive subtractive methods [1]. With the years going by and the technique continually developing, additive

manufacturing has moved further to the production end, and is disseminating into the industry and the business world. As a main advantage, additive manufacturing can fabricate very complex geometries which are difficult or impossible to build using conventional manufacturing process [2]. This can bring more profit in some cases for parts made via additive manufacturing than subtractive methods. However, the real integration of additive manufacturing techniques into commercial production is a matter of complementing traditional manufacturing rather than entirely replacing them at the moment [2].

As one of the AM methods, Selective Laser Melting (SLM) is a process for producing metal parts. It is a laser based additive manufacturing technique, which is able to build complex geometries directly from 3D CAD models, thereby allowing for great design freedom [3-5]. Selective Laser Melting relies on the generation and distribution of laser generated heat to raise the temperature of a region of a powder bed to above its melting point. Due to the high energy input to enable full melting of the powder bed materials, SLM is able to build fully dense metal parts without post heat treatment or infiltration of finished components required [6].

Successful fabrications of parts by SLM require a comprehensive understanding of the main process controlling parameters such as energy input, powder bed properties and build conditions. The microstructure in SLM parts is a key issue of the process as it strongly affects the final mechanical properties. It is valuable to control the parts' microstructure through controlling the process parameters to obtain acceptable mechanical properties for end-users. It is important to investigate details of microstructure such as grain size distribution, phase transformation, forming trend on solidification direction, characterisation under different processing parameters, etc. A clear knowledge and reliable prediction of the microstructure forming process will give a better understanding of the SLM process and help other research such as process stability and repeatability study.

In the SLM process, microstructure evolution depends on the thermal history of the process. The temperature distribution in the build area can significantly influence the melting pool behaviour. Due to the high energy input per unit area, non-uniform temperature distribution and fast solidification process, a high thermal gradient may be introduced into the SLM component. This thermal gradient causes residual stresses and affects the final part's quality [7]. Also the presence of a fully molten melt pool makes the process very difficult to control due to increased thermocapillary effects [8]. Therefore, it is important to have an accurate prediction of the temperature distribution history during the process.

1.2 Scope of Research

The aim of this research is to gain a better understanding of the process control parameters in SLM process, and to develop a modelling methodology for the prediction of the foundation of part microstructure. The following objectives were identified to achieve the overall scope of the research.

- Investigation of the main laser energy density input control parameters, such as laser power, scanning speed, lens focus position, hatch spacing, etc.
- Investigation of the effect of building conditions to the process.
- Raw materials characterisation, including powder particle shape and size distribution, flowability, sustainability and their effects to the final parts quality.
- Heat transfer model inputs characterisation, such as defining and measuring and the material properties, input loads and boundary conditions.
- Establishment of a Finite Element model of moving heat source.
- Adding states variable material properties to the heat transfer model.
- Establishment of multi-layers heat transfer model.
- Validation of heat transfer modelling work using relative experiments.

- Microstructure prediction based on the knowledge of main process control parameters and results from heat transfer modelling work.

1.3 Research Methodology

The research is comprised of an experiment and a finite element modelling part.

Experimentation was carried out to understand the effect of each processing control parameters on the final part quality, and to characterise the model inputs. Laser energy input, build conditions and powder bed properties were investigated. Samples were built and tested to gain the knowledge of the relationship between samples' density and mechanical properties and each process control factor. For laser energy input parameters, laser energy output, scanning strategy and building direction were studied. Build condition investigation includes oxidation control, gas flow in the process chamber and pre-heating study. The powder bed properties study characterises the raw material, which includes chemical composition, particle shape and size distribution, flowability and sustainability examinations. Heat transfer model inputs characterisation, such as defining and measuring the material properties, input loads and boundary conditions were investigated via experiment.

For the predictive modelling of microstructure, a methodology for predicting the temperature distribution history and temperature gradient history during the SLM process has been developed. Moving heat source and states variable material properties were studied and applied to the heat transfer model for reliable prediction. A Multi-layers model was established to simulate the layer by layer process principles. Microstructure was predicted by simulated melting pool behaviour and the history of three dimensional temperature distribution and temperature gradient distribution. These results were validated by relevant experiment examination and measurement.

1.4 Research Novelty

Previous work in the SLM field has focused on the part quality and microstructure control by optimising the laser energy input. This research studies not only the laser energy input, but also raw material properties' effect on the SLM build quality. Raw material properties are also taken into thermal modelling work for the temperature and microstructure prediction. This research involves a multi-layer heat transfer modelling work to give three dimensional temperature history predictions, while most previous models did not include this layer by layer manner. The results from the model are used for predicting the melt pool behaviour during the SLM process and the microstructure of SLM parts.

1.5 Thesis Structure

Each aspect of this research is described in detail and results are discussed in the remaining chapters of this thesis. A brief description of the contents is given below, with the main structure shown in Figure 1-1.

Chapter 2 Literature Review provides a review of the literature to validate the relevance of this research. Some of the basic concepts of additive manufacturing process are introduced in the chapter. Previous studies on process control parameters and working principles of SLM are reviewed. Laser manufacturing relevant heat transfer models are studied. The gap of knowledge based on the literature review is identified.

Chapter 3 Experimental Research Methods introduces the research methods for the experiments in this research. The main equipment is introduced at the beginning, followed by SLM process optimisation, raw material characterisation and model inputs identification methods. Microstructure examination methods are presented at the end.

Chapter 4 Finite Element Modelling Methods introduces the research methods on simulation establishment. Geometry used in the model, meshing method, boundary condition selection are discussed, as well as the methods on applying the moving heat source, states variable material properties and multi-layers to the model.

Chapter 5 Results & Discussions – SLM Process Control Parameters studies the effect of laser energy input strategy and building conditions in the SLM process on the final built part quality.

Chapter 6 Results & Discussions – Raw Material Characterisation characterises the powder's chemical and physical properties, such as shape, size distribution, flowability, etc. Two samples with different particle size distribution are used in the research. Effects of different particle size distribution on processing parameters optimisation and powder sustainability are investigated.

Chapter 7 Results & Discussions – Model Inputs Characterisation describes the measurement and calculation of the main heat transfer model inputs, which including input heat source, base material properties and boundary conditions.

Chapter 8 Results & Discussions – Heat Transfer Model Establishment provides the main work on the heat transfer model establishment – the procedure of applying moving heat source, states variable material properties and boundary conditions into the simulation. This chapter also presents the multi-layers model establishment procedure and discusses the results from simulation.

Chapter 9 Results & Discussions – Microstructure Prediction and Validation focuses on the microstructure prediction using the results obtained from previous chapter, and the validation through experiment examinations.

Chapter 10 Discussions discusses the experimental and the modelling results presented in previous chapters and their connections.

Chapter 11 Conclusions and Future Work presents the main conclusions from the research, along with the suggested future work.

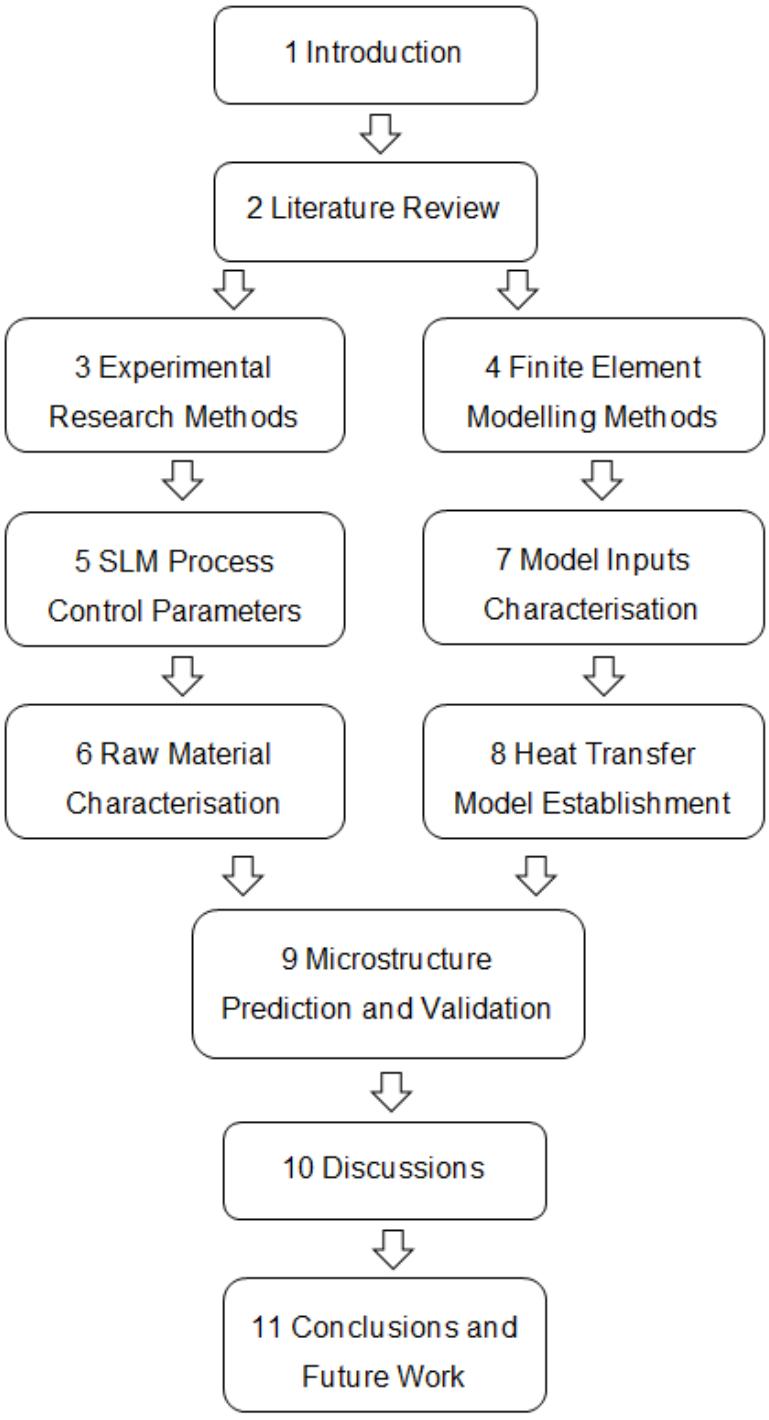

Figure 1-1 Main thesis structure

2 Literature Review

2.1 Additive Manufacturing

Additive Manufacturing (AM) is a group of manufacturing technologies which are capable of producing 3D solid parts by adding successive layers of material. Parts are fabricated in an additive manner, layer by layer; and the geometric data can be taken from a CAD model directly [3, 4, and 9]. The main revolutionary aspect of AM is the ability of quickly producing complex geometries without the need of tooling, allowing for greater design freedom [5]. The other advantages include the reduction in manufacturing steps and use of materials; therefore causing reduction in fabricating cost. Additive Manufacturing is also referred to as Solid Freeform Fabrication (SFF) [10], Layered Manufacturing (LM) [11], and e-Manufacturing [12].

Additive Manufacturing can go back to the late 1980's, early 1990's [13, 14]. In 1991, CIRP's STC-E devoted a first keynote paper on a survey of additive manufacturing, which surveys one decade of innovation in AM [13]. Although most processes were already known in 1991, most of them were still in a pre-commercial stage, with some of them reaching the commercialisation stage painfully [15]. The first successful process, Stereolithography from 3D systems, came out in 1991. Followed by other companies, there is a clear breakthrough in 1994 in AM at which time machine sales took off exponentially [15]. Many AM techniques existing today can process materials such as polymers, metals, ceramics and composites. The bonding of material can be achieved by different physical and chemical methods.

2.1.1 Classification

The classification of AM technologies can be based on the raw material used in the process [16], which divides these technologies into three different categories: Liquid-based processes, Powder-based processes and Solid-based processes. Figure 2-1 shows a family tree of AM technologies. It may not cover all current technologies, but it shows the categorisation of major AM techniques.

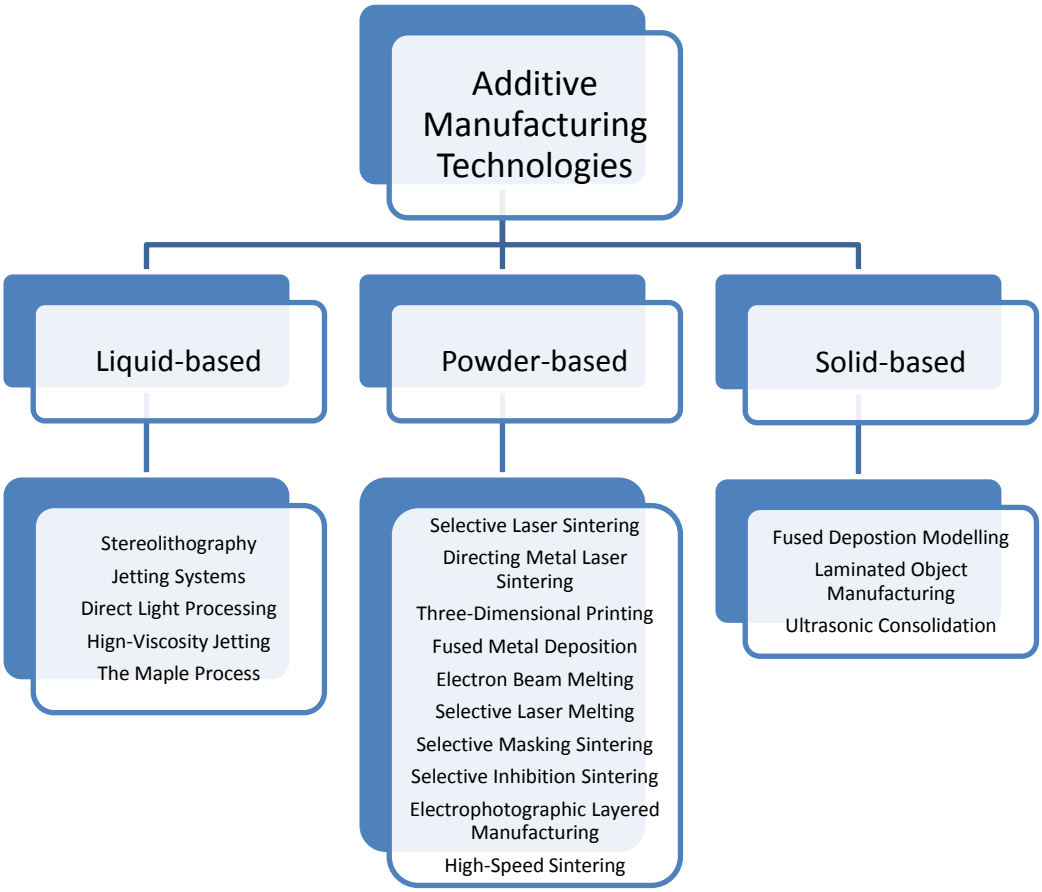

Figure 2-1 Family tree of Additive Manufacturing Technologies [16]

2.1.2 Liquid-based processes

Most Liquid-based AM systems form solid parts by selectively curing regions of photosensitive polymers using a particular wavelength of light. The light source can be either a scanning laser beam or a wide area light source. Photocurable resins which can achieve stable properties over time and in different environments are widely used in Liquid-based additive manufacturing technologies [16].

Stereolithography (SLA) system, released by 3D systems in 1987, is widely considered to be the founding process within the field of AM [17]. The stereolithography process uses an ultraviolet (UV) laser to cure a photocurable resin. Parts can be built from a CAD model and the whole process can be controlled by the machine's software, including automatically generating the supports.

2.1.3 Solid-based processes

AM processes which use solid raw materials in non-powder form have been an integral part of the AM industry since early 1990s [16]. They are still developed and improved by both the suppliers and academic institutions today.

Fused Deposition Modelling (FDM) was commercialised by Stratasys Inc. in 1991 [8, 18]. In this process, solid wire-shaped materials are heated to a semi-molten consistency before depositing using single or multi nozzle systems. The nozzle systems traverse in X and Y direction to create a two-dimensional layer. FDM can process materials such as polycarbonate, polyphenylsulfone and acrylonitrile butadiene styrene (ABS). This process can build solid parts with little waste, but the size of the extrusion limits the size that any features smaller than double the track width cannot be produced [18].

Ultrasonic Consolidation (UC) is also a solid-based technology developed by Solidica Inc. in 2002 [19]. It combines the ultrasonic welding of metal foils and additive manufacturing techniques to produce solid parts. The process applies sonic oscillations to metal foil under an applied load. The oscillation bonds the thin metal foil together with a very low heat. This process is capable to process a range of metals such as Iron, Copper, Nickel and dissimilar combinations like Al/Stainless steel and Al/Ni [20].

2.1.4 Powder-based processes

Powder-based additive manufacturing technologies offer a wide range of material possibilities such as polymers, metals and ceramics. Parts can be built with similar material properties and stability compared with solid material. These technologies can be divided into two main types: powder feed deposition and powder bed deposition.

Based on powder feed deposition, a number of processes have been developed, such as **Three-Dimensional Laser Cladding (3D LC)** which is also called Laser Engineered Net Shaping (LENS) [21]. In the process, the powder is delivered in a gas jet through nozzles, coaxially with the laser beam. The powder in the melt pool created by the laser can form a cladding line and then cool to form a solid structure when the laser moves away. It is important to melt the powders and homogenise the melt pool for successful building [4]. Fully dense parts can be achieved by this technique [22-24].

Three-Dimensional Printing (3DP) developed at MIT is the basis of a number of technologies that use the application of a binder to a powder layer to construct parts [16-18, 25]. In the process, a thin powder layer is selectively bonded by ink-jet droplets of adhesive binder. A range of materials can be used in this technique, including metals. But the parts fabricated by this technique usually have high surface roughness and need further post processing operations to obtain final properties [26, 27].

Selective Laser Sintering (SLS) is an important additive manufacturing technique widely used today, which is referred to as powder bed deposition. It was first invented in 1979 by Ross Householder, and commercialised in the late 1980s by the University of Texas at Austin, when the first machine came out in 1992 developed by DTM Corporation [28-30]. The process is in many ways similar to Stereolithography; but is capable of processing a variety of materials including polymers, metals and ceramics. The powdered raw material is sintered or partially melted by a laser which selectively scans the surface of the powder bed to create a two-dimensional solid shape, and then a fresh layer of powder is added to the top of the bed to form another solid layer which can be traced by the laser bonding it to the layer below. It is basically a one-step process and you can get the final parts directly from a CAD model. To minimise the required laser output energy and to reduce thermal stresses, the powder is normally maintained at an elevated temperature, just below its fusing point [28-32]. To avoid oxidation problem during the process, it usually operates in an inert protect gas environment [18].

Electron Beam Melting (EBM) is a process very similar to SLS but replaces the laser with an electron beam. It was developed by Arcam in Gothenburg Sweden in 1997 [33].The electron beam is stationary and there is no need for scanning mirrors as the beam can be directed by changing an electromagnetic field, which allows for high scanning speed and fast build rates [34]. The technique offers the ability to fully melt a wide range of metal powders due to the high power developed by the electron beam. However the process is limited to conductive materials and surfaces [16].

Selective Laser Melting (SLM) is also a process very similar to SLS, but it uses a higher energy density to enable full melting of the powder. This technique is capable of building fine details such as thin vertical walls, complex lattice structures and fine cylindrical struts [35, 36]. SLM is capable of processing many standard metal materials like Stainless Steel, Inconel, Titanium alloys and Aluminium alloys [16, 25]. Due to the high temperature involved in processing metals, the use of a protecting gas is important to avoid oxidation. It can also enhance the wet-ability of the molten material and

reduce the porosity caused by oxidation [37]. However, due to full melting process and high temperature, there can be big thermal stresses and large shrinkage after solidification, which need to be improved.

2.2 Direct Metal Laser Fabrication

Direct Metal Laser Fabrication (DMLF) is a group of laser based additive manufacturing technologies for producing metal components. The laser beam is delivered to the surface of the material, and the heat generated by the laser causes the material to sinter or completely melt. When the laser beam moves away, the material can be cooled and forms solid parts. The material type can be in powder or wire form, and the laser types and material deposition methodology can vary [4]. Due to the accuracy, stability and versatility of the laser beam, DMLF processes are capable of building end-use parts with acceptable accuracy and resolution just in one step. Also, these technologies can fabricate parts with improved mechanical properties compared to the conventionally processed, such as casting and forging [38, 39].

2.2.1 Laser scanning systems

DMLF processes can vary due to system configuration. The type of laser used within the system is a significant factor that greatly affects the capabilities of the system. With the continuous development of laser technology, many kinds of lasers have been used in laser direct manufacturing. Commercial sintering and melting machines have used Carbon Dioxide (CO_2), Neodymium-doped Yttrium Aluminium Garnet (Nd:YAG) and Ytterbium (Yb) fibre lasers. The main difference between these lasers is their wavelength. CO_2 lasers have a wavelength of 10.6μm while Nd:YAG and Yb fibre lasers have wavelengths in the range of 1.06 to 1.1μm.

As a gas laser, CO_2 lasers are one of the highest-power continuous wave lasers that are currently available. It is also quite efficient: the ratio of output power to pump power can be as large as 20% [40]. Nd:YAG lasers are solid-state lasers, which can operate in both pulsed and continuous mode. Pulsed Nd:YAG lasers are typically operated in the so called Q-switching mode, which can generate high intensity [41]. Yb fibre lasers are capable of producing several-kilowatt of continuous power, having 70-80% optical-to-optical and up to 25% electrical-to-optical efficiency [42]. The advantage of the fibre laser is that the light can be coupled into the flexible fibre and can be delivered to a movable focusing element with high output power and high optical quality [43].

The Gaussian distribution is the most widely adopted model for laser intensity distribution, which utilises the symmetrical distribution to describe laser intensity across the laser beam [44]. It assumes that in most cases the maximum laser intensity is at the centre of the beam. Figure 2-2 shows three different Transverse Electromagnetic Mode (TEM) radial intensity distributions. The TEM_{00} profile is the one suited for laser machining due to high energy concentration in the central area and also the energy is gradually emitted from the centre, which delivers enough and smooth energy to the substrate [45].

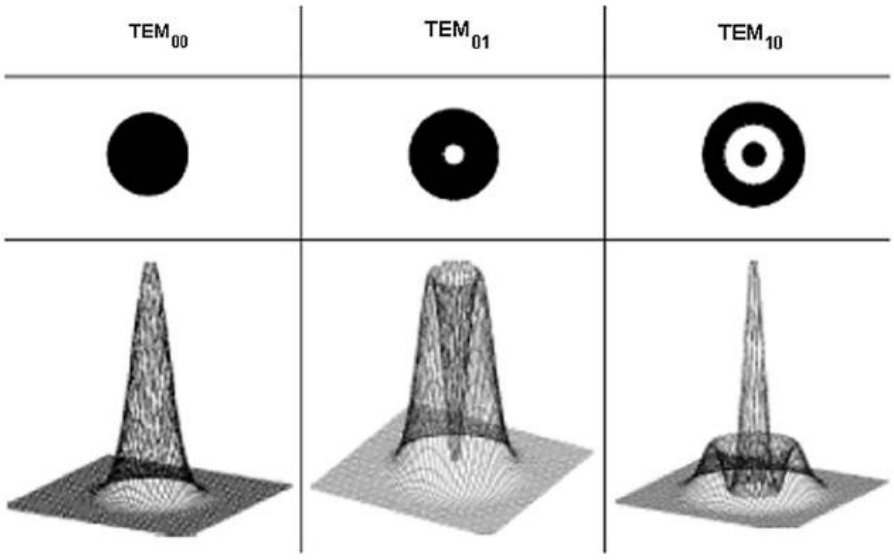

Figure 2-2 Gaussian beam mode profiles [46]

Based on the Gaussian function, the corresponding time-averaged intensity distribution can be given by Equation (2.1) [44].

$$I(r,z) = \frac{|E(r,z)|^2}{2\eta} = I_0 \left(\frac{w_0}{w(z)}\right)^2 \exp\left(\frac{-2r^2}{w^2(z)}\right) \quad (2.1)$$

where *r* is the radial distance from the centre axis of the beam, *z* is the axial distance from the beam's narrowest point (the "waist"), $I_0 = I(0,0)$ is the intensity at the centre of the beam at its waist, w(*z*) is the radius at which the field amplitude and intensity drop to 1/*e* and 1/e^2 of their axial values respectively, and w_0 = *w*(0) is the waist size. The constant is the characteristic impedance of the medium in which the beam is propagating, and for free space, $\eta = \eta_0 \approx 377\Omega$.

For a Gaussian beam of wavelength λ at a distance z along the beam from the beam waist, the variation of the spot size w(z), can be given by Equation (2.2).

$$w(z) = w_0\sqrt{1 + \left(\frac{z}{z_R}\right)^2} \quad (2.2)$$

Where z_R is the distance along the propagation direction of the laser beam from the waist to the place where the area of the cross section is doubled, and is called the Rayleigh range [47], given by Equation (2.3). The distance b between two Rayleigh range points is the depth of focus of the beam, where $b=2z_R$.

$$z_R = \frac{\pi w_0^2}{\lambda} \quad (2.3)$$

The waist size, which is the minimum spot diameter to a Gaussian beam, can be given by Equation (2.4) [48].

$$w_0 = \frac{4M^2 f_1 \lambda}{\pi D_1} \quad (2.4)$$

Where M^2 is the beam propagation factor, f_1 is the focal length of the lens, λ is the laser wavelength and D_1 is the beam diameter at the lens. Figure 2-3 shows these beam parameters stated above.

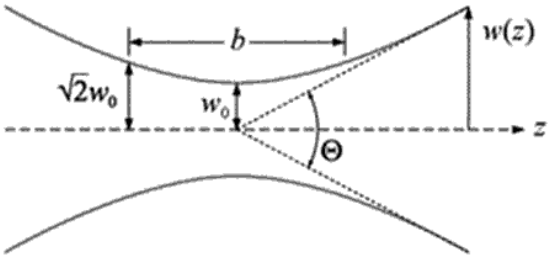

Figure 2-3 Gaussian beam parameters after focusing [49]

The power P passing through a circle of radius r in the transverse plane at position z can be given by Equation (2.5) [44].

$$P(r,z) = P_0\left[1 - e^{-2r^2/w^2(z)}\right] \tag{2.5}$$

where P_0 is the total power transmitted by the beam, given by Equation (2.6) [44].

$$P_{0=}\frac{1}{2}\pi I_0 w_0^2 \tag{2.6}$$

Similarly combining these two functions can find that about 95% of the beam's power will flow through a circle of radius r=1.224w(z) [50].

The peak intensity at an axial distance can be calculated using L'Hôpital's rule, given by Equation (2.7), which is twice the average intensity [49].

$$I(0,z) = \lim_{r\to 0}\frac{P_0\left[1-e^{-2r^2/w^2(z)}\right]}{\pi r^2} = \frac{2P_0}{\pi w^2(z)} \tag{2.7}$$

A whole laser scanning system usually has several optical components. A beam expander is often used where the beam path is long or the laser produces such a small beam diameter which is very difficult to focus without

having the focal lens close to the work piece. Different types of reflecting mirrors are used to direct the laser beam in the X and Y axis. A focal lens is used to focus the laser beam where the minimum spot size can be on the surface of the building platform.

2.2.2 Laser-Material interactions

Laser light is a form of energy or electromagnetic radiation generated by Light Amplification Stimulated by Emission of Radiation (LASER). It can also be considered as moving particles with very high energy values. The process of melting using a laser begins by converting the laser's photons into kinetic energy [51]. The photons can excite electrons which are in the outmost shell of surface atoms of the target material, including the release and excitation of conduction electrons. This energy transfer usually takes a very short time, about 1ps in metals [52]; so it is revealed as rapid heating or thermalisation. The heat generated by the laser will travel through the target material by thermal conduction, and can completely liquefy the material to form a melt pool.

When the laser transfers energy to a material, the energy cannot be fully absorbed by the material. The absorption of a material is defined as the ratio of the absorbed radiation to the incident radiation [53]. The value of the absorption coefficient will vary with the same effects that affect the reflectivity. For most materials,

$$\text{Reflectivity} = 1 - \text{absorptivity} - \text{transmission} \quad [54] \qquad (2.8)$$

In actual processes, the energy loss contains radiation, convection with the surrounding atmosphere and expulsion of materials [55]. However, the main loss of the laser energy is reflection [54].

In general, the absorption depends on the laser wavelength, the nature of the material, surface geometry, surrounding gas and temperature, etc. [56-59] It is

believed that at longer wavelengths metallic materials generally have an increased reflectivity and consequently the laser processing of metals is more difficult, so it is preferable to process metals using lasers with shorter wavelengths as the metal can absorb more energy from the laser [60]. This is because of resonance and scattering effects of the laser wavelength [61].

Unlike an opaque continuous medium, the powder bed allows a certain penetration of the light energy of the laser beam through gaps between particles and mutiple reflection into particles. This penetration allows more laser energy absorption into the powder bed rather than a continuous medium. In order to describe how the energy will be absorbed in depth, an "energy penetration" parameter was introduced [62]. Table 2-1 shows the absorption of some typical powder materials at different wavelengths.

Material	λ= 1.06μm	λ= 10.6μm
Cu	59%	26%
Fe	64%	45%
Sn	66%	23%
Ti	77%	59%
Ni-alloy	64%	42%
$NaNO_3$	16%	80%
NaCl	17%	60%

Table 2-1 Absorption of powder materials at different wavelength [62]

2.2.3 Binding mechanisms

There are many ways to consolidate metal powder material pre-deposited on a building platform with a laser. Classification of laser based powder

consolidation mechanisms can be based on the powder material state, which divides these ways into three different categories: Solid State Sintering, Liquid Phase Sintering/Partial Melting and Full Melting [63].

Solid State Sintering is a consolidation process occurring below the material's melting temperature. This binding creates "necks" between powder particles without the presence of a liquid phase at the contact areas [64, 65]. This method is rarely used in additive manufacturing as diffusion of atoms is very slow and not compatible with the desired high laser scanning speed which will increase the process productivity and economic feasibility [63].

Liquid Phase Sintering and Partial Melting include many binding mechanisms in which part of the powder material with low melting temperature is melted while the remaining material with a higher melting temperature remains solid. There is a limited degree of rearrangement of the solid particles due to the short interaction time; so that the metal part produced directly using partial melting will contain a high level of porosity [8]. It may need post-processing operations in order to reduce the part porosity and improve mechanical properties.

Full melting is a consolidation mechanism which is capable of producing fully dense parts without the need of any post-processing. It can achieve this by completely melting the powder particles with the use of high laser energy densities. However, due to the high temperature gradients and densification ratio during the process, high internal thermal stresses can be generated [66, 67]. Also, balling and dross formation from the melt powder materials in the melt pool may result in poor surface finish [63]. Explanation on the balling effect can be found in section 2.3.3.

2.3 Selective Laser Melting

Selective Laser Melting (SLM) is a powder bed process which is very similar to Selective Laser Sintering (SLS), but uses a different laser energy density

to enable full melting of the powder; a schematic of the process is shown in Figure 2-4. Theoretically the fabricated parts can exhibit full or near-full density without any post processing work such as heat treatment or infiltration of finished components required [6].

SLM can process standard metal powder materials like stainless steel, Inconel, titanium alloys and aluminium alloys. These powders are processed directly without the addition of a binder. The ability to fabricate parts using single type of metal powder material is one of the biggest advantages of SLM [68]. Recently, it has been found that SLM can also build from mixture powder [8].

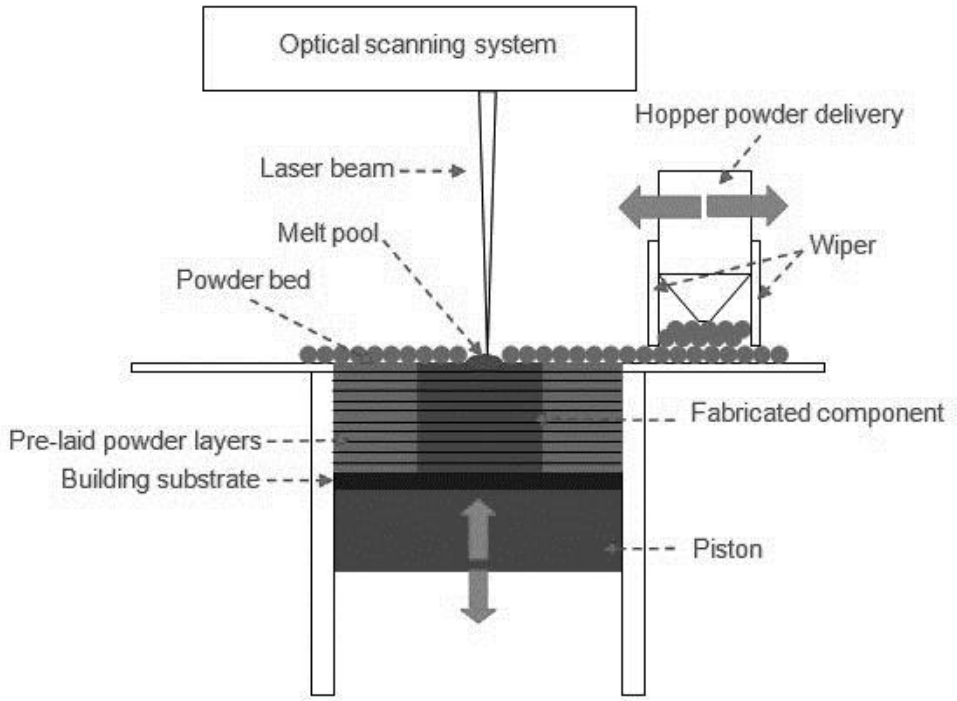

Figure 2-4 Schematic of the Selective Laser Melting process

2.3.1 Process control factors

The SLM control factors which influence part physical and mechanical properties include laser energy input strategy, raw material properties, powder bed properties, building strategy and atmosphere [69]. Previous

studies performed using SLM have shown that important part features such as porosity, surface roughness, geometry, parts dimensional accuracy and microstructure are strongly dependent on the system's laser processing parameters such as laser power, scanning speed, layer thickness, scan overlap, etc. [70-72]

Some factors in the process are controllable, while some not. Table 2-2 shows the main SLM control parameters classified by controllability and also different control parts in the process.

Control Systems	**Variable Parameters**	**Non-variable Parameters**
Optical scanning system	Laser power Laser focus position Beam energy intensity	Laser efficiency Laser beam profile Focal lens properties
Process scanning strategy	Scanning speed Hatch distance Layer thickness Scanning direction Re-melting scan	
Processing environment	Gas flow Pre-heating Building substrate thickness Inert gas	
Raw material & powder bed	Particle shape Particle size distribution Powder flowability Density of the powder bed	Chemical compositions Laser energy absorption

Table 2-2 Main SLM process control factors

2.3.2 Optical scanning system

Optical scanning systems used in SLM today for processing metals usually contains a short pulse or continuous wave of laser energy, a beam expander, a dual axis scanning mirror system and a F-Theta focal length lens. The use of F-theta lens can provide a flat field at the image plane of scan, delivering the laser energy uniformly throughout the powder bed, shown in Figure 2-5. The development of F-Theta lens covers a wider spectral range of laser and provides a larger working area, which increases the efficiency of laser material processing techniques [73].

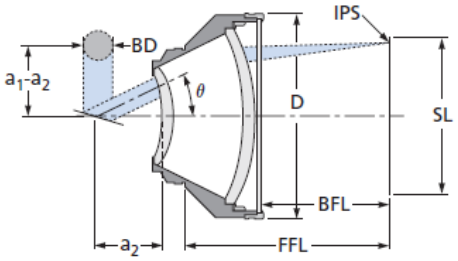

EFL	Effective Focal Length
BFL	Back Focal Length
SL	Scan Length
BD	Input Beam Diameter
IPS	Input Spot Size
D	Assembly Diameter
FFL	Flange Focal Length
θ	Scan Angle (±)

Figure 2-5 Working principle of F-theta lens [74]

The main feature of a continuous wave laser is it has a continuous laser output due to the continuous excitation of the reactive medium where the energy output is theoretically constant. In this case, the powder bed can receive a continuous stable energy input and be heated and melt continuously [75]. However, in some SLM processes, laser energy is emitted in a pulse mode by setting the exposure time and the distance between exposures. This method of laser energy delivery is carried out such that heat build-up and melt pool width is minimised [69].

In SLM processes, laser energy density, E_ρ, is a key factor that affects the final part's quality. Laser energy density is defined by the incident laser power P (W), laser scanning speed u (mm/s) and laser beam spot size on the powder bed ð (mm), given by Equation (2.9) [3].

$$E_\rho = \frac{P}{u\delta}\ (J/mm^2) \tag{2.9}$$

The process parameters, laser power and scanning speed can be controlled during the process through machine control software. Laser beam spot size on the powder bed can also be controlled by adjusting the lens position or the distance between lenses in the beam expander. In some systems, beam offset is used to compensate for the laser beam focal diameter at the boundaries of the scanned section [68].

2.3.3 Process scanning strategy

In SLM processes, the input process parameters can be controlled and varied to achieve the resultant parts. Many previous input parameter control works have been carried out to improve the material properties such as density, surface finish, accuracy and mechanical properties. These machine controllable input parameters include laser exposure time and point distance, powder layer thickness, hatch type, hatch distance, beam offset, and other strategies. Table 2-3 and Figure 2-6 show the description of some brief parameters.

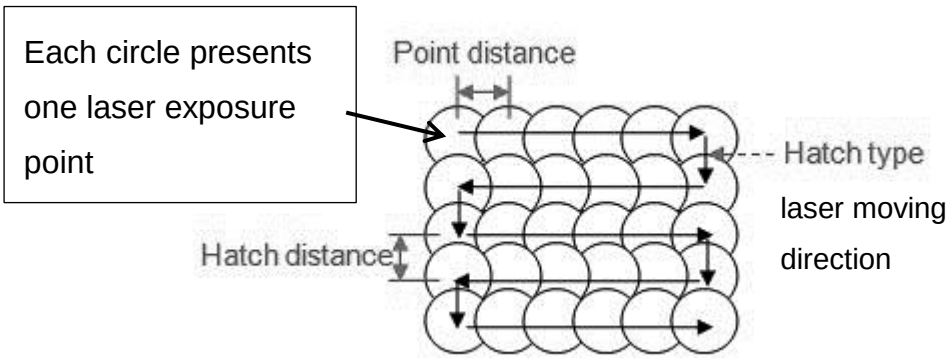

Figure 2-6 Schematic of some input process parameters

Input Parameters	Description
Exposure time	Determines the time of laser exposure into each point.
Point distance	Each hatch line is divided into a series of points, point centres are separated by the point distance.
Scanning speed	Defines the speed of the scanning laser movement.
Layer thickness	Specifies the layer incremental distance during process.
Hatch type	Controls the scanning strategy, such as scanning direction, re-melting scan, chessboard scan, etc.
Hatch distance	Controls the distance between two adjacent lines of the scan.

Table 2-3 Input process parameters of SLM

A characteristic of the SLM process is the combination of exposure time and point distance, which is used to define the scanning speed of the laser beam:

$$scanning\ speed = \frac{pointdistance\ (\mu m)}{exposuretime\ (\mu s)} \tag{2.10}$$

Scanning speed is a main factor than can affect the laser energy density. It must be mentioned that a range of laser powers and scanning speeds can produce the same energy density. However, the effect on the powder can be variable as some significant effect factors such as radiation and absorption can be different [4]. Hatch distance also affects the laser energy density.

The main aim of controlling the energy density is to make sure the heat absorbed by the powder is enough for producing dense parts without over-

heating. High energy density can cause the surface powder to begin to vaporise before a significant depth of molten material is achieved. It can also cause deformation of the parts due to high thermal stresses. Reducing the energy density can be achieved by reducing the laser power, increasing the scanning speed and increasing the hatch distance. The melt powder layer thickness decreases with increasing the scanning speed due to the shorter interaction time, this thickness also decreases with increasing hatch distance [4, 76].

Controlling the process parameters needs to consider the wet-ability for avoiding balling phenomenon. Balling is when melting is induced by the laser beam, the molten powder quickly consolidates into spheres of diameter approximately equal to the diameter of the laser beam, rather than consolidating into the previous layer. Previous work showed that the spherical structure increased with decreasing the scanning speed and increasing the laser power [77-79]. Recent investigation indicated that the scanning speed is the main factor in determining / avoiding the balling phenomenon [68]. Suitable higher scanning speed can reduce balling, even when the energy densities are the same.

Many scanning strategies can affect the melt pool behaviour and material properties of the parts [80]. A widely used re-melting strategy is used to re-melt the surface of the part to reduce the top surface roughness [70]. It needs a control of the process parameters like scanning speed and input power to ensure the efficient re-melting results.

2.3.4 Process environment

In the SLM process, the gas chamber should be filled with a protecting gas to aid reduced oxidation during the process. Oxygen can react with the molten material causing the surface to oxidise which will affect the final part properties. Oxidation can cause the reduction of molten material wet-ability, which can be a barrier to successful layer fusion and can cause porosity,

balling, delamination and tearing due to surface tension effects [37]. It is stated that the O_2 level within a SLM process should be below at least 0.3% to aid reduction in oxidation [81].

Different types of protect gases can be used to surround the building area such as argon (Ar), nitrogen (N_2), helium (He) or Carbon Dioxide (CO_2). Ar is heavier than air enabling an effective shielding for molten material and greater resistance to cross-draft [82]. N_2 can react and form nitrides with several elements such as Ti, Mn and Cr [83]. N_2 cannot be used in processing carbon steel as it can also react with Fe and C, causing porosity in the part. He is lighter than air making it difficult to protect molten material in powder bed based process. Due to the low price compared with other protect gases; Ar is widely used in commercial SLM systems.

Some academic works believed that pre-heating the building substrate can reduce the surface roughness and improve the part accuracy due to reduced thermal gradients and shrinkage, as less heat input is required by the laser to change the powder from a solid to liquid phase [84-86]. But some research indicated that pre-heating the powder bed does not necessarily improve the part properties as pre-heating only raise the temperature to 100-250°C, while the fully melting temperature of metals is above 1000°C [87]. Pre-heating processes can improve the powder flowability as it reduces the moisture content of the powder, also it can slightly improve spreading behaviour of a melt pool due to reduced temperature variation between solid parts and melt pool [69].

2.3.5 Raw material used in SLM process

Metals powders are the largest group of materials developed for the SLM process today. There has been a number of academic works on SLM to process stainless and tool steel, iron, copper, aluminium and aluminium alloys, nickel alloys, titanium and chromium [70, 88-92]. Most metal powders can be processed to produce fully functional parts directly; however, processing

highly reactive metals such as aluminium may have more processing difficulties. Powder properties such as Particle Size Distribution, density of the powder bed, laser energy absorption, melting temperature, boiling temperature and other thermal properties, should be considered before processing as the characteristics of the powder have a critical effect on the process [93].

With development in the powder fabrication techniques, atomization techniques are widely used in recent years and become the major techniques for fabricating metal powders [94]. Atomization processes involve the formation of powder from molten material using a spray of droplets. It can be classified by the medium used for breaking up the molten material steam, which divided these techniques into three main methods: gas atomization, water atomization and centrifugal atomization. Most commercial used metal powders can be produced by gas atomisation, while some special materials such as hard ceramic materials need to be produced by water atomisation or centrifugal atomisation [94]. Gas atomized metal powders can have acceptable packing properties and flowability, and exhibit apparent and tapping densities in the 60-65% of theoretical range (bulk material) [94].

Particle size distribution is a key factor in powder characterisation. It has a significant effect on powder bed density and fluidity. It also affects the density and surface roughness of the parts, layer thickness determination and energy input determination. Having a wide range of particle sizes can result in a higher packing density as the smaller size particles can fill the gaps in between larger particles. A wide range of particle sizes may conversely lead to increased porosity as larger particles could melt or partially melt while smaller particles may vaporise [71]. Previous research believed that using a particle size range of 20-50μm can meet the basic acceptance when producing fully functional high density metal parts [87, 95, 96].

Use of smaller powder requires less heat input for melting. The efficiency of the laser reduces if the particle size becomes smaller as absorption becomes smaller. In general, the smaller particle size can form parts with higher

surface quality both on the top and side of a part as the stair stepping effect is reduced due to the ability of depositing thinner layers [4, 18, 97]. Also, by using smaller particles and layer thickness, the beam diameter can be reduced as it has a shorter distance to diverge [98]. So it can improve the part accuracy as the shrinkage and the width of melt area difference between the bottom and top of each layer is smaller [99].

2.3.6 Powder flowability

During the SLM process, the powder layer should be spread uniformly by the wiper. Therefore the powder flowability is a main powder characteristic which can affect the melting process, particle distribution on the powder bed, laser energy absorption and laser-powder interaction. The flowability can be significantly affected by powder particle size distribution, particle morphology and inter-particle friction [94]. It is believed that spherical particles with smooth surfaces and a uniform size move more easily within the powder system and tend to create a uniform bed density. The high flowability occurs when the powder contains a narrow particle size range. However, maximum powder bed density occurs when the powder contains a mixture of different sized particles. Therefore, for optimum SLM processing, a fine balance between these two is required [68]. Particles with a perfectly round shape flow smoothly as the flow motion is not hindered by angle contacts [87]. Also the smooth surfaces reduce the inter-particle friction.

Moisture can also affect the flowability of the powder. It is important to store the powder in a dry place to avoid moisture. Pre-heating the substrate can also help to reduce the moisture during the process.

2.3.7 Effect of chemical elements

Few metals are used in their pure state. They always have other elements added to them for turning them into alloys and giving them better mechanical properties. The alloying elements usually dissolve in the basic metal to form solid solution, and the solubility can vary depending on different elements [100]. These elements can influence the bonding mechanism and finally microstructure of the alloy.

In the SLM process, dissolved elements can cause solidification problem such as delamination and solidification cracks due to its significant effect on the material convection in melt pool [8]. Also the difference on melting temperature of each element and inter-reaction between them can result in the formation of a heterogeneous microstructure. Some elements may have high reflectivity of the laser beam and cause a negative effect on densification, while some elements can affect melt pool behaviour causing porosity and high roughness on the top surface [8].

2.3.8 Laser energy absorption

In the SLM process, the energy or heat input depends both on the laser energy density incident on the work material surface and the energy absorption. The study of whole process laser energy absorption is important for obtaining a more uniform and reproducible laser melting process.

Unlike fully dense materials, only part of the incident radiation is absorbed by the outer surface of the particles in a loose powder. As the laser is a light source, the incident radiation can penetrate through the inter-particle pores to be absorbed by the underlying particles. So powder materials exhibit a higher absorption than the same bulk material. It must be remembered that the powder structure changes with exposure, so the energy absorption will change with time during the process [53]. Due to phase changes of the metal powders from solid to liquid, the density of free electrons in liquid is higher

than that in solid according to the decrease of Fermi's energy [101]. This can increase the absorption of laser energy as the collision frequency between photons and heat carrier electrons increases which can also cause an increase in conductivity [82, 102].

Previous works have focused on the laser energy absorption measurement on the powder beds. However, during the SLM process, when the metal powders become molten, there is an increase of energy absorption. There may also be a problem when melting material next to previously melted material. The powder melting and consolidation mechanisms happen in a very short time, as well as the area of melting powder under a certain exposure time is difficult to measure and calculate, it is difficult to get the value of the laser energy absorption of the whole process.

2.3.9 Microstructural development

The microstructure of a material, which is the number of presented phases, phase distribution, volume fraction, phase grain shape and size, is essential knowledge as many physical and mechanical properties are structurally sensitive [103].

In the SLM process for metals, solidification conditions such as the cooling rate determine the microstructure of the part produced. After the laser moves away from the melt pool, the highly disordered liquid phase material transfers to an ordered solid phase, accompanied by the release of thermal energy [104]. During solidification processes, crystalline nuclei form and these crystalline regions can grow due to the removal of thermal energy. In the general case of solidification within the bulk of molten metal, few crystalline nuclei form independently at random points. But in the SLM processes, rapid cooling rates reduce the time for nuclei formation and may cause non homogeneous nucleation [104].

Some metals have more than one crystal structure. It is a fact that changing temperature can control the crystal structure effectively. This can change material properties as different crystal structures have different mechanical properties application conditions. For example, at low temperatures, steels which have a face-centred cubic (fcc) structure have much better ductility and toughness than steels which have a body-centred cubic structure (bcc) [100].

The iron rich corner of the C-Fe-Cr-Ni system forms the basis of the wide range of commercial alloy stainless steels. The major solid state transformations involve the allotropic forms of iron, which are ferrite (bcc), α-iron and δ-iron, and austenite (fcc), γ-iron [105]. The binary equilibrium phase diagrams of C-Fe (Carbon-Iron), Fe-Cr (Iron-Chromium) and Fe-Ni (Iron-Nickel) are shown in Figure 2-7 to Figure 2-9.

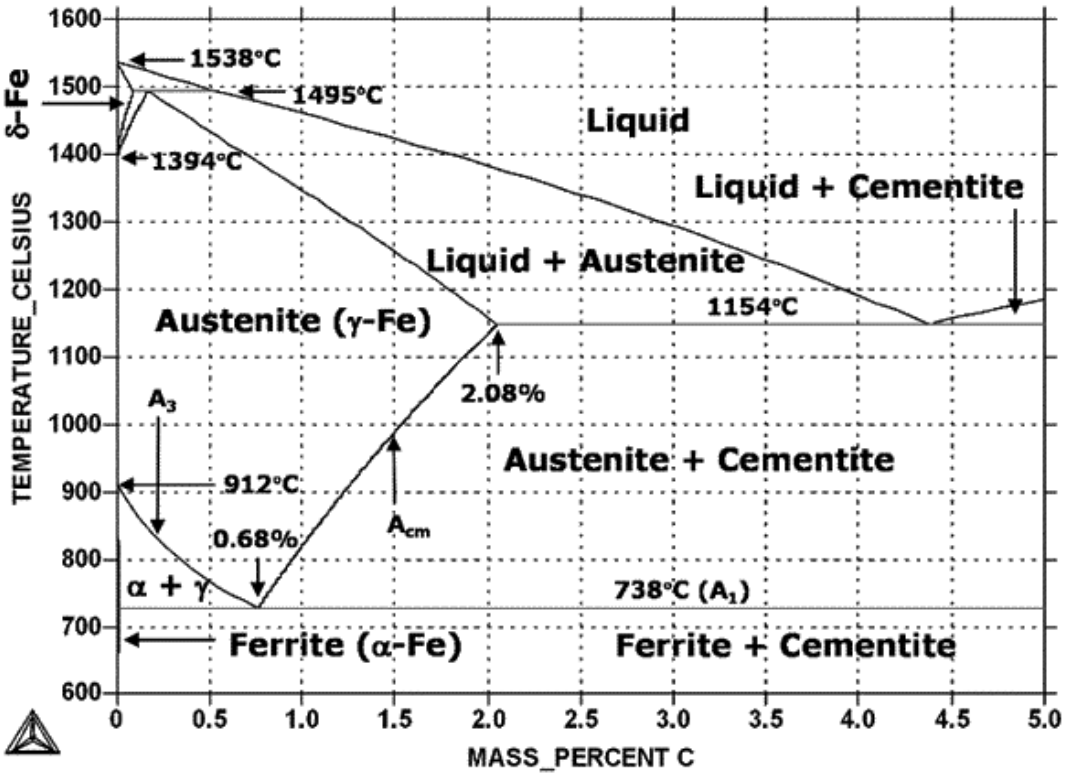

Figure 2-7 C-Fe phase diagram [106]

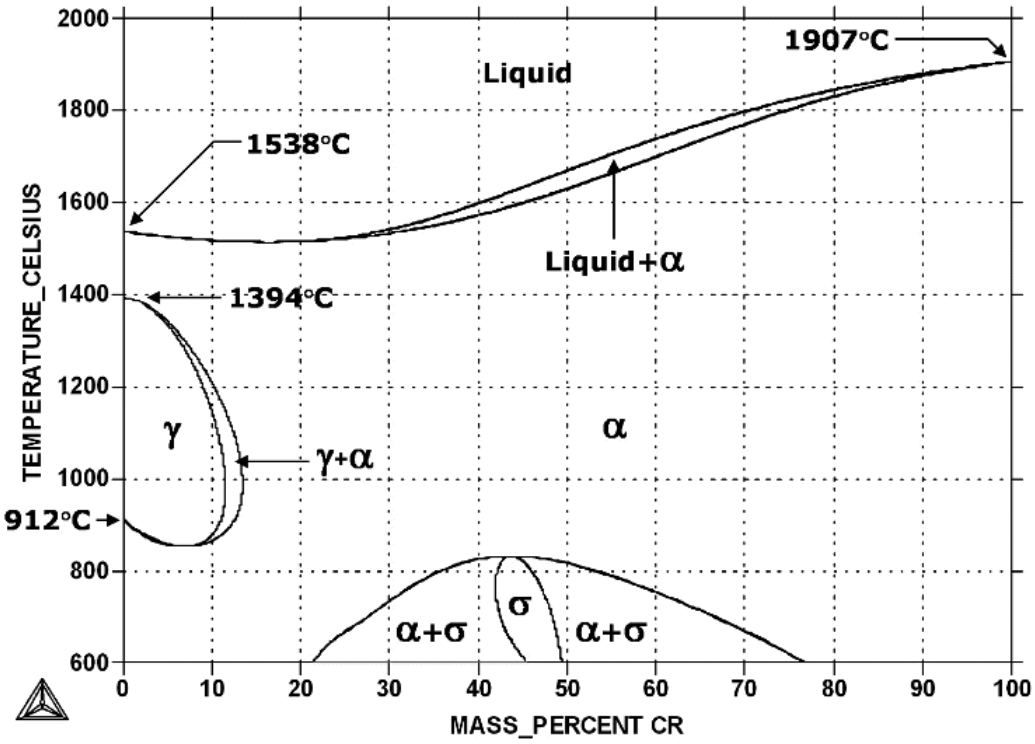

Figure 2-8 Fe-Cr phase diagram [106]

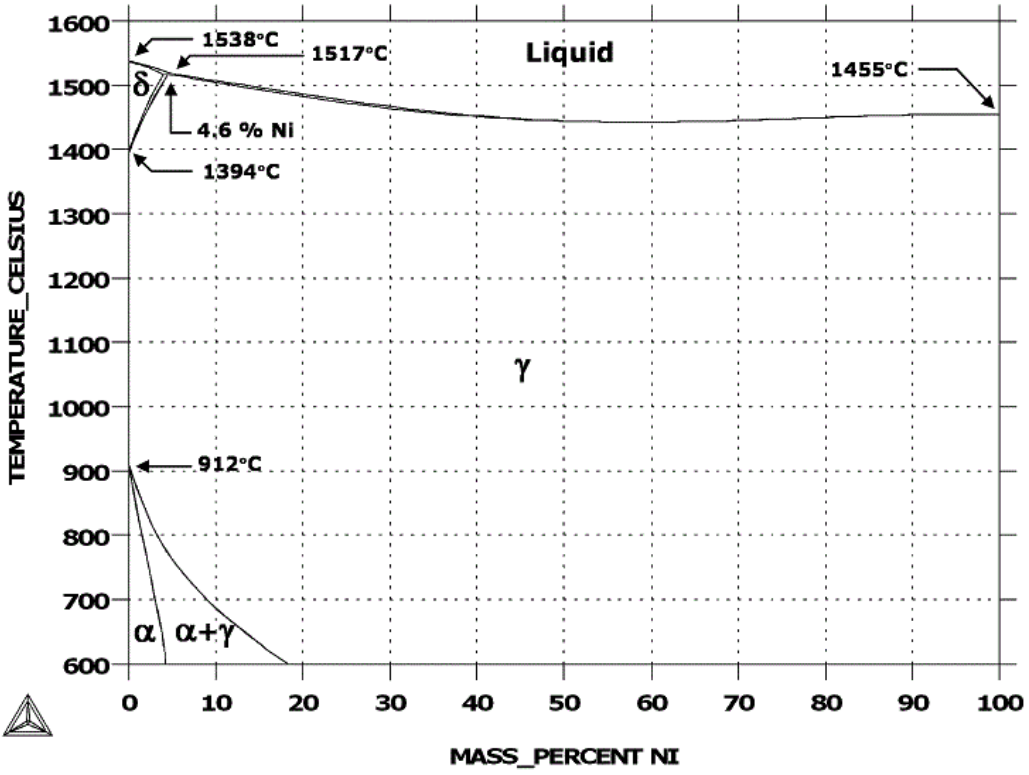

Figure 2-9 Fe-Ni phase diagram [106]

The phase diagrams are used for determining the phase generated under certain temperatures and cooling rates. The binary equilibrium phase diagrams are the most widely used ones which still need further combined analysis to determine the actual phase. A quaternary equilibrium phase diagram for system Fe-Cr-Ni-C was developed by SGTE FactSage, which gives essential information in one diagram, shown in Figure 2-10 [107].

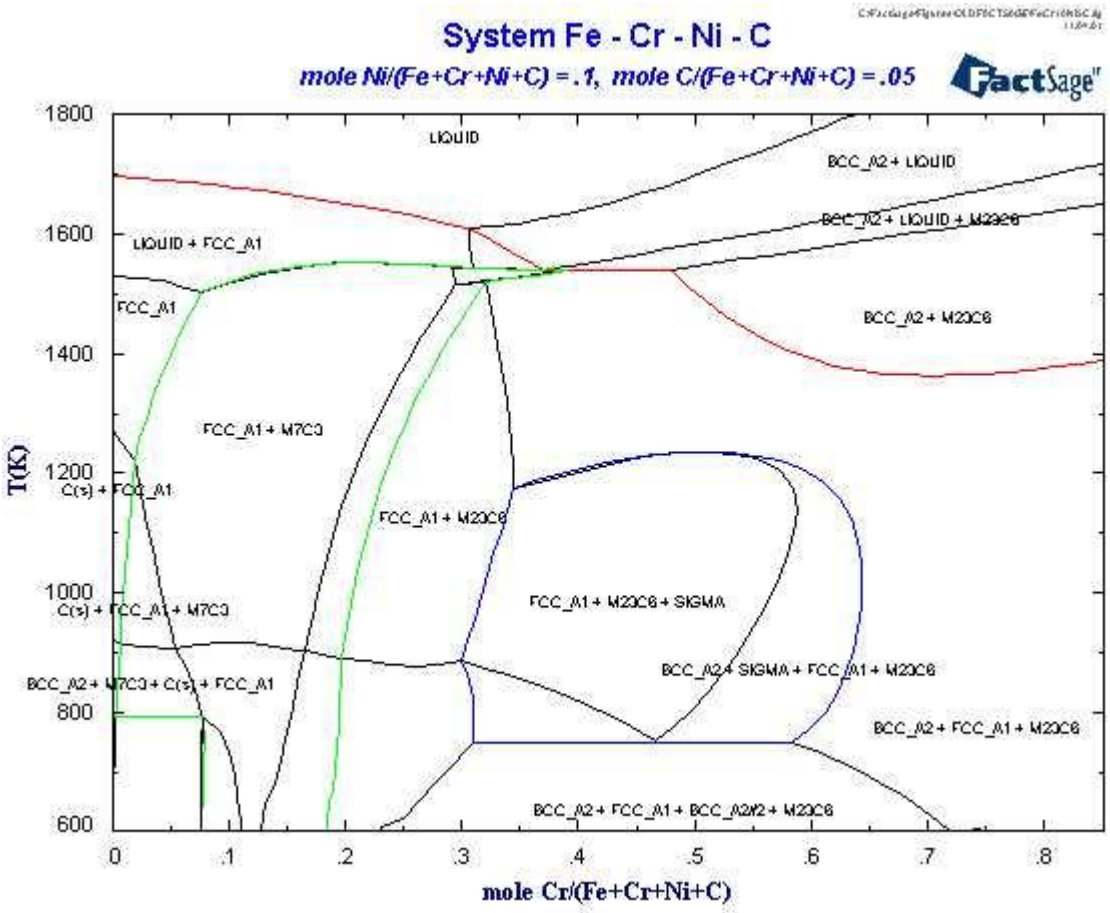

Figure 2-10 Fe-Cr-Ni-C phase diagram [107]

In the SLM process, thermal transport in liquid and solid phases controls the solidification processes, and therefore impacts the microstructure and mechanical properties of the SLM parts [108]. It has been shown that temperature gradient and heat transfer conditions determine the cooling rate, grain growth and the microstructural formation [109]. Therefore, changing the processing parameters in the SLM process would affect the final

microstructure and mechanical properties. Microstructural characterisation was investigated in correlation to the changes of the SLM processing parameters, to quantify the effect of these factors [27, 109-111].

2.4 Heat transfer in the powder bed

2.4.1 Thermal conductivity

Selective Laser Melting techniques require the correct amount of energy at the right place and at the right time to ensure successful processing. The thermal mapping of the process influences the melt pool behaviour and further the microstructure of the parts. Therefore the energy delivery determines the final mechanical properties such as strength, hardness, elongation, impact strength, fatigue behaviour and accuracy. Thermal properties of the raw material such as thermal conductivity and specific heat capacity can be used to explain and evaluate the melt area distribution as well as the underlying solid layer and neighbouring particles that can be melted or re-melted by heat conduction.

Thermal conductivity influences the heat transfer in the SLM process. Usually, the heat flows via conduction down thermal gradients according to Fourier's theory of heat transfer. However, the thermal properties of the powders are not the same as bulk materials as they are not homogenous. The powder's thermal conductivity depends on the number of contacts made between powder particles with more contacts equating to an improved conductivity [69]. It is reported that heat is conducted almost exclusively within the highly conductive particles, to the core of particles [112]. And when the temperature within the particle becomes homogenous, the heat conducts into other conductive particles. The value of thermal conductivity changes significantly with the material phase and temperature. The conductivity of metals generally increases with increasing temperature [113].

On the powder bed, laser radiation can pass through the gaps between particles and generate multiple reflections [112]. Therefore, although the heat conducts away from the centre of laser beam, the powder bed can reduce the temperature gradient further. Heat distribution in the powder bed is shown in Figure 2-11.

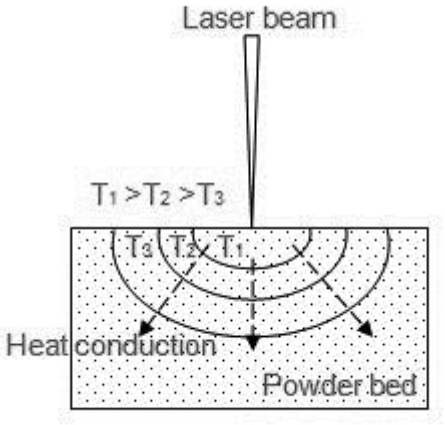

Figure 2-11 Heat distribution in the powder bed

2.4.2 Melting energy

The energy required to melt a particle can be given by Equation (2.11) [101], which is based on the energy required to melt material equation.

$$\Delta H = \rho V_p \left(C_p \Delta T + L_f\right) = \frac{4}{3}\pi\rho r_p^3 E \qquad (2.11)$$

Where ΔH is the energy required, ρ is the density, V_p is the volume, r_p is the radius, and C_p is the specific heat capacity of the particle. ΔT is the temperature difference between ambient and material melting temperature, L_f is latent heat of fusion and E is melt energy.

According to the equation, pre-heating the powder can reduce the required melt energy due to the reduction of ΔT. However, this effect is very small. Elsen found that the reduction in melt energy required for melting stainless

steel powder with a pre-heating temperature 500°C on the powder bed was just 22% compared with no pre-heating used [81].

2.4.3 Residual stresses

It is important to investigate the thermal stresses developed in the SLM process which can cause unsuccessful manufacturing. In SLM, large heat intensities are generated rapidly within a small area; due to non-uniform heating, variable cooling and repetitive heating cycles, a steep thermal gradient can be developed across the powder bed. This thermal gradient induces stresses that can cause shrinkage, solidification cracks and layer delamination [101]. Cooled parts manufactured by SLM contain residual stress that can reduce their fatigue strength [7].

Residual stresses are stresses that remain after the original cause of the stresses has been removed. They remain along a cross section of the component, even without the external cause. In SLM processes, residual stresses occur because of the heat from the melting process. This can cause localised expansion, which is taken up by either the molten metal or the placement of parts being melted. When the laser moves away, areas cool and contract more than others, leaving residual stresses.

Residual stresses can reduce the performance or cause failure of manufactured parts. They may increase the rate of damage by fatigue, creep or environmental degradation [114]. Residual stresses can also cause elastic deformation and cracks in the parts during post-processing by machining [115].There are many ways to reduce residual stresses today, and it is believed that post-heating treatment, re-scanning each layer by laser and pre-heating the powder bed can reduce residual stresses effectively [116].

2.4.4 Thermal shrinkage

Shrinkage occurs when material cools and contracts, which often leads to unacceptable dimensional loss and stresses. It can affect the part microstructure and final mechanical properties, causing many important stability problems.

In the SLM process, the level of shrinkage can vary due to different materials used, melting condition and process parameters used [117]. The methods that can control or reduce the shrinkage include reducing the laser beam spot size [24], pre-heating the powder bed [24] and using a near zero shrinkage powder [112]. Also, by using correct process parameters, shrinkage due to the liquid phase can be completely compensated by an expansion of the material caused by the diffusion of the component, so that the final parts may have no net volume changes [4, 118].

Solidification cracks and layer delamination may occur due to the thermal shrinkage strain during the cooling and solidification procedure [91]. Cracks usually happen along grain boundaries or interfaces between different materials. Reducing the thermal shrinkage or thermal residual stresses can help to avoid solidification cracks and layer delamination during the SLM process.

2.5 Heat Transfer Modelling in Selective Laser Melting

Mathematical models can be used to gain insight into SLM. A reliable and accurate prediction of the temperature distribution can be useful for further SLM investigation.

Heat conduction simulation can also help to investigate the melting efficiency. It is useful to apply the simulation results on energy reduction to avoid over-heating. During the SLM process, the end of each hatch and also in the last few scans, the part may have already been preheated due to the thermal

conduction. The process parameters can be adapted to compensate for the heat accumulation, which is in fact a recuperation of already used heat [55].

Previous numerical solutions on laser processing work focused on the input heat source development for the temperature distribution prediction. Goldak introduced a 3D moving heat source which is used widely in both welding and laser processing areas [119]. The building medium for the input heat source applied onto has also been developed to fit the powder bed in the solutions on laser sintering and laser melting [120]. Contacts conductivity was introduced for simulation the powder bed thermal properties [120, 121].

2.5.1 Heat transfer theory on general laser processing work

Heat transfer is the transition of thermal energy from a hotter object to a cooler object. It always occurs from a higher temperature object to a cooler temperature one as described by the second law of thermodynamics [122]. As long as there is a temperature difference between objects, heat transfer can never be stopped; it can only be slowed. Heat can be transferred by conduction, convection or radiation. Although usually more than one of these processes occurs in a given situation, heat radiation and conduction are major heat flow in laser processing work.

As laser processing is usually a fast heating process, the heat flow by conduction is relatively confined and represents an approximately constant fraction of the delivered power. So it is possible to use lumped heat capacity calculations for prediction purpose [54]. The models used in prediction of heat flow should solve Fourier's Law of heat conduction, which is given by Equation (2.12), where q is the local heat flux and k is material's thermal conductivity, T is the temperature. Fourier's law states that the time rate of heat transfer through a material is proportional to the negative gradient in the temperature and to the area, at right angles to that gradient, through which the heat is flowing [123]. It is a rate equation that allows determination of the

conduction heat flux from knowledge of the temperature distribution in a medium.

$$q = -k\frac{dT}{dx} \tag{2.12}$$

When heat flows through an element, the heat balance can be written as,

$$heat\ in - heat\ out = heat\ accumulated + heat\ generated \tag{2.13}$$

The difference between the heat in and the heat out depends on the total conduction in all three dimensions, which can be given by Equation (2.14).

$$heat\ in - heat\ out = k\left[\frac{\partial^2 T}{\partial x^2} + \frac{\partial^2 T}{\partial y^2} + \frac{\partial^2 T}{\partial z^2}\right]\delta x\delta y\delta z \tag{2.14}$$

Heat accumulated can be given by Equation (2.15), where ρ is density and C_p is specific heat capacity.

$$heat\ accumulated = \rho C_p\frac{\partial T}{\partial t}\delta x\delta y\delta z \tag{2.15}$$

Heat generated can be given by Equation (2.16), H is the amount of the heat flow.

$$heat\ generated = H\delta x\delta y\delta z \tag{2.16}$$

Thus the basic equation in heat flow modelling can be given by Equation (2.17). This is the 3D extension of Fourier's second law.

$$k\left[\frac{\partial^2 T}{\partial x^2} + \frac{\partial^2 T}{\partial y^2} + \frac{\partial^2 T}{\partial z^2}\right] = \rho C_p\frac{\partial T}{\partial t} + H \tag{2.17}$$

2.5.2 Previous solutions of laser processing simulations

Numerical solutions were developed to simulate moving laser heat source working on different mediums. A series of heat source geometries and

profiles were developed to present the moving laser. Typical solutions are listed below.

Moving point source in a medium of infinite thickness is one of the earliest analytic solutions applicable to similar melting process such as welding [124]. This solution simulates surface melt and can be rendered finite in depth and width by using the method of images. However, it is not accurate in the region where the point source is incident, as the temperature there would be infinite.

Moving line source in an infinite or semi-infinite material is developed from one dimensional solution [124]. An infinite line source with its axis perpendicular to the top and bottom surfaces extends through the depth of material. This two dimensional solution can simulate full penetration melting of the sheet with any thickness. It is still has the problem that it leads to infinite temperatures at the source.

Continuous Gaussian surface source in an infinite solid material is another solution based on point and line source solutions. A steady state temperature distribution due to a stationary Gaussian beam in a semi-infinite medium has been studied [125], and a three dimensional solution for a moving elliptical Gaussian heat source has been presented [126].

Periodic moving point and line source solutions for a medium of semi-infinite thickness are solutions for the temperature field in infinite area and semi-infinite thickness [127]. They are based on the solutions for combined point and line source [128] and for a medium of finite thickness [129].

Moving heat source in a semi-infinite medium is a three dimensional solution developed recently for studying different heat source geometries [55]. The model is based on the previous moving point source and semi-ellipsoidal source solutions, and has been used on studying the melting efficiency and the effects of latent heat.

2.5.3 Input heat source development for laser processing work

Heat transfer modelling work has been successfully used in the field of laser processing of materials to aid successful fabrication of part. Much of the previous work has been concerned with the solution of the heat conduction equations [130-132]. The heat sources used have been point sources, line sources and plane sources as they are amenable to direct analytical solution.

If the heat is liberated at the rate of $Ø(t)\rho C_p$ per unit time from t=0 to t=t' is constant and equal to q, we have:

$$T = T_0 + \frac{q}{4(\pi\alpha)^{\frac{3}{2}}} \int_{\frac{1}{t}^{\frac{1}{2}}}^{\infty} exp\left[\frac{-r^2(t-t\prime)^{-1}}{4\alpha}\right] d\left[(t-t')^{-\frac{1}{2}}\right] = \frac{q}{4\pi\alpha r} erfc\left[\frac{r}{(4\alpha t)^{\frac{1}{2}}}\right] \quad (2.18)$$

where r is radial distance from point source, T_0 is environment temperature, α is thermal diffusivity, and q is the heat flux.

When $t \to \infty$,

$$T = T_0 + \frac{q}{4\pi\alpha r} = T_0 + \frac{P}{2\pi k r} \quad (2.19)$$

where P is the point source power, k is the thermal conductivity and Equation (2.19) is the analytical solution of stationary point heat source.

In 1946, Rosenthal developed the analytical solution for a moving point heat source [124], the Equation is shown below:

$$T = T_0 + \frac{P}{2\pi k r} exp\left[\frac{u}{2\alpha}(x-r)\right] \quad (2.20)$$

where u is the constant moving speed in the same direction of x, x is the axis of movement.

The Rosenthal solution is suitable to predict the temperature distribution at a large distance from the source. However, the solution loses accuracy when near the heat source as the predicted temperature there tends to infinity [55].

To overcome this problem, 2D and 3D heat sources have been introduced [119, 133].

2D Gaussian heat source is the Gaussian distribution extension of point source based on the laser intensity equation. From Equation (2.7), solution of stationary Gaussian distribution source can be obtained by solutions below:

$$I(0,z) = \lim_{r\to 0} \frac{P_0\left[1-e^{\frac{-2r^2}{w^2(z)}}\right]}{\pi r^2} = \frac{2P_0}{\pi w^2(z)} \quad \Rightarrow I(0,0) = \frac{2P_0}{\pi w_0^2}$$

$$\Rightarrow T(0,0,t) = T_0 + \frac{2PD}{\pi D^2 k T^{\frac{1}{2}}} \tan^{-1}\left[\frac{2(\alpha t)^{\frac{1}{2}}}{D}\right]$$

$$\Rightarrow T(0,0,\infty) = T_0 + \frac{P}{Dk\pi^{\frac{1}{2}}} \tag{2.21}$$

where $D=2w_0$ – beam diameter, other definitions of the symbols can be found in section 2.2.1.

Expanding the Rosenthal solution using a Gaussian distribution, the solution of a moving Gaussian distribution heat source can be obtained:

$$T = T_0 + \int_{t'=0}^{t'=t} dT_{t'}$$

$$= T_0 + \frac{q}{\rho\pi C_p (4\pi\alpha)^{\frac{1}{2}}} \int_0^t \frac{dt'(t-t')^{\frac{1}{2}}}{2\alpha(t-t')+2w_0^2} exp\left[-\frac{(x-ut')^2+y^2}{4\alpha(t-t')+2w_0^2} - \frac{z^2}{4\alpha(t-t')}\right] \tag{2.22}$$

Goldak introduced a 3D moving heat source with a Gaussian distribution inside a double-ellipsoidal volume [119], shown in Figure 2-12.

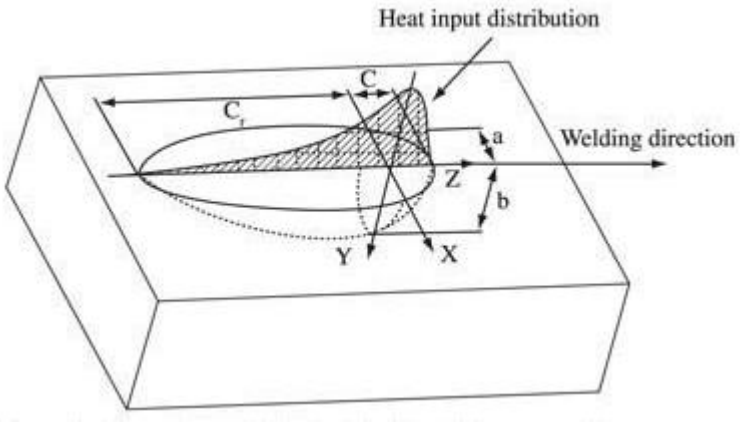

Figure 2-12 Schematic model for Goldak heat source [134]

The model gives a Gaussian distribution and has features of power and energy density distribution control in the melting pool and heat affected zone. It has been widely used in heat transfer modelling as it has the properties close to a real laser beam spot.

The heat distribution in a moving frame can be calculated with the Equation (2.23) and (2.24) [134].

$$q_f = \frac{6\sqrt{3}\eta Q f_f}{\pi\sqrt{\pi} a_f bc} exp\left[-3\left(\frac{x^2}{a_f^2} + \frac{y^2}{b^2} + \frac{z^2}{c^2}\right)\right] \quad (2.23)$$

$$q_r = \frac{6\sqrt{3}\eta Q f_r}{\pi\sqrt{\pi} a_r bc} exp\left[-3\left(\frac{x^2}{a_r^2} + \frac{y^2}{b^2} + \frac{z^2}{c^2}\right)\right] \quad (2.24)$$

where Q is the total heat input (watts), η is the thermal efficiency. The factors f_f and f_r denote the fraction of the heat deposited in the front and rear quadrant respectively. The a_f, b, c and a_r are source constant parameters that define the size and shape of the ellipses.

Nguyen at al. used this 3D heat source to develop models in a semi-infinite body and predict the melting pool geometry in laser welding [135, 136]. A recent research in laser process modelling about moving heat source indicated that in order to achieve a reliable estimate of the peak temperature or an estimate

of the thermal gradient near the spot, a suitable choice of heat source is necessary [55].

2.5.4 Powder bed studies for the thermal properties

The choice of modelling body is also important for thermal mapping prediction. As most previous works in heat flow modelling were focused on particular problems, i.e. shrinkage investigation or thin wall investigation, 2D body like single line or single layer were widely used. The most developed model used in laser melting is in a semi-infinite body or a thick plate [135, 136].

Unlike bulk materials, a non-homogeneous powder bed causes difficulties in investigating heat transfer processes due to a variety of heat conduction mechanisms. Previous theoretical models studied the effective heat conductivity of granular material were mainly based on the generalized conductivity principle [137]. It is believed that the conductivity of a continuous medium is greater than that of a dispersed one [138].

A uniform bulk medium with linear thermal properties was used to describe the powder bed until Maxwell started to look at non-continuous states [139]. Recent research to simulate the powder bed has considered the gas filling of the pores [140, 141], and the contacts between particles [120, 121]. In contacts between particles, a contact radius a is introduced, and the effective contact conductivity, λ_e, of simple equal overlapped spheres, shown in Figure 2-13 can be calculated using the Reimann-Weber equation [121]:

$$\lambda_e = \lambda \left(\frac{R}{a} + \frac{1}{\pi} \ln \frac{2R}{a} \right)^{-1} \tag{2.25}$$

Where λ is the thermal conductivity of bulk material and R is the radius of the sphere.

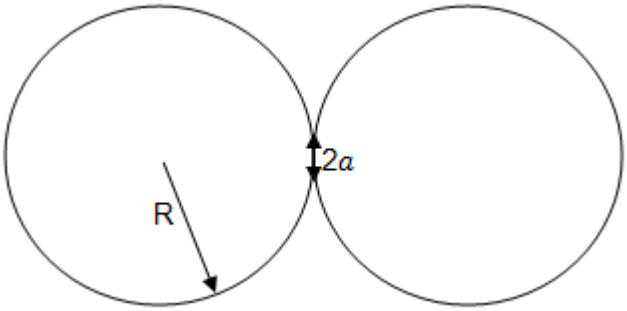

Figure 2-13 Contact radius between two spherical particles with the same radius R

Considering that small particles can fill in the gaps between big particles, a close-packed structure, shown in Figure 2-14 was used to describe the relative powder bed structure, and gives an effective thermal conductivity of $\lambda_e = 2\sqrt{2}\lambda\frac{a}{R}$.

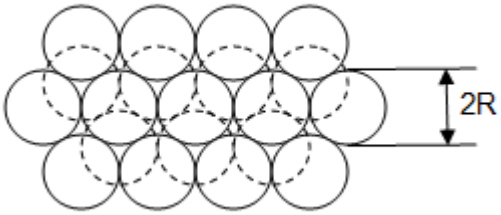

Figure 2-14 Close-packed structure of particles

There are also models on studying the effects of geometrical and physical characteristics of the powder on heat transfer. They provide good agreement with experimental data when the process is governed mainly by conduction at high temperatures. At low temperatures the process is mainly limited by heat transport through contact spots, and the predictions of the models are in less agreement with experiments due to the lack of information on the powder structure [141].

A thin layer of uniform powder bed solution was developed for studying the laser energy absorption and heat transfer [142]. Gusarov did further study on the structure of the powder and believed that the thermal conductivity in the powder bed is highly affected by the particles shape, size and their arrangement. The results from this model have a good agreement with experiments but are limited to deep powder bed as well as non-uniform powder bed.

2.5.5 Previous modelling works for the SLM process

The modelling of the SLM process and the related SLS technique, for both metal and polymer, are widely reported in the literature. Computer modelling of heat and mass transfer in the SLM process can help to predict the temperature field, and to choose the optimal laser energy input to achieve desirable microstructure and quality of manufactured parts [91]. In order to optimise the SLM process and to avoid unwanted defects, there is an increasing interest in understanding the process dynamics of laser melting , especially the mechanisms of defect formation.

For describing the process dynamics of SLM, a simulation model should include energy input, medium material properties as well as relevant boundary conditions. The input heat source development for the SLM process has been discussed in section 2.5.2 and 2.5.3. The medium development for applying the heat source has been discussed in section 2.5.2 and 2.5.4. In SLM process, the initial state of the medium material is powder; while after melting and solidification, certain areas of the medium change to solid, and the effective thermal properties change. Therefore, numerical methods were developed to study the powder consolidation kinetics and the effect of changing medium states [142-145]. A number of models have been proposed for the relationship between powder bed and solid thermal conductivities [146, 147]. A finite element model for SLM process studied this temperature dependant thermal property, and considered the

thermal conductivity of the medium as a field property which is dependent on porosity [148].

A good understanding of the phenomena happened during the SLM process is important for controlling the properties of the produced parts. Simulations of heat transfer in the laser-powder interaction zone have been applied to predict the temperature field as well as the laser radiation transfer into the powder bed [142, 143, and 149-152]. Models are also used for predicting the melting efficiency and the melt pool size [55, 144 and 153]. Some models focused on predicting the defects formation, such as balling, shrinkage and evaporation during the SLM process [144, 153 and 154]. The heat transfer models in the SLM process also studied the masses of the layers and predicted surface roughness [155, 156].

2.6 Summary

The fabrication of fully functional metal parts using SLM process is very difficult to control. Although successful fabrication of many metals such as steels, nickel alloys, titanium alloys and aluminium alloys have been reported, as well as some composite parts like Cu-TiB_2 and TiC-Al_2O_3 [68]; there are still many problems within the part such as high residual stresses, solidification cracks, unacceptable surface roughness and dimensional accuracy. Also, the SLM process is still not stable and repeatable enough for mass production.

Recently many investigations on SLM have been focused on controlling the laser process parameters for obtaining acceptable mechanical properties, such as reducing the porosity of the parts. Limited academic work has focused on microstructure characterisation and prediction. Research has shown that different process control parameters can affect melt pool behaviour and the solidification process, but limited in-depth research has investigated the relationship between the process parameters and microstructure distribution.

The majority of academic work on the SLM process has successfully connected the laser process parameters to final parts quality. However, little work has previously been reported on the basic principles of this process and raw material effect on the process and the powder bonding mechanisms. This may be attributed to the complex nature of the process, which exhibits multiple modes of heat, mass and momentum transfer, and chemical reactions [54]. Although some efforts were put in the enhancement of the basic knowledge, significant research and development are still required for the fabrication of high performance engineering parts with controlled microstructure.

As a laser based fabrication technology, there is a gap of knowledge on laser-material interaction history. Due to the powder bed characterisation and rapid melting and cooling procedure, it is difficult to quantify the laser energy absorption and conduction process as well as the powder bed temperature. This also causes a lack of knowledge on temperature distribution history during the whole process.

There are many models studied for heat conduction solutions in laser fabrication process. The main drawback of previous models is that the base material properties change has not been taken into account. The behaviour of molten material is needed to be considered as it can affect the thermal conductivity after solidification. A further improvement of the modelling body need to be work out to suit this state changing powder bed.

The reliable and accurate prediction of microstructure forming during the process will help to understand more on the basic principles of SLM process, give a better idea on the mechanical properties prediction. Microstructure prediction of parts fabricated by laser sintering/melting process is a newly developed research target which can assist SLM process become more controllable. This is the final aim of this research.

3 Experimental Research Methods

3.1 Introduction

This chapter describes the equipment, methods and procedures used during the experiments carried out in this research. The experimental programme has four main parts, which help to understand the SLM process for establishing the model for the heat transfer and microstructure prediction, characterise and measure the model inputs, and validate the modelling results.

The first part is SLM process understanding and optimisation. Successful fabrication of parts requires a comprehensive understanding of the main processing control factors. In the SLM process, energy input, build conditions and raw material properties are the three leading factors that can affect a part's quality, such as density and mechanical properties. Energy input and build conditions are able to be controlled by the equipment. Energy input can be studied by characterising the optical scanning system, and the SLM scan strategy. Parts need to be built under different energy inputs and then tested to identify the relationship between processing factors and SLM part properties. Environmental factors such as bed temperature, protection gas and gas flow need to be considered as well.

The second part is raw material characterisation. The powder material used in the SLM process is machine independent, which is not controlled by the SLM equipment. The effect of shape and size distribution of the raw material used in the SLM process on the quality of built parts is worthy of investigation, because the powder bed's density and thermal properties can change due to different particle shape and size distribution. This will affect the laser-powder bed interaction and laser radiation. Powders used in the SLM process are normally recycled and reused, and may face degradation after long process

periods; therefore raw material sustainability in the SLM process requires study.

The third part is model input characterisation. To establish a heat transfer model for predicting the microstructure and mechanical properties of SLM parts, reliable and accurate model inputs need to be examined and measured. These inputs include geometry used in the model, material properties, loads and boundary conditions. Relevant experiments should be carried out to obtain these values for the modelling work. Due to non-continuous, non-homogeneous specificity of powder bed, its material properties are not available from the literature, and cannot be measured using direct methods either. Specific design of measurement methods need to be worked out.

The fourth part is microstructure examination. The aim of the heat transfer model is to predict the thermal history and microstructure generation during the SLM process. Therefore experimental microstructure examination needs to be carried out as a validation procedure for the modelling prediction work.

3.2 Selective laser melting equipment

Samples were built using a commercial Selective Laser Melting workstation ‘MCP SLM-Realizer 100’ developed by MCP-HEK Tooling GmbH, shown in Figure 3-1. It contains a central control system, a main computer with monitor for the operating software, a control computer which controls the build process, a process chamber and a monitor displaying the current parameters and measurement value.

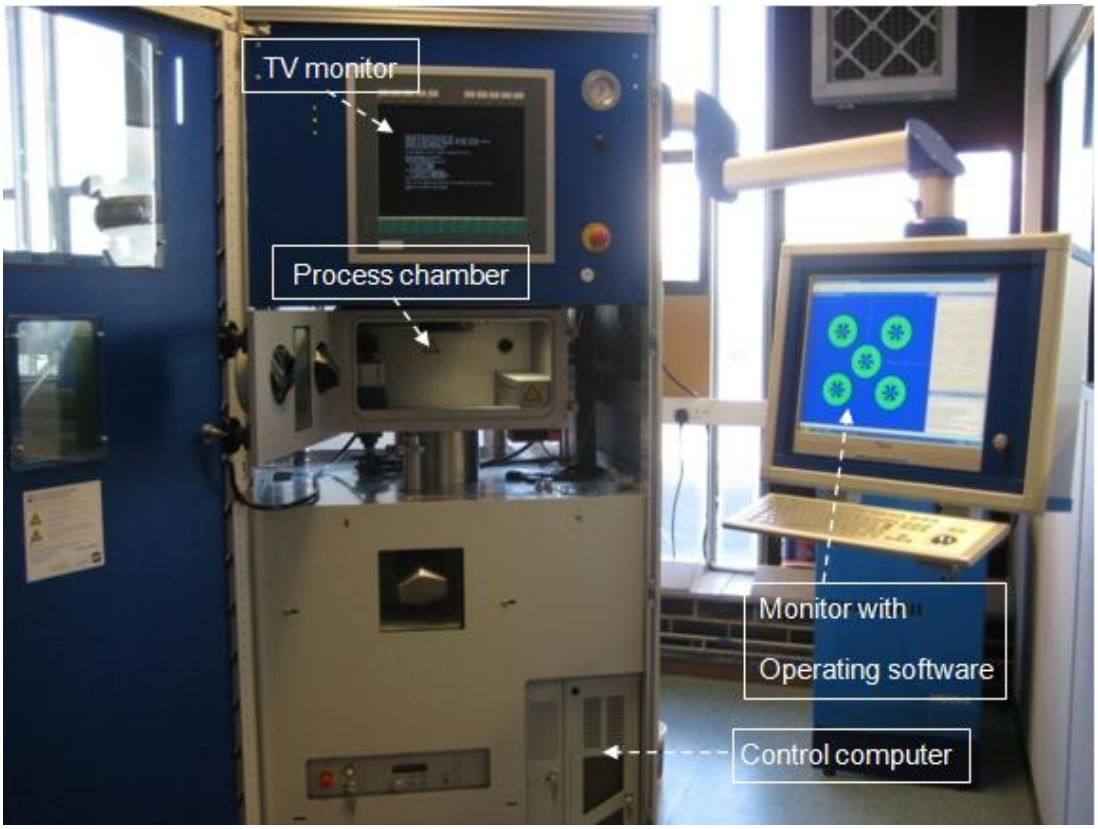

Figure 3-1 MCP SLM-Realizer 100

3.2.1 Optical scanning system

The MCP SLM 100 was equipped with a Continuous Wave Ytterbium fibre laser made by IPG® Photonics, which has central emission wavelength in the range of 1.07-1.09µm, a TEM_{00} Gaussian profile and 50 Watts output power [157]. An adjustable beam expander is also equipped on the laser beam path for adjusting the focused laser spot size on the top surface of the building area. The scanning system includes a dual axis mirror positioning system and a galvanometer optical scanner provided by Cambridge Technology, which directs the laser beam in the X and Y axis. The focusing component is a 120mm F-Theta focal length lens, which produces a focused laser beam with a spot size from 30µm to 300µm [158]. A schematic optics system is shown in Figure 3-2.

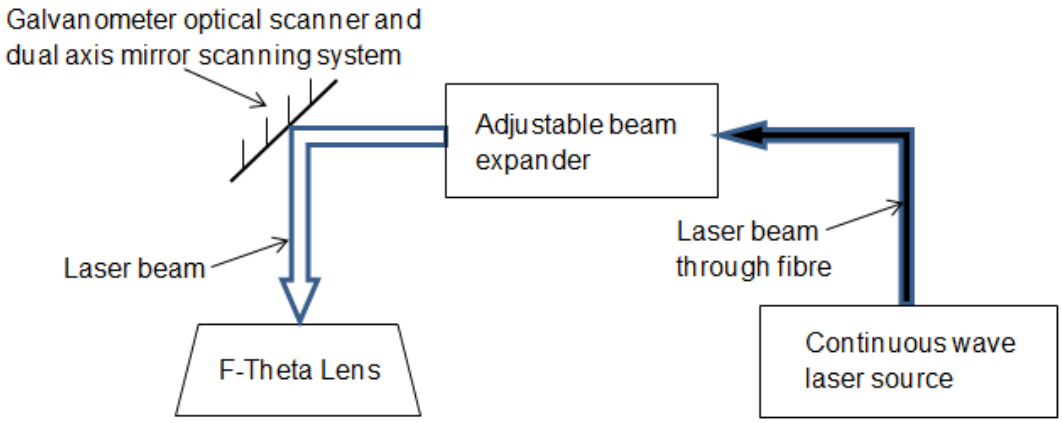

Figure 3-2 Optics system inside MCP SLM-Realizer 100

3.2.2 Building chamber

Figure 3-3 shows the components in the main process chamber. The maximum part build area is (Ø x Z) 125 x 70mm [158]. It needs two screws to hold the building substrate on the building table. The metal powder is deposited via a hopper, which has a capacity of 0.5 litres and five Ø2mm holes allowing the powder to flow out. A 0.64 litre expander has been added to the hopper to hold more powder for high builds or large part. The metallic powder is spread by a delivery blade, and the gap between the blade bottom and the top surface of the powder bed should be adjusted to the layer thickness in the building process, to make sure the first layer has the same amount of the powder as other layers. The speed of the delivery blade can be controlled by the operating software. There is a “super air knife” using Argon inside the process chamber to partition and protect the build area from oxidation during the building process. Compressed Argon flows from five holes set on the right side of the chamber. The gas flows across the building area, to a filter on the left of the chamber through two holes.

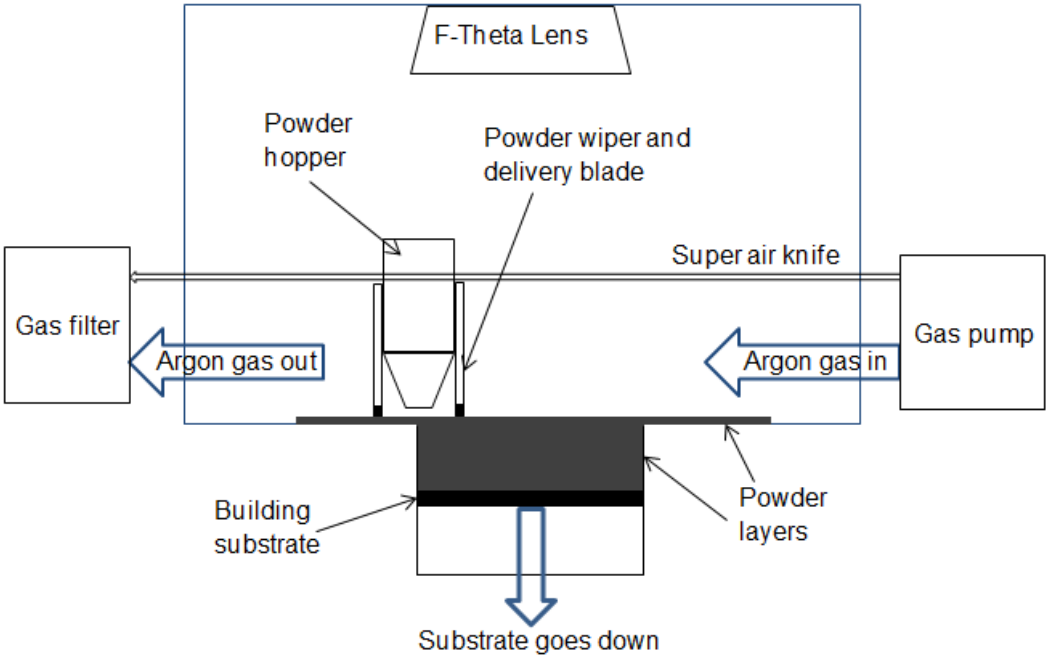

Figure 3-3 Process chamber in MCP SLM-Realizer 100

3.2.3 Machine operating software

The structural information of the desired part is generated using a CAD program, which is produced independently of the machine and requires conversion to a .STL file. The supports which are used to hold the part to stop deformations can be generated by Magics™, a well-established AM software package provided by Materialise. To build the parts, further process and machine-specific operations are necessary in addition to the three dimensional data. The whole building process is controlled using a control software, 'Realizer', provided by Realizer GmbH, which controls all process parameters and machine operations. The Realizer operating window is shown in Figure 3-4.

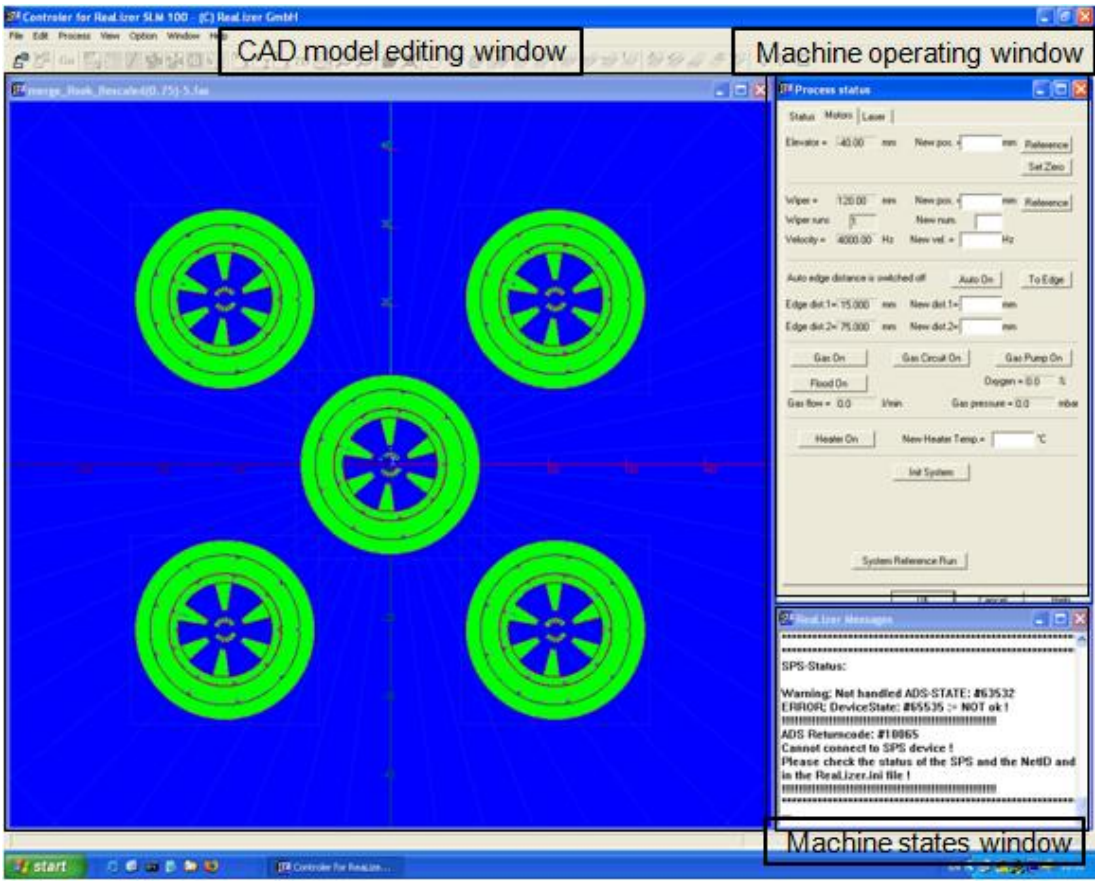

Figure 3-4 Operating software in MCP SLM-Realizer 100

3.2.4 Process control parameters file

An adjustable material file containing all the controllable process parameter data is used in Realizer [158], shown in Figure 3-5, Figure 3-6 and Figure 3-7. The main aim of processing parameters optimisation is to set a reliable material file to get desirable part quality. In the material file, controllable process parameters include laser power, laser lens focus position, layer thickness, scanning speed (obtained by point distance/exposure time), scanning strategy, and scan overlapping (hatch distance and hatch offset); descriptions can be found in Section 2.3.3. They control the parameters for internal solid hatch scan, outside contour and boundary scan, part's support scan and skin scan. Skin scan is the re-melting process for the last layer to improve the surface quality. Supports are needed when some areas of the part deform because the powder bed cannot hold the solid part, or when

some areas of the part start curving due to the thermal stresses. Energy input for support scan should be lower than internal solid hatch scan for easy removal after the builds.

Figure 3-5 shows the sentences controlling the point distance for different scans. The same format is used for controlling the other parameters such as laser power, lens focus position, exposure time, etc.

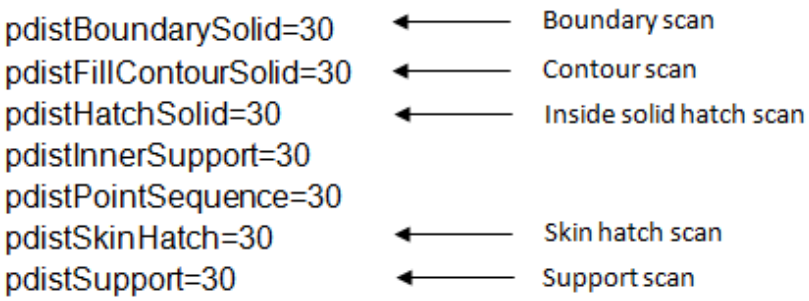

Figure 3-5 Material file description Part 1, point distance setting for different scans

Figure 3-6 shows the sentences for editing major controllable parameters, including layer thickness, laser power and lens focus position, scanning speed and scanning strategy.

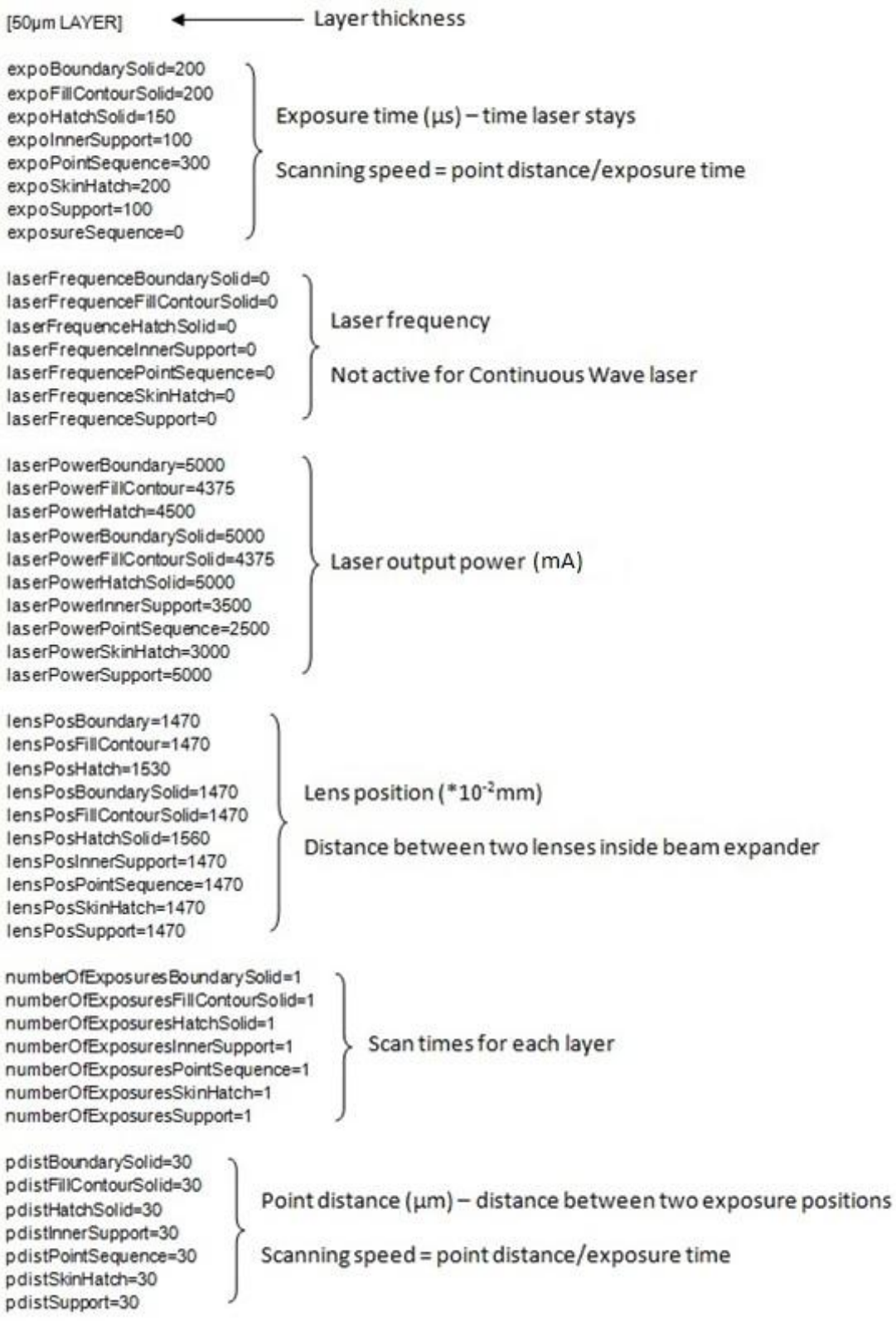

Figure 3-6 Material file description part 2, major controllable parameters settings

Figure 3-7 shows the sentences controlling the scanning strategy and scan overlapping.

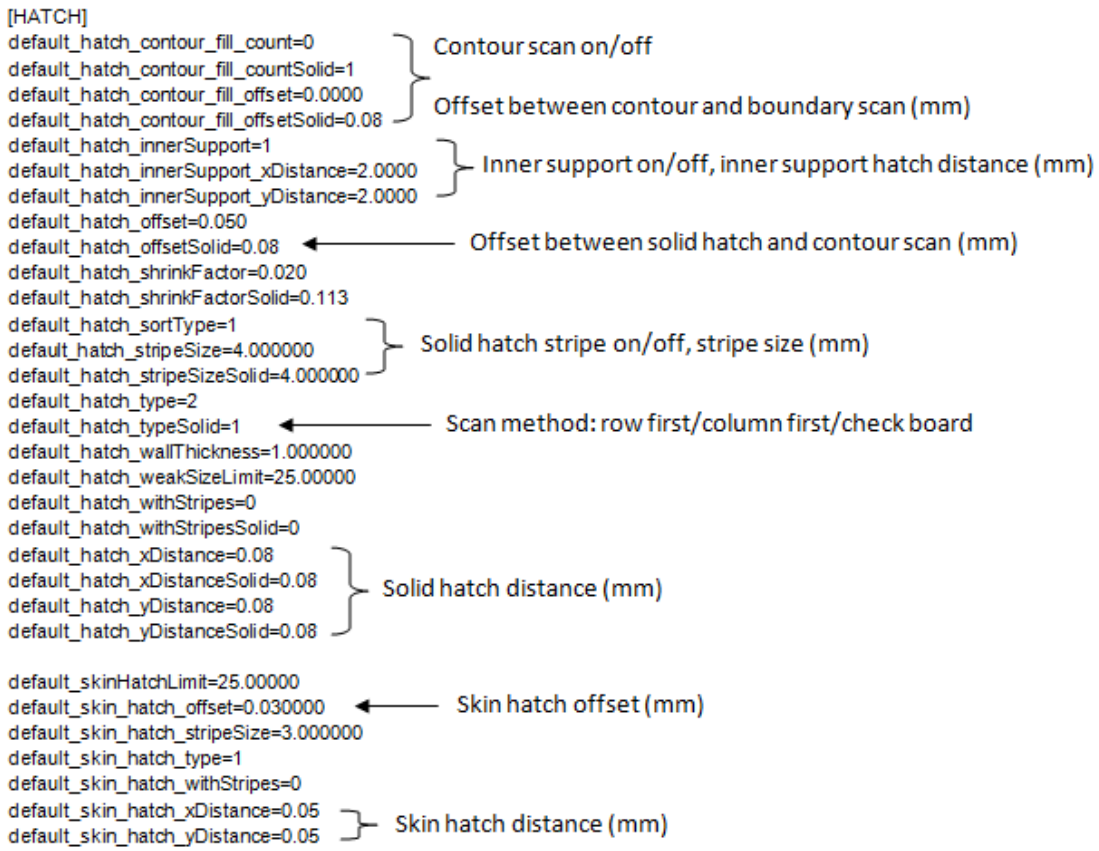

Figure 3-7 Material file description part 3, scan strategy control

By adjusting all the controllable process parameters in the material file, the SLM process can be optimised to get desirable part quality.

3.3 SLM Process Understanding and Optimisation

3.3.1 Optical scanning system examination

The optical scanning system provides two key factors which affect the SLM process energy input – laser power and focus position. A study on laser profiles helps to gain better understanding on how to control these two

factors. Laser profiles usually include laser working mode, power and beam profile.

The laser working mode which includes whether the laser operates in pulse or continuous mode can be tested using an oscilloscope, Teledyne LeCroy Wavejet 324A, to detect the laser firing signal. The results of the recorded signal can also show if there is any delay when setting the laser on and off. Laser power can be measured by a laser power meter which contains a detector and a handheld reading device. The beam profile can be examined by a camera based laser beam profiler. The beam profiler can also measure the laser beam diameters on the building substrate.

According to the solution of laser energy density in Equation (2.9), laser beam diameter affects the energy intensity delivered to the powder bed. Different lens focus position settings by the machine in SLM process will introduce different laser beam diameters in the build area. To obtain high laser energy intensity, the laser should be focused on the surface of the powder bed, where the narrowest beam width can be found.

The relationship between laser energy intensity and machine controllable laser focus position setting requires investigation before building parts. It can be done by measuring the laser beam diameter using either a beam profiler or firing the laser to the laser sensitive paper. 3M™ Laser Markable Label can be used for checking these issues by scanned in single line. It is a specialty film label material that can be imaged by the laser beam, with dual layers of acrylate. The top layer is 10μm matte black acrylate which is engineered to be ablated by a laser beam, and the base layer is 50μm white acrylate which is not sensitive to the beam in comparison with the top layer [159]. When firing the laser on it, the laser beam can generate a shape, as shown in Figure 3-8, and the experimental results can be obtained by observing the brightness and measuring the width of bright parts through an optical microscope.

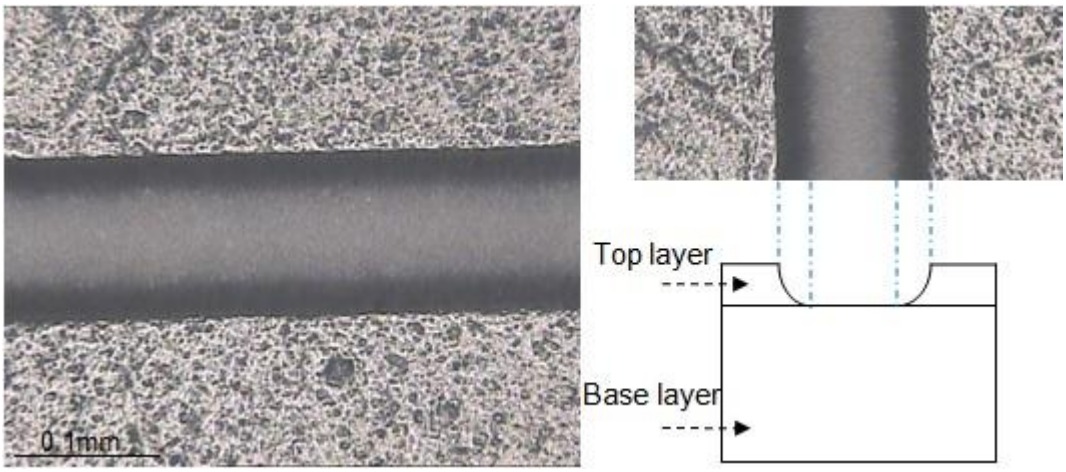

Figure 3-8 Laser mark on the laser markable label

Laser effect on SLM build quality

Based on the laser beam diameter measurement results, samples should be built to find out the relationship between laser power or lens focus position and the SLM part's density. Density was measured by cross sectioning the sample, and examining the porosity using an optical microscope and image processing software Adobe Photoshop. The influence of optical scanning system to the SLM process can be significant. It is necessary to find out the proper value for these two factors, and it is the first step in processing parameters optimisation.

Building area variation study

The use of an F-theta lens in the SLM process provides a flat field at the image plane of the scan, delivering the laser beam vertically to the powder bed. Depending on the quality of F-theta lens, the laser energy density delivered may be not uniform throughout the whole build area, with higher energy density in the centre and lower energy density at the edge. Also, due to the incidence angle, the laser beam spot shape can change from a circle in the centre to an ellipse at the edge of the building area, which will reduce the built part's size accuracy.

Therefore, a building area variation study needs to be developed. Samples can be built on a series of concentric circles. Even if the laser energy delivered in the whole build area is not the same, it should be uniform within a circle when the centre of the building area is the centre of the circle. At least four specimens should be built in each circle to avoid any error in examination. Building parameters and conditions can be found in Chapter 5. Physical and mechanical properties of each specimen are checked and compared to study the variation. Specimens' dimensions were measured using vernier caliper; density was checked by examining the cross sections and ultimate tensile strength (UTS) was measured using Instron 3369.

3.3.2 Process scanning strategy study

Process scanning strategy includes laser scanning speed, hatch distance, layer thickness, hatch type, and build direction. The processing parameters and conditions for building the samples for process scanning strategy study can be found in Chapter 5.

Scanning speed

Scanning speed is another key factor in laser energy density determination. High scanning speed can reduce the whole build time, but can cause poor material properties of the built parts. Based on optical scanning system studies, selected laser scanning speeds were used on studying the effect on built samples' physical and mechanical properties. Tensile test specimens were built as both density and tensile strength were tested.

Hatch distance

The hatch distance can be determined based on a thin wall study. Thin walls can be built by scanning a single line at constant position on each layer. A minimum value of thin wall thickness is required for a hatch distance study. In 3D builds, a scan overlap of 20%-50% is common [4, 26]. Therefore, the hatch distance should be 50%-80% of minimum thin wall thickness. Thin

walls were built based on the laser scanning parameters study. After thin wall thickness values were obtained, cubic blocks were built based on the thin wall processing parameters to study the effect of hatch distance on built parts density.

Layer thickness

Layer thickness can affect the built part's density and side surface finish. It is determined firstly by the powder particle size distribution. To spread powder uniformly on the powder bed, the layer thickness should not be less than the majority of particle sizes. But under certain powder delivering speed, using larger layer thickness may cause powder shortage problem on the building area. Also, thicker layers need more energy input compared with thinner layers; which means under the same laser energy intensity input, it is easier to melt thinner layer and form fully dense part.

The melt pool in the build process has a shape of half-ellipsoid, shown in Figure 3-9. Thinner layer thickness increases the overlapping between two layers, and can reduce the sawtooth effect caused by ellipsoid shape at the boundary. Smaller layer thickness will help to reduce the side surface roughness. Therefore, determining layer thickness should follow two basic rules: no less than the majority of particle sizes; choose thinner layer rather than thicker layer.

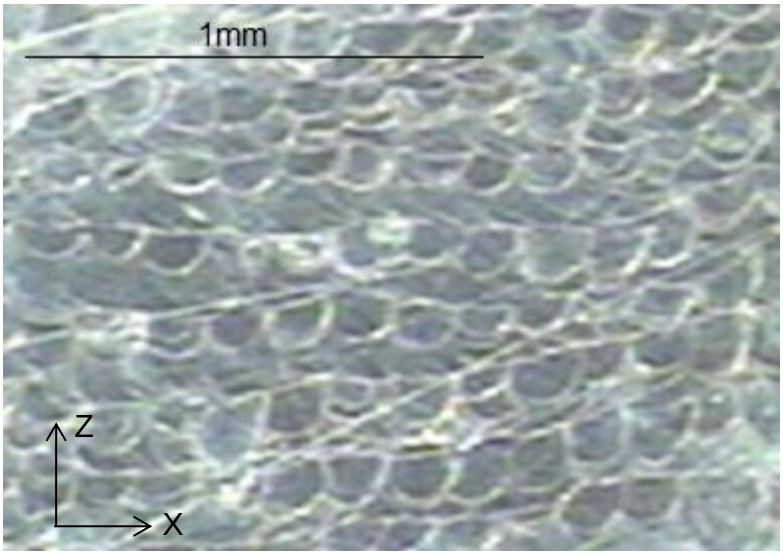

Figure 3-9 Microstructure of part shows melting pool shape in vertical view

Re-melting study

A re-melting process can reduce the top most layer surface roughness by replacing the top melted layer with a more homogeneous one and releasing residual stresses [160]. The process parameters used in the re-melting process is important as it can affect the final part quality. Through observation of the SLM process, it is found in previous practise that using a larger laser spot size during a re-melting process helped to reduce the roughness. Therefore, the experiment for studying the re-melting effect was carried out by controlling lens position to the value when the laser was out of focus on the top surface of the powder bed; other process parameters for re-melting process stayed same. Surface roughness was measured by Talylor Hobson Form Talysurf 50, a bench-top mechanical surface form profilometer.

Building direction

In a SLM process, parts are fabricated in an additive manner, layer by layer. Between two layer scans, the delivery blade needs to move to deliver the powder uniformly on the powder bed. The delay of scan causes the previous layer to cool, and the bond between two layers may become weaker

compared with other build directions. To study this building direction effect, tensile test specimens were built on both X direction (in parallel with gas flow direction) and Z direction (perpendicular with powder bed surface) using the same processing parameters. Tensile strength was compared using Instron 3369.

3.3.3 Building conditions investigation

Processing environment

During the SLM process, the process chamber needs to be filled with a protective gas during the whole building process. Oxygen levels within the chamber can be detected by an oxygen sensor set inside the processing chamber, and should stay below 0.3% during the whole process [81]. Usually, argon is used as the protecting gas as it is an inert gas and heavier than air. To maintain the accuracy of detected oxygen level, the oxygen sensor should be maintained on a regular basis.

Gas flow effect

During the SLM process, there is gas flowing across the building area. It may cause the parts built on the near flow side of the building substrate to cool faster than the parts built on the other side. Also, due to the circulation path inside the processing chamber, parts built in the front side of the building platform may cool quicker than the parts built in the back side. To understand the variation caused by the gas flow, an advanced experiment based on the optical scanning system building area variation study was designed. The building platform was divided into four main areas: left back, left front, right back and right front. Specimens with the same processing parameters were built in the four areas. These specimens were also built in the same circles for a reliable comparison with previous results. Building parameters and conditions can be found in Chapter 5.

Pre-heating study

A pre-heat treatment can be applied to the build substrate during the building process. Since the maximum pre-heating temperature provided by the SLM system used in the study is not high compared with the most metal melting temperature. It may or may not improve the part's density, surface finishing and size accuracy due to the reduced thermal gradients and shrinkage. To study the pre-heating effect on the built part's quality, tensile test specimens were built using 250ºC pre-heating during the whole building process, and a further group of specimens were built without pre-heating at the same positions on the building platform with all the processing parameters remaining constant. Density and tensile strength were tested and compared.

3.4 Raw material characterisation

3.4.1 Material used in the study

Stainless steel 316L was processed in the whole study. It is a low carbon version of Austenite stainless steel. It has 16-18.5% chromium (Cr) content with 10-14% nickel (Ni) and 2-3% molybdenum (Mo) additions for corrosion resistance [161]. The presence of Cr resists corrosion by forming a thin but highly tenacious layer of chromium (III) oxide (Cr_2O_3) when exposed to oxygen. It is impervious to water and air, protecting the metal beneath; and also can quickly reform when the surface is scratched.

When processing austenitic stainless steel, a major problem can be caused by carbon which is known as sensitisation effect should be considered. Sensitisation of metals involves the creation of galvanic corrosion cells within the microstructure of an alloy. When austenite stainless steel is processed, if it is heated to a critical temperature range 425-870°C, carbon can precipitate out at grain boundaries reacting with Cr [162] and form Chromium Carbides, due to the high temperature produced by the melting process. This will reduce the Cr concentration which is necessary for corrosion resistance. The

“L” in 316L means that the carbon content of this stainless steel is below 0.03%, and this will reduce the sensitisation effect [162].

Two sets of gas atomised Stainless Steel 316L powders obtained from two suppliers, Sandvik Osprey Ltd and LPW Technology Ltd were used in the study. These were chosen for their similar chemical composition, data provided by the suppliers, shown in Table 3-1, but different particle size distribution, as measured by the suppliers. Supplier data indicated that Sandvik Osprey (SO) particle size was in the range 0-45µm and LPW Technology (LPW) in the range 15-45µm. Actual particle size distribution was measured by Malvern Mastersizer 2000 before using the powder, results are shown in Chapter 6.

Brand	Fe	Cr	Ni	Mo	Mn	Si	P	S	C
Osprey	69.613	16.3	10.3	2.1	1.21	0.41	0.031	0.016	0.020
LPW	69.512	16.5	10.1	2.06	1.30	0.47	0.028	0.007	0.023

Table 3-1 Chemical composition provided by suppliers (unit: wt%)

3.4.2 Storage and preparation

All the raw materials should have a proper storage condition to protect them from being mixed or destroyed. The main storage method is using the original package with different labels outside describing the current states, shown in Figure 3-10. All the powder which is not going to be processed in the next 24 hours should be stored inside the package.

Figure 3-10 Store package for the powder used in the study

Before SLM processing, the powder should be sieved through a 75μm sieve to avoid any dust, hair, damaged or large particles affecting the part's quality. Water content in the powder can be measured by A&D MS-70 moisture analyser. Based on a series measurements and powder flow testing, to obtain enough flowability for the powder flowing out from the hopper, the powder should be warmed to reduce the water content to less than 0.01%. The powder being processed in the next 24 hours can be left inside the oven with special tray and warning card describing the powder states, shown in Figure 3-11.

Figure 3-11 Reduction of moisture and temporary storage

3.4.3 Particle shape, size distribution and powder bed density

Upon receipt, the powders required characterisation by examining the particle shape and size distribution. Particle shape was examined by LEO 440 Scanning Electron Microscope (SEM). The shape of the powder can not only affect the packed structure, but also the flowability. Particle size distribution was measured using the Malvern Mastersizer 2000 with Scirocco dry dispersion accessory, a laser diffraction based particle size analyser. Particle size distribution is a key factor in powder characterisation. It has a significant effect on powder bed density and fluidity. It also affects the density and surface finish of the built parts, layer thickness determination and energy input determination. Having a wide range of particle sizes can result in a higher packing density as the smaller particles can fill in the gaps between larger particles.

It is necessary to determine the powder bed density during the manufacturing process, as the powder bed density can affect the interaction between the laser beam and the powder, and also the conduction of the heat through the powder bed. Powder bed density is mainly determined by particle size distribution of the powder. It can be any value between the powder apparent density and tapping density (where the tapping density refers to the apparent density of the powder after a specified compaction process). During the SLM process, the metallic powder is spread by a delivery blade, and the gap between the blade bottom and the top surface of the powder bed is the layer thickness in the building process. As the delivery blade moves across the powder bed, it may also deliver a pressure on to the powder bed increasing the powder bed density. Therefore, a reliable measurement method was developed to get a realistic value of powder bed density within the SLM 100.

A container was produced by SLM with internal dimensions of 30mm(X), 30mm(Y), 30mm(Z), shown in Figure 3-12, with average surface roughness R_a less than 20μm on both bottom and sidewall surfaces, measured by Talylor Hobson Form Talysurf 50. During the building process, the blade

delivers the powder uniformly across the powder bed, but only the container is melted, leaving the unaffected powder within the container. Therefore, the powder inside the box should have the same density as the powder bed. After the build, the powder inside the box was weighed using a scale with an accuracy of 0.1mg and the packing density determined. All the dimensions of the box were measured again using vernier caliper to avoid any error in the calculation.

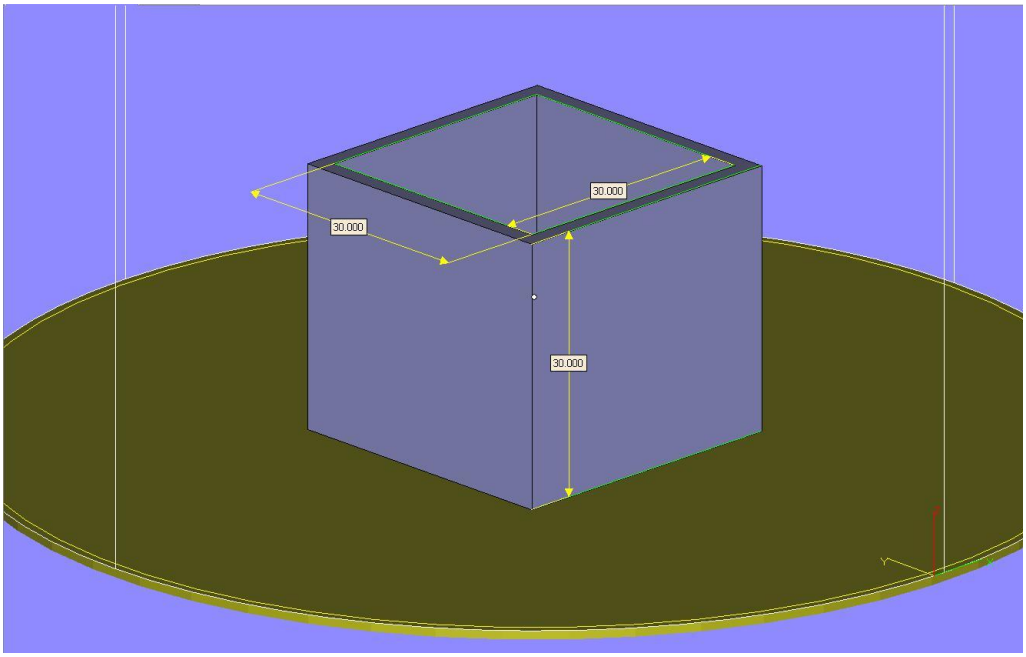

Figure 3-12 Design of container built for powder bed density measurement

Internal surfaces' roughness and the curving bottom surface can affect the accuracy of the measurement result. To avoid the deformation, the container was built directly on the substrate without any supports. To minimise the surface roughness effect and other measuring errors, 3 containers was built and an average result was obtained. The powder bed density measurement result is also required for the heat transfer modelling work, and is discussed in chapter 7.

3.4.4 Powder flowability measurement

The powder flowability is a powder characteristic which can affect the particle distribution on the powder bed; therefore affecting the melting process, laser energy absorption and laser-powder interaction. For SLM, enough powder flowability is required to achieve uniform thickness of powder layers, which allows uniform laser energy absorption in the processing area. If the powder cannot be spread uniformly on the build area, the processing layer cannot have a uniform thickness, which will leave the finished layer with a rough surface and the next layer rougher. Therefore, when the laser scans across the powder bed, the energy cannot be absorbed uniformly, and porosity can be created. The highest powder flowability occurs when the powder contains a narrow particle size range. However, maximum powder bed density occurs when the powder contains a mixture of different sized particles. Therefore, for optimum SLM processing, a balance between these two is required.

To measure the powder flowability during the build process, a simple method is developed. Recording the build time for the whole process, measuring the weight of powder used during the process, then the flowability by time can be calculated.

Another way to characterise the powder flowability can be achieved by calculating the Hausner ratio. The Hausner ratio is a number which is correlated to the powder flowability. It is calculated using the equation shown below [163]:

$$H = \frac{\rho_T}{\rho_A} \tag{3.1}$$

Where ρ_T is the tapped density of powder, and ρ_A is apparent density of powder. A Hausner ratio greater than 1.25 is considered to be an indication of poor flowability [163]. Powder apparent and tapped densities were measured according to ASTM D7481 to calculate the Hausner ratio.

3.4.5 Effect of particle size distribution on parts quality

Powder particle size distribution plays an important role in sintering kinetics and powder bed formation [94, 164]. Investigations on the effect of particle size and size distribution have been carried out for sintering ceramics [165-167]. However, the effect of particle size distribution on laser sintering/melting has not been well documented, especially in SLM processes [168, 169]. Also, investigations which compare the laser sintering/melting behaviour of powders with similar average size, but different size distribution range are limited. This is the reason for choosing separate suppliers of powders with similar average size but different particle size distribution in this study.

To study the effect of powder particle size distribution on part quality and energy input optimisation, cubic blocks and tensile test specimens were built separately using powder supplied by Sandvik Osprey and LPW. Different groups of samples were built on the constant position of the building substrate, and under the same processing parameters for both brands. Building parameters and conditions can be found in Chapter 6. Density, ultimate tensile strength (UTS), elongation at break, hardness and surface roughness were measured for the comparison. UTS and elongation were measured by Instron 3369, surface roughness was measured by Talylor Hobson Form Talysurf 50, and hardness was measured using a Rockwell hardness testing machine Avery 6402.

3.4.6 Powder sustainability study

One main advantage of powder based additive manufacturing technology is reducing the raw material cost by recycling and reusing the un-melted/sintered powder. But actually the powder used in the process cannot be used indefinitely. There have been reports on polymer degradation occurring during the fabrication of objects by selective laser sintering [170, 171], and the degradation may happen to metals after a long processing period. During the building process, fine particles can be sintered together to form

bigger particles, that may break at some point by the inter-friction between particles. Therefore, after several builds, the particle shape and size distribution may change.

An example of a possible powder degradation phenomenon was found under SEM examination after the stainless steel 316L powder had been used for more than one year, shown in Figure 3-13. The particle started to peel off the outside skin, and can cause the powder stop flowing due to the increased powder inter-friction. This appearance may be caused by the friction between particles, the friction between powder and delivery blade or sieve, break between sintered particles, or the laser-powder interaction. The appearance of this degradation phenomenon was the reason for the powder sustainability study.

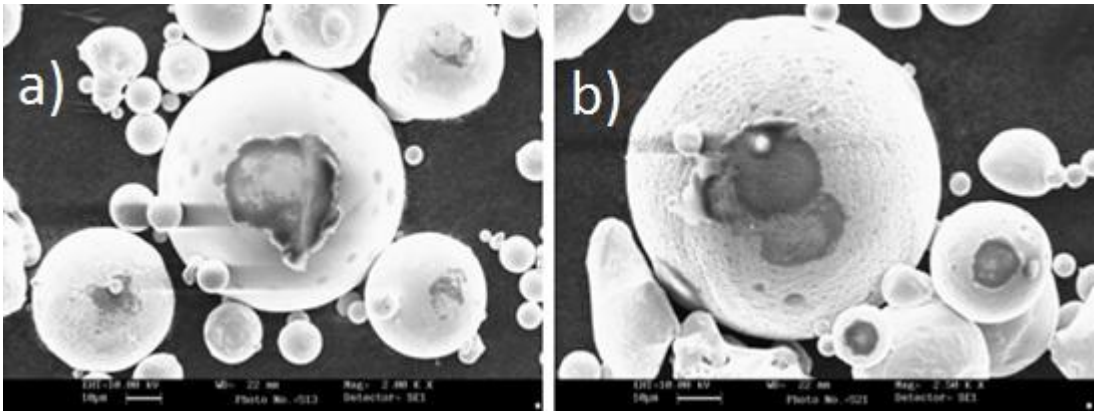

Figure 3-13 Powder degradation after one year processing, a) and b) are showing different particles with same degradation

A powder sustainability monitoring study was developed to investigate the life time of the raw material used in the SLM process until degradation. 15kg of stainless steel 316L powder provided by LPW technology as well as 15kg of stainless steel 316L powder provided by Sandvik Osprey technology were used in the study, and never mixed with any other powder. The powders were processed from their virgin states, and for both general build and experiment uses. The total build time was recorded when using the monitored powder. After a certain amount of build time, the sample powder

was taken out from the whole batch for examining the particle shape and size distribution. At the same time, tensile test specimens were built to examine the tensile strength (UTS) and surface roughness. All the specimen builds used the same processing parameters on the constant position of the building substrate. Due to the research time limitation, the total powder sustainability monitoring study time was 800 hours for LPW powder, and 300 hours for Sandvik Osprey powder.

A further examination on the particle microstructure was carried out by using Electron backscatter diffraction (EBSD), which is a microstructural-crystallographic technique used to examine the crystallographic orientation of metals. The equipment used was FEI Nova 600 Nanolab Dual Beam system. Powders supplied by LPW technology in both virgin and 800 hours processed states were examined by EBSD.

3.5 Model inputs characterisation

Reliable and accurate model inputs are key factors to gain accurate results from finite element models. These inputs include the geometry used in the model, material properties, loads and boundary conditions. Geometry and boundary conditions are described in Chapter 7; loads which are the input laser energy are discussed in section 3.3; material properties are measured during experimental programme described in this section.

For a heat transfer analysis only model, three material properties – density, thermal conductivity and specific heat capacity are required. In contrast to a solid medium, powder bed properties cannot be obtained directly from the literature or handbook, and can be affected by particle shape and size distribution. Therefore, experimental measurements were designed to gain these properties of the powder used during the SLM process.

3.5.1 Powder bed density

Powder bed density was measured by the method in section 3.4.3.

3.5.2 Thermal conductivity

Thermal conductivity can be measured by the Thermal Conductivity Apparatus Model P5687 supplied by Cussons Technology Ltd. This apparatus is designed for the determination of coefficient of thermal conductivity for both good conductors and thin specimens of insulators. The solid samples should follow the dimensions shown in Figure 3-14 to fit inside the apparatus [172].

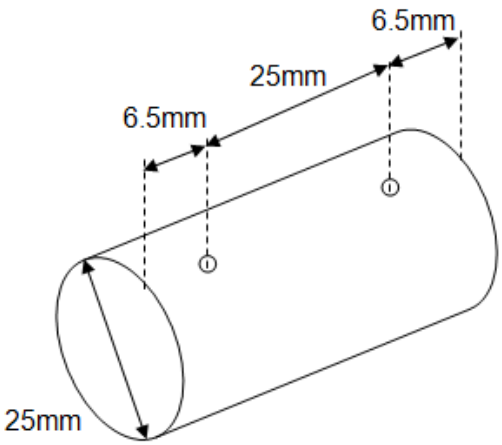

Figure 3-14 Sample dimensions for thermal conductivity apparatus

To measure the powder bed thermal conductivity, a sealed container with the same dimensions in Figure 3-14 should be used. To maintain the same density in the container as the actual powder bed density, the method used in section 3.4.3 was repeated. The container was produced by SLM with external dimensions of Ø25mm x 38mm (Z).

The container was built with 1mm thick top and bottom lid, and a series of sidewall thicknesses, which were 1mm, 1.5mm, 2mm, 2.5mm and 3mm. Using this container in the apparatus, the measured thermal conductivity is a consolidated result of solid sidewall and internal powder. To clear away the effect of solid sidewall from the measurement, different sidewall thickness of the containers were built, and the results were analysed by a linear function.

The temperature measurement range of the thermal conductivity apparatus is 0-300°C [172], which is much lower than the stainless steel 316L's melting temperature around 1400°C. Since the thermal conductivity of the stainless steel 316L is temperature dependent, the measurement results obtained from the experiment cannot be used in the modelling work directly. The conductivity at higher temperature should be calculated by the solution for solid stainless steel temperature dependent thermal conductivity, Equation (3.2), which can also be used for the powder bed [107]:

$$k = a + b \times T \tag{3.2}$$

where k is the thermal conductivity, T is the temperature, a and b are constant numbers. The values of a and b for the powder bed can be calculated based on the measurement results in section 7.2.2.

3.5.3 Specific heat capacity

The specific heat capacity of the powder bed can be determined by using Differential Scanning Calorimetry (DSC). Specific heat capacity thermal curves, which shows heat flow as function of temperature can be obtained. Using the data from the curves, the specific heat capacity can be calculated by the Equation (3.3) [173]:

$$C_p(T) = \frac{{}^{dq}/_{dt}}{m\,{}^{dT}/_{dt}} \tag{3.3}$$

Where $^{dq}/_{dt}$ is measured differential heat input, $^{dT}/_{dt}$ is temperature scanning rate, and m is mass of sample.

Due to limited access to a DSC for metallic materials with wider temperature range, a Shimadzu DSC-60 with temperature range -150 to 600°C, heat flow range ±40mW was used for measuring the specific heat capacity thermal curves. It requires a DSC pan with 5mm in diameter for powder samples, and the density of powder inside the pan could not be the same as the actual powder bed density during the SLM process. An estimate of the volume of powder inside the DSC pan was calculated based on the post-sealing container shape. Therefore the relative weight of the powder in the DSC pan can be calculated by the measured powder bed density and the estimate volume, and this is the weight of the powder should be in the DSC pan. The powder weight was measured using Mettler Toledo AL 204, a high precision laboratory balance with readable display of 0.0001g and a weighing range of up to 210g, an accuracy of 0.1mg. With this calculated amount of powder set inside the DSC pan, the measurement result may not be strictly accurate due to the estimate volume, but provides an indication of likely value.

The specific heat capacity of the stainless steel 316L is also temperature dependent, and therefore the measurement should not be used in the modelling work directly either. It should be calculated by the solution for solid stainless steel temperature dependent specific heat capacity, Equation (3.4), which can also be used for the powder bed [107]:

$$C_p = a' + b'T + c' \times T^2 \tag{3.4}$$

where C_p is the specific heat capacity, T is the temperature, a', b' and c' are constant numbers. The values of a', b' and c' for the powder bed can be calculated based on the measurement results in section 7.2.3.

3.6 Microstructure examination

The microstructure of the SLM parts strongly influences their physical and mechanical properties. The examination of the microstructure can help understand the effect of the laser beam on the powder bed and the melting pool behaviour during the SLM build.

To examine the microstructure of the SLM parts under Nikon Optiphot optical microscope and LEO 440 SEM, the samples were cut, polished and etched based on the practice standard ASTM E407. Thin wall samples were selected for checking the phase, grain size and grain growth direction under single laser moving track on each layer. Since the laser tracks started and ended in the same position and moved in the same direction on each layer for building thin wall in SLM process, it was possible to examine a whole layer in one horizontal view. Also choosing thin walls rather than cubic blocks allowed clear details discovered in both horizontal and vertical directions by removing the scan overlap effect.

FEI Nova 600 Nanolab Dual Beam EBSD used in powder sustainability study was also used to investigate the phase, grain size and grain growth direction of the SLM thin wall parts. It detected the crystallographic orientation which can be used on phase identification, and also showed clear grain boundaries. The information given by EBSD can be a supplement to optical microscopy and SEM examination.

3.7 Summary

Experiments were carried out to gain better understanding on the main factors which affect the SLM process. This knowledge helps to optimise the SLM manufacturing process and control the final part's quality.

Firstly, the equipment controllable SLM processing parameters were investigated. The optical scanning system was examined to find the

relationship between the input laser energy density and the manufactured part's physical and mechanical properties. Then different process scanning strategies were studied and their effects on the manufactured part's quality were investigated experimentally. Building conditions were studied to gain the knowledge of their influence on the melting process.

After studying the main SLM process parameters, an experimental programme continued to investigate the raw material's effect on SLM build quality. As base materials used in the manufacture process, the powders' performance when they are spread and placed on the laser processing area can impact the laser melting process and the final part's quality. The powder's particle shape and size distribution, powder bed density, powder flowability and sustainability were investigated for their effect on SLM parts quality.

Material properties needed in the simulation work, especially the density and thermal properties of the powder bed were experimentally measured for use in the heat transfer model. Particular measurement experiments were designed and relevant calculations were used to obtain reliable values.

Finally, the microstructure of the built parts was examined experimentally by optical microscope, SEM and EBSD. Results obtained in this experiment process gave better understanding of the laser melting process, and also were used to validate the prediction from the heat transfer model.

These experiments enable to understand the key factors which affect the SLM process and final parts quality. This helps to obtain an idea on which process parameter needs to be considered and involved in the modelling work. The experimental programmes also provide the correct model inputs for a reliable and accurate simulation, as well as the validation for the prediction from the heat transfer model. These are the main contributions to this research.

4 Finite Element Modelling Methods

4.1 Introduction

The effect of the main SLM processing parameters on the manufactured part's quality can be investigated from experiments. By controlling these parameters, the whole SLM process can be optimised. However, key factors which describe and determine the melting process such as the melting pool behaviour and thermal history on the powder bed are not easy to be measured and investigated from an experimental programme. A reliable analysis model can simulate the melting process, predict essential behaviours during the manufacturing, and therefore give in-depth knowledge of the SLM process for better control. This chapter describes the methods to establish a heat transfer analysis model for simulating the laser melting process and predicting the temperature distribution and part's microstructure in the SLM process.

Compared with analytical models, finite element model establishment requires more efforts on the inputs and model structure study, and can provide accurate and detailed results for further analysis. The heat transfer model in the study was established in ABAQUS/CAE v6.9-6.11 which is a software application used for both the modelling and analysis of mechanical components and visualizing the finite element analysis result. It was developed and released by Dassault Systèmes as a main component of brand SIMULIA™.

A complete finite element model for heat transfer analysis establishment should contain model inputs characterisation, meshing method selection, geometry, material properties, heat source and boundary conditions application, heat transfer analysis, and post-processing if needed. Therefore, the methods for establishing and developing the model include 5 main steps.

Step 1 is to characterise and determine the geometry and the boundary conditions used in the model, followed by step 2 meshing method and choice of elements. Step 3 is to apply the moving heat source to the model. A moving heat source will need to include the shape, energy input and velocity of the laser beam. Step 4 is to apply the states variable material properties to develop and adjust the model for the powder bed. The states of the material used in the SLM process may experience changes when the temperature increases or decreases, and this state change should be accounted for in the model. Step 5 is multi-layer model establishment, which is a further step to develop the model into a 3D analysis, and simulate the layer by layer manner of the SLM process.

An overall methodology for the SLM process heat transfer modelling is shown in Figure 4-1. The flowchart shows the main working order for the models developed in step 4 and 5.

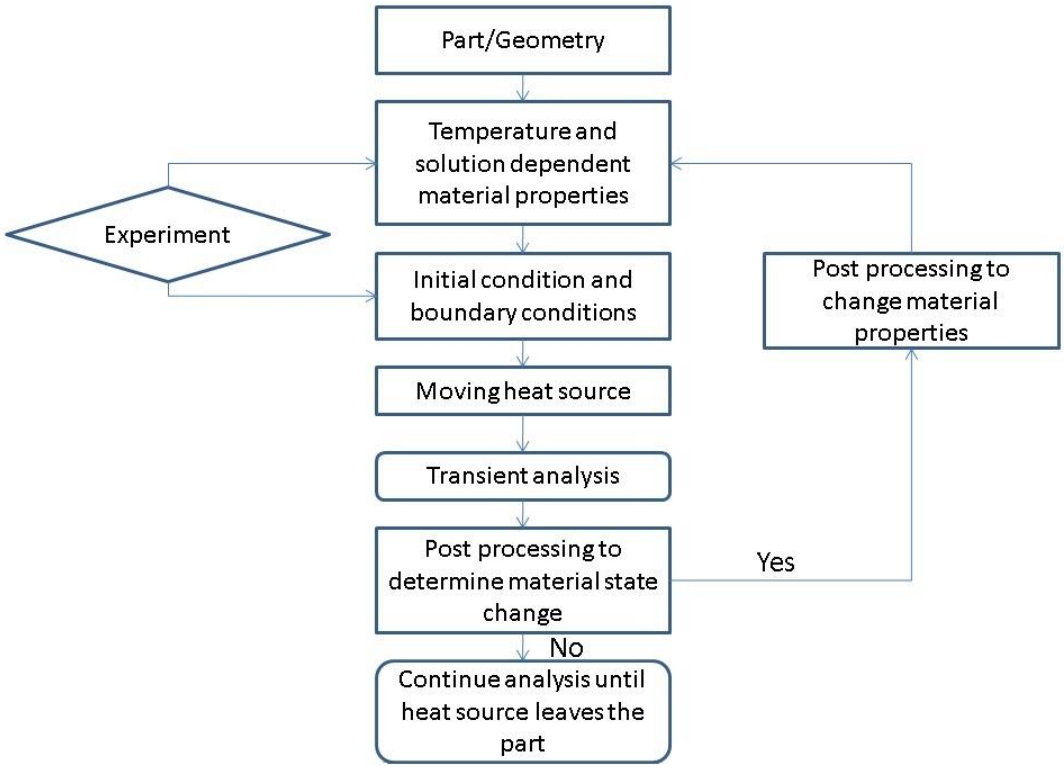

Figure 4-1 Overall methodology of the heat transfer model

4.2 Geometry and boundary conditions

In the MCP SLM-100, the maximum building volume filled by the powder during the SLM process is (Ø x Z) 125 x 70mm [158]. The width of melting pool generated by the laser track would have similar dimension to the thickness of thin walls built in SLM process, and normally the value was between 0.15-0.3mm. Considering the size comparison between the whole building volume in the SLM process (125 x 70mm) and the heat affected zone generated by laser scanning (width around 0.15-0.3mm), the heat affected zone is much smaller than the whole building volume. Therefore, the dimensions of the analysis zone used in the model should be relative to the dimensions of the heat affected zone to obtain temperature results for further analysis. The geometry used in the heat transfer model can be a regular shaped cuboid which is standard and simple but still appropriate for the heat transfer analysis of the SLM process. To avoid complicating the whole model by generating a non-homogeneous and non-continuous powder bed, the powder bed was approximated using a solid bed with powder properties, i.e. powder bed density, thermal properties, etc.

The boundary conditions of a heat transfer model analysis involve two main situations: constant temperature and continuous heat conduction. Predefined fields such as the initial temperature and interaction such as environment temperature, surface radiation and surface film condition can also be defined as boundary conditions. The geometry used in the finite element model is a regular shaped cuboid, with each surface having different boundary conditions, shown in Figure 4-2.

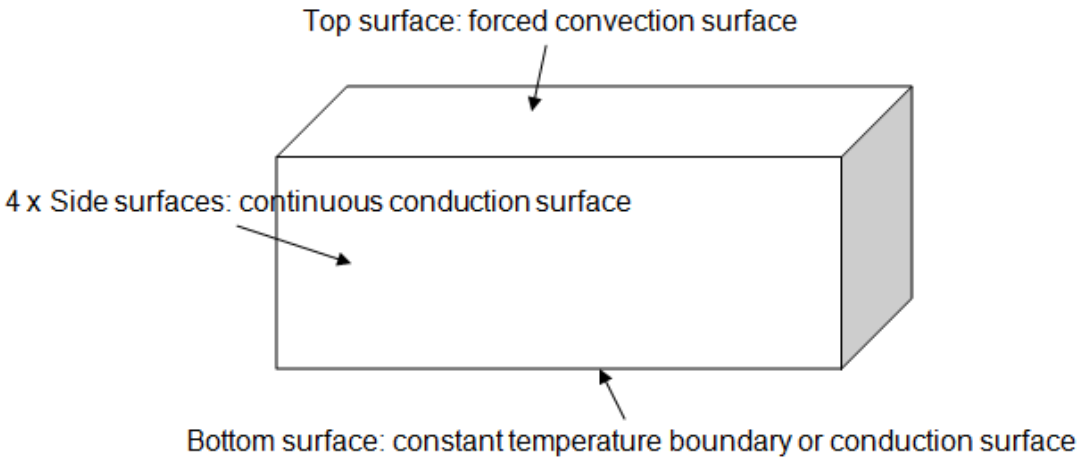

Figure 4-2 Boundary conditions for each cuboid surface

The top surface is a forced convection surface with argon gas flows across the building area. The typical equation for calculating the forced convection heat transfer is Newton's Law of Cooling, and the convection heat transfer coefficient which determines the calculation is required for the heat transfer model. The convection heat transfer coefficient is dependent on the type of media, the flow properties such as velocity, viscosity and other flow and temperature dependent properties [174]. These correlations are usually expressed in terms of dimensionless numbers. The dimensionless numbers used for forced convection heat transfer coefficients are Nusselt number (Nu), Prandtl number (Pr) and Reynolds number (Re) [175]. Definitions of these numbers are shown in Equation (4.1), (4.2) and (4.3).

$$Nu = \frac{hD}{k} \tag{4.1}$$

$$Pr = \frac{v}{\alpha} = \frac{\mu C_p}{k} \tag{4.2}$$

$$Re = \frac{DV\rho}{\mu} \tag{4.3}$$

where h is the heat transfer coefficient, k is the thermal conductivity of the fluid, D is the characteristic length parameter, μ is the viscosity of the fluid,

C_p is the heat capacity of the fluid, V is the velocity of the fluid and ρ is the density of the fluid. Since the heat transfer coefficient, h, appears in the Nusselt number, so the correlations are typically in the form of an equation for Nu in terms of Re and Pr [175].

The forced convection in the SLM process can be described as a fluid flowing parallel to a flat surface and Blasius similarity solution for a laminar flow can be used [176], which gives the correlation shown in Equation (4.4).

$$Nu = \frac{hD}{k} = 0.664 Re^{1/2} Pr^{1/3} \quad (4.4)$$

Experimentally, the flow rate of the protective argon gas was determined by reading the gas flow meter during the SLM process. The reading was repeated 4 times to avoid any reading error.

The four side surfaces are continuous heat conduction surfaces with the same thermal properties as the powder bed.

The bottom surface is a constant temperature boundary when pre-heating applied to the build substrate during the SLM process. With no pre-heating applied to the build substrate, the bottom surface is a conduction surface as the heat will transfer from the powder bed to the solid build substrate. During the SLM process, the build substrate goes down when the layers of powder increase. The substrate leaves the building chamber and enters into a zone where it is affected by the MCP SLM 100 equipment working temperature. This action may change the temperature of the substrate, and affect the conduction state for the bottom surface. Therefore, the temperature of the substrate needs to be monitored, and its influence on the bottom surface boundary conditions needs to be quantified. Thermal-couples are equipped under the build substrate and the temperature can be read through the SLM 100 control software, shown in Figure 4-3. Build chamber temperature (the environment temperature) can also be read in the same process properties information window. These temperature readings were checked on a regular frequency – every 30 minutes during the whole SLM process, and

calculations were carried out using Fourier's Law (Equation 2.12) to obtain the heat affected depth into the build substrate, shown in chapter 7 section 7.3.2. If the heat affected depth compared with the thickness of build substrate is relative small, then the effect of equipment working temperature can be ignored, and the bottom surface of the modelling cuboid is a conduction surface where heat transfers from the powder bed to the solid build substrate.

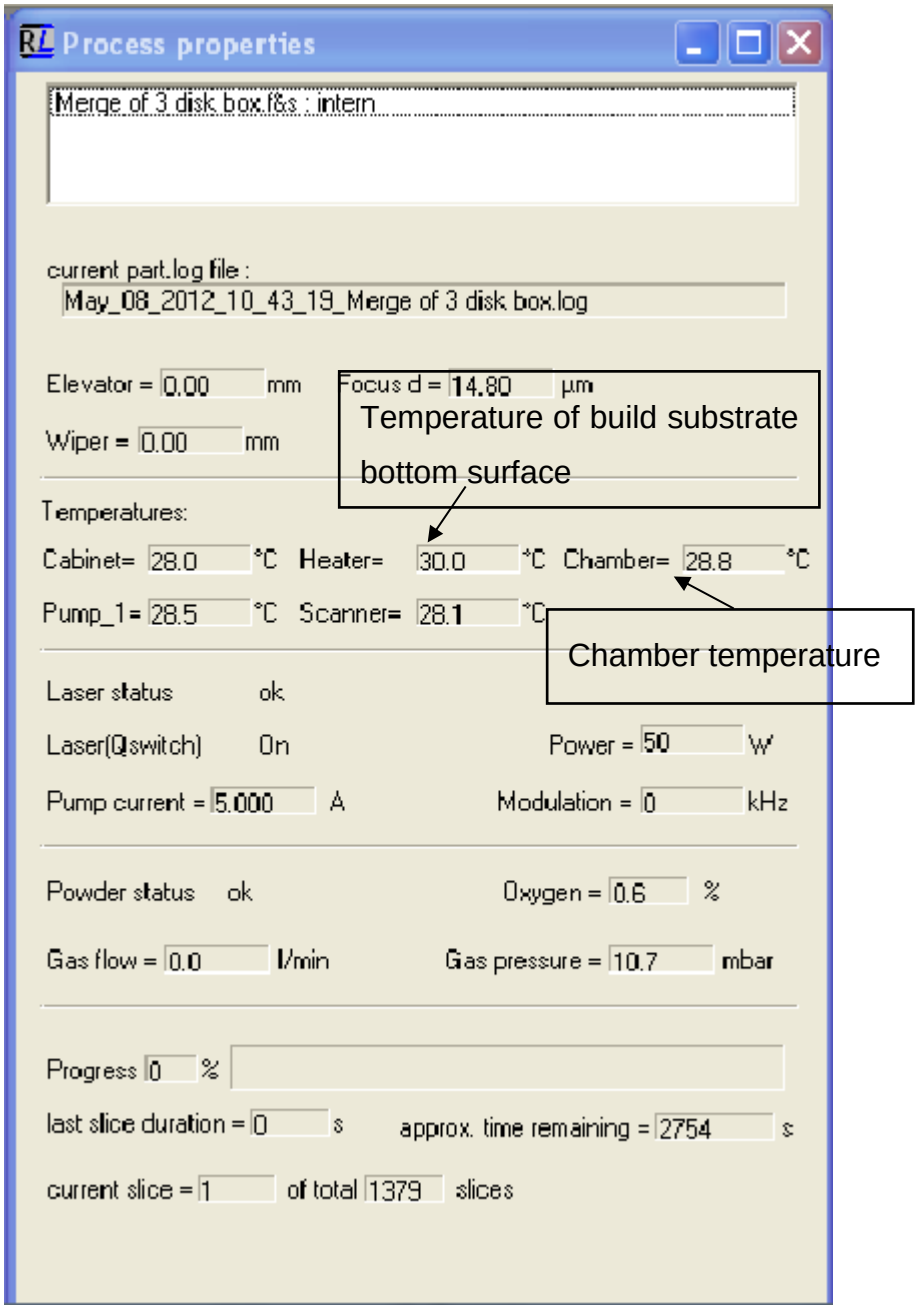

Figure 4-3 Process properties during the SLM process

4.3 Meshing methodology and choice of elements

Meshing of the analysis zone can be a challenge due to the balance between modelling results accuracy and analysis time. A number of meshing methods are available in ABAQUS/CAE based on the geometric region and material properties applied. Since the geometry used in the heat transfer modelling was a regular shape cuboid with unique powder bed properties applied to it, a standard continuous mesh was chosen.

Two seeding methods were considered, one with constant distance between seeds throughout the whole analysis region, the other one with graded distance between seeds starting from the laser material interaction point/line to the edge of the analysis region. Graded distance seeding methods are useful when the heat concentrates in one area and generates a high temperature gradient in that area. However, a constant distance seeding method is more appropriate if the heat concentration area's size varies. The temperature in the melting zone can be significantly higher than the edge of heat affected zone, but the size of the melting zone varies due to the heat input parameters. Also, considering the material states changes during the process and multiple layers analysis needs, seeds with constant distance throughout the whole analysis region were used.

ABAQUS/CAE provides different element shapes which can be used in meshing the part, shown in Figure 4-4 [177]. Element shape needs to be carefully selected to obtain reliable and accurate results, at the same time avoiding long calculation and analysis time. Mesh size dependency needs to be checked and analysed. Smaller meshes provide greater resolution and increase the results accuracy, but also increases the calculation time. Therefore, a balance between mesh size and results accuracy needs to be studied.

Element type selection was carried out by applying a point heat source on a two dimensional square region (5x5mm) with solid stainless steel 316L material properties. All types of two dimensional element provided by

ABAQUS/CAE were studied. Modelling results were compared with the Rosenthal solution on a stationary point heat source, shown in Equation (4.5).

$$T = T_0 + \frac{P}{2\pi kr} \tag{4.5}$$

Where T_0 is the environment temperature, P is the point heat source power, k is the thermal conductivity of the medium and r is the radial distance from the point source.

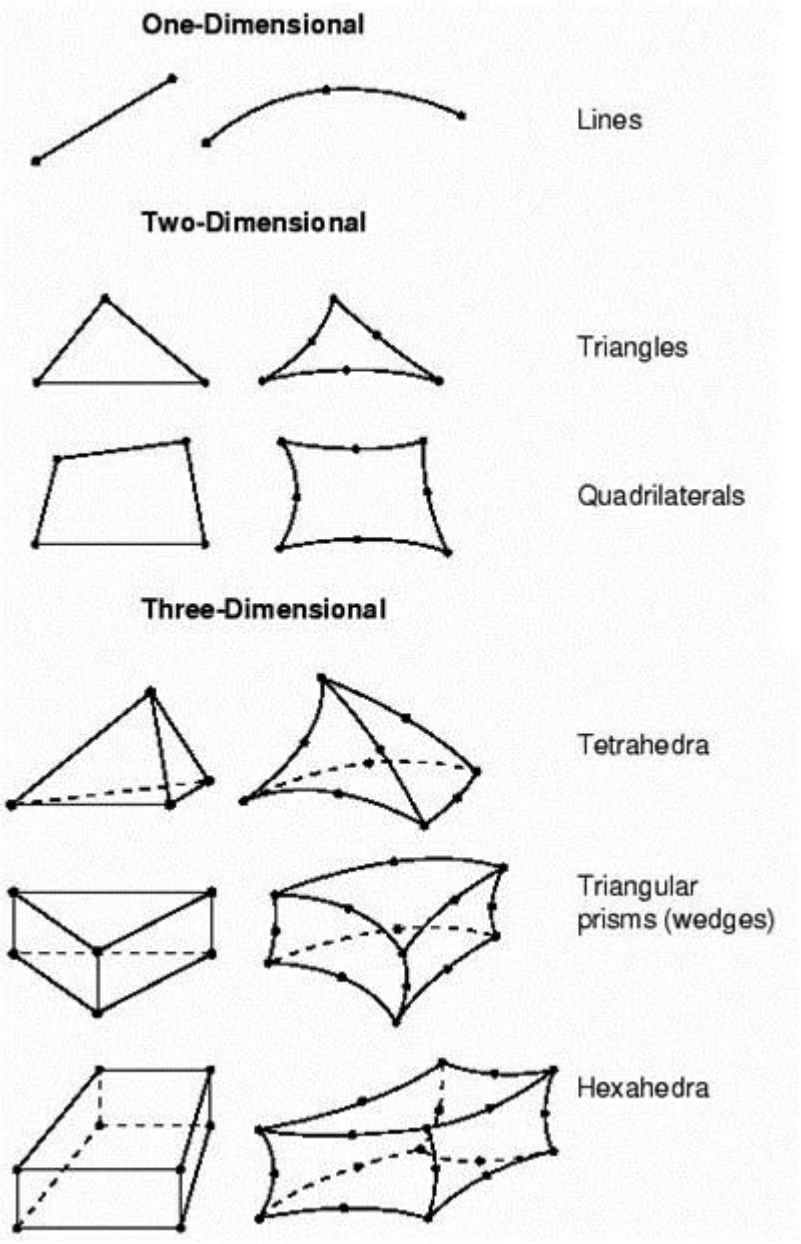

Figure 4-4 Element types provided by ABAQUS/CAE [177]

4.3.1 Two dimensional Tri 3

Tri 3 is a 3-node linear heat transfer triangle. Different Tri 3 element sizes (resolution 2x2, 4x4, 8x8 and 16x16) in a two dimensional part, which has a point heat source applied in the left down corner, have been studied, shown in Figure 4-5.

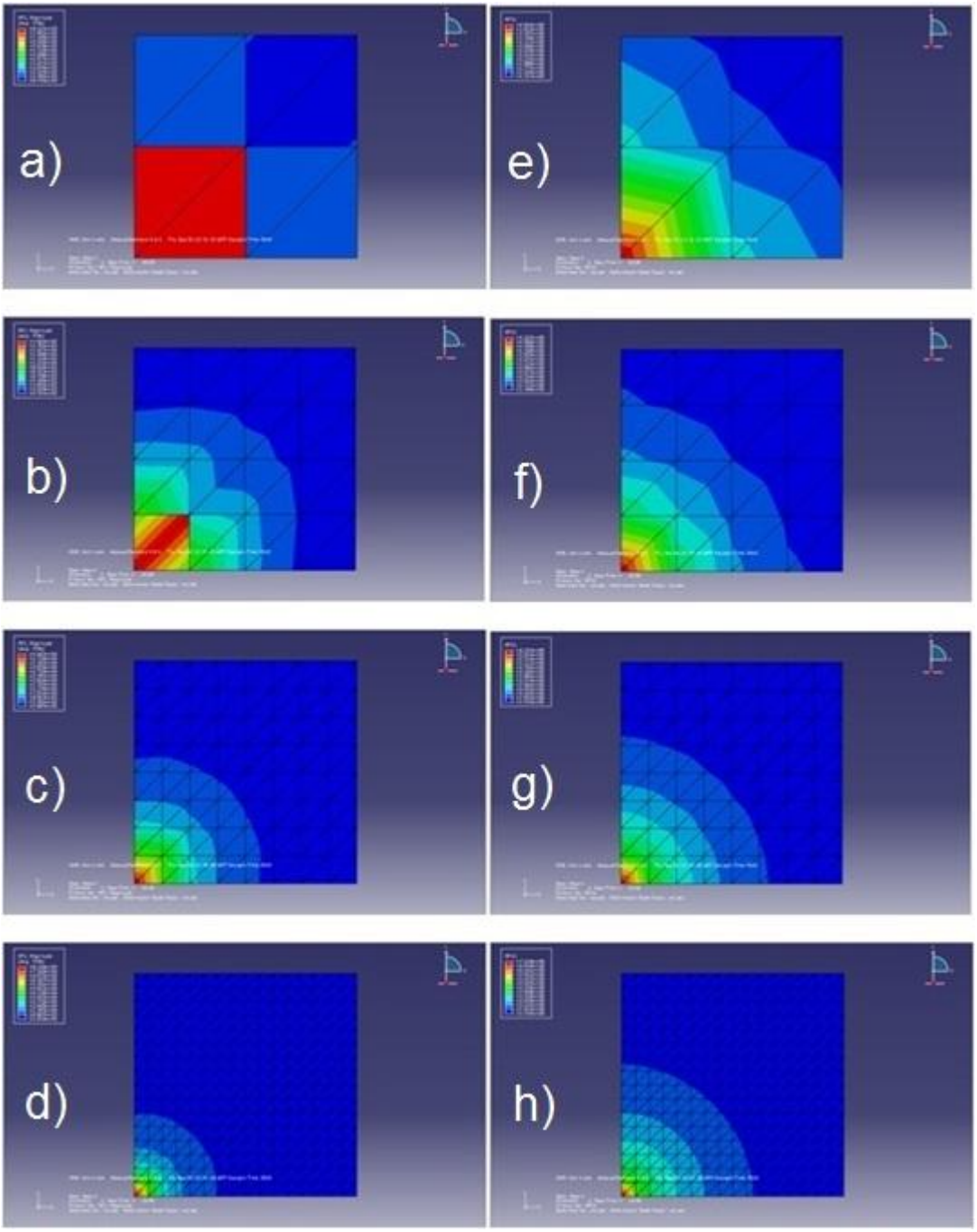

Figure 4-5 Tri 3 element size study, figure a) to d) are heat flux results, figure e) to h) are temperature results at different mesh sizes

4.3.2 Two dimensional Tri 6

Tri 6 is a 6-node quadratic heat transfer triangle based on Tri 3. It can create higher accuracy than Tri 3 but also increasing the calculation time. Study of Tri 6 is shown in Figure 4-6.

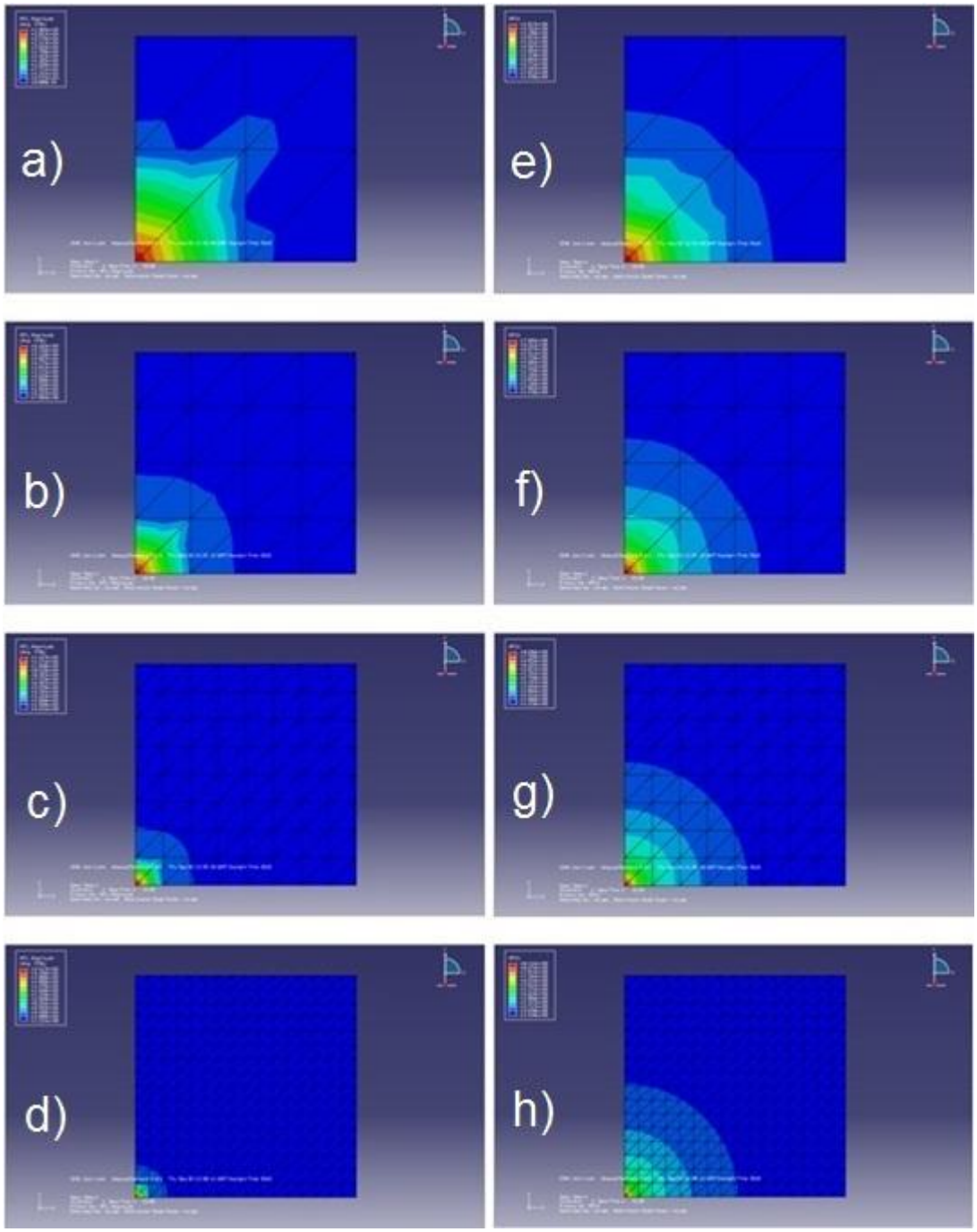

Figure 4-6 Tri 6 element size study, figure a) to d) are heat flux results, figure e) to h) are temperature results at different mesh sizes

4.3.3 Two dimensional Quad 4

Quad 4 is a 4-node linear heat transfer quadrilateral. It is widely used in Finite Element modelling due to its high accuracy, but less calculation time compared with Tri 3, Tri 6 and Quad 8. Study of Quad 4 is shown in Figure 4-7.

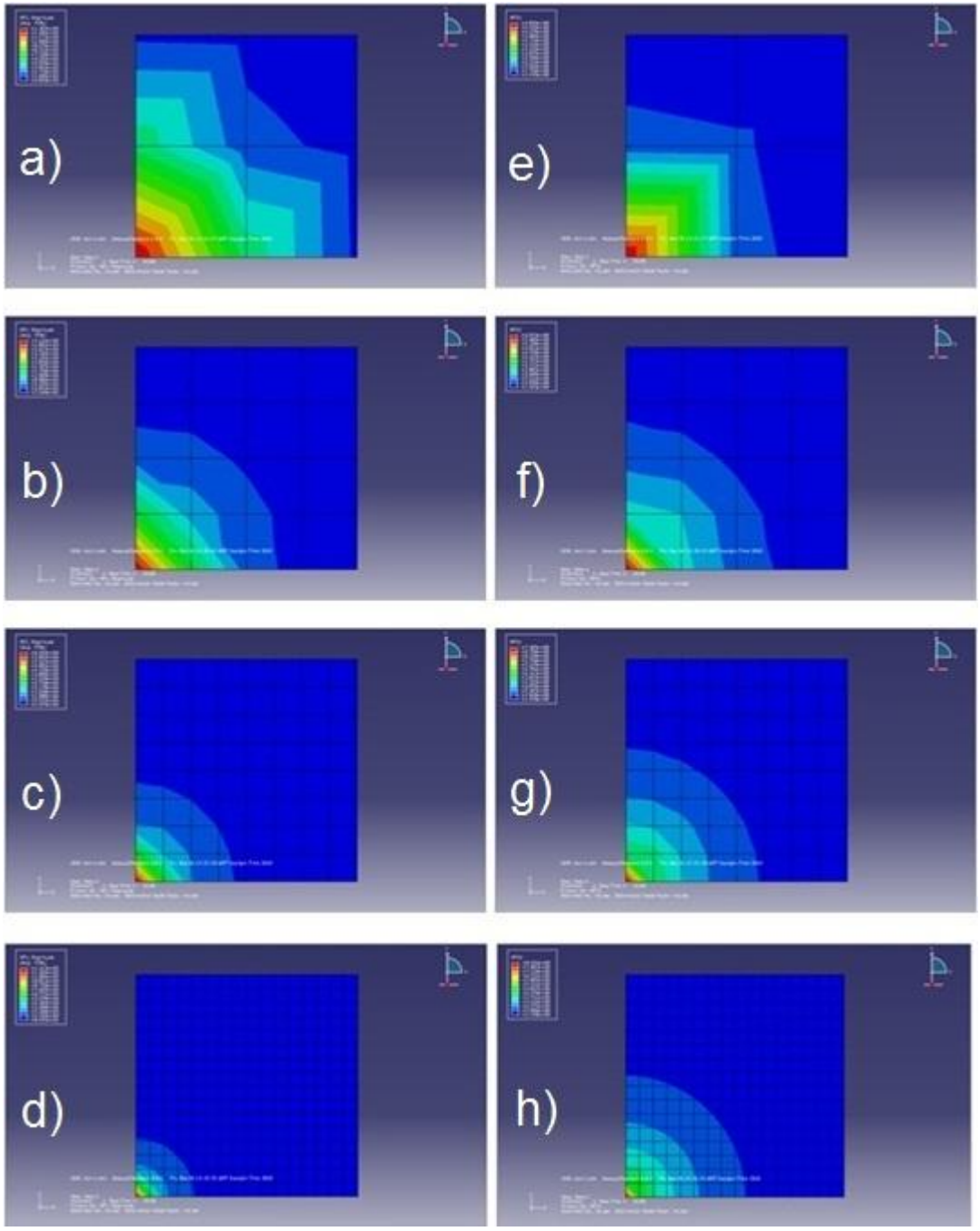

Figure 4-7 Quad 4 element size study, figure a) to d) are heat flux results, figure e) to h) are temperature results at different mesh sizes

4.3.4 Two dimensional Quad 8

Quad 8 is an 8-node quadratic heat transfer quadrilateral. Using this mesh type will have higher accuracy, but longer calculation time. Study of Quad 8 is shown in Figure 4-8.

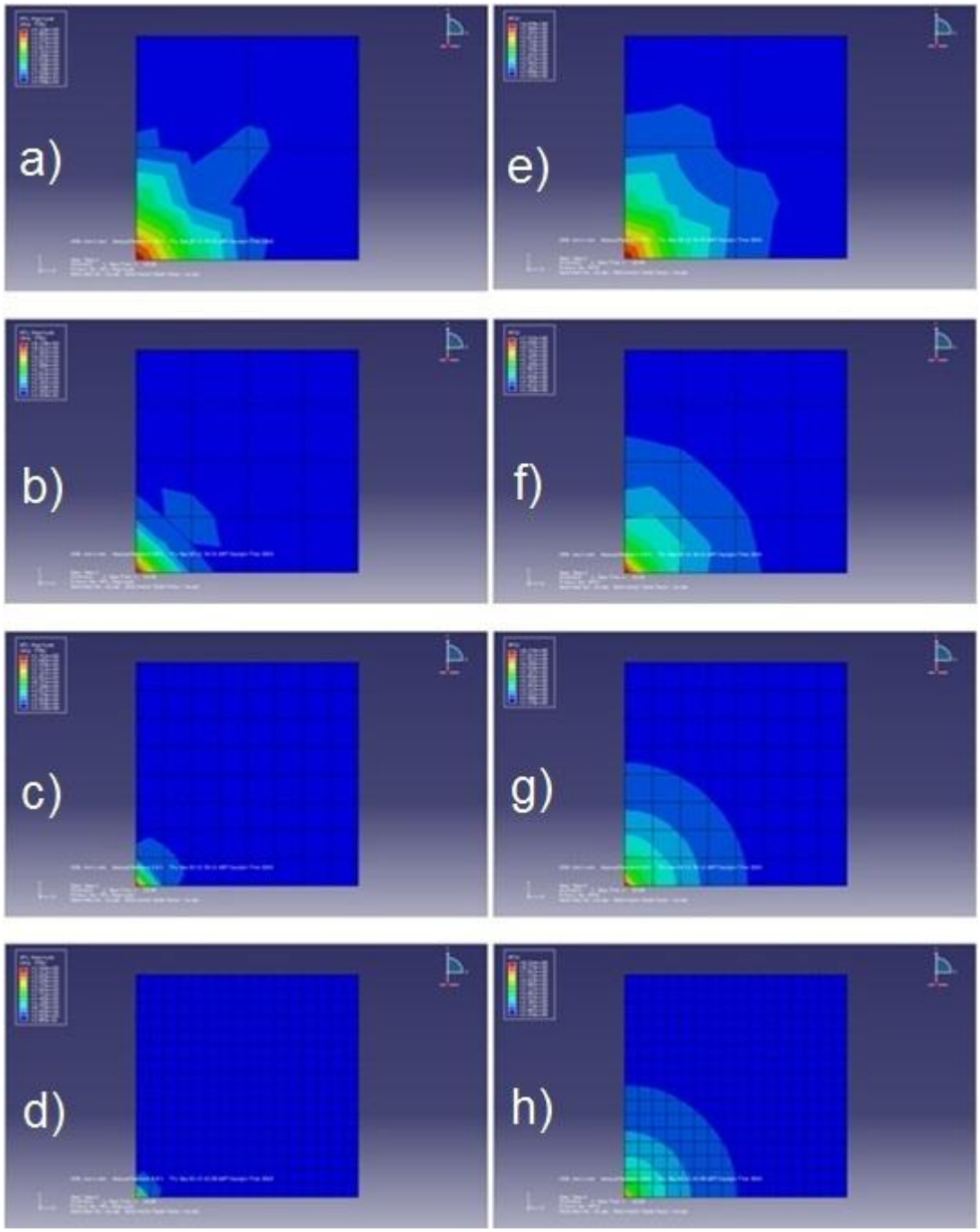

Figure 4-8 Quad 8 element size study, figure a) to d) are heat flux results, figure e) to h) are temperature results at different mesh sizes

4.3.5 Element type and results accuracy

Temperature results of the nodes for different element types and sizes were plotted in Figure 4-9. Temperature distribution obtained from Rosenthal solution was also plotted for a comparison.

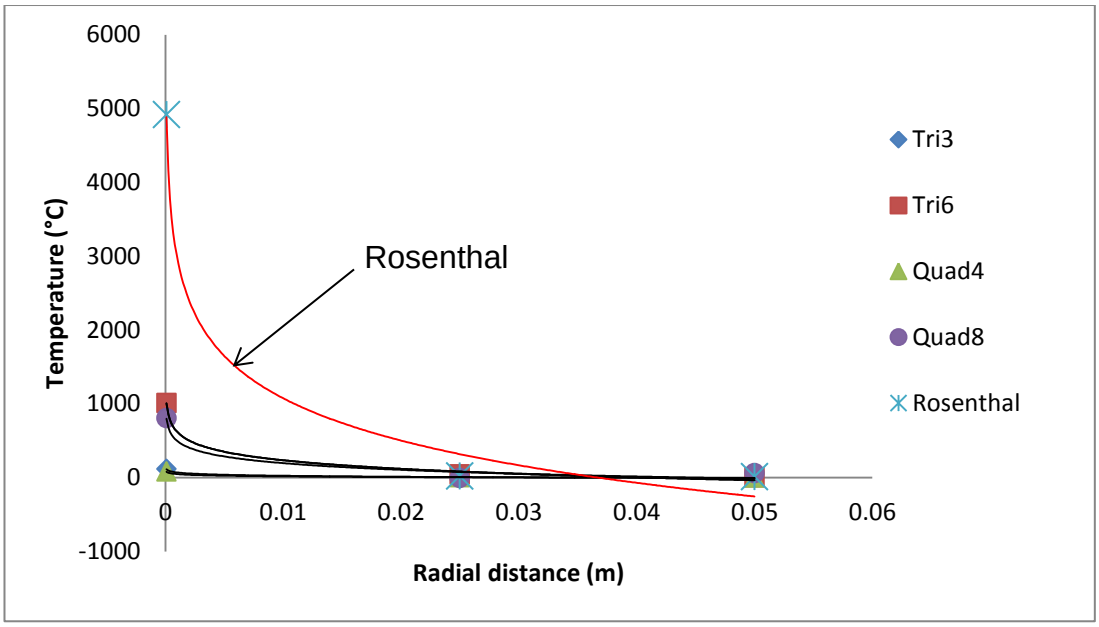

a) Temperature distribution for different element types, resolution 2x2

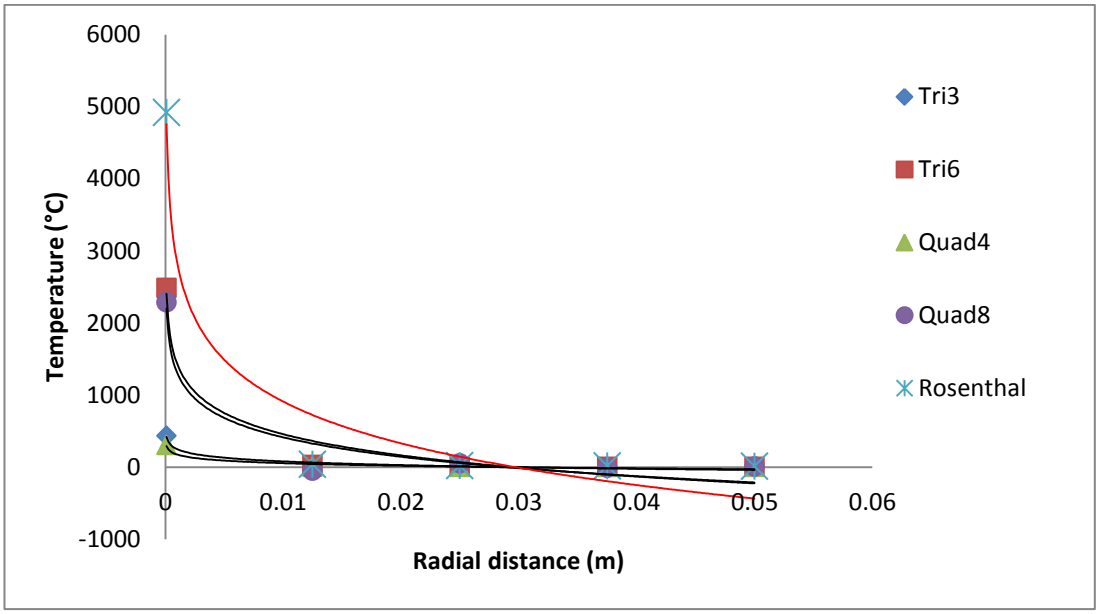

b) Temperature distribution for different element types, resolution 4x4

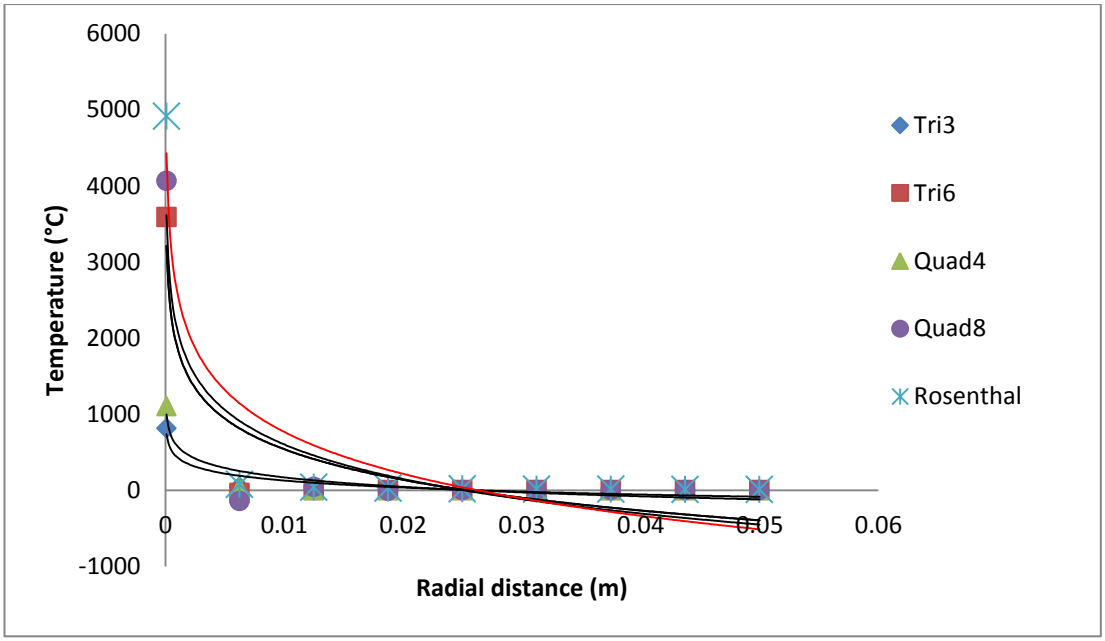

c) Temperature distribution for different element types, resolution 8x8

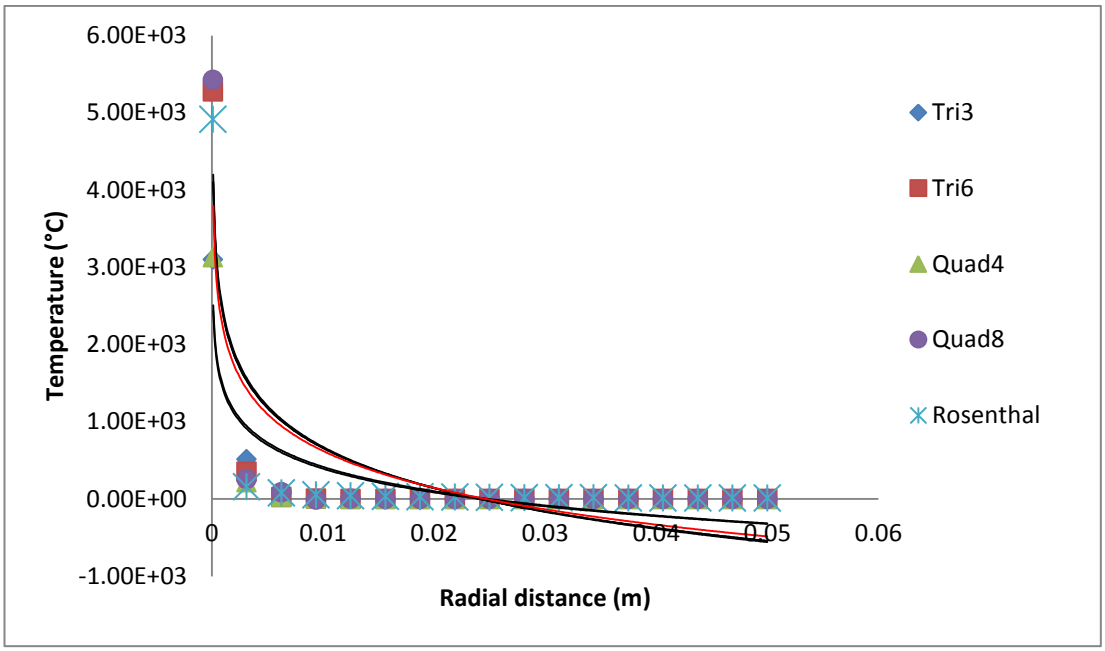

d) Temperature distribution for different element types, resolution 16x16

Figure 4-9 Compare different element type and size for result accuracy examination

Although Tri 6 and Quad 8 element type delivered the temperature results closer to the Rosenthal solution than Tri 3 and Quad 4 element type, negative values of the temperature were found which broke the heat conduction rule and was not acceptable. Using Tri 3 and Quad 4 element type needs higher resolution to get more accurate result. In resolution 2x2 and 4x4, Tri 3 delivered the results closer to the Rosenthal solution; while in resolution 8x8 and 16x16, Quad 4 is closer. Also, using Quad 4 mesh type needs less calculation time than the other three types according to the ABAQUS record. Therefore Quad 4 was chosen for two dimensional element type, and related to three dimensional modelling, Hex 8 element type was chosen. To obtain accurate results from the model working, relevant high resolution meshing methods was used, with each element size of 0.025mm. This size was chosen based on the layer thickness used in the experiment.

4.4 Moving heat source application

The load used in the heat transfer modelling is the input heat source, which contains input heat or power, shape and moving speed of the heat source. Input power and shape of the laser can be measured by the methods used in section 3.2.1, and moving speed can be defined by the user.

ABAQUS/CAE provides three default defined heat sources, which are concentrated (point) heat flux, surface heat flux and body heat flux. All default heat sources have a uniform distribution, which is not applicable to a moving laser.

To describe complex distribution and moving heat source, a user subroutine DFLUX (Defined Heat Flux) was written in FORTRAN. The DFLUX program contained DFLUX interface, user defined moving speed with initial coordinates and processing coordinates, input heat and user defined heat distribution. In all three dimensional modelling works in this thesis, a Goldak body heat source was used. The description and solution of the Goldak heat source can be found in section 2.5.3.

DFLUX subroutine presents the moving heat source is shown below:

```
DFLUX(FLUX,SOL,JSTEP,JINC,TIME,NOEL,NPT,COORDS,JLTYP,TEMP,
PRESS,SNAME)

    INCLUDE 'ABA_PARAM.INC'

    parameter(one=1.d0)

    DIMENSION COORDS(3),FLUX(2),TIME(2)

    CHARACTER*80 SNAME

      q=5000

      v=0.2

      d=v*TIME(2)

      x=COORDS(1)

      y=COORDS(2)

      z=COORDS(3)

      x0=0

      y0=0

      z0=0.05

      a=0.0028

      b=0.0034

      c=0.0032

      PI=3.1415

      heat=6*sqrt(3.0)*q/(a*b*c*PI*sqrt(PI))

      shape=exp(-3*(x-x0)**2/c**2-3*(y-y0-d)**2/a**2-3*(z-z0)**2/b**2)

      JLTYP=1

      if (JSTEP. eq. one) then
```

*FLUX(1)=heat*shape*

endif

RETURN

END

An initial model for a moving heat source application was established on a solid material state medium. It helped to analyse the laser processing parameters rather than material properties in the SLM process, and obtain reliable results related to the experiments. The moving speeds of the heat source were 150mm/s, 200mm/s, 250mm/s and 300mm/s, set the same as in the experiments. The energy of heat source was calculated based on a laser power of 50W with relevant beam diameter. Considering the laser energy absorption, a measured coefficient of 67% [53] was used.

4.5 States variable material properties study

In the SLM process, the powder melted by the laser will transfer to the solid when the laser moves away and the melt region cools. So during the whole process, three material states – powder, liquid and solid exist, and need to be considered for the heat transfer modelling. There are significant differences of physical and thermal properties between powder and solid material, which affect the analysis results. To have a reliable and accurate model, material properties would need to be updated to reflect the state (powder, liquid and solid) at that point (element) in space and time.

To define states variable material properties, user subroutine UMAT (User Defined Material Property) was written in FORTRAN. The overall structure of the UMAT file is shown in Figure 4-10.

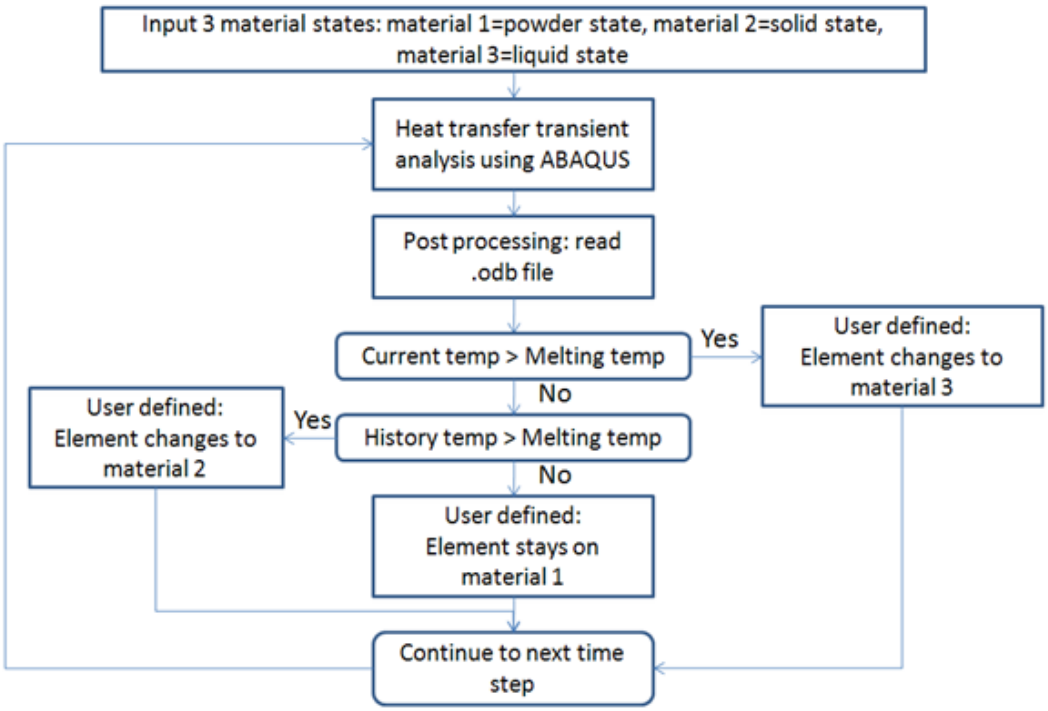

Figure 4-10 UMAT structure for states variable material properties

A model for the moving heat source applied on states variable material properties medium was established. Another two models for moving heat source applied on solid material state medium and powder state medium were also established as comparisons. The heat input for all three models were the same, which were the moving speeds of the heat source of 250mm/s, laser power of 50W with a beam diameter of 0.03mm. Considering the laser energy absorption, a measured coefficient 67% [53] was used. The boundary conditions for all three models were kept constant. Results for the comparisons can be found in chapter 8.

4.6 Multi-layers model establishment

A Multi-layer model was established based on the single layer modelling results. In the SLM process, after laser scanning of the current layer

completes, powder within the melting zone transfers to solid, while powders outside the melting zone remain in the same state. When the next powder layer is delivered to the build area, the analysis zone should a have top layer applied on states variable material properties, part of the underneath layer applied on states variable material properties, and part of the underneath layer applied on solid material properties. The area of solid material region can be obtained from the previous layer analysis. A schematic of multi-layers model establishment is shown in Figure 4-11.

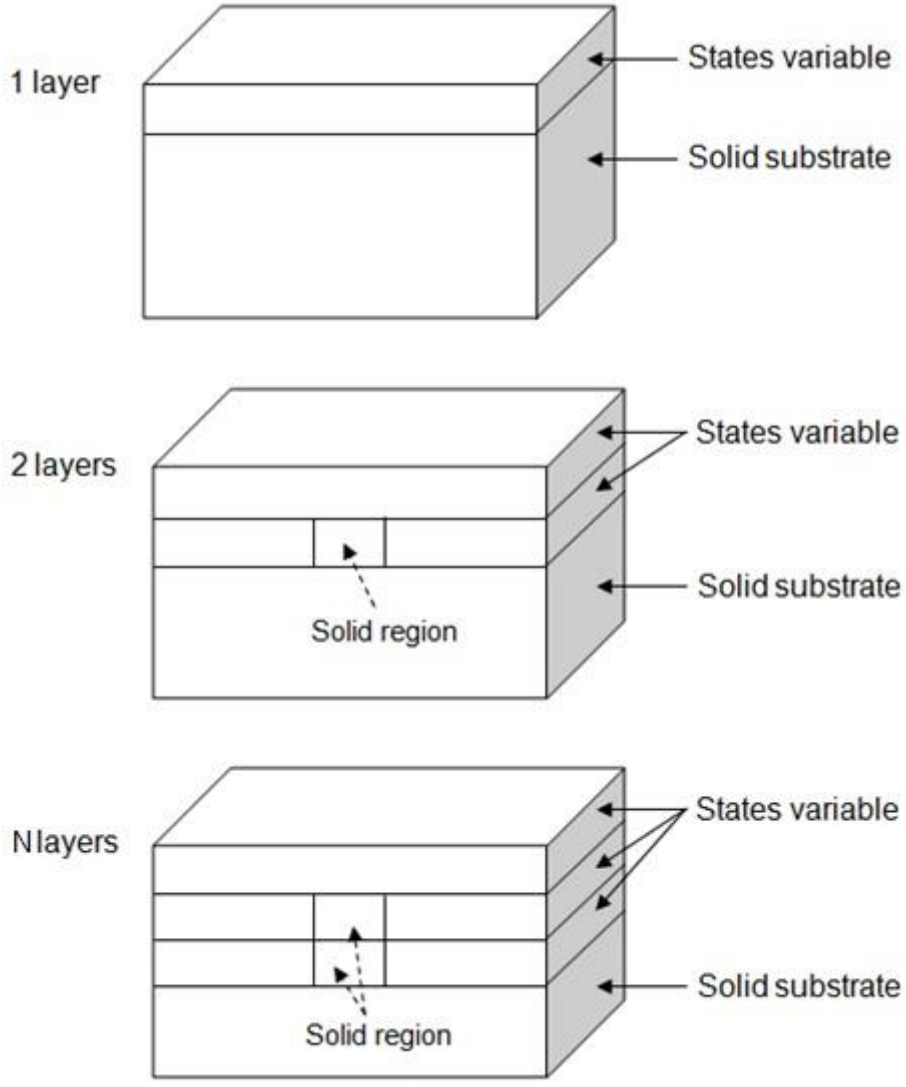

Figure 4-11 Schematic for establishing multi-layers model

4.7 Summary

FEA heat transfer models were established to simulate the laser melting process and predict the melting pool behaviour, temperature distribution on the powder bed and part's microstructure in the SLM process. The results obtained from the modelling work provided in-depth knowledge for manufacturing parameters optimisation and part's quality control.

A regular shaped cuboid was selected for the geometry used in the model. It was a full solid geometry with powder properties applied to simulate the powder bed.

Different types of boundary conditions were investigated and applied to each side of the cuboid. The top surface was a forced convection surface, while the four side surfaces were continuous heat conduction surfaces with the same thermal properties as the powder bed. The bottom surface could be a constant temperature boundary or a conduction surface depending on if pre-heating was applied.

A meshing method was discussed as it was important for a FEA model. Constant distance between seeds was selected for seeding the whole geometry. Element type Quad 4 was chosen for 2D geometry, and Hex 8 was chosen for 3D geometry.

A moving heat source applied to the model was defined by the DFLUX subroutine, which contained the shape, energy input and velocity of the laser beam, to simulate the laser scanning process. The material properties of the model were states variables to reflect the material state changes during the build. This states variable was defined by a UMAT subroutine.

A multi-layer model was established as a further step to develop the model into 3D analysis, and simulate the layer by layer manner of the SLM process.

5 Results & Discussions - SLM Process Control Parameters

5.1 Introduction

This chapter presents the results and analysis from first part of the experimental programme – SLM process understanding and optimisation. The overall experiment method for this part was described in section 3.3. The results of the energy input study are presented and analysed in the next section, followed by the build condition investigation and discussion.

In the energy input study section, experiments were carried out on examining the optical scanning system and comparing different scanning strategies. Samples were built and tested with these controllable process parameters to study their influence. Trends for each process factor's effect on the built parts' physical and mechanical properties are obtained and discussed.

In the build conditions study section, the processing environment was investigated and discussed. The results show the effects of gas flow in the processing chamber and pre-heating applied to the build substrate on the built parts' physical and mechanical properties. There are also results that present the issues happened during the melting process when improper energy input was delivered and when the equipment failed to detect the right oxygen level in the chamber. These results were analysed and possible reasons are discussed.

5.2 Energy input study

5.2.1 Laser profiles examination

The laser working mode was tested using an oscilloscope, Teledyne LeCroy Wavejet 324A. A stable and continuous signal with constant power was detected during the testing, which indicated that the laser used in MCP SLM 100 worked on a continuous mode.

The laser power was tested under static mode and scanning mode. Five different laser output powers 10W, 20W, 30W, 40W, 50W (1A, 2A, 3A, 4A, 5A) were set for static mode, and three of the most often used different scanning speeds 150mm/s, 200mm/s, 250mm/s all under a constant power output of 50W (5A) were set during the scanning mode. Results are shown in Table 5-1 and Table 5-2. The detected power was stable under both static mode and scanning mode.

Output power setting	Detected power	Constant value or change
10W	7.2W	Constant
20W	17.6W	Constant
30W	27.8W	Constant
40W	37.9W	Constant
50W	47.5W	Constant

Table 5-1 Laser power detected under static mode

Scanning speed	Output power setting	Detected power
150mm/s	**50W**	46.8~48.7W
200mm/s	**50W**	46.5~49.4W
250mm/s	**50W**	46.7~49.3W

Table 5-2 Laser power detected under scanning mode

The laser beam profile was examined by setting the laser in the static mode and firing the laser only. To avoid damage to the detector, a maximum power of 25W was set according to the beam profiler user manual. Due to the characteristic of the laser, the beam width was wider when increasing the power to 50W, which is the power used in the experiments for building samples in this research. Based on the Gaussian solution, equation (2.5) to equation (2.7), proportional relation between the power P and the beam width w_0 is shown in equation (5.1). Therefore, the beam width at 50W can be calculated based on the beam width result measured at 25W.

$$P \propto w_0^2 \tag{5.1}$$

The measurement results were obtained and processed by BeamStar software, provided by Ophir Optronics™. Results from setting the power outputs at 25W, lens focus position 14.50mm are shown in Figure 5-1. A commonly used definition of the beam diameter is the width at which the beam intensity has fallen to $1/e^2$ (13.5%) of its peak value [178]. This is derived from the propagation of a Gaussian beam and is appropriate for lasers operating in the fundamental TEM_{00} mode or closely [179]. Another common definition of the beam diameter is the full width at half-maximum (FWHM) diameter, which the beam intensity has fallen to 50% of its peak value [180]. A problem with this type of definition is that the result does not depend on how quickly the intensity decays in the wings of its intensity profile [178,181]. Therefore, 13.5% of peak was used for defining the beam diameter in this research. The laser used in MCP SLM 100 has a relatively standard Gaussian TEM_{00} distribution, with beam diameter around 0.03mm when setting lens focus position at 14.50mm.

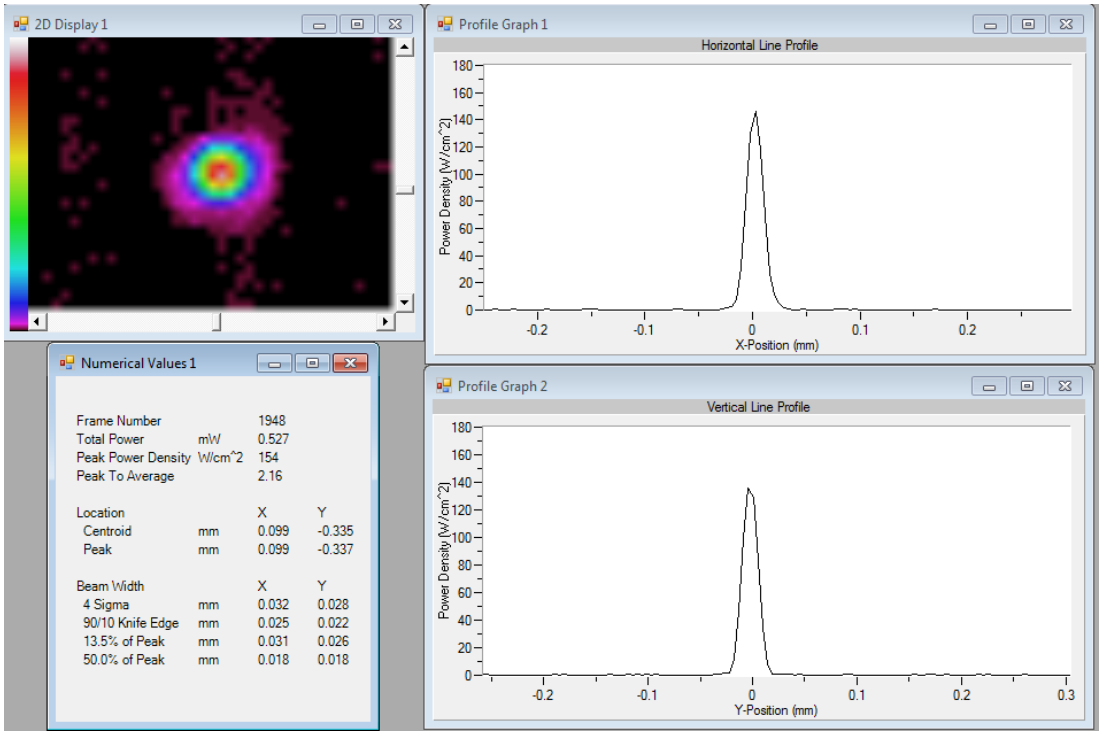

Figure 5-1 Laser beam profile under 25W power, 14.50mm lens focus position

5.2.2 Laser focus position and energy intensity study

In the MCP SLM-Realizer 100, the laser beam diameter on the top surface of the powder bed can be controlled by changing the distance between two lenses inside the beam expander. Modifying the distance between two lenses can change the output laser beam width from the beam expander. When the laser beam reaches the focusing lens, a different beam width has different focus position, then the laser beam delivered on the top of the powder bed has a different diameter. A process parameter named “lens position” in the material file which controls the distance between lenses of the adjustable beam expander.

Lens position values were adjusted from 13.80mm to 14.90mm under static output laser power 25W for beam profile measurement. Typical results are shown in Figure 5-2, Figure 5-3 and Figure 5-4.

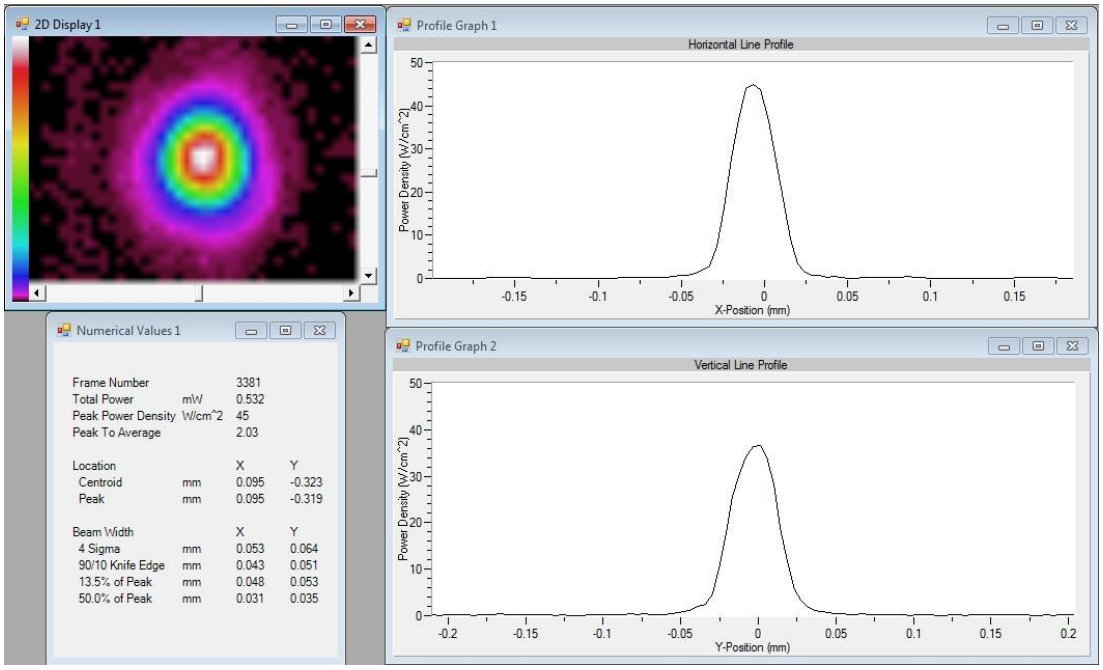

Figure 5-2 Laser beam profile under 25W power, 14.00mm lens focus position

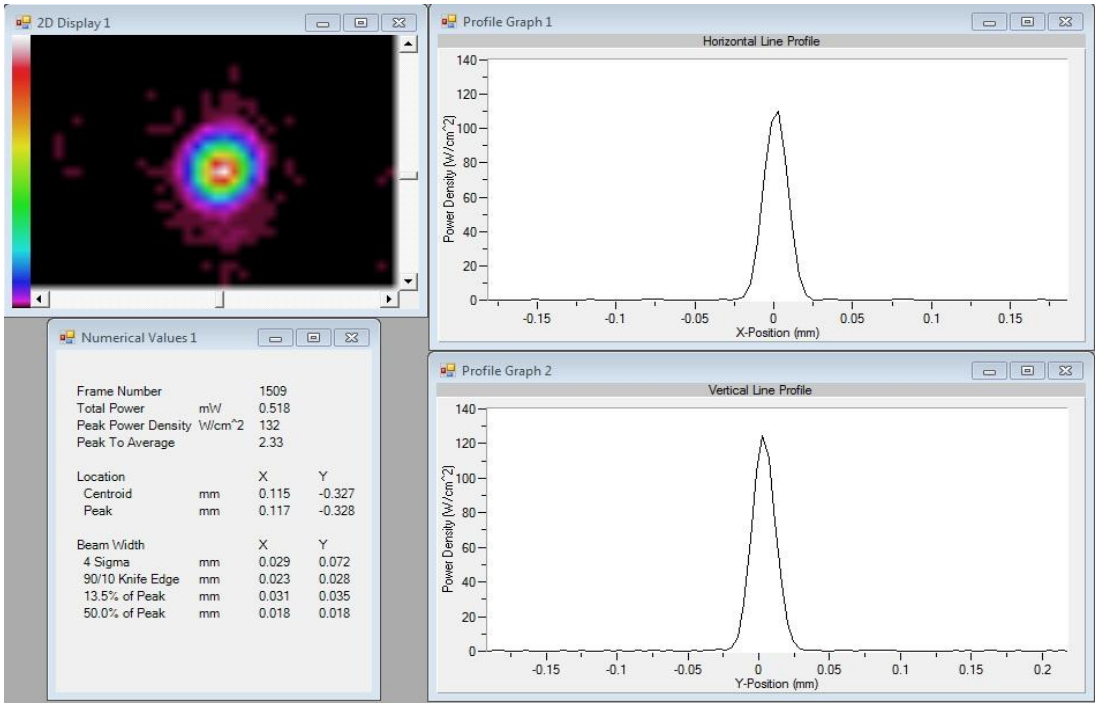

Figure 5-3 Laser beam profile under 25W power, 14.30mm lens focus position

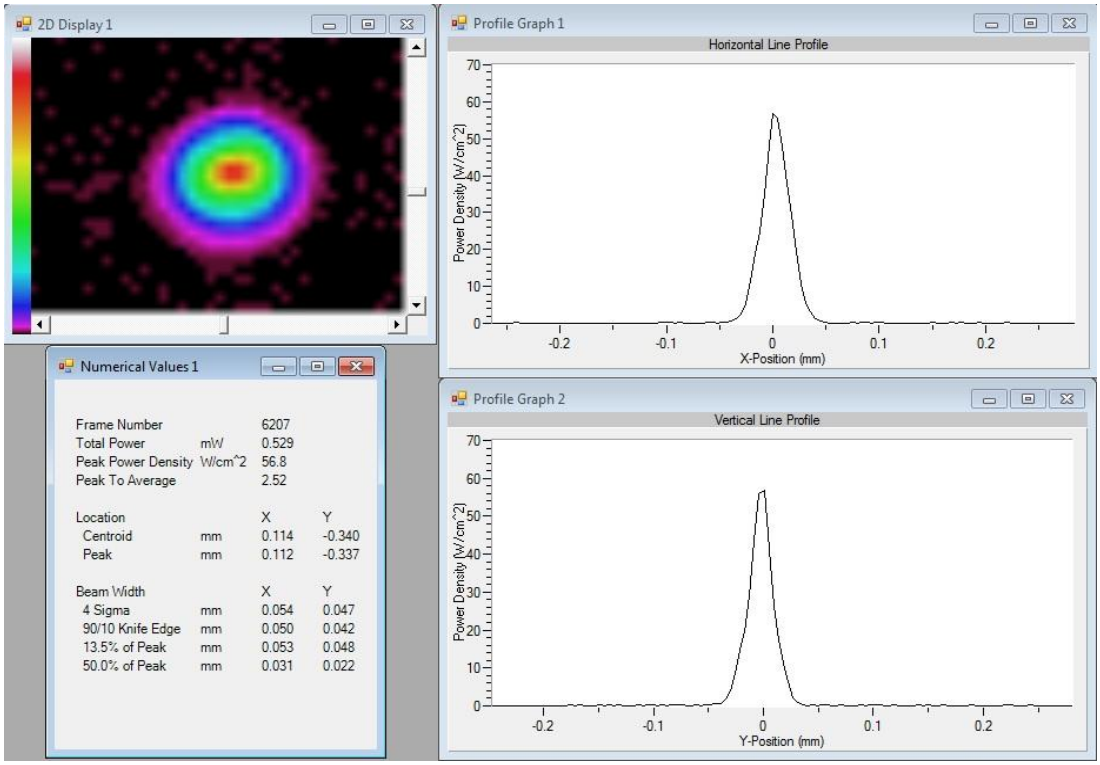

Figure 5-4 Laser beam profile under 25W power, 14.80mm lens focus position

The detected beam dimensions and power densities showed significant differences based on different lens position valued. A peak power density 154W/cm^2 was obtained when setting the lens position at 14.50mm, while the narrowest beam width 0.026mm-0.028mm was achieved when setting the lens position at 14.40mm and 14.50mm under the power of 25W. The measurement results indicate that the laser focused on the top surface of the powder bed when setting the lens position at 14.50mm.

Suggested by MCP engineer, to find the lens position value for focusing the laser beam on the top of the build surface, 3M™ Laser Markable Label was ablated by the laser beam under lens position values from 13.70mm to 15.70mm, as shown in Figure 5-5. Due to temperature sensitivity of the top layer of the laser paper, a very low laser power of 5W was used in the experiments. After scanning, the laser paper with all the marks on it was examined under an optical microscope. It was observed and measured that using value 14.50mm resulted a brightest and narrowest bright section

compared with others, as shown in Figure 5-6, which has agreement with the beam profiler measurement results.

Figure 5-5 Firing laser onto laser markable label under different lens position value

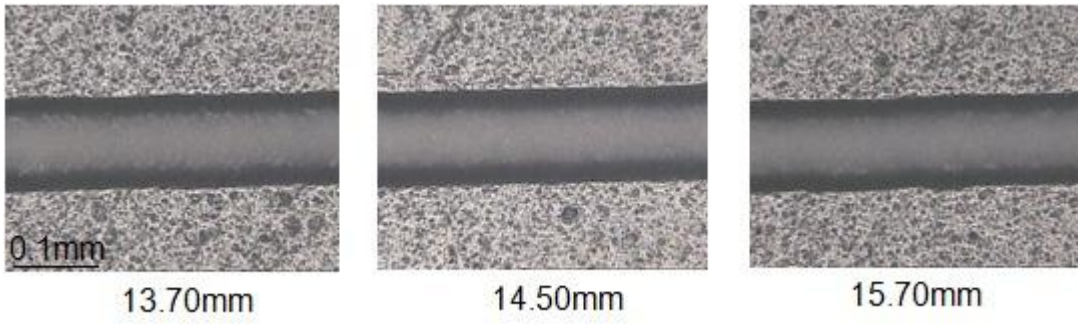

Figure 5-6 Marks on the laser paper under optical microscope, same magnification for all three images

Based on the results in Figure 5-6, 3 sets of eight 10mm cuboid blocks were built using lens position values of 14.10mm, 14.20mm, 14.30mm, 14.40mm, 14.50mm, 14.60mm 14.70mm and 14.80mm to find the highest density. The laser equipped in the MCP SLM-Realizer 100 has the maximum power of 50W, which is not a high power used in SLM process compared with other commercial equipment. Therefore, during the process parameters optimisation study, the output laser was always set to 50W. All other

processing parameters were kept the same in the lens position study, such as scanning speed of 200mm/s, solid hatch distance of 0.08mm, layer thickness of 0.05mm, single scan per layer and no pre-heating process. Stainless steel 316L virgin powder supplied by LPW technology Ltd was used to build samples. The average measured density for each lens position value is shown in Table 5-3.

Lens position	**14.10 mm**	**14.20 mm**	**14.30 mm**	**14.40 mm**	**14.50 mm**	**14.60 mm**	**14.70 mm**	**14.80 mm**
Density	96.72% ±0.28	97.98% ±0.47	99.02% ±0.25	99.87% ±0.19	99.93% ±0.22	99.18% ±0.3	98.63% ±0.33	97.59% ±0.45

Table 5-3 Average density of samples built under different lens positions

Density was measured by cross sectioning the sample, and examining the porosity using an optical microscope and image processing software Adobe Photoshop CS4. The maximum density was obtained when the lens position value was 14.50mm. From beam profile measurement results, a lens position value of 14.50mm shows a laser focused on the top surface of the powder bed. When the laser is focused on the powder bed, the delivered energy to the powder bed is at its highest due to the narrowest beam width. High laser energy helps to fully melt the powder along the laser scanning track, therefore very few stainless steel 316L particles can remain unmelted. When the laser is out of focus, the delivered energy decreases even if the power remains constant. Lower energy input decreases the built part's density as the energy delivered to the powder bed cannot generate enough heat to fully melt all the particles. The trend observed from Table 5-3 shows agreement with the beam diameter measurements, while narrowest beam width presents the highest part’s density and the density decreases when the beam becomes wider, i.e. out of focus.

5.2.3 Building area variation

During the build area variation study, round tensile test specimens with a gauge length of 16mm and neck diameter of 4mm, designed according to ASTM E8-09 were built as a set of concentric circles with radius 18mm, 36mm and 54mm, as shown in Figure 5-7. Four specimens were built in each circle to avoid any error in examination. Stainless steel 316L virgin powder supplied by LPW technology Ltd was used to build the samples. The main processing parameters include laser power of 50W, lens position of 14.50mm, scanning speed of 150mm/s, solid hatch distance of 0.08mm, layer thickness of 0.05mm, single scan per layer and no pre-heating process. Gauge area diameter, density and tensile strength of each specimen were tested and compared to study the variation. Tensile strength (UTS) at break was tested using Instron 3369.

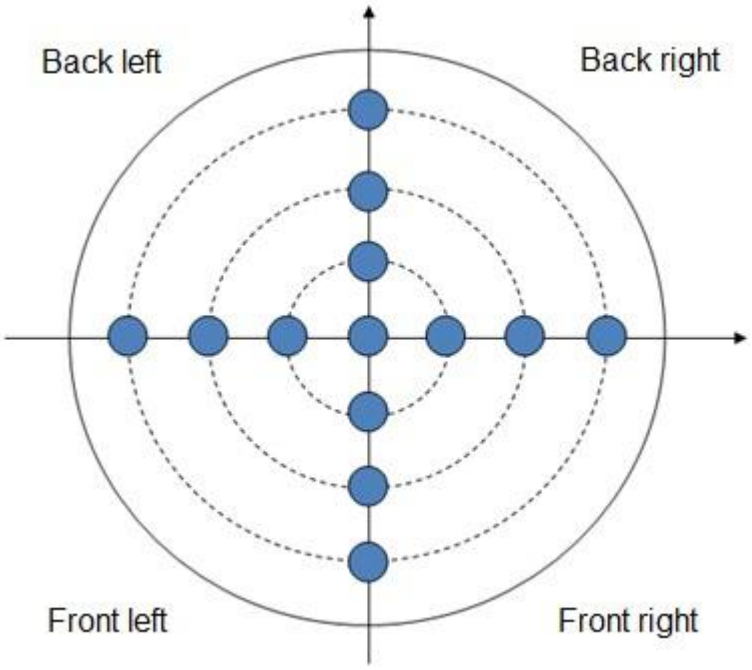

Figure 5-7 Top view of building area variation study orientation

Results from the build area variation study experiment are shown in Table 5-4 (Gauge area diameter), Table 5-5 (Density) and Table 5-6 (Tensile strength).

Position	No.1 (back)	No.2 (right)	No.3 (front)	No.4 (left)	Average
Centre	4.03mm	-	-	-	-
18mm circle	4.03mm	4.03mm	4.03mm	4.03mm	4.03mm
36mm circle	4.03mm	4.03mm	4.03mm	4.02mm	4.03mm
54mm circle	4.03mm	4.04mm	4.03mm	4.03mm	4.03mm

Table 5-4 Measured gauge area diameter of specimens

The measured gauge area diameters stay close for all 13 specimens. The average value is 4.03mm, with a standard deviation of 0.004mm. The variation for the built part's size is 0.1% and can be ignored. It indicates that there is no effect of the laser incidence angle, and the laser spot shape on the top surface of the powder bed stays nominally circular.

Position	No.1 (back)	No.2 (right)	No.3 (front)	No.4 (left)	Average
Centre	99.1%	-	-	-	-
18mm circle	99.1%	99.0%	99.1%	98.8%	99.0%
36mm circle	98.6%	99.6%	99.3%	98.8%	99.1%
54mm circle	99.2%	99.5%	99.3%	98.7%	99.2%

Table 5-5 Measured density of specimens

The measured density varies among all 13 specimens. It also varies between 4 specimens in the same circle. This can be caused by the density measurement method error, and is difficult to avoid. The average value was 99.1%, with the standard deviation of 0.3%. The density result here was lower than the ones in Table 5-3, and was mainly caused by the focal position change in the machine. The variation for the built part's density is relatively low. Therefore, the energy intensity delivered to the powder bed does not vary throughout the whole building area.

Position	No.1 (back)	No.2 (right)	No.3 (front)	No.4 (left)	Average
Centre	672.4MPa	-	-	-	-
18mm circle	672.7MPa	672.2MPa	676.1MPa	672.3MPa	673.3MPa
36mm circle	668.5MPa	677.8MPa	675.1MPa	672.4MPa	673.4MPa
54mm circle	672.9MPa	675.3MPa	673.3MPa	670.7MPa	673.1MPa

Table 5-6 Tensile strength (UTS) of specimens

The average value of tensile strength (UTS) at break is 673.2MPa, with the standard deviation of 2.4MPa. The variation of tensile strength is minimal, which proves that the laser energy delivered to the powder bed does not vary significantly throughout the whole building area.

A statistical hypothesis test, one-sample t-test, was performed in Microsoft Excel 2010 to study the significance level of the UTS results variation. The analysis results show a t statistic value of 0.0115, which is smaller than the t critical value of 1.7823. Also the p-value is 0.4955, which is larger than the common significance level 0.05 [182]. Therefore, the data analysis showed the variation of the UTS results was not significant at a significance level of 5%.

All the measurement results indicate that the F-theta lens equipped inside MCP SLM-Realizer 100 works well to provide a flat field at the image plane of scan, and deliver the laser energy uniformly to the powder bed throughout the whole building area.

5.2.4 Scanning speed

Four different scanning speeds of 150mm/s, 200mm/s, 250mm/s and 300mm/s were used on processing the stainless steel 316L virgin powder supplied by Sandvik Osprey Ltd. Flat tensile test specimens with a gauge length of 25mm and thickness of 3mm, designed according to ASTM E8-09, were built in parallel with gas flow direction to examine the density and tensile strength (UTS), shown in Figure 5-8.

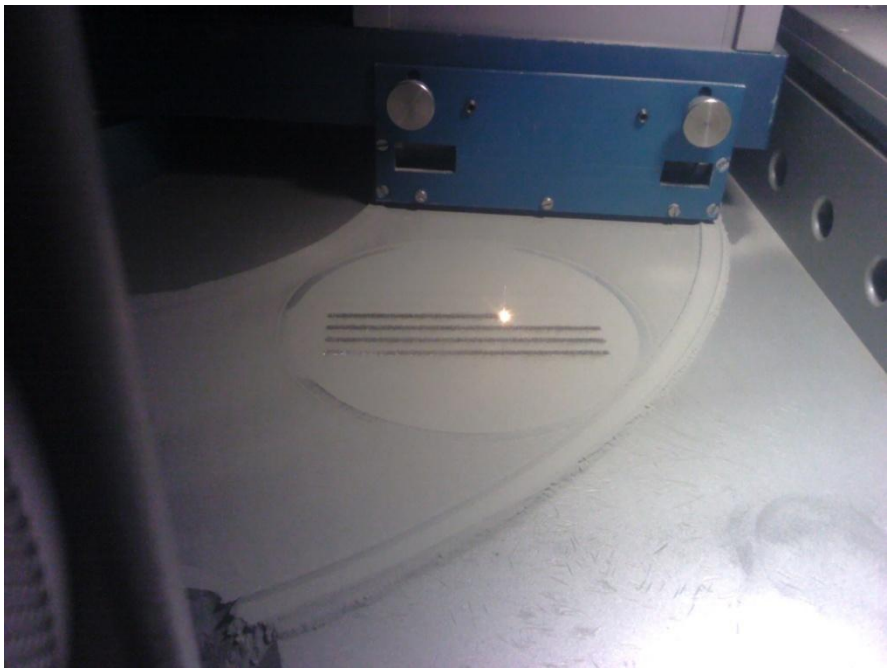

Figure 5-8 Tensile test specimens built in parallel with gas flow direction

In each group, 6 specimens were built on the constant position using the same processing parameters. All groups were built using the same

processing parameters except for scanning speed. The main processing parameters include laser power of 50W, lens position of 14.50mm, solid hatch distance of 0.08mm, layer thickness of 0.05mm, single scan per layer and no pre-heating process. In the material file which controls the machine processing parameters, scanning speed is obtained by point distance divided by exposure time. In this study, point distance was kept constant, and exposure time was varied.

Figure 5-9 shows the cross section images of specimens built by four scanning speeds and Table 5-7 shows the average density value. Generally, density increases while decreasing the scanning speed. There is a significant increase in density from 250mm/s (98.54%) to 200mm/s (99.65%). According to the solution of laser energy density, a decrease in scanning speed can increase the energy input per unit, which enables higher temperature created and more powder melted. Using faster scanning speed decreases the melt pool's width and depth due to the shorter interaction time [4], and generates a smaller heat affect zone while more particles remain unmelted.

There is a small drop in density from 200mm/s to 150mm/s with even more energy delivered on the powder bed. This can be caused by small particles vaporising during the laser-powder interaction process due to the high energy intensity [71], and leaving small pores inside the part. It can also be caused by the balling issue that can occur during the consolidation process. Previous work showed that molten powder consolidates more preferentially to a spherical structure rather than consolidating into the previous layer when decreasing the scanning speed [77]. This indicates that the scanning speed is the main factor in determining the balling phenomenon [68]. Therefore even though a slow scanning speed generates more heat in the powder bed, it may be less helpful on producing fully dense parts in the SLM process.

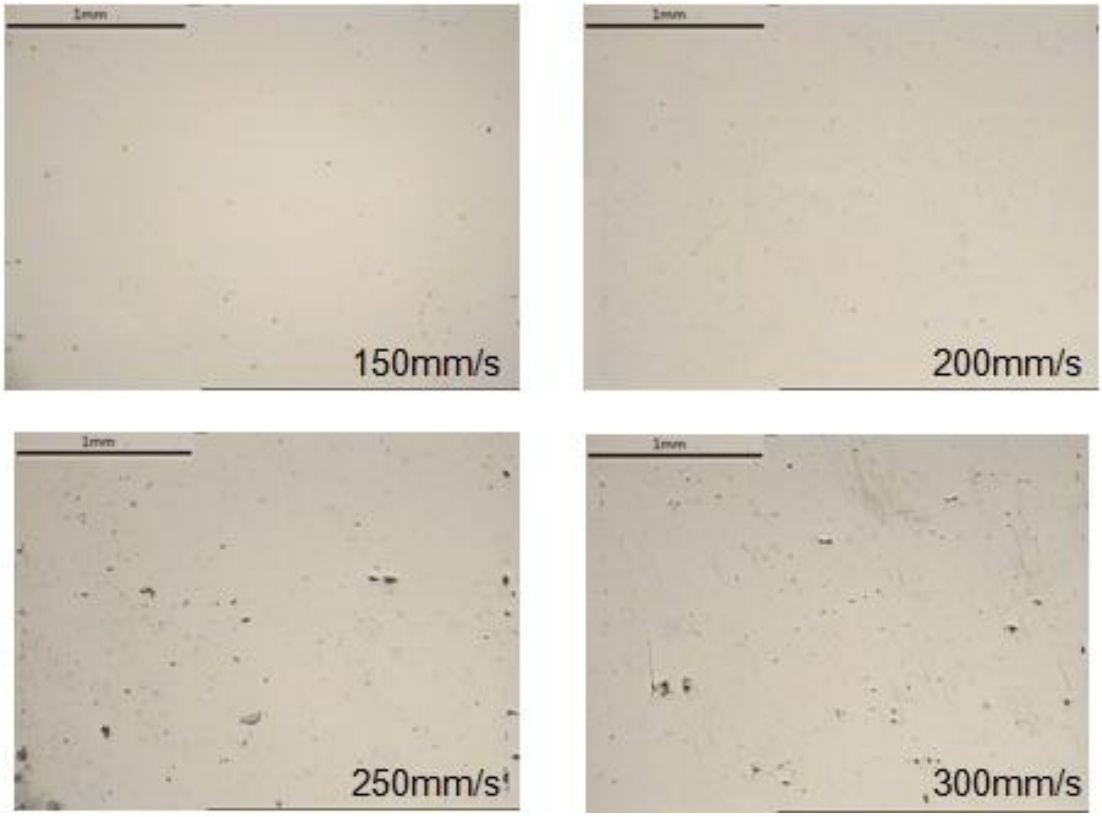

Figure 5-9 Cross sections of parts built by 4 different scanning speeds

Scanning speed	150mm/s	200mm/s	250mm/s	300mm/s
Average density	99.27% ±0.36	99.65% ±0.19	98.54% ±0.25	98.13% ±0.38

Table 5-7 Average densities of parts built by 4 different scanning speeds

Table 5-8 shows the average tensile strength (UTS) and elongation at break values with standard deviation. When the density increases, UTS and elongation increase relatively; while density decreases, they decrease too. All these results show that even high energy density may not create high quality part. Therefore, it is important to investigate all the processing parameters to obtain suitable energy input, rather than simply delivering high energy intensity into the powder bed.

Scanning speed	150mm/s	200mm/s	250mm/s	300mm/s
UTS (MPa)	594.81±3.52	609.59±3.31	564.49±1.91	554.87±2.53
Elongation (%)	33.04±0.79	36.65±1.90	29.04±1.05	25.53±1.08

Table 5-8 Tensile strength and elongation at break of parts built by 4 scanning speeds

5.2.5 Hatch distance

The production of thin walls is the initial study for hatch distance determination. Different samples were built throughout the control of laser scanning speed on processing the stainless steel 316L virgin powder supplied by Sandvik Osprey Ltd. The main processing parameters include laser power of 50W, lens position of 14.50mm, layer thickness of 0.05mm and no pre-heating process. The laser scanning speeds were 158mm/s, 176m/s, 200mm/s, 230mm/s, 250mm/s, 273mm/s and 300mm/s.

Built thin wall parts are shown in Figure 5-10, with a length and height of 10mm. Five samples on each scanning speed were built. Both the density and the thickness of the thin wall were measured. Density was measured by analysing the light transmittance of the thin wall samples. This method allowed a quick examination, but could not detect the closed cell porosity generated by particles evaporation. The thickness measurements were taken at three heights along each sample. Average measurement results of the density and thickness on each scanning speed are shown in Figure 5-11 and Figure 5-12.

As discussed in the last section, the melt powder layer thickness decreases while increasing the scanning speed, generating less overlap between layers in the Z direction. This can result the porosities between layers that can be

observed through light transmission. The thin walls also become thinner with high scanning speed applied due to smaller melt pool.

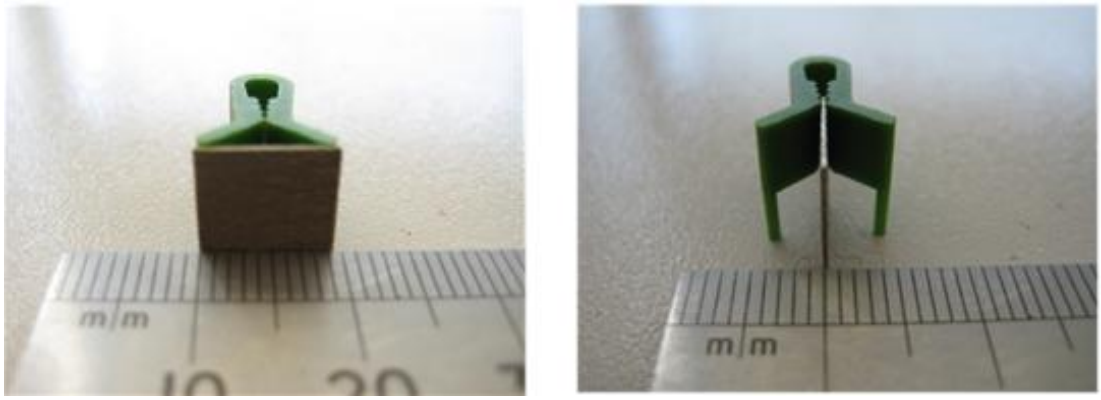

Figure 5-10 Thin wall built for hatch distance study

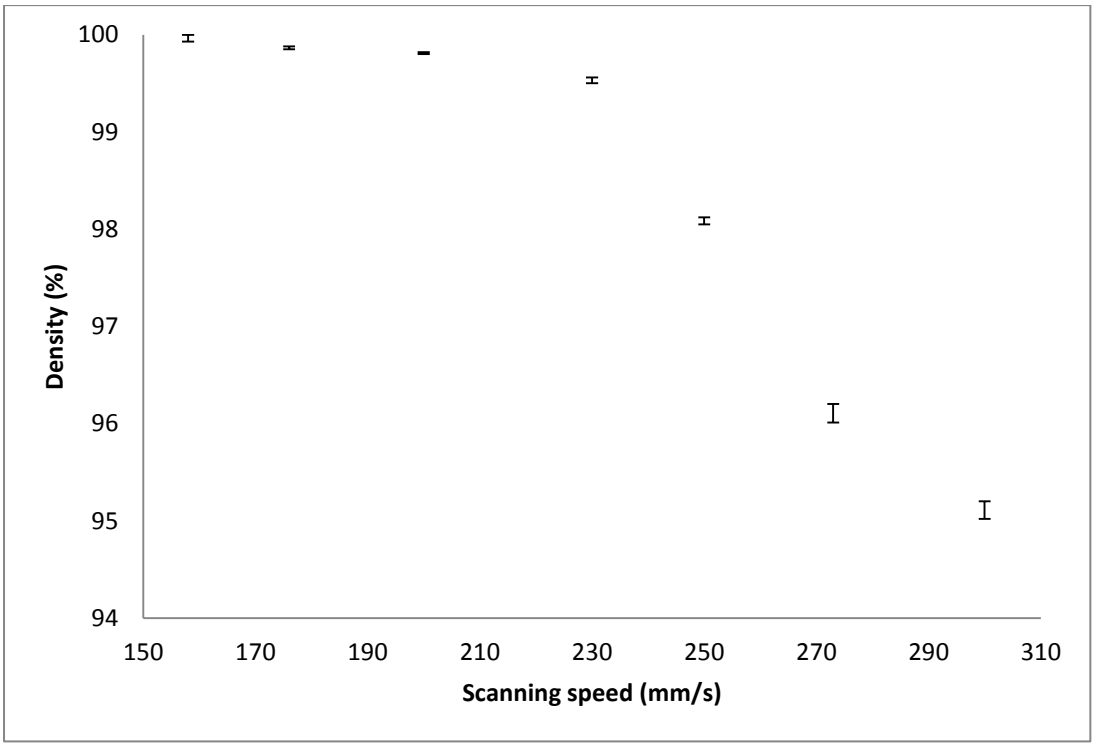

Figure 5-11 Measured densities of thin walls by different scanning speeds

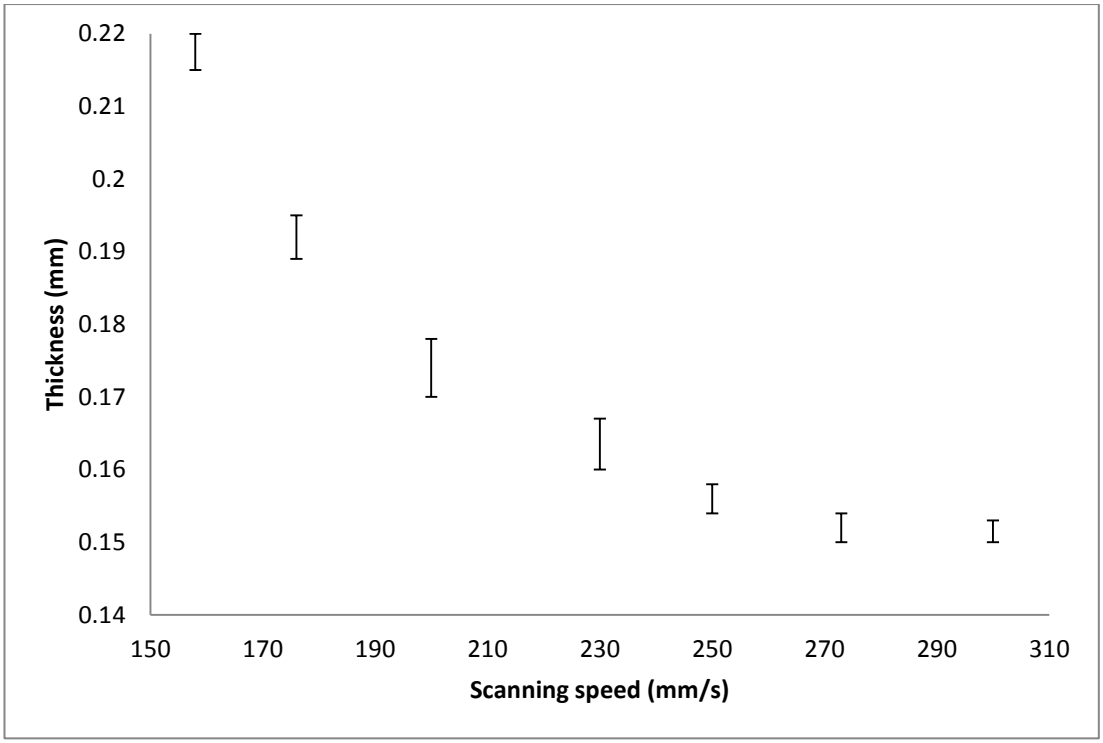

Figure 5-12 Measured thickness of thin walls by different scanning speeds

A fully dense thin wall with thickness of 0.175mm can be built on MCP SLM-Realizer 100 based on the processing parameters provided above. A minimum thickness of 0.15mm can be used in a joining scan/hatch distance study. The hatch distance should be 50%-80% of minimum thin wall thickness [4, 26], which are from 0.075mm to 0.12mm.

Three hatch distance values 0.08mm, 0.1mm and 0.12mm were picked for solid hatch distance study on stainless steel 316L virgin powder supplied by Sandvik Osprey Ltd. The main processing parameters stayed constant within thin wall study, but used a constant laser scanning speed of 200mm/s. Three cuboid blocks on each hatch distance were built, and average density results are shown in Figure 5-13.

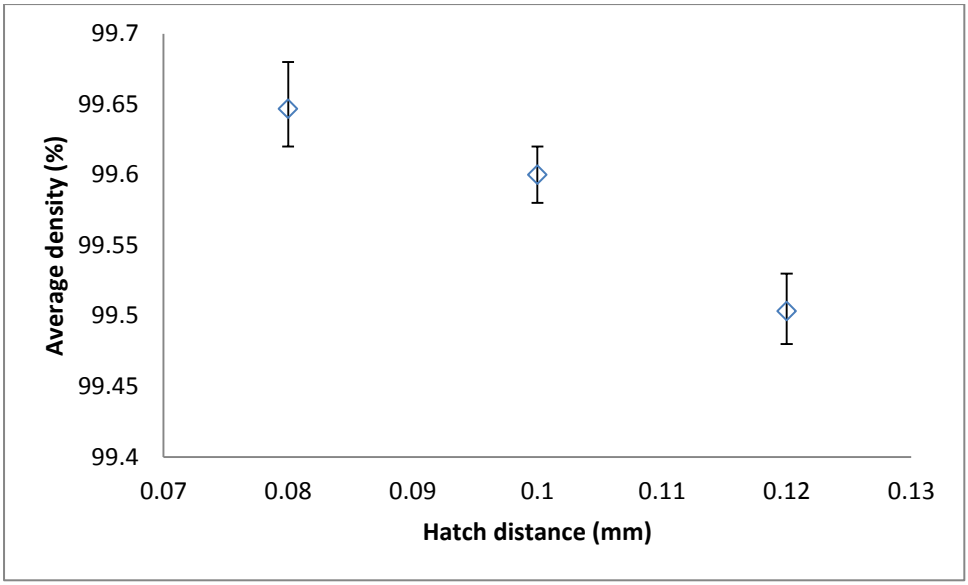

Figure 5-13 Average density on different hatch distance

Increasing the hatch distance decreases the melt powder layer thickness as less overlap between scan tracks separates the heat affected zone [76]. Therefore, hatch distance also controls the energy intensity on the powder bed and the size of the heat affected zone. Hatch distance can be involved in calculating the laser energy density in the SLM process, which develops Equation (2.9) into an area energy density solution showed in Equation (5.2), where D_h is the hatch distance. The unit for area energy density stays the same, because the unit directions of the laser beam diameter and hatch distance are the same.

$$E_\rho = \frac{P}{u\delta D_h} \ (J/mm^2) \tag{5.2}$$

Results showed that hatch distance affects the built part's density, but has less density control than scanning speed or lens focus position. Increasing the hatch distance from 0.08mm to 0.12mm caused 0.18% of a density drop, and the average density is still in higher than 99%. To get high density part, the value of 0.08mm was used on processing all the stainless steel powder.

5.2.6 Re-melting process

An experiment for studying the re-melting process was carried out by increasing the lens position value to 15.00mm to generate a larger laser energy affected zone for the re-melting process, and to help reduce the melt pool overlap effect on the top surface roughness. The other process parameters for skin hatch and processing parameters for inside solid hatch stayed constant. Surface roughness was measured by a Talylor Hobson Form Talysurf 50. Re-melt of the final layer in the SLM process introduced a significant decrease on average surface roughness of the top layer from 31.563μm to 12.912μm, as shown in Figure 5-14. The two parts shown in Figure 5-14 have the same shape, and compared areas are in the same position on the building platform. The part on the right was scanned by re-melting the last solid layer under lens position value of 15.00mm; with the left hand part did not have any re-melting scan. Parts were built using stainless steel powder provided by Sandvik Osprey Ltd.

Figure 5-14 Top surface improvement through re-melting process, L is the original part, R has been re-melted on the top surface

Re-melting the surface of the part was reported as an efficient way to reduce the top surface roughness [70]. It is also reported to reduce the residual stresses in the top layer [183]. There are also studies on combining the SLM

process and laser re-melting to improve the surface quality of outer surfaces of the SLM parts, while also improve the inner density of the part [184]. The pores formed in between neighbouring melt pools disappear after laser re-melting each layer generated in the SLM process. The re-melting process also improves the current layer's surface roughness to allow the powder deposition more uniform for the next layer. Therefore, it is found that the laser re-melting after every layer is a promising method to increase the density of the SLM parts and to enhance the surface quality, especially top surface [184, 185].

5.2.7 Building direction

In the build direction study, tensile test specimens were built in both the X direction (parallel with gas flow direction) and Z direction (vertical to the powder bed surface) using the same processing parameters. Due to the build limitations of the machine, Z direction build cannot be higher than 70mm [173]. Therefore, flat tensile test specimens with a gauge length of 25mm and thickness of 3mm, designed according to ASTM E8-09 were built in the X direction, and round tensile test specimens with a gauge length of 16mm and neck diameter of 4mm, designed according to ASTM E8-09 were built on Z direction, shown in Figure 5-15.

Figure 5-15 Tensile test specimens built for build directions study

Round tensile test specimens were not suitable for building in the X direction. A vertical cross section was done on a round tensile test specimen built on X direction, shown in Figure 5-16. The cross section can be divided into two parts by a line going through the centre of the circle. The upper part has a regular circular shape, while the lower portion is more like an ellipse. This can be caused by not enough support force from the powder bed to support the solidified section, as the edge of the lower part is always built on the powder bed rather than a solid layer. Residual stresses which are reinforced by the high thermal gradients from melting to solidification in a short time also deform the part. Significant porosity between the boundary and internal solid scan can be observed in the lower part. This is also caused by the deformation during the process.

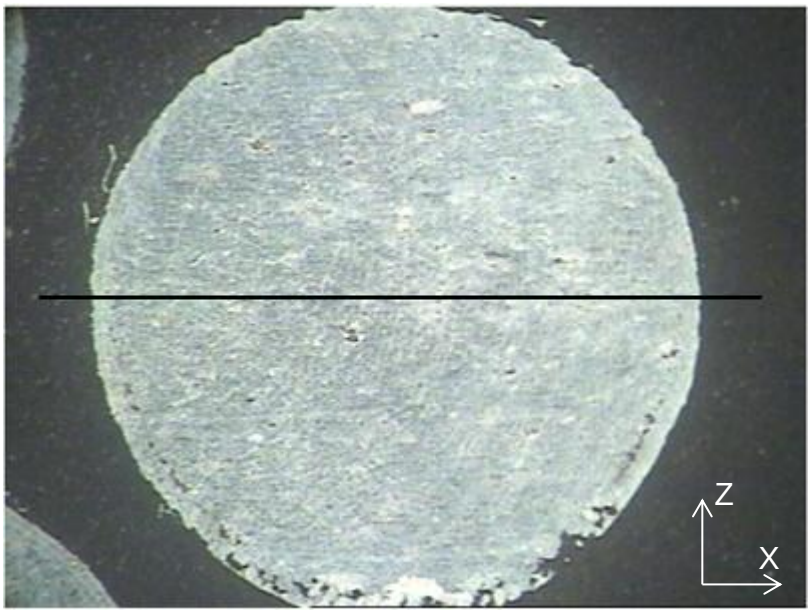

Figure 5-16 Cross section of round tensile test specimen built on X direction

Specimens were built using the stainless steel 316L virgin powder supplied by LPW Technology Ltd. The main processing parameters include laser power of 50W, lens position of 14.50mm, scanning speed of 200mm/s, solid hatch distance of 0.08mm, layer thickness of 0.05mm, single scan per layer

and no pre-heating process. All the tested parts were built in one build to avoid any build condition effect. Six tensile test specimen of each direction were built. Measured UTS and elongation at break of parts built on both X and Z directions are shown in Table 5-9.

Build direction	**X**	**Z**
UTS (MPa)	667.54±4.38	675.21±3.41
Elongation (%)	34.75±1.87	33.25±0.93

Table 5-9 Tensile strength and elongation at break under different build directions

The results of Z direction did not show significant decrease compared with X direction; and even slightly higher in UTS. The short time scan delay (10-15 seconds for depositing a layer of powder) did not decrease the bond strength between layers, and also the layer thickness of 0.05mm used in the process was small enough to allow a melting pool overlap between two layers. High energy input can also create a deeper melting pool, therefore, the bond between two layers was not weaker than the bond between two exposure points.

Due to the limitation of the powder container inside the processing chamber, topping up in the middle of building process with prepared powder was needed when building high parts (>30mm). The action of the topping up requires the machine to be paused until the topping up ends. This process can generate 20-30 minutes scan delay for the next layer. To study the effect of topping up on the bond strength between layers, tensile test specimens with topping up processes were built and tested. The specimens after being pulled are shown in Figure 5-17. From left to right, sample 1 and 2 were built with topping up delay during the process when building the gauge length

area, sample 3 to 6 were built without topping up delay during the process when building the gauge length area.

Figure 5-17 Tensile test specimens with/without topping up delay during the process have been pulled

Sample number	**1**	**2**	**3**	**4**	**5**	**6**
UTS (MPa)	496.55	512.87	678.23	673.44	672.28	676.52
Elongation (%)	5.62	6.01	34.12	33.78	33.25	33.39

Table 5-10 Tensile strength and elongation at break with/without topping up delay, samples were built in Z direction

Specimens with the topping up delay (20-30 minutes) can fail at the beginning of the test even with high density, resulting in low tensile strength and elongation, as shown in Table 5-10. They always break near the topping

up layer, while no topping up delay specimens would usually break close to the middle of the gauge length. This indicates that the topping up delay decreases the bond strength between layers. By providing the top layer enough time to completely cool, the top layer material has less activity with solidification procedure completes and the grains settle down. Residual stress in the top layer also affects the surface roughness to prevent uniform deposition of the powder material for the next layer. Therefore, to keep the bonding strength for the next layer, higher energy intensity should be delivered.

Topping up process can only affect the bond strength between two layers. Tensile test specimens built on X direction always break in the middle of the gauge length no matter with topping up process or not, shown in Figure 5-18. From top to bottom, sample 1 and 2 were built with a topping up delay during the process, sample 3 to 6 were built without topping up delay during the process. The delay did not affect the bond strength between two exposure points as they are not in the same vector direction. The UTS and elongation at break also remained similar for all six samples, as shown in Table 5-11.

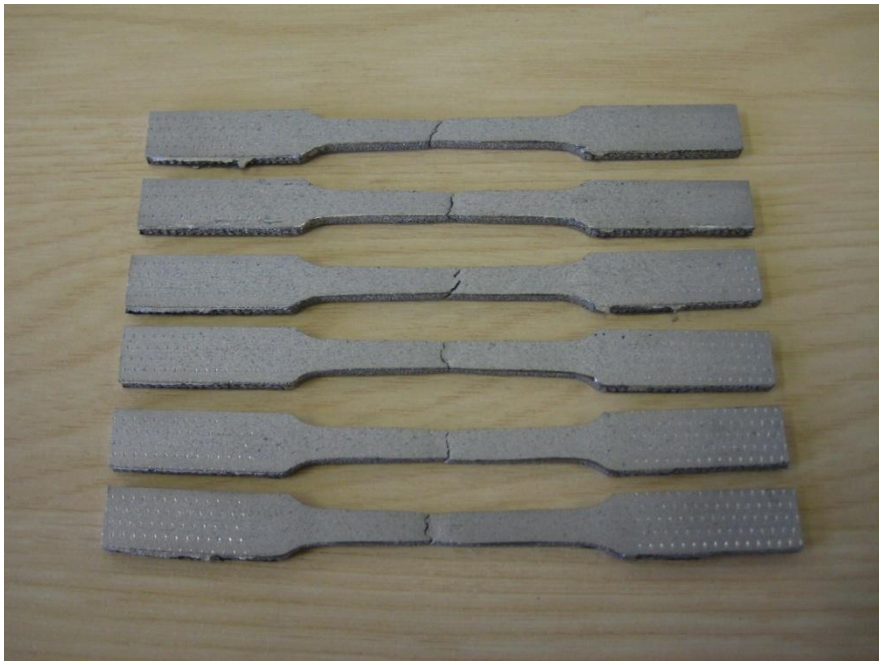

Figure 5-18 Tensile test specimens with/without topping up delay during the process have been pulled

Sample number	1	2	3	4	5	6
UTS (MPa)	661.48	662.39	665.33	660.54	668.25	671.33
Elongation (%)	34.12	33.98	34.17	33.78	34.23	34.59

Table 5-11 Tensile strength and elongation at break with/without topping up delay, samples were built in X direction

5.3 Building conditions

5.3.1 Processing environment

In the SLM process, the oxygen level in the chamber, detected by an oxygen sensor, should stay below 0.3% during the whole process [81]. The MCP SLM-Realizer 100 will not start building work until the oxygen sensor's reading is less than 1%, as an efficient way to protect the processing environment. To maintain the accuracy of the detected oxygen level, the oxygen sensor should be replaced after a certain period.

It has been observed that significant oxidation phenomenon happened when the oxygen sensor failed to detect the accurate oxygen level during the process. This produced darker powders when scanning, and caused porosity and delamination of the parts. The chemical composition of a collection of the 'darker powder' was measured by EDX, and the results showed a great increase in oxygen compared with fresh powder and recycled powder without oxidation, shown in Table 5-12 and Figure 5-19. SEM was used to present the images of several oxidised particles, shown in Figure 5-20. The dark spots on the particles contain high levels of oxygen, where a chemical reaction between the stainless steel 316L particle and oxygen happened.

This may due to the higher temperature at the shell of the particles provides more oxidation chances [112].

Oxidation can cause the reduction of molten material wet-ability, which can be a barrier to successful layer fusion and can cause porosity, balling, delamination and tearing due to surface tension effects [37]. Therefore, it is very important to avoid oxidation during the SLM process.

Element	C	O	Si	Cr	Mn	Fe	Ni
Weight %	2.38	14.62	7.29	15.1	6.85	46.6	7.15
Atomic %	7.23	33.31	9.46	10.59	4.55	30.42	4.44

Table 5-12 Chemical composition of one oxidised stainless steel 316L particle

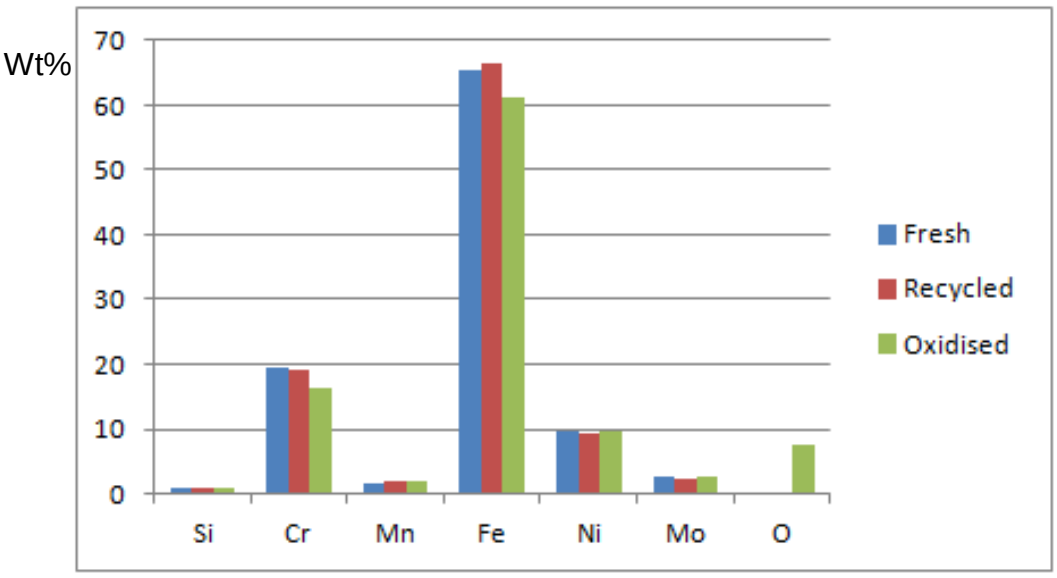

Figure 5-19 Chemical composition comparison between fresh, recycled and oxidised stainless steel 316L powder

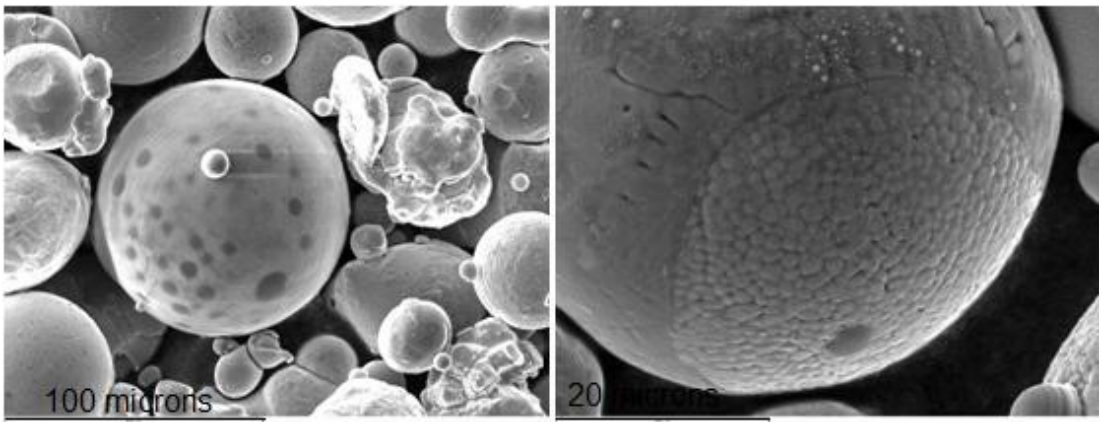

Figure 5-20 SEM images of oxidised stainless steel 316L particles

When improper high laser energy intensity was delivered to the powder bed, boiling pool or even plasma formation could be generated [54, 72]. The vaporised particles or plasma formation above the powder bed decrease the laser energy absorption, which generated dark particles during the process, shown in Figure 5-21. Collected dark particles were examined by SEM, shown in Figure 5-22.

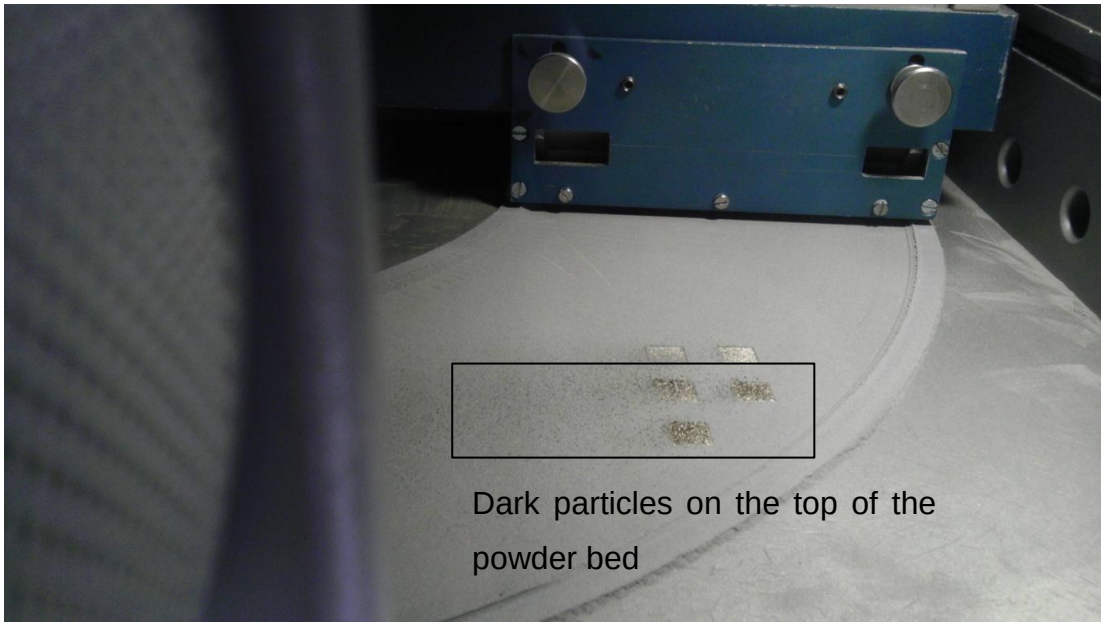

Figure 5-21 Dark particles generated by improper high laser energy intensity

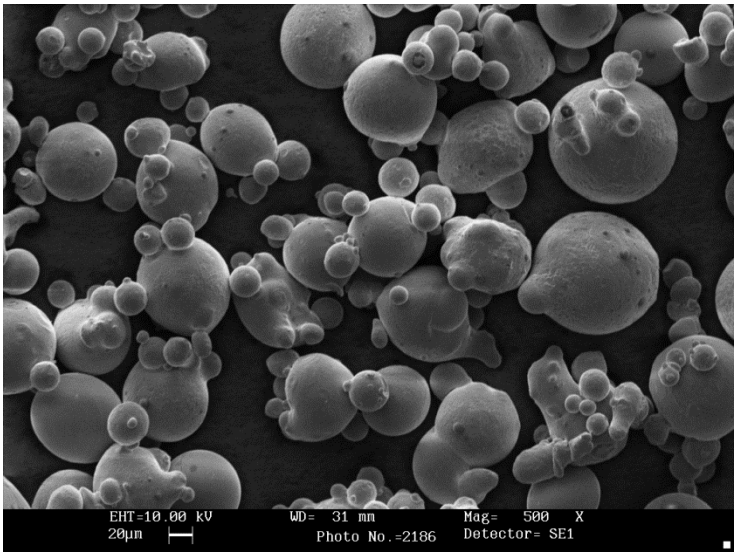

Figure 5-22 SEM image of dark particles generated by improper high laser energy intensity

Dark particles generated by improper high laser energy intensity in this case were not oxidised, since the dark dots on the particles in Figure 5-20 were not found in Figure 5-22. They are formed by series sizes of sintered particles generated during the boiling or plasma formation. These dark particles remained on the processing area while the laser was scanning, and caused a rough surface finishing, porosity and delamination of the parts.

During the laser melting process, the temperature of the exposed particles usually exceeds the melting temperature [91]. A further increase of the temperature to around 2900°C causes the material to evaporate. When this phase transformation occurs, the rapidly moving vaporised particles expand and generate a recoil pressure on the molten pool [91]. Nd:YAG laser can generate high energy intensity at 10^5 to 10^6 W/mm^2. At this high incident energy intensity, the vapour interacts with the laser radiation and becomes ionized, then a plasma is formed [102, 186]. The plasma decreases the energy intensity delivered to the powder bed and the laser energy absorption. Therefore, the laser sintered the particles rather than fully melting them. Vaporised particles are also evaporated, consolidated, sintered and left on the top of the powder bed.

Lowering of the power intensity by some orders of magnitude lower than the plasma threshold, it is reported that only evaporation takes place [91]. The evaporation decreases the density of the part in the SLM process and should be avoided. Therefore, to avoid the formation of boiling pool, evaporation or plasma formation during the melting process, suitable laser energy intensity should be delivered to generate a stable melting pool during the SLM process.

5.3.2 Effect of gas flow

Based on the building area variation study, an additional 8 tensile test specimens were built to study the variation caused by the gas flow. Stainless steel 316L virgin powder supplied by LPW technology Ltd was used to build samples. The main processing parameters include laser power of 50W, lens position of 14.50mm, scanning speed of 150mm/s, solid hatch distance of 0.08mm, layer thickness of 0.05mm, single scan per layer and no pre-heating process. Gauge area diameter and tensile strength of each specimen were tested and compared to study the variation. Results are shown in Figure 5-23, the green circles were the positions of additional 8 specimens.

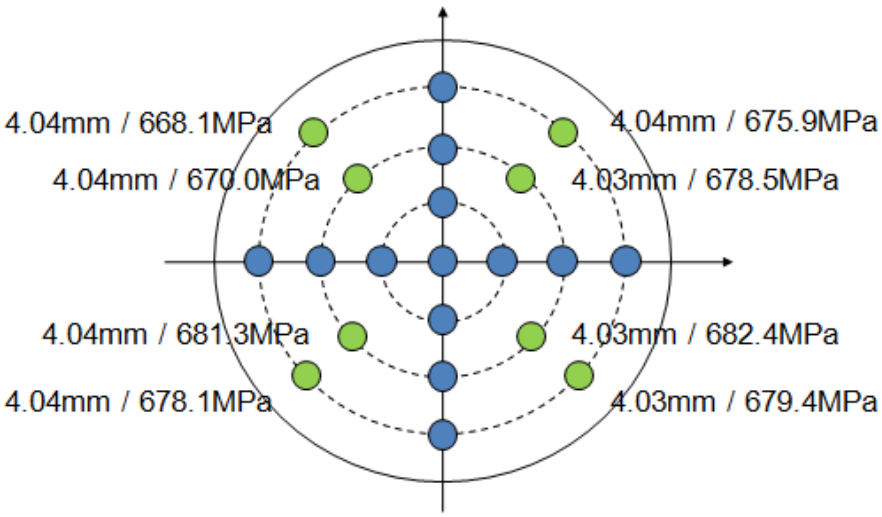

Figure 5-23 Results from gas flow effect study

The measured gauge area diameters stay close for all 8 specimens, and also close to the 13 specimens built for building area variation study. The average value is 4.036mm, with the standard deviation of 0.005mm. The variation for the built part's size is so small that can be ignored. It indicates that gas flow has no effect on the built part size accuracy.

The average value of tensile strength (UTS) at break was 676.7MPa, with a standard deviation of 5.15MPa. The parts built in the left back area did have smaller tensile strength compared with the parts built in the other areas, but the difference of 1.48% of the average value is still not significant. A statistical hypothesis test, one-sample t-test, was performed in Microsoft Excel 2010 to study the significance level of the UTS results variation. The analysis results show a t statistic value of -4.9×10^{-5}, which is smaller than the t critical value of 1.7247. Also the p-value is 0.4999, which is larger than the common significance level 0.05 [182]. Therefore, the data analysis showed the variation of the UTS results was not significant at a significance level of 5%.This shows that the gas flow did not affect laser-powder interaction and cooling process throughout the building area. But to achieve the acceptable mechanical properties, it is better to avoid building parts in the left back area if possible.

As discussed in section 5.3.1, when improper high laser energy density was delivered to the powder bed, a series of sizes of sintering particles could be generated and remained on the powder bed. Because of the gas flow, these particles can be blown to the left area of the building substrate, and affect part quality. To study the effect of these 'dark particles', 3 sets of tensile test specimens were built from left to right on the building substrate, shown in Figure 5-24. Stainless steel 316L virgin powder supplied by LPW technology Ltd was used to build samples. The main processing parameters include laser power of 50W, lens position of 14.50mm, scanning speed of 100mm/s, solid hatch distance of 0.08mm, layer thickness of 0.05mm, single scan per layer and no pre-heating process.

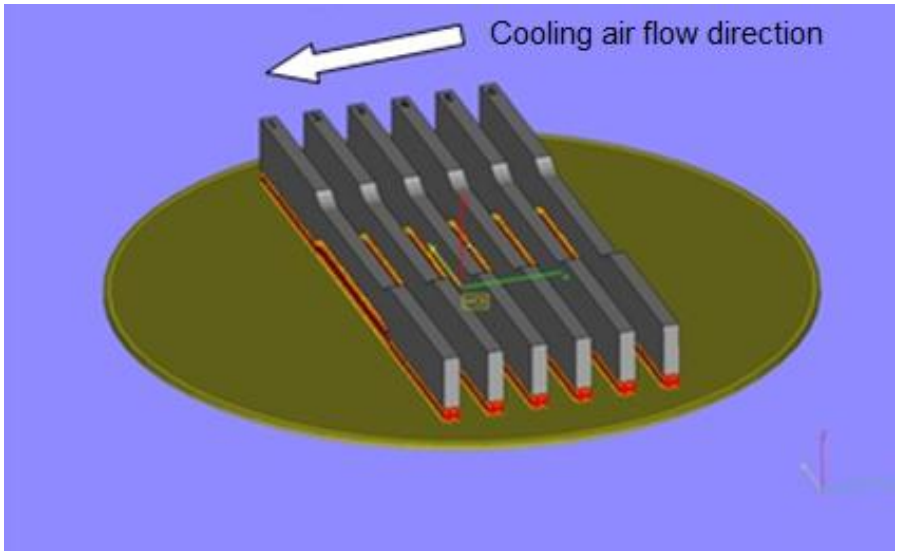

Figure 5-24 Tensile test specimens were built for dark particles effect study

The specimens were labelled as No.1 for the left to No.6 for the right. The average tensile strength for each number can be found in Table 5-13. A group of specimens after break are shown in Figure 5-25. There was a significant decrease in tensile strength at break of No.1 and No.2 specimens, which had most of dark particles covered during the process. No.4, No.5 and No.6 specimens which did not have dark particles remained on the process area because of the gas flow, had similar tensile strength at break. Figure 5-25 also showed this trend as the elongation at break of sample 1, 2 and 3 is lower compared with sample 4, 5 and 6.

	No.1	**No.2**	**No.3**	**No.4**	**No.5**	**No.6**
UTS (MPa)	363.43 ±18.35	556.98 ±6.79	630.23 ±4.2	660.53 ±4.88	661.93 ±3.84	657.73 ±5.29

Table 5-13 Average tensile strength of specimens built for dark particles effect study

Figure 5-25 Break specimens built for dark particles effect study

5.3.3 Pre-heating study

A pre-heat of 250°C, according to the maximum value recommended by the machine operating manual [173], can be applied to the bottom of the build substrate during the whole SLM process. A group of 6 tensile test specimens were built using 250°C pre-heating during the whole process, and another group of specimens were built on the same position of building substrate without pre-heating. Stainless steel 316L virgin powder supplied by LPW technology Ltd was used to build samples. The main processing parameters include laser power of 50W, lens position of 14.50mm, scanning speed of 250mm/s, solid hatch distance of 0.08mm, layer thickness of 0.05mm, single scan per layer and no pre-heating process. The results for pre-heating study are shown in Table 5-14. With the limited 250°C on the building substrate, while stainless steel melting temperature is around 1400°C, it is difficult to see any significant improvement compared with non pre-heating process.

	Density	Tensile strength	Elongation
250ºC pre-heating	99.4% ±0.23	609.59MPa ±3.35	36.65% ±1.40
Non pre-heating	99.4% ±0.28	605.19MPa ±4.59	36.14% ±1.71

Table 5-14 Average density, tensile strength and elongation for pre-heating study

Some academic works suggested that pre-heating the building substrate can reduce the surface roughness and improve the part accuracy due to reduced thermal gradients and shrinkage, as less heat input is required by the laser to change the powder from a solid to liquid phase [84-86]. Some other research indicated that pre-heating the powder bed does not necessarily improve the part properties when the temperature difference between pre-heating and the material melting temperature is large (>800°C) [87]. The results shown in Table 5-14 have a good agreement with the latter comments, and suggest the pre-heating in this research does not improve the built part's quality significantly.

5.4 Summary

The results of the first part of the experimental programme were presented and analysed in this chapter. Knowledge on each process parameter's effect on the SLM process and final part's physical and mechanical properties was obtained, discussed and used for the process optimisation.

Laser energy density is a key factor which affects the final parts quality. It is controlled by four main process parameters – laser power, beam width on the powder bed (lens position), laser scanning speed and scan hatch distance. The main aim of controlling the energy density is to make sure the

heat absorbed by the powder is enough for producing dense parts without over-heating. Suitable energy intensity can generate parts with densities very close to 100% (99.93%), as well as high strength. Low energy density resulted in porosity and low strength in the part, while improper high energy densities can cause the surface powder to begin to vaporise and even generate plasma.

Controlling the process parameters needs to consider the wet-ability for avoiding balling phenomenon. The laser scanning speed is the main factor in determining the balling phenomenon during the SLM process. Lower scanning speed increases the risk that the molten powder consolidates more to a spherical structure rather than consolidating into the previous layer.

Building direction did not affect the built part's quality. The bond between two layers was not weaker than the bond between two exposure points. However, a topping up delay does reduce the bond strength between layers.

The F-theta lens equipped inside MCP SLM-Realizer 100 works well to provide a flat field at the image plane of scan, and deliver the laser energy uniformly to the powder bed throughout the whole building area. The gas flow did not affect laser-powder interaction and cooling process throughout the building area. But it did affect the parts built on the left of the building substrate when evaporation and plasma take place under improper high energy intensity. Re-melting the surface of the part is an efficient way to reduce the top surface roughness.

Oxidation needs to be avoided during the process, as it degrades the powder material, as well as causes porosity and delamination of the parts. A pre-heat of 250°C in this research did not improve the part's quality significantly, as it is far away from the stainless steel 316L melting temperature.

6 Results & Discussions - Raw Material Characterisation

6.1 Introduction

This chapter presents the results and analysis from the second part of the experimental programme – raw material (powder used in SLM process) characterisation. The overall experimental method for this part was described in section 3.4. The results include the examination and measurement of the powder's fundamental properties, the effect of particle size distribution on part quality and the metal powder's sustainability in the SLM process.

Experiments were carried out on stainless steel 316L powder supplied by two suppliers, LPW Technology Ltd and Sandvik Osprey Ltd, with different particle size distributions. Results show the different behaviours of the powder bed density and powder flowability. Effects of the particle size distribution on the final part's quality are presented, compared and discussed.

Powder material sustainability was studied by monitoring the powder particle shape, size distribution and built part's physical and mechanical properties after a certain usage time. Results are presented on both LPW and Sandvik Osprey powders.

6.2 Particle shape and size distribution

Particle shapes examined by SEM are shown in Figure 6-1. Both the Sandvik Osprey and the LPW powder appear to be close to spherical with smooth surfaces. Visual inspection suggests that the Sandvik Osprey powder consists of a wider range of particle sizes than the LPW.

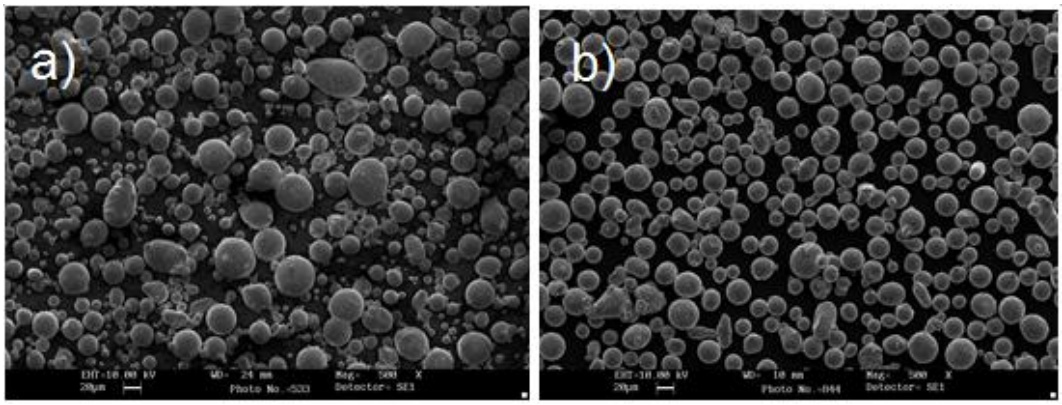

Figure 6-1 a) Osprey, b) LPW powder under SEM, mag=500x

Measured particle size distributions of Sandvik Osprey and LPW powders are shown in Figure 6-2. Clearly, the two powders have a distinctly different distribution. The Sandvik Osprey powder has a wider range and contains significantly more fine particles (<10μm). The mean sizes are close, 27.533μm (SO) and 29.294μm (LPW).

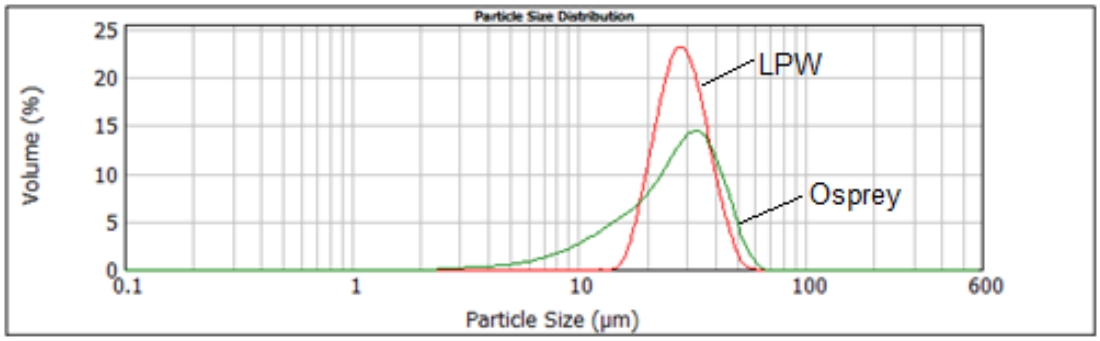

Figure 6-2 Particle size distribution measured by Mastersizer 2000

6.3 Powder bed density and powder flowability

Apparent density, powder bed density and tapped density of the powders are shown in Table 6-1. A wider range of particle sizes usually allows a higher density to be achieved as the smaller particles can fit in the gaps between the larger particles and this is reflected in the generally higher bed density

observed for the SO powder. This is likely to be beneficial for the final part. However, the higher density will result in greater friction and more possibilities for particles to "lock" together during flow, and thus reduced flowability is seen for the SO powder, shown in Table 6-2.

Brand	Apparent density (g/ml)	Powder bed density (g/ml)	Tapped density (g/ml)
Osprey	4.54	5.312	5.54
LPW	4.33	4.88	5.03

Table 6-1 Measured apparent density, powder bed density and tapped density

Brand	Flowability by time (kg/hour)	Hausner ratio
Osprey	0.54	1.22
LPW	0.67	1.16

Table 6-2 Measured powder flowability

The flowability can be significantly affected by powder particle size distribution, particle shape and inter-particle friction [94]. It is believed that spherical particles with smooth surfaces flow well as the flow motion is not hindered by angle contacts [87], also the smooth surfaces reduce the inter-particle friction. In the SEM images, both LPW and SO powders observed have particle shapes that are relatively spherical with smooth surfaces. Therefore, the difference between their particle size distributions is the main reason for different flowability. High flowability occurs when the powder contains a narrow particle size range, and LPW powder has this advantage compared with SO powder. Hausner ratios for both powders are less than 1.25, indicate that they both have acceptable flowability [163].

6.4 The effect of particle size distribution

Tensile test specimens with a gauge length of 25mm and thickness of 3mm, designed according to ASTM E8-09, were built for the effect of particle size distribution study. For each brand's powder, five groups of specimens were built using five different scanning speeds: 100mm/s, 150mm/s, 200mm/s, 250mm/s and 300mm/s. Another five groups of specimens were built with five different lens focus position 14.40mm, 14.50mm, 14.60mm, 14.70mm and 14.80mm.

To plot the results as a function of laser energy intensity in this study, lens focus position values were converted to the laser beam diameters. Measurement results using the camera based laser beam profiler, are 0.026mm, 0.028mm, 0.030mm, 0.035mm, 0.048mm for the above lens position values under 25W. Equation (5.1) is used for calculating the beam width under 50W. The laser beam diameter and scanning speed are parameterised into a laser energy density using the Equation (2.9), while hatch distance is set to a constant value.

Within each group the processing parameters were the same for all 5 specimens, all the specimens were built in a constant position of the build substrate, and these are shown for each experiment in Tables 6-3 and Table 6-4. Final part density was measured by cross sectioning specimens and examining the porosity using an optical microscope. Five cross sections were examined to obtain average density values for each sample. Surface roughness was measured by Talylor Hobson Form Talysurf 50. UTS and elongation at break were tested using an Instron 3369 and hardness was measured using a Rockwell hardness testing machine (Avery 6402).

Scanning speed variation	
Laser power	50W
Laser beam diameter	0.040mm
Scanning speed	100mm/s, 150mm/s, 200mm/s, 250mm/s, 300mm/s
Layer thickness	0.05mm
Hatch distance	0.08mm
Scanning strategy	One scan each layer
Pre-heating substrate	None

Table 6-3 Specimens built parameters using different scanning speeds for particle size distribution effect study

Laser beam diameter variation	
Laser power	50W
Laser beam diameter	0.037mm, 0.040mm, 0.042mm, 0.049mm, 0.068mm
Scanning speed	200mm/s
Layer thickness	0.05mm
Hatch distance	0.08mm
Scanning strategy	One scan each layer
Pre-heating substrate	None

Table 6-4 Specimens built parameters using different laser beam diameters for particle size distribution effect study

6.4.1 Density of the finishing parts

Table 6-5 shows the average measured density of the final parts, as a percentage of the full density. Generally a downward trend in density was observed with increasing scanning speed, reflecting the reduced energy input into the material. In addition, the LPW powder, which was previously observed to have a lower powder bed density, is typically found to have a lower part density than the SO parts, suggesting a possible link between the powder bed density, and thus the particle size distribution and the final part density. Typical cross-sections of the samples are shown in Figure 6-3. There is a small drop in average density for SO parts from 150mm/s to 100mm/s with even more energy delivered, and can be caused by fine particles vaporisation due to the high temperature generated on the powder bed.

Scanning Speed	100mm/s	150mm/s	200mm/s	250mm/s	300mm/s
Osprey	99.45%	99.93%	99.55%	99.37%	99.30%
LPW	99.85%	99.65%	99.02%	97.91%	97.22%

Table 6-5 Average density of parts built using different scanning speeds

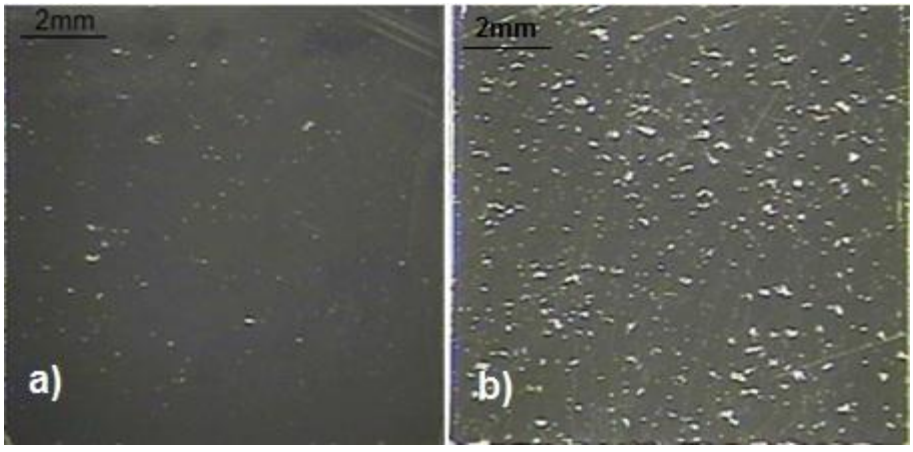

Figure 6-3 Cross section of parts built on 300mm/s, a) Osprey, b) LPW

Table 6-6 shows the average density of parts built using five laser beam diameters.

Beam diameter	0.037mm	0.040mm	0.042mm	0.049mm	0.068mm
Osprey	99.90%	99.55%	99.45%	99.26%	98.53%
LPW	99.93%	99.02%	98.63%	97.98%	96.72%

Table 6-6 Average density of parts built using different laser beam diameters

A similar trend is observed for varying the laser beam diameters. As the diameter is increased, then for the same power, the density tends to decrease. This reflects the same trend in the energy intensity as the beam diameter or the scanning speed increased. The same trend was observed for samples built under different scanning speeds: the Osprey samples give higher densities than LPW's when using larger laser beam diameters.

6.4.2 Surface roughness of the finishing parts

Figure 6-4 and Figure 6-5 show measured side and top surface roughness R_a for both SO and LPW parts.

The results for roughness are more confused. There are suggestions of an increase in roughness as the laser energy intensity is decreased, though there is some significant variation from this, particularly for the top surface roughness of parts built using both SO and LPW powder.

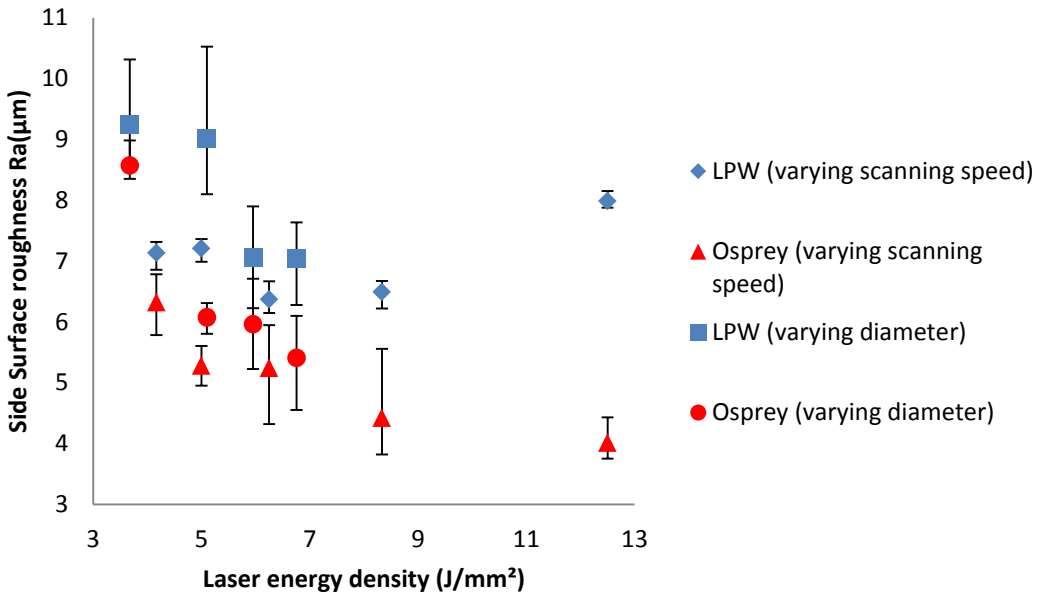

Figure 6-4 Side surface roughness for both SO and LPW parts

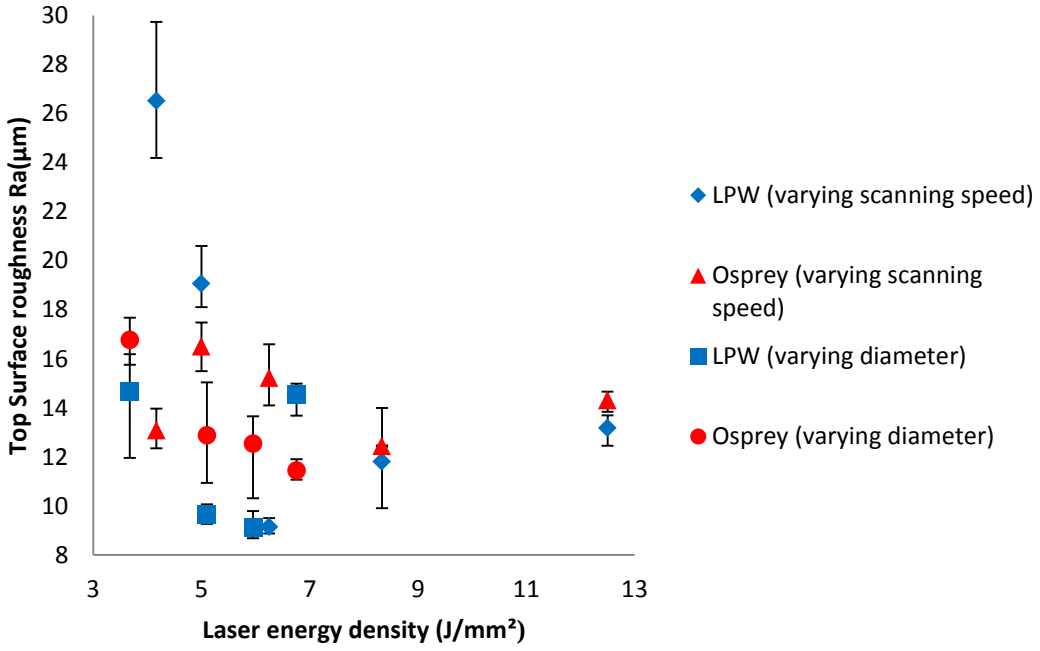

Figure 6-5 Top surface roughness for both SO and LPW parts

SO parts had a generally smoother side surface finish than the LPW parts, and suggested a possible link between the particle size distribution and the

final parts side surface finish. The wider particle size range of SO powder presents higher powder bed density, and smaller gaps between particles. When the particles are melted and consolidated, the shrinkage for each layer could be lower compared with the LPW powder. This allows the powder deposition for the next layer to deliver similar amount of the powder each time. Therefore, the laser melts a near constant amount of powder and generates similar melting pool size for each layer. Constant melting pool depth presents constant overlapping between layers and helps to reduce the stair stepping effect on the side surface finishing [18].

The top surface is usually rougher than side surface on SLM built parts, as can be seen from Figure 6-4 and Figure 6-5. The lowest R_a of top surface was observed between the input laser energy density from 5J/mm^2 to 7J/mm^2 for both SO and LPW parts. Higher energy intensity input introduced a rougher top surface due to high thermal stresses and non-uniform solidification rate across the powder bed. Also the vaporisation during the melting process when high energy intensity is delivered increases the top surface roughness. Top surface roughness of SO parts varies in a smaller range compared with LPW parts, which indicates the effect of energy intensity on top surface finish is larger on a lower density powder bed.

6.4.3 Tensile strength and elongation of the finishing parts

Figure 6-6 and Figure 6-7 show the UTS and elongation at failure of the samples built using both SO and LPW powders.

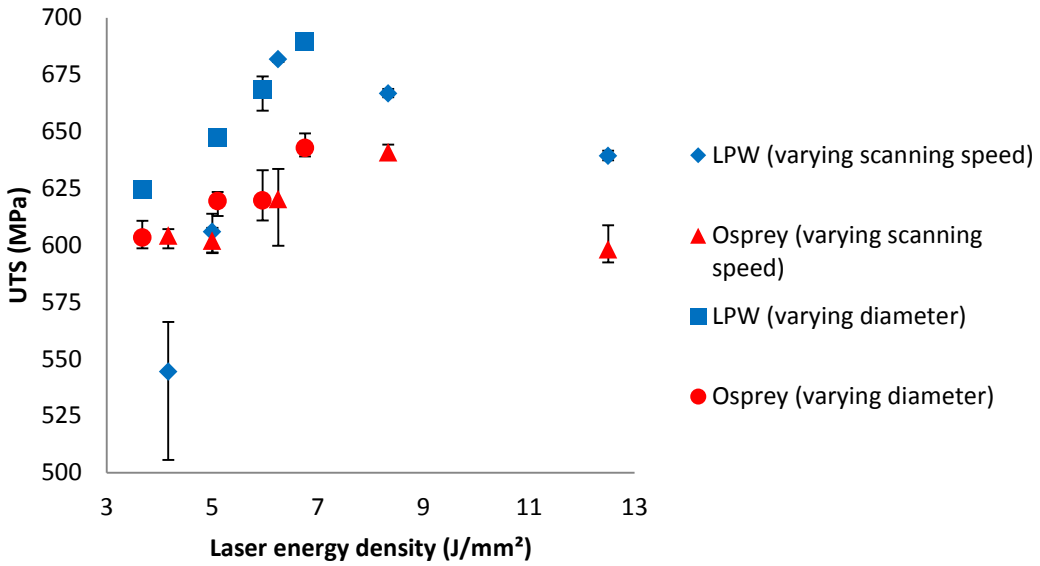

Figure 6-6 UTS of both SO and LPW parts

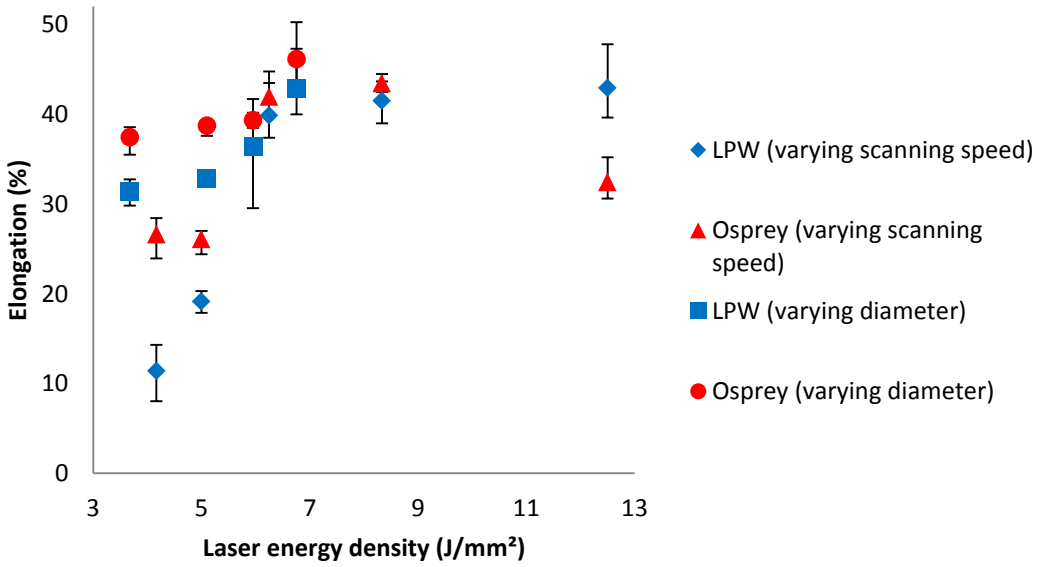

Figure 6-7 Elongation of both SO and LPW parts

Both SO and LPW parts experienced first an increase and then decrease in UTS with increasing the laser energy density. A drop in UTS under higher energy intensity input was observed for both SO and LPW parts. The results

show a good agreement with the density results. Low energy input generates porosity inside the part and decrease the UTS; while high energy input also generates porosity by vaporising the particles or forming plasma, and reduces the UTS too. Observed from Figure 6-6, LPW parts have higher tensile strength than SO parts, and may be caused by different chemical compositions of two powders.

The results for elongation show the similar trend as the UTS results of both SO and LPW parts. SO parts have higher elongation than LPW parts in most energy intensity, which is opposite to the UTS results, as can be seen from Figure 6-7. Parts built by LPW powder are more brittle compared with the SO parts.

6.4.4 Hardness of the finishing parts

Figure 6-8 shows measured Rockwell B hardness of both SO and LPW parts.

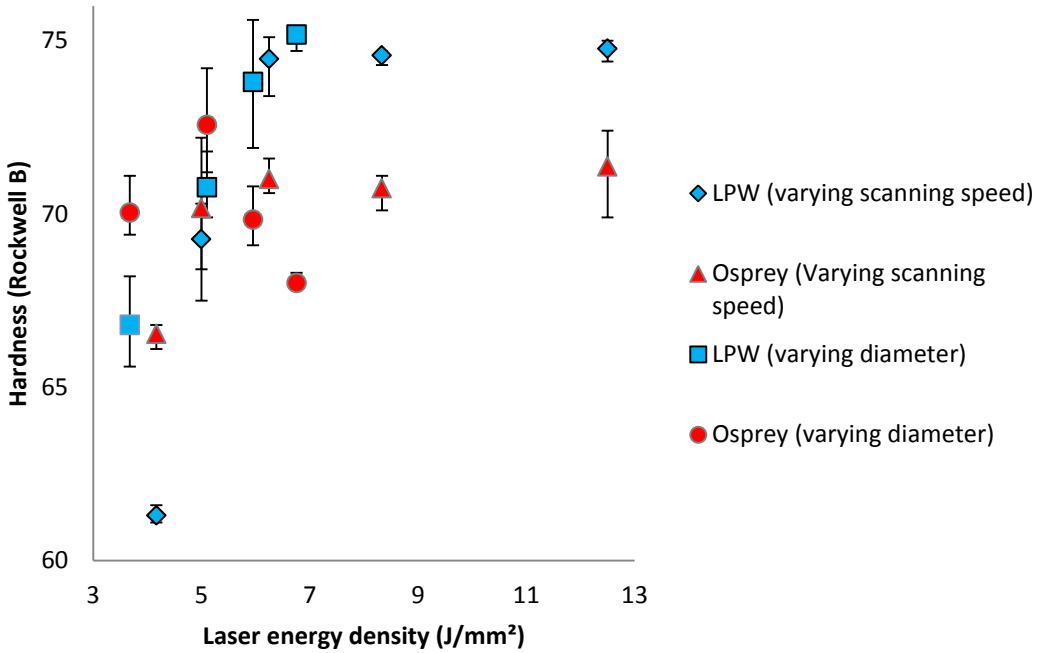

Figure 6-8 Hardness under different scanning speeds

The results for hardness are also confusing. There are suggestions of an increase in hardness as the energy intensity is increased, although there is significant variation for parts using SO powder. Rockwell B hardness of SO parts stayed in a small range between 68 and 72, but did not form a clear trend under different laser energy density, observed from Figure 6-8.

Previous work indicated a hardness increase along with the density increase when higher energy intensity was delivered to the powder bed [187]. Presented in section 6.4.1, SO parts have densities which were less variable than LPW parts in the laser energy density range used in the experiment. This small change in density results the hardness of SO parts remaining similar. LPW parts have the hardness increase well agreed with their density increase.

LPW parts have larger hardness than SO parts when high energy intensity was delivered. SO powder has more fine particles than LPW powder, and has higher chance to evaporate these fine particles to generate porosity inside the built part, resulting lower hardness.

In the UTS, elongation and hardness results shown in Figure 6-6 to 6-8, there was an out of trend drop for LPW parts built at 300mm/s scan speed and 0.04mm beam diameter. The values are lower than the results from a part built with lower laser energy intensity (200mm/s scan speed, 0.068mm beam diameter). This indicated that scan speed affected the LPW parts mechanical properties more than focus position in low energy density area.

To sum up, Powders with different particle size distribution behave differently in selective laser melting process, and introduce differences in powder bed distribution and built part's quality. With similar mean size, powder with wider range of particle size provides higher powder bed density, while powder with narrower range of particle size provides better flowability. They are main factors which generates the differences in built part's quality.

Powder with wider range of particle size performs better under low laser energy intensity, which generates higher density parts. Also parts built by wider range particle size powder have smoother side surface finishing.

Powder with narrower range of particle size performs better under high laser energy intensity, which generates parts with higher UTS, larger hardness and smoother top surface finishing.

6.5 Powder sustainability study

6.5.1 LPW powder monitoring

Powders supplied by LPW technology for the powder sustainability monitoring study was processed for over 800 hours. Samples were examined after every 200 processing hours to check for differences. Particle shape changes were examined by SEM, shown in Figure 6-9, and particle size distribution changes were tested by Mastersizer 2000, shown in Figure 6-10.

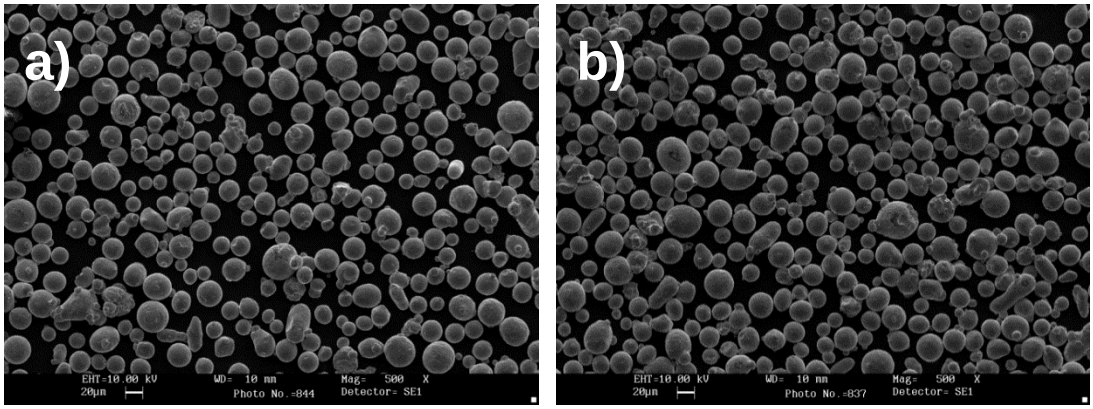

a) virgin powder; b) processed after 200 hours

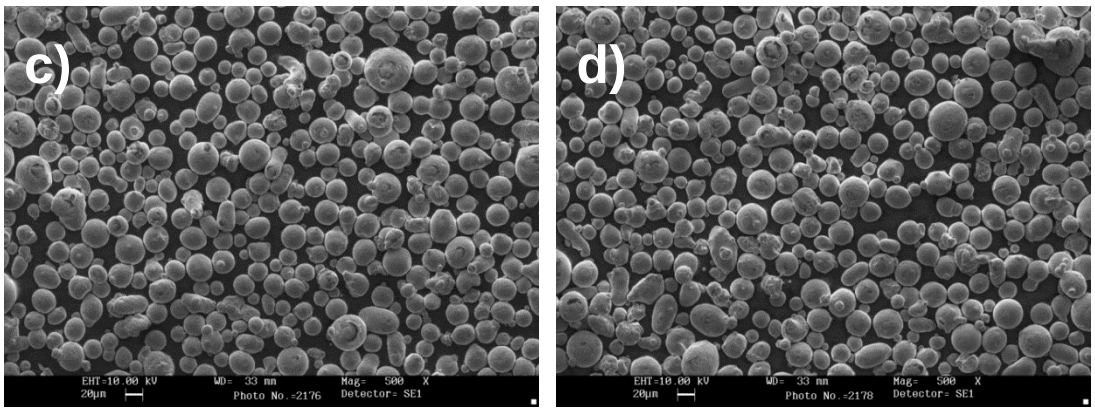

c) processed after 400 hours; d) processed after 600 hours

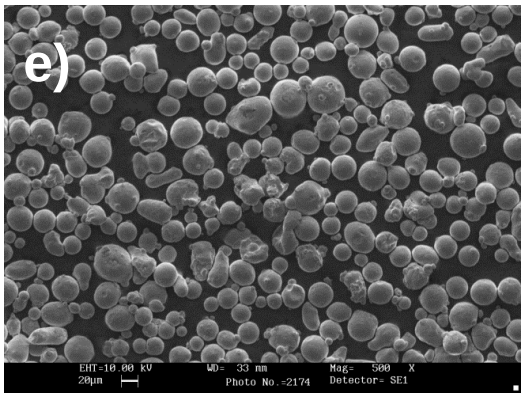

e) processed after 800 hours

Figure 6-9 LPW powder in different stages, examined by SEM

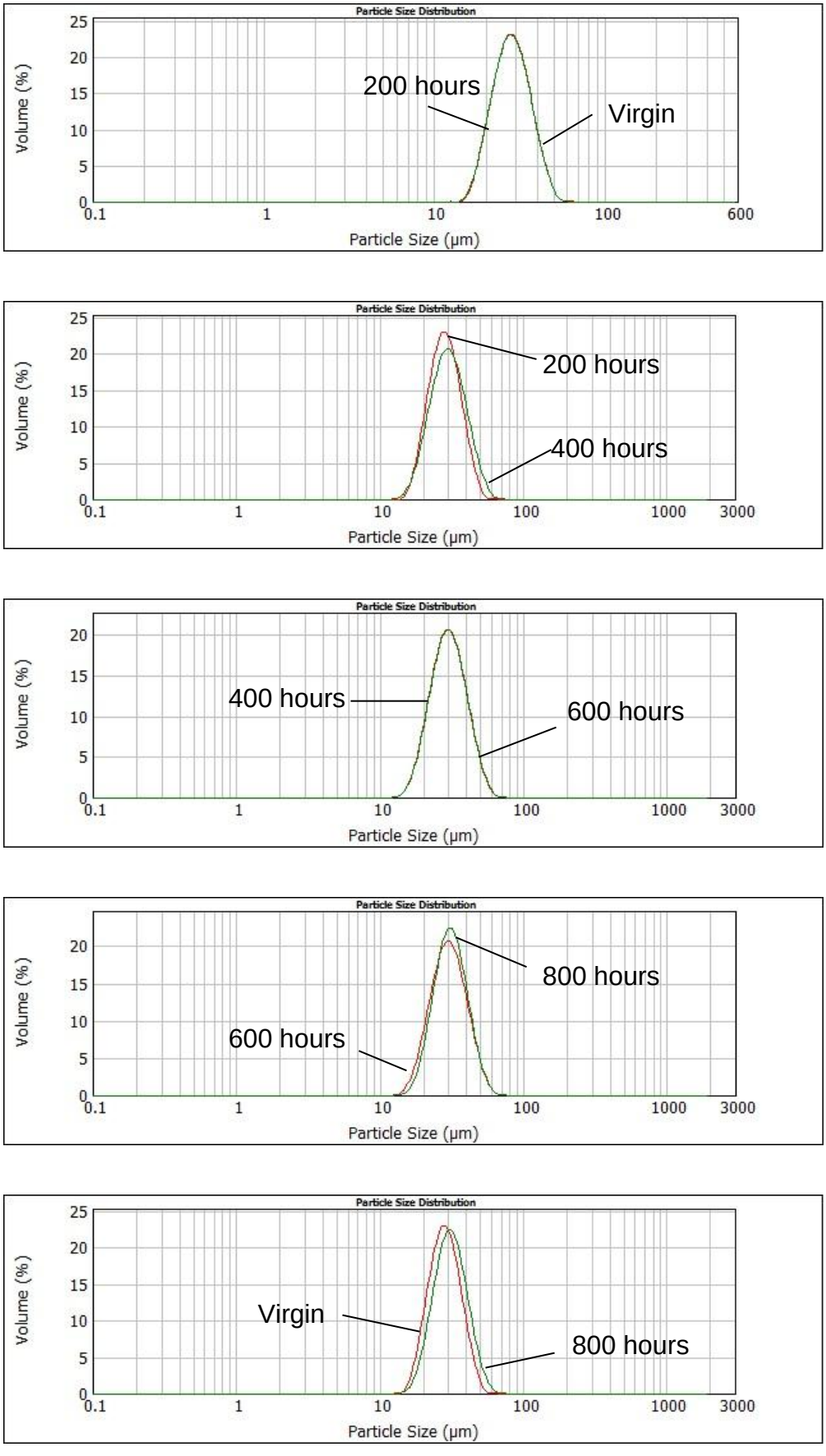

Figure 6-10 Particle size distribution comparisons for LPW powder

After 800 hours of processing, the particle shape did not show significant change when compared with the virgin LPW powder. The majority of particles stayed spherical, with a few particles began to form un-spherical shapes because of sintering or heat affecting during the process.

Particle size distribution result showed slight movement on the x-axis after 800 hours processing time. The shape and width of the distribution curve stayed similar to the virgin powder. The results indicated a trend that the particles would become relative larger in a slow-moving process during the SLM building process.

Besides the particle shape and size distribution examination, mechanical properties of the parts built by the sample powders were also examined. 3 sets of flat tensile test specimens with a gauge length of 25mm and thickness of 3mm, designed according to ASTM E8-09, were built in parallel with the gas flow direction to examine any differences for both tensile strength and surface roughness. They were built on the same position of the substrate under the same building conditions. The main processing parameters include laser power of 50W, lens position of 14.50mm, scanning speed of 200mm/s, solid hatch distance of 0.08mm, layer thickness of 0.05mm, single scan per layer and no pre-heating process. UTS and surface roughness were measured, and the average results were shown in Table 6-7.

Average results	Virgin	200 Hours	400 Hours	600 Hours	800 Hours
Tensile strength	680.63MPa	686.57MPa	684.33MPa	680.79MPa	683.21MPa
Top surface roughness	12.6054µm	10.2486µm	11.6549µm	11.3244µm	10.7108µm
Side surface roughness	6.4131µm	6.3798µm	6.5232µm	6.4419µm	6.5655µm

Table 6-7 Average mechanical properties comparison for LPW parts

As shown in Figure 6-9 and 6-10, the particle shape and size distribution of the powder provided by LPW Technology did not show a significant change after 800 hours processing time, the measured tensile strength and surface roughness also did not show a significant increasing or decreasing trend. The average tensile strength stayed relatively constant as well as the average side surface roughness. The top surface roughness showed a slight improvement after 200 processing hours, but did not form a trend during the whole 800 processing hours.

To investigate if there was any difference of the powder particle's microstructure due to the heat effect during the SLM process, sample powders were examined by EBSD for their crystallographic orientation. Powders supplied by LPW technology in both their virgin and 800 hours processed states were examined by EBSD. The results were shown in Figure 6-11 and Figure 6-12.

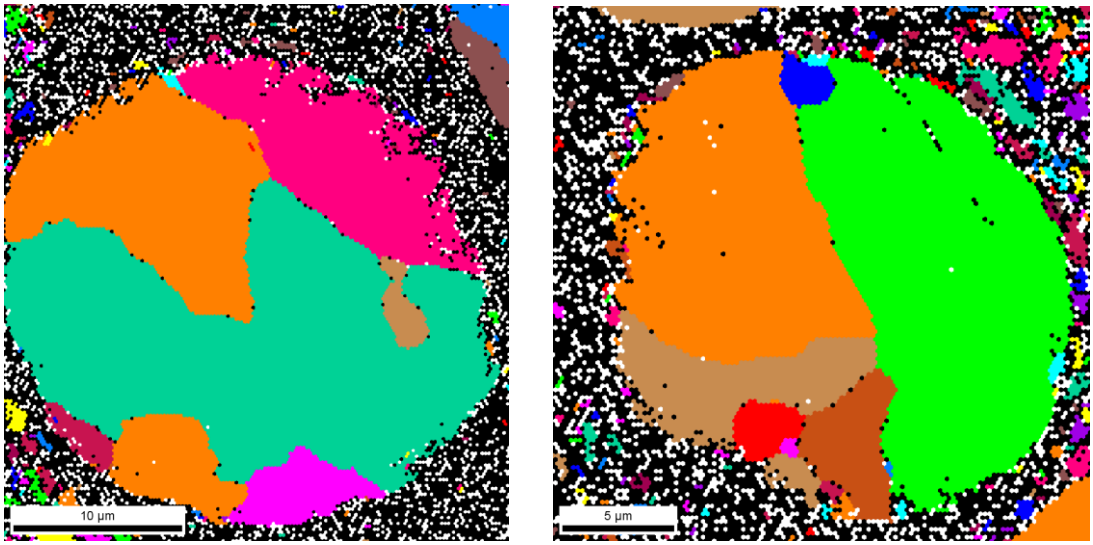

Figure 6-11 Crystalline orientation maps of two particles random selected from LPW virgin powder

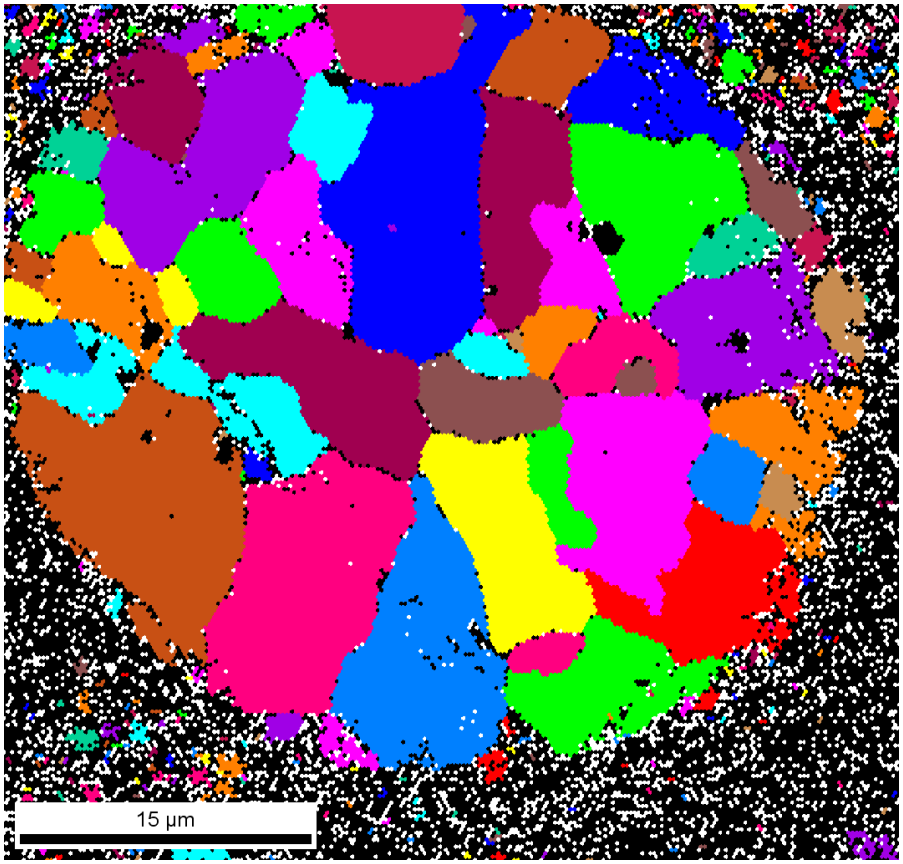

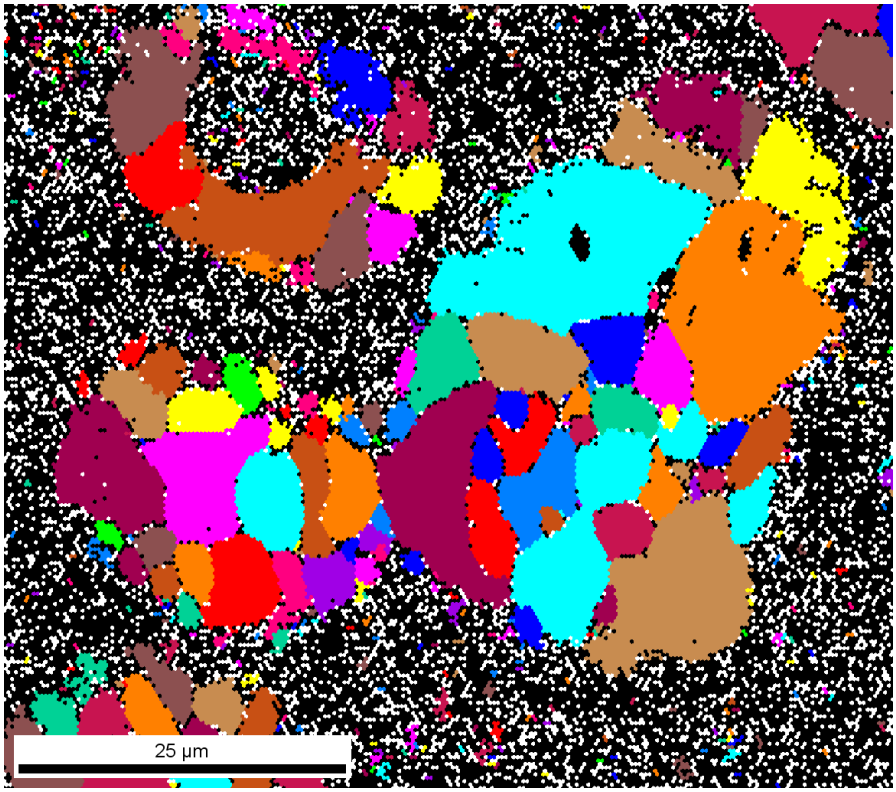

Figure 6-12 Crystalline orientation maps of two particles random selected from LPW powder after 800 hours processing

Particles shown in Figure 6-11 and Figure 6-12 were selected randomly from sample powders which contained a large amount of particles for each state. All the particles contained over 99.7% of γ-iron (Gamma ferrite) phase, which was austenite.

Virgin powders were formed by several large grains, most of them larger than 20μm, while the powders after 800 processing hours were formed by various sizes of grains, from 5μm to 15μm. It could be assumed that there was recrystallization happened to the heat affacted zone particles during the SLM process, and small size of grains were formed due to very high cooling rate [83, 111].

The second image in Figure 6-12 shows a large particle formed by three small particles sintered together. A strong necking formed between right top particle and right bottom particle can be observed with the grains growing through these two particles. A weak necking formed between left particle and right bottom particle can also be observed since the grains still stayed in their original particles in the necking area.

6.5.2 SO powder monitoring

Due to the research time limitation, powder supplied by Sandvik Osprey Ltd for powder sustainability monitoring study was processed for over 300 hours. Samples were examined after every 100 processing hours to check the shapes and particle size distributions. Powders were used for general building work under around 1,000 processing hours in MCP SLM 100 were also examined as a reference in this study. These powders had been found to start to degrade, and were presented in section 3.4.6. Particle shape changes were examined by SEM, shown in Figure 6-13, and particle size distribution changes were tested by Mastersizer 2000, shown in Figure 6-14.

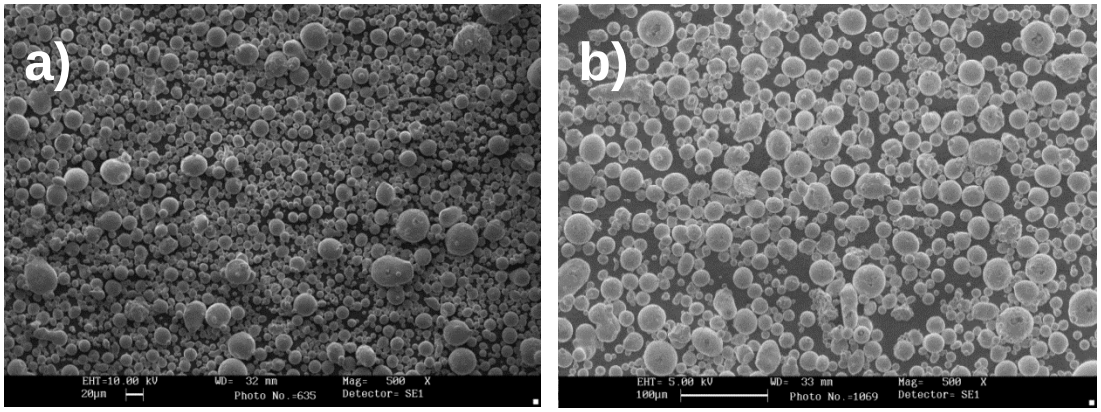

a) virgin powder; b) processed after 100 hours

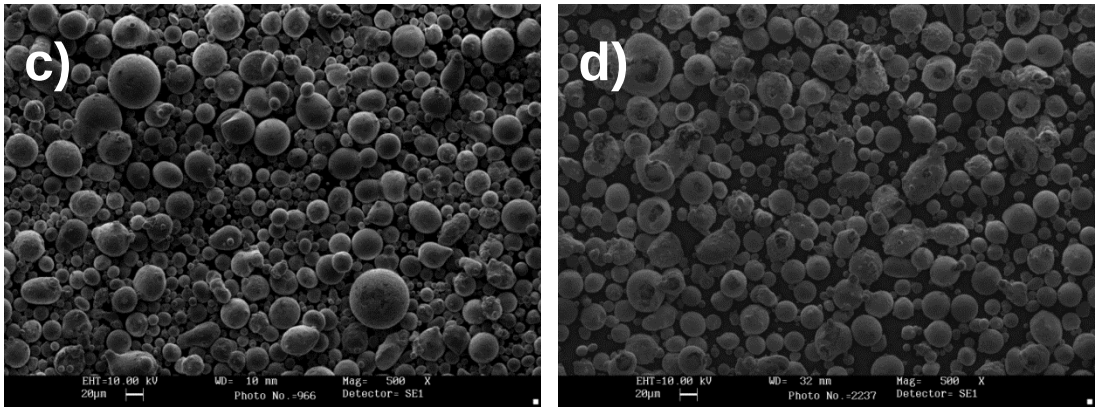

c) processed after 200 hours; d) processed after 300 hours

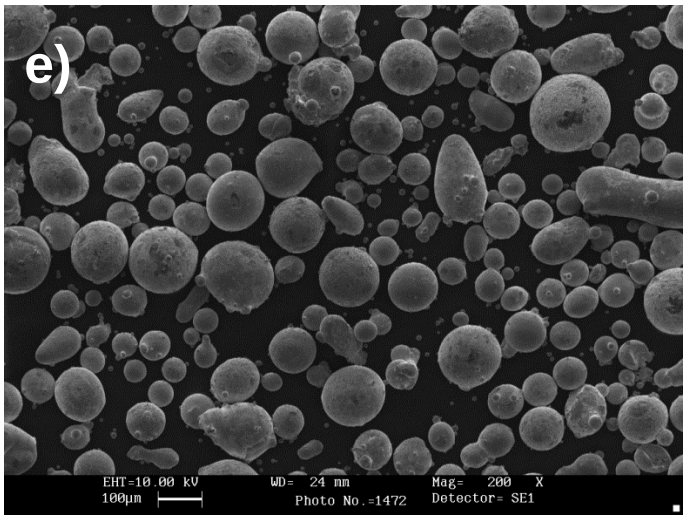

e) processed after 1,000 hours for general building propose in SLM 100

Figure 6-13 SO powder in different stages, examined by SEM

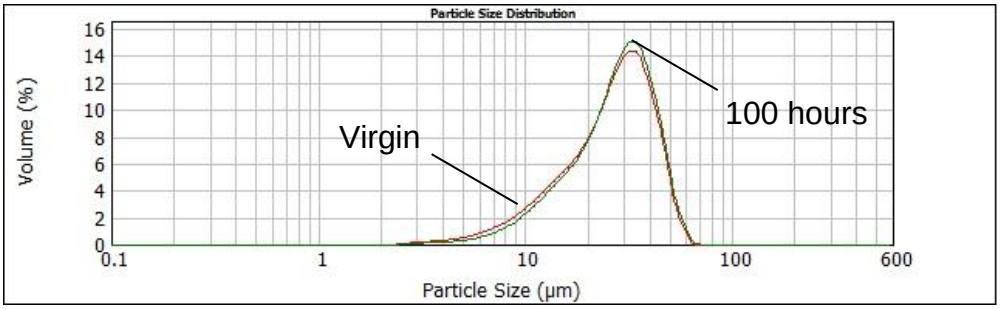

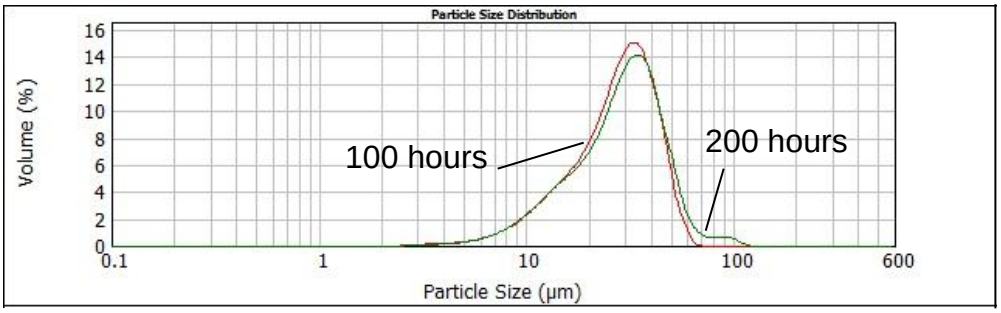

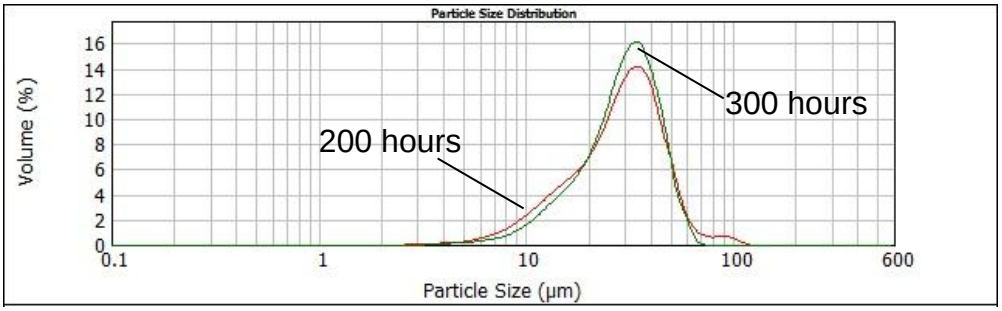

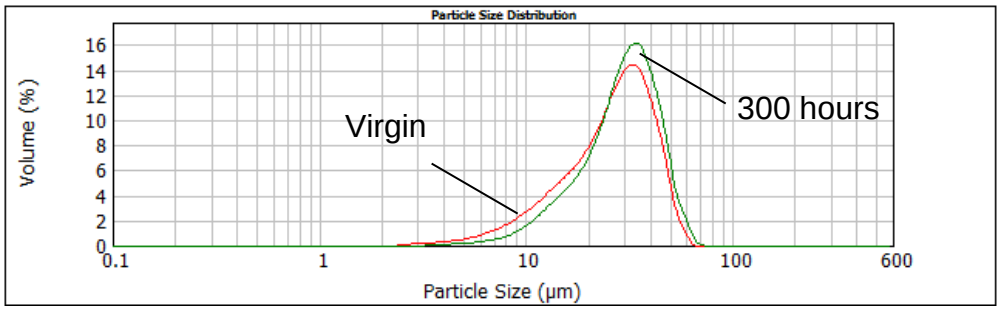

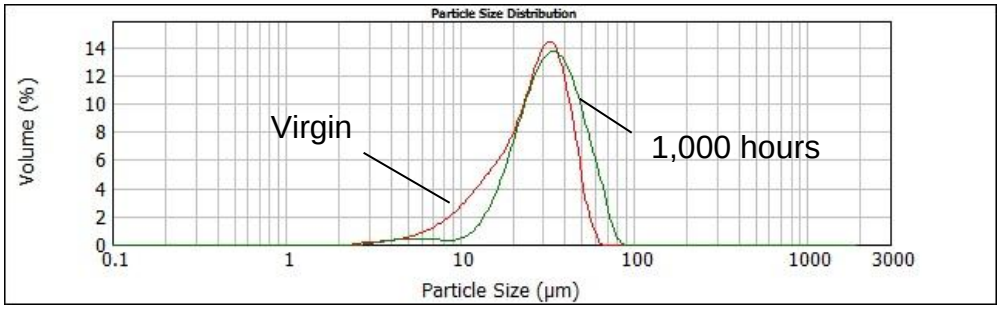

Figure 6-14 Particle size distribution comparison for SO powder

As shown in Figure 6-13 and 6-14, after 300 hours of processing, the particle shape did not show significant change when compared with the virgin SO powder. The majority of particles stayed on spherical shape, with a few large particles began to form un-spherical shapes because of sintering or heat affecting during the process. It can be observed from the SEM images that after 300 processing hours, the amount of large particles with diameters over 80μm started to increase and the fine particles with diameters smaller than 15μm started to disappear. After 1,000 hours processing, the amount of fine particles was much smaller compared with virgin SO powder.

Particle size distribution result showed an observed difference after 300 hours processing time, and a significant difference after 1,000 hours. The trend of fine particles decreasing and large particles increasing can be obtained. After 1,000 hours processing time, the fine particles with diameters smaller than 10μm were nearly gone, and it could be caused by vaporisation and sintering during the SLM process.

Besides the particle shape and size distribution examination, mechanical properties of the parts built by the sample powders were also examined. 3 sets of flat tensile test specimens with a gauge length of 25mm and thickness of 3mm, designed according to ASTM E8-09, were built in parallel with gas flow direction to examine any differences for both tensile strength and surface roughness. They were built on the same position of the substrate under the same building conditions. The main processing parameters include laser power of 50W, lens position of 14.50mm, scanning speed of 200mm/s, solid hatch distance of 0.08mm, layer thickness of 0.05mm, single scan per layer and no pre-heating process. UTS and surface roughness were measured, and the average results were shown in Table 6-8.

Average results	Virgin	100 Hours	200 Hours	300 Hours	1,000 Hours
Tensile strength	626.33MPa	628.37MPa	623.53MPa	618.79MPa	612.56MPa
Top surface roughness	12.8685μm	12.2576μm	12.6845μm	13.3274μm	14.7117μm
Side surface roughness	6.0758μm	6.3723μm	6.9234μm	7.4417μm	9.2320μm

Table 6-8 Average mechanical properties comparison for SO parts

Due to the changes in particle size distribution of the powder provided by Sandvik Osprey Ltd, the measured tensile strength and surface roughness showed relative changes too. The change in particle size distribution did not generate significant effect on the average tensile strength as well as the top surface roughness; and a decrease trend on the tensile strength and an increase trend on the top surface roughness was obtained. Side surface roughness showed a slight increase after 300 processing hours and an obvious increase after 1,000 processing hours.

6.6 Summary

The results of the second part experimental programme were presented and analysed in this chapter. Two brands of powder were used in the experiments. The powder particle shape, size distribution, flowability and the behaviour on forming the powder bed were examined. Particle size distribution effects on the final part quality were studied. Powders were monitored under a certain period for investigation their sustainability.

SO powder with wider range of particle size provides higher powder bed density, generates higher density parts under low laser energy intensity, and generates smoother side surface finishing parts. LPW powder with narrower range of particle size provides higher flowability, generates parts with higher UTS and greater hardness under high laser energy intensity.

Main powder degrade phenomenon is the change in powder particle shape and size distribution. LPW powder did not degrade in the monitoring period 800 hours with no significant changes happened in particle shape, size distribution and built part's quality. SO powder started to degrade after 300 hours with an observed difference in particle size distribution, and this difference was enhanced after 1000 hours of processing. The degradation results the lower tensile strength and higher surface roughness of the built parts.

7 Results & Discussions - Model Inputs Characterisation

7.1 Introduction

This chapter presents the results and analysis from third part of the experimental programme – model inputs characterisation. These inputs include the material properties, loads and boundary conditions, and are essential for the simulation. The overall experiment method for this part was described in section 3.4.

Since the powder bed properties cannot be obtained directly from the literature, relevant measurements were carried out. The results of density, thermal conductivity and specific heat capacity for the powder bed are presented.

Loads and boundary conditions are also discussed in this chapter.

7.2 Material Properties

The finite element model for heat transfer analysis was established using the material properties of the stainless steel 316L powder supplied by LPW Technology. The powder state and solid state of stainless steel 316L are two stable states which exist in the SLM process and their physical and thermal properties should be measured in order to accurately describe the physical process during the SLM manufacture.

The liquid state of stainless steel 316L can only exist when the temperature is above the melting temperature 1400°C [188]. The liquid state's physical and

thermal properties are hard to measure due to the limited access to the suitable equipment. In the simulation work, proper assumption based on the current knowledge for the inputs is allowed, and can be validated later from the modelling results accuracy. Therefore, the solid state's physical and thermal properties were used in the modelling work for the liquid state as an assumption due to their close density.

7.2.1 Density

The bulk density of stainless steel 316L is 8000kg/m^3 [188]. Since the built part's density in SLM process have been shown to reach a maximum of 99.93%, the value used for the FE model was 7994kg/m^3.

The powder bed density during the SLM process has been measured by the method described in section 3.4.3, and the result shown in section 6.3 presented that the stainless steel 316L powder supplied by LPW Technology formed a powder bed density of 4880kg/m^3.

7.2.2 Thermal conductivity

Stainless steel 316L is a temperature dependent material where its thermal properties vary at different temperatures. The thermal conductivity of fully solid stainless steel 316L is 16.2W/m·K at 100°C, and 21.5W/m·K at 500°C [188]. Therefore, Equation (3.2) is converted to Equation (7.1) for calculating the thermal conductivity k_S (S for solid) at different temperatures for the bulk stainless steel.

$$k_s = 11.26 + 1.325 \times 10^2 T \quad (7.1)$$

The parts generated by the SLM process have a maximum density of 99.93%. The gas in the pores also has temperature dependent conductivity, making it complicated to calculate the combined thermal properties. Since

the density of built part is close to the bulk material, the conductivity of the gas in the pores is ignored due to its minimal effect, 0.02622W/m·K at 25°C, 0.0457W/m·K at 325°C and only being 0.07% in the part [110]. Therefore the values for full solid stainless steel 316L were used in the heat transfer modelling.

To measure the powder bed thermal conductivity, containers shown in Figure 3-15 were built with 1mm thick top and bottom lid, and a series of sidewall thickness 1mm, 1.5mm, 2mm, 2.5mm and 3mm. Due to the accuracy and limitations of the thermal conductivity apparatus[172], three measuring temperatures 100°C, 200°C and 300°C were selected. Each measurement was repeated twice to obtain a reliable range of the readings, and the results were shown in Figure 7-1.

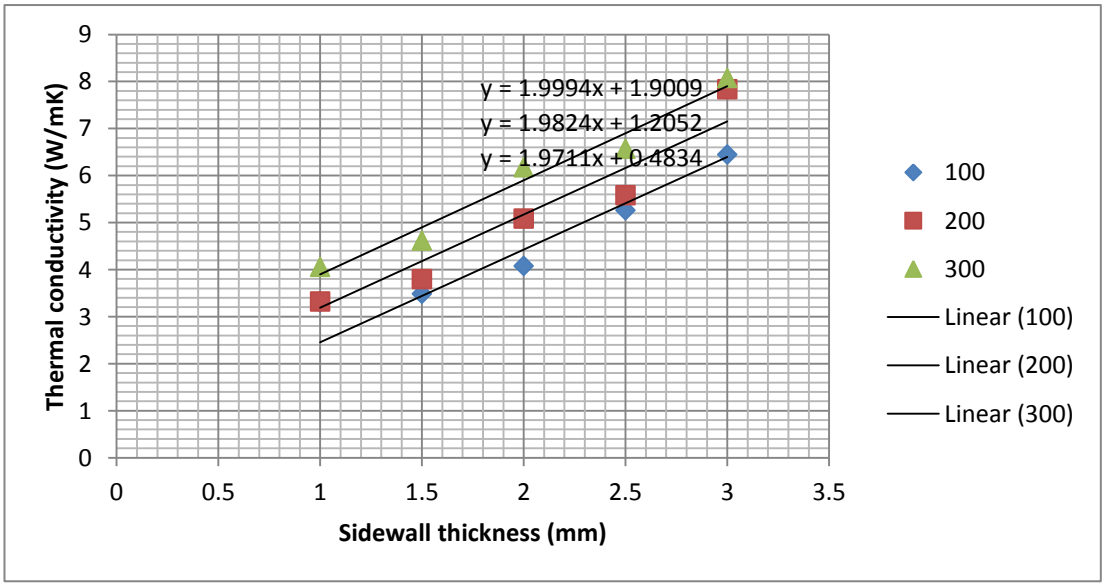

Figure 7-1 Powder bed thermal conductivity based on different sidewall thickness

In Figure 7-1, the sidewall thickness shows a linear effect on the measurement results, and the powder bed thermal conductivity was obtained when the sidewall thickness was zero. The results show the LPW powder bed has thermal conductivity of 0.5W/m·K at 100°C, 1.2W/m·K at 200°C and

1.9W/m·K at 300°C. These values were inputted into Equation (3.2) to calculating the thermal conductivity k_p (P for powder) at different temperatures for the powder bed, shown in Equation (7.2).

$$k_{P=} - 2.111 + 0.7 \times 10^2 T \tag{7.2}$$

7.2.3 Specific heat capacity

The specific heat capacity of solid stainless steel 316L is 500J/kg·K at the temperature 0-100°C [188]. The parts generated by the SLM process have a maximum density of 99.93%, and only 0.07% porosity. The remaining 0.07% of air has specific heat capacity 1005J/kg·K in the temperature range [189], and its specific heat capacity is also temperature dependent [190]. The influence rate of the air on the built part specific heat capacity is calculated below:

$$Influence\ rate\ of\ the\ air = \frac{1005 \times 0.07\%}{1005 \times 0.07\% + 500 \times 99.93\%} = 0.14\%$$

As discussed in section 7.2.2, due to the small influence rate of the air and the complex calculation for the combining properties, the specific heat capacity of the gas in the pores is ignored, and the values for fully solid stainless steel 316L were used in the heat transfer modelling.

Based on the temperature dependent specific heat capacity values obtained from the metal handbook [188], the Equation (3.4) is converted to Equation (7.3) for calculating the specific heat capacity C_{pS} (S for solid) at different temperatures for the bulk stainless steel.

$$C_{pS} = 365.43 + 0.40649T - 1.732 \times 10^{-4} T^2 \tag{7.3}$$

A Shimadzu DSC-60 with temperature range -150 to 600°C, heat flow range ±40mW was used for measuring the specific heat capacity thermal curves of the stainless steel 316L powder provided by LPW Technology [191]. The heat

flow as a function of temperature is shown in Figure 7-2. The measurement was repeated to reduce any reading or operating errors, and the results are shown in Figure 7-3.

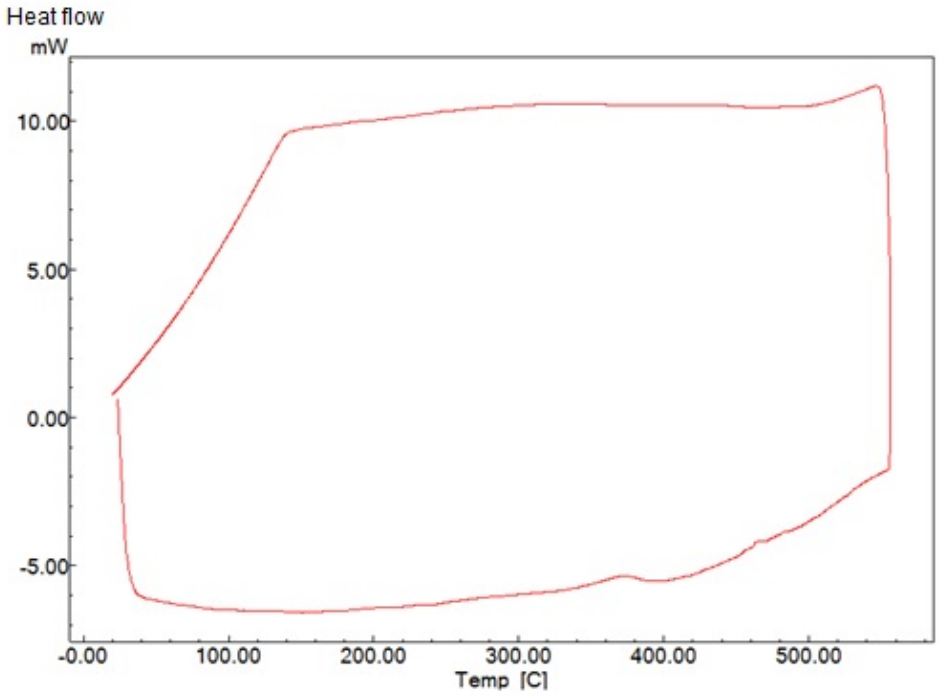

Figure 7-2 Specific heat thermal curve for stainless steel 316L powder

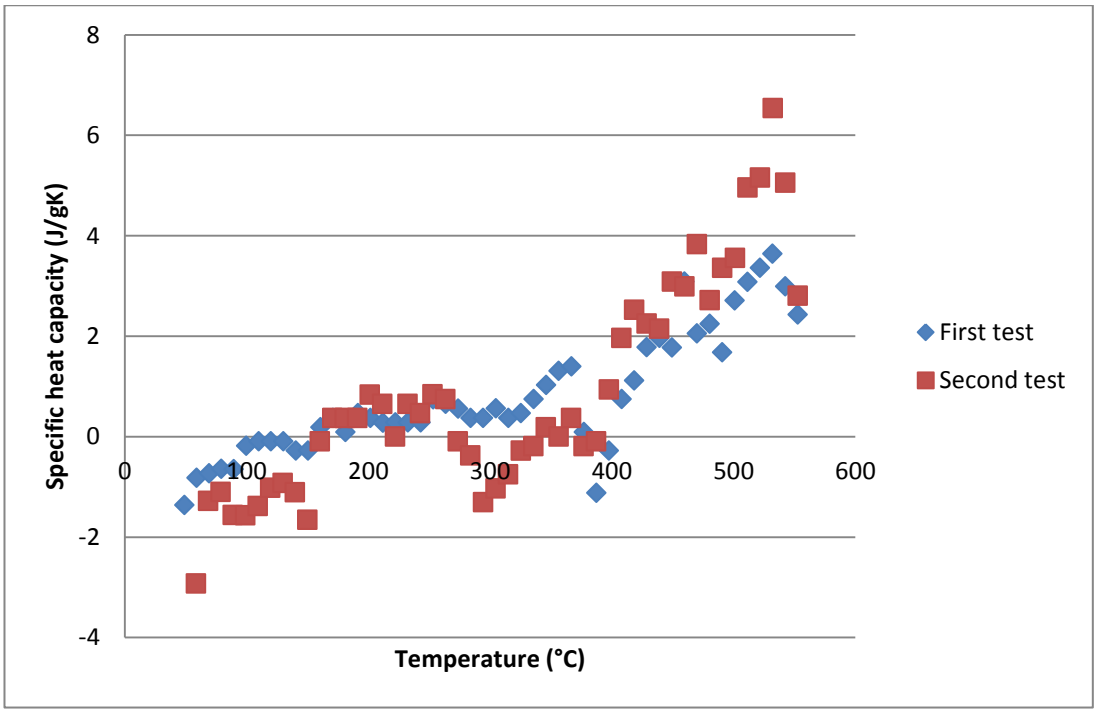

Figure 7-3 Calculated specific heat capacity of powder bed

The calculated specific heat capacity of stainless steel 316L powder bed is between 0-654J/kg·K at the temperature 0-550°C with temperature dependent property. Measurement errors between temperature range 0-180°C resulted in negative values. These errors appear in the range when the heat flow increased gradually in Figure 7-2 at the beginning of the measurement, where this increase rate did not repeat when the samples were cooled down at the end of the measurement.

Due to the large measuring error by the experiment above, another estimation method for the specific heat value at typical room temperature conditions was developed. The powder bed can be defined as a mixture of powder and air, and the specific heat capacity of the powder bed may be calculated by two main medium values – solid stainless steel 316L and air. The measured powder bed density is 4880kg/m^3, which is 61% of solid full density 8000kg/m^3 with specific heat capacity 500J/kg·K; the remaining 39% of air has specific heat capacity 1005J/kg·K[192]. So the estimated specific heat capacity value can be calculated by the equation below:

$$61\% \times 500 + 39\% \times 1012 = 699.68 J/kg \cdot K$$

Considering the temperature dependence, the estimation solution used above is converted to Equation (7.4) to calculate the specific heat capacity C_{pP} (P for powder) for the powder bed at a given temperature T.

$$C_{pP}(T) = C_{pS}(T) \times 61\% + C_{pA}(T) \times 39\% \quad (7.4)$$

Where C_{pA} (A for air) is the specific heat capacity for the air, and it has the same relationship with the temperature described in the Equation (3.4) [193]. Based on the temperature dependent specific heat capacity values obtained from the reference [190], the Equation (3.4) is converted to Equation (7.5) for calculating the specific heat capacity C_{pA} (A for air) at different temperatures for air.

$$C_{pA} = 1008 - 0.07T + 2 \times 10^{-4} T^2 \quad (7.5)$$

7.3 Loads

The load used in the heat transfer model is a moving heat source which simulates the moving laser passing through the powder bed. Due to the laser penetration phenomenon, a Goldak body heat source was selected for the model establishment. The description and solution of the Goldak heat source can be found in section 2.5.3. Input heat or power, shape of the input heat distribution and the moving speed of the heat source require definition.

The input power and shape of the laser were measured by the methods described in section 3.3.1. Output power was 47.5W when setting at 50W. The detected laser beam profile had a standard Gaussian TEM_{00} distribution on both X and Y directions. When setting the lens focus position value at 14.50mm and output power at 25W, the beam width at 50% of peak was 0.018mm on X direction and 0.018mm on Y direction; the beam width at 13.5% of peak was 0.031mm on X direction and 0.026mm on Y direction. The beam width on output power 50W would be relatively larger than 25W, and is calculated by Equation (5.1). The beam width at 50% of peak was 0.025mm on X direction and 0.025mm on Y direction; the beam width at 13.5% of peak was 0.044mm on X direction and 0.037mm on Y direction at 50W.

7.4 Boundary Conditions

7.4.1 Top surface

The top surface is a forced convection surface due to the inert gas flowing across the building area. Gas flow meter readings were checked every 30 minutes during the whole build. Results showed a stable reading on 12Liters/hour, which was used for calculating the heat transfer coefficient. The protective argon gas has a density of 1.67kg/m^3, a thermal conductivity of 17.80x10^{-3}W/m·K, a specific heat capacity of 0.52J/g·K and a viscosity of 22.7241μPa·s at a chamber temperature of 30°C during the build [194, 195].

Using the equation (4.2) – (4.4), the heat transfer coefficient used in the model was calculated to be 14.73W/m^2·K.

7.4.2 Bottom surface

With no pre-heating applied to the build substrate, the bottom surface of the geometry used in the melting process simulation can be seen as a conduction surface, as the heat will transfer from the powder bed to the solid build substrate. The bottom surface temperature of the build substrate was read every 30 minutes during an 8 hour build and the results are shown in Figure 7-4.

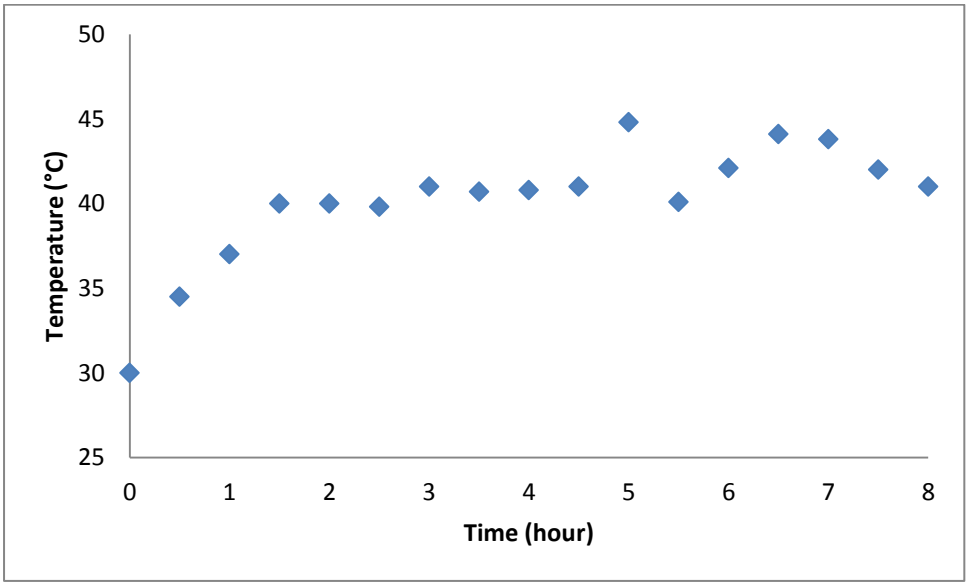

Figure 7-4 Bottom surface temperature of the build substrate monitored during an 8 hour build

Figure 7-4 showed, after around 1.5 hours, the substrate bottom surface temperature could reach 40°C to 45°C, and maintained at this temperature range until the build completed.

A finite element model was established to calculate the depth of the heat affected zone due to substrate bottom surface temperature increase during the build. The model was based on solving the Fourier's Law of heat conduction. The geometry used in this model has the same size and shape of the building substrate used in the experiment. Top and side surfaces of the build substrate are both conduction surfaces to allow the heat flowing from the build substrate to the surrounding environment. Bulk stainless steel 316L's material properties were used as the material property inputs.

The load in this model is the temperature applied to the bottom surface of the build substrate. Since the maximum temperature from the record was 45°C, the model presumed there was a constant 45°C temperature applied onto the bottom surface of the build substrate. A temperature distribution result at the steady state is shown in Figure 7-5.

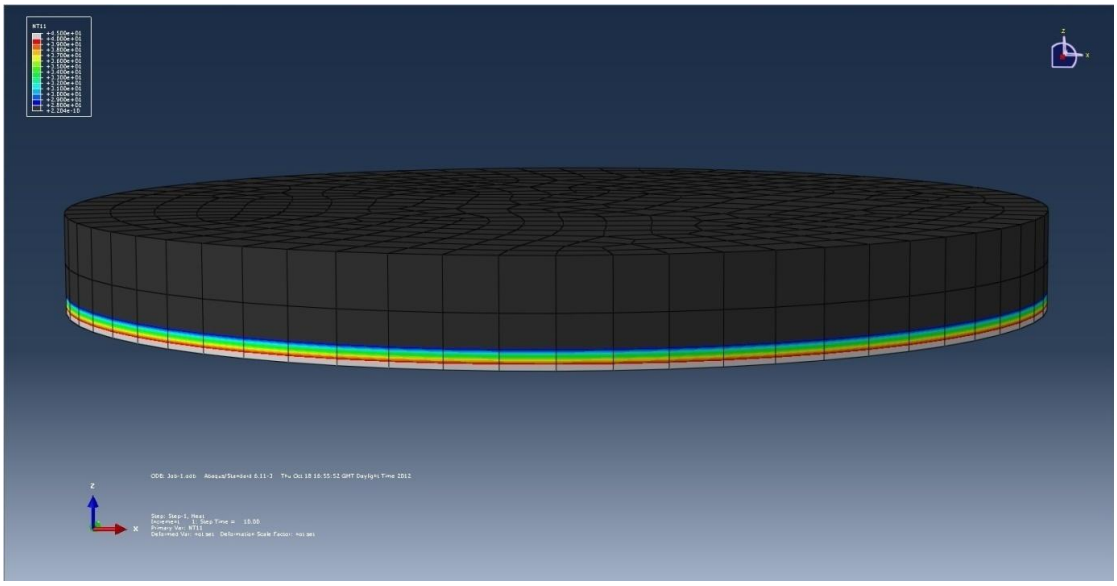

Figure 7-5 Temperature distribution on the build substrate when a constant 45°C temperature applied onto its bottom surface

In Figure 7-5, the black area in the geometry has a temperature below 30°C, which is the chamber temperature during the SLM process. The temperature distribution result shows the heat affected depth of the build substrate was relative small compared with the substrate thickness, and did not affect the

top surface at all. So when no pre-heating was applied to the build substrate, the bottom surface of the modelling cuboid was a conduction surface where heat transferred from the powder bed to the solid substrate.

7.5 Summary

The results of the third part experimental programme were presented in this chapter. Essential model inputs were measured, calculated and discussed.

The solid state stainless steel 316L's physical and thermal properties were used in the model for the liquid state as an assumption due to their close density. The density value of 7994kg/m^3 is used for the solid state, and 4880kg/m^3 is used for the powder state. Equations were developed for solving the temperature dependent conductivity and specific heat capacity of both solid state and powder state stainless steel 316L.

The input heat source is a Goldak body heat source, and has a power of 47.5W, a beam width of 0.025mm on both X and Y directions at 50% of peak, and a beam width of 0.044mm on X direction and 0.037mm on Y direction at 13.5% of peak.

Boundary conditions were also clarified. The top surface of the modelling cuboid is a forced convection surface with the heat transfer coefficient of 14.73W/m^2·K. The four side surfaces are continuous heat conduction surfaces, as well as the bottom surface.

8 Results & Discussions - Heat transfer Model Establishment

8.1 Introduction

This chapter presents the results and analysis from the modelling work. The overall modelling method was described in chapter 4. Three main steps on the heat transfer model establishment are presented, and the results from each step are discussed.

The first step of heat transfer model establishment was to apply a moving heat source on a solid material state medium. It helped to analyse the effect of laser processing parameters on the heat affected area without considering the material properties, giving a trend related to the experiments.

The second step was to apply the moving heat source on a medium with state variable material properties. The temperature distribution results are compared with applying the moving heat source to the medium which has solid material state or powder state only.

The third step was a multi-layer model establishment. Melt pool behaviour changes due to the increase of layers are presented and discussed. The nodes in each layer have different temperature distributions, and the results are analysed.

8.2 Moving heat source application

8.2.1 Melt pool formation

The moving heat source was applied on a solid material state medium. The results from heat transfer modelling are focused on the melt pool behaviour, such as shape, size and temperature. From calculated temperature distribution results, the area marked in the Figure 8-1 with temperature higher than stainless steel melting temperature 1400ºC at the origin is the predicted melt pool.

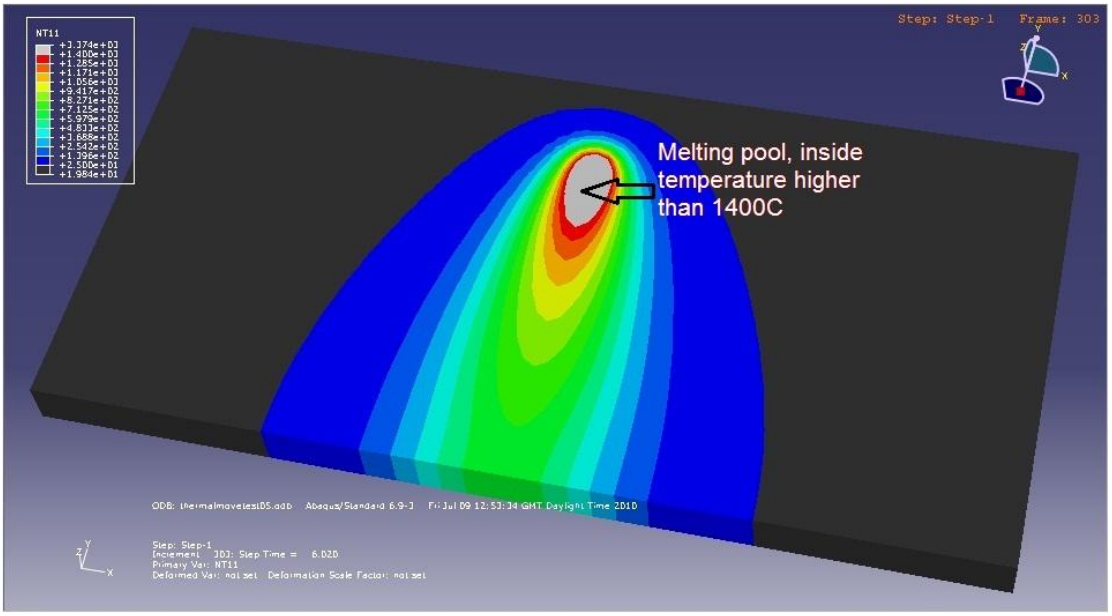

Figure 8-1 Melting pool formation from FE modelling

Figure 8-2 shows different temperature distributions picked at different times using a 200mm/s laser scanning speed, and the maximum temperatures were recorded. During the whole thermal history, the melt pool shows a very stable size with the width and length in equilibrium except for the initial time period. The maximum temperature inside the melting pool stayed in a narrow range with the standard deviation of 41.07ºC (1.2% of the average value). This indicates that each hatch line will have a stable straight shape and can

provide reliable size accuracy for the part under continuous moving heat source.

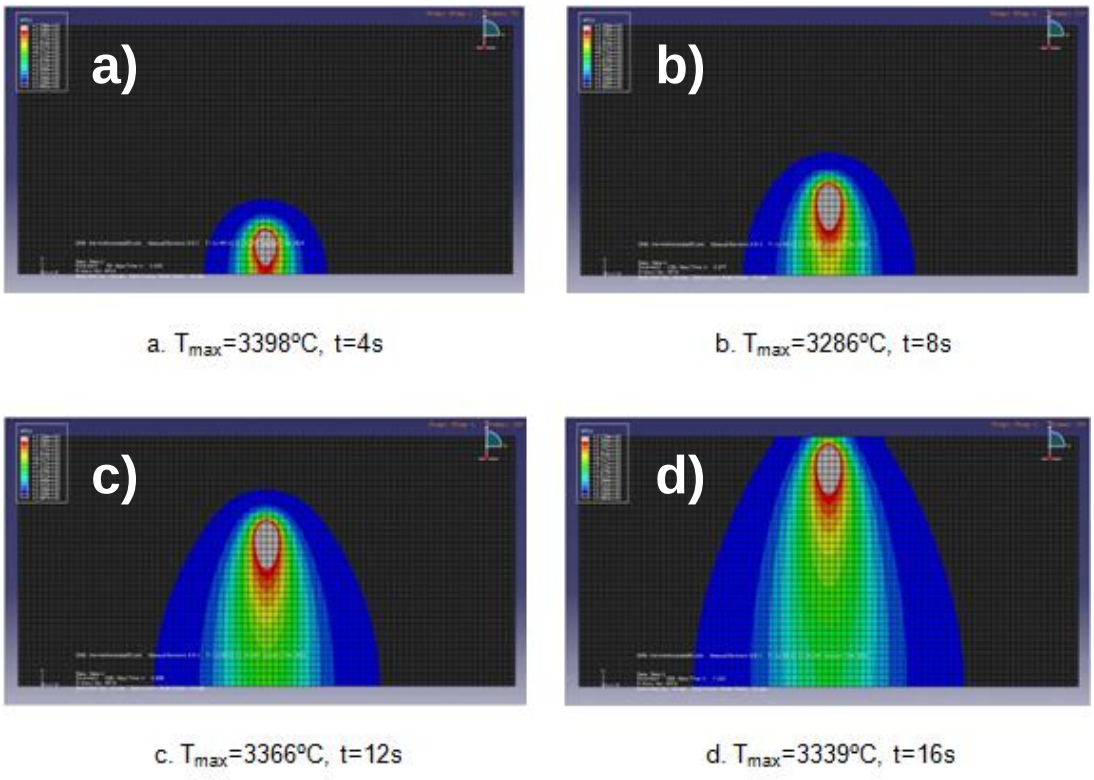

Figure 8-2 Temperature distribution at different recording time using 200mm/s scanning speed, a at 4s, b at 8s, c at12s, d at 16s

8.2.2 Laser processing parameters effect

As a main factor in determining the laser energy density, the effect of the laser scanning speed on the temperature distribution was studied. Four laser moving speeds 150mm/s, 200mm/s, 250mm/s and 300mm/s were used in the heat transfer modelling work to present different behaviours of melting pool. The main difference between different scanning speeds is the melt pool size, where lower speeds leading to an increase of the size, as shown in Figure 8-3. According to energy density definition described in Equation (2.9), with laser power and laser beam diameter remaining constant, lower scanning speed will create higher energy density, which will increase the

temperature in the laser-material interaction area and therefore increase the melting pool size.

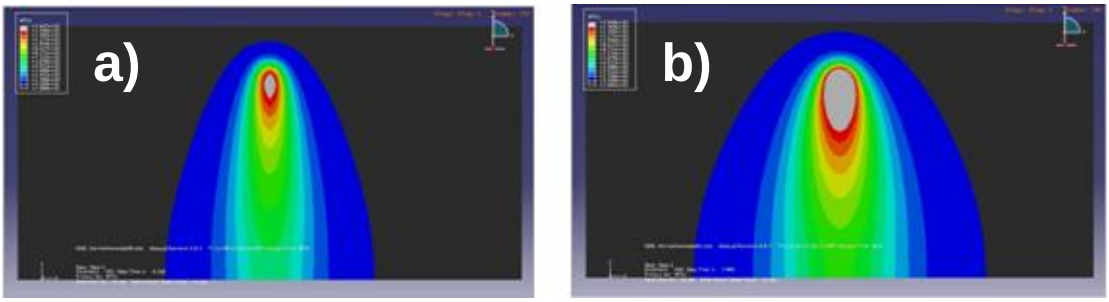

Figure 8-3 Temperature distribution under 300mm/s (a) and 150mm/s (b)

With an energy intensity increase, not only does the melting pool size increase, but also the maximum temperature inside melting pool. The melting pool size and maximum temperature under four scanning speed were compared and shown in Figure 8-4. The predicted melt pool length is larger than the width in the selected scanning speeds range. However, the trends in Figure 8-4 present a faster decrease in the melt pool length than the width. This indicates the melt pool size will become more circular when increasing the scanning speed. Under certain high scanning speed, a circular melt pool with diameter close to the laser beam diameter can be anticipated.

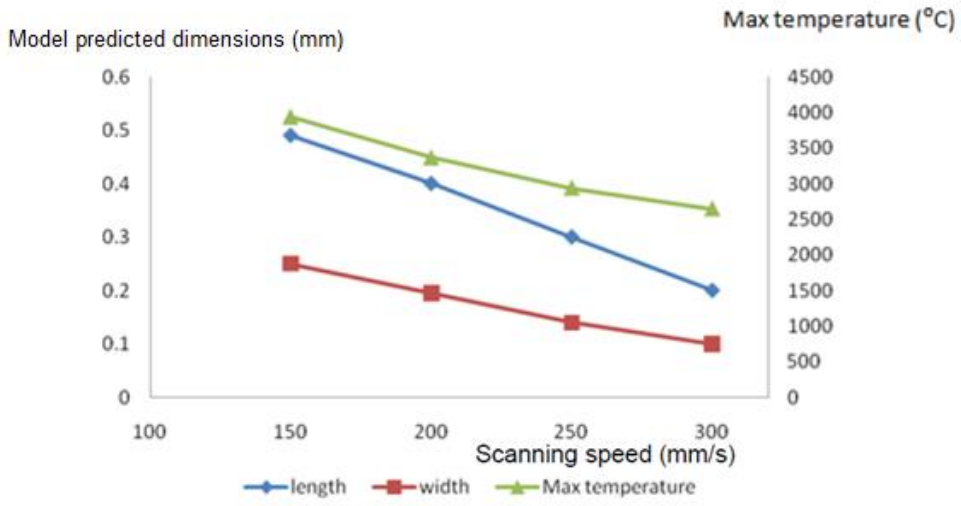

Figure 8-4 Melting pool size and maximum temperature under four different scanning speeds

In the SLM process, the laser scanning speed is determined by the point distance between two spots and the exposure time that the laser stays at each spot, calculated in Equation (2.10). Also a hatch distance is set to control the scan overlap, presented by Figure 2-6 in section 2.3.3. With a lower scanning speed, a larger melt pool is generated. Under a certain hatch distance, larger melt pool can generate more overlap between neighbouring melt pools, and the pores formed in between neighbouring melt pools will become smaller or disappear, leading to a low porosity in the part built by SLM. Therefore, in a processing parameters optimisation study, decreasing the scanning speed until the melting pool is big enough to create suitable overlap in the building area is one efficient method to improve the density and mechanical properties. This prediction shows agreement with the experiment results presented in section 5.2.4. However, improper low scanning speed will increase the temperature inside the melt pool. In some areas the temperature can go over the material's boiling temperature 2900°C and form material evaporation. This prediction is also agreed with the experiment results presented in section 5.2.4 and 5.3.1.

8.3 States variable material properties application

Three FE models with a moving heat source applied to a solid material state medium, a powder state medium and a state dependant medium were established. The temperature distributions results are shown in Figure 8-5, Figure 8-6 and Figure 8-7. The purpose of modelling a single layer with three material states is to show the importance of using state variable material properties in the simulation, by comparing the differences in the temperature distributions results. The other model inputs stay the same for these three FE models.

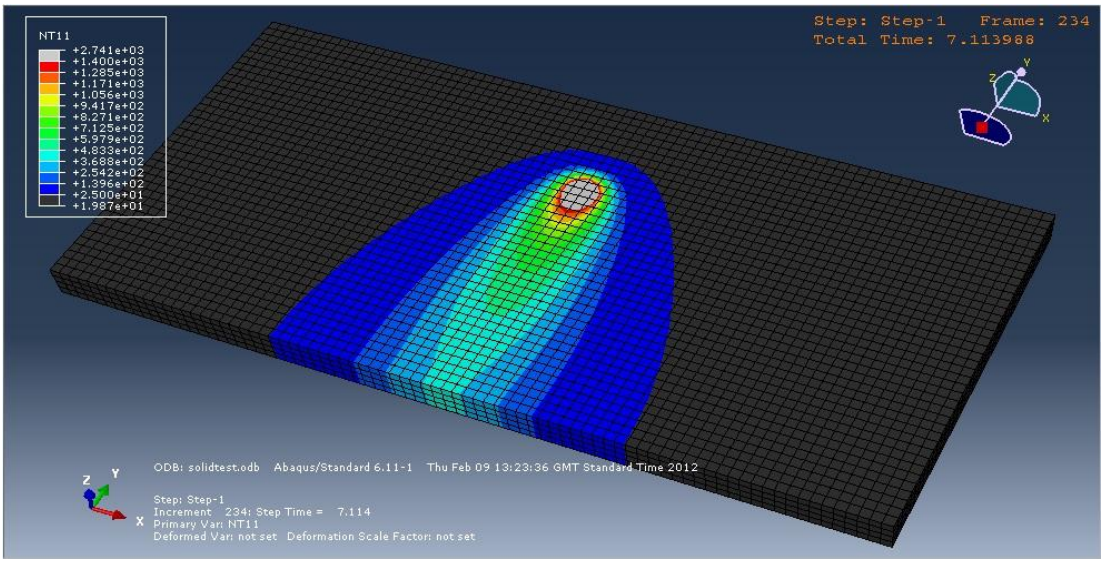

Figure 8-5 Moving heat source applied to a solid material state medium

When the moving heat source was applied to the solid material state medium, the formed melting pool had a shape close to that of the heat source, and a maximum temperature around 2800°C. The heat was transferred widely throughout the whole geometry, forming a quarter of the ellipsoidal heat affected zone.

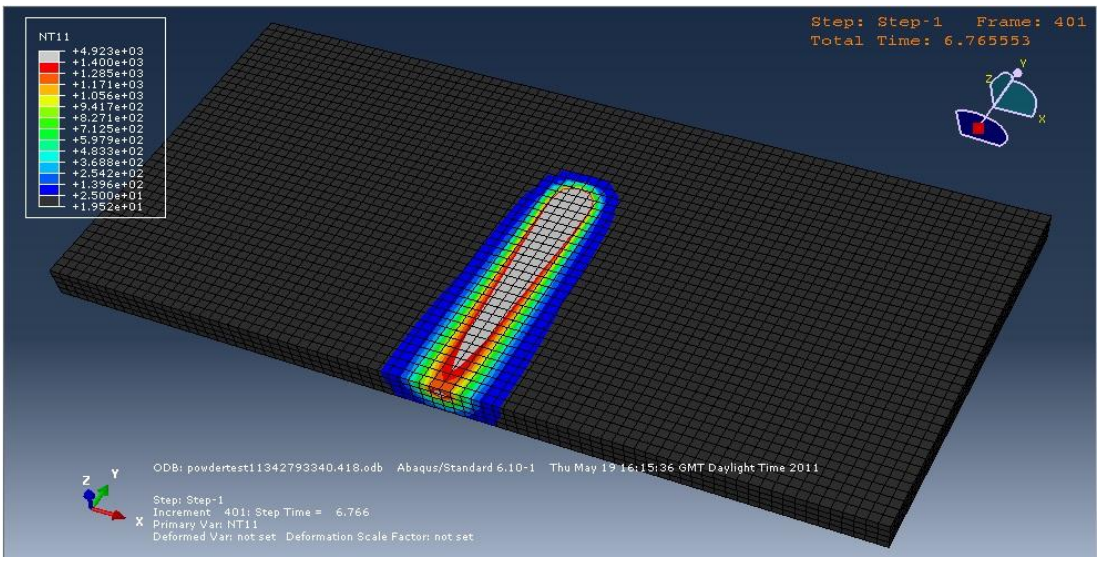

Figure 8-6 Moving heat source applied to a powder state medium

When the moving heat source was applied on the powder state medium, the temperature distribution was significantly different. Due to the relatively low thermal conductivity of the powder bed compared to the solid material, the heat had less freedom to be transferred further into the geometry. Most of the heat was contained in a small area, forming a long narrow melting pool, with a maximum temperature around 5000°C. The heat affected zone was also narrower compared with the one in the solid material state medium.

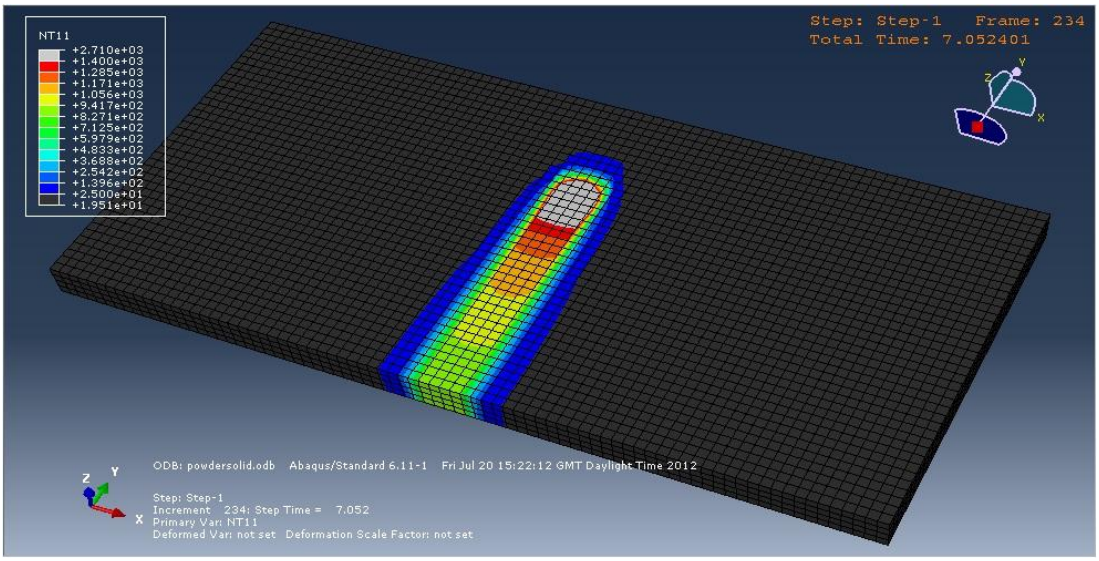

Figure 8-7 Moving heat source applied to the states variable medium

When the moving heat source was applied to the states variable medium, the shape of the heat affected zone was very similar to the one in the powder state medium. This was mainly because the powder bed has relatively low thermal conductivity, and the heat was not being transferred further into the geometry as well as in the solid state. Since the powder material in the melt pool moving path was transferred to a solid state after the laser passed, heat was easily conducted through the solid path, reducing the length and temperature of the melting pool. The maximum temperature of the melting pool was around 2800°C, which is closer to the one on the solid material state medium.

The results present that the sizes and shapes of both melt pool and the heat affected zone are very different when the moving heat source is applied to different material states. The temperature distribution results predicted by the model will be used for further analysis and the microstructure prediction. Therefore, states variable material properties need to be applied in the model to result accurate prediction.

8.4 Multi-layers model establishment

A multi-layers model was established based on the single layer modelling results. The element size used in the model is 0.025mm, while the building layer thickness set in the experiment is 0.5mm. Therefore each layer contains 2 layers of the elements and 3 nodes in the vertical direction.

In the SLM process, the laser generated heat affected zone can only reach a certain depth with a few powder layers involved, leaving the rest of the powder layers unaffected. To obtain a single node or element's temperature history due to the layers building, 3 continuous vertical arrangement nodes in the central melting pool moving path were selected, shown in Figure 8-8 and Figure 8-9 (the rest can be done in the same manner), and their temperatures as a function of time were recorded. The multi-layer analysis continues layer by layer until the elements' temperatures remains unaffected by the laser energy.

A time period of 50 seconds was used for plotting the nodes' temperatures as a function of time, since it is a typical time period for laser scanning and powder depositing in each layer during thin wall building. Although the cooling step which includes the powder deposition for the next layer is much longer compared with the heat moving step, the temperature of the nodes before the next layer started may not be able to decrease to the surrounding temperature 30°C. But the elements melted by the laser should be consolidated already, so a solid state material property can be applied. The powder deposited for the next layer has a temperature of 30°C, the same as

the process chamber temperature. Therefore, to avoid complicating the whole model by adding the thermal history results from the previous layer analysis to the next layer and affecting the boundary settings, a complete cool down step was assumed before applying the moving heat source to the next layer. The aim of this multi-layers modelling work is to obtain the melt pool behaviour and temperature distribution trend when building up the layers.

Figure 8-8 to Figure 8-16 show temperature distributions on the whole geometry, and 3 nodes' temperature recorded curves from 1 layer to 9 layers.

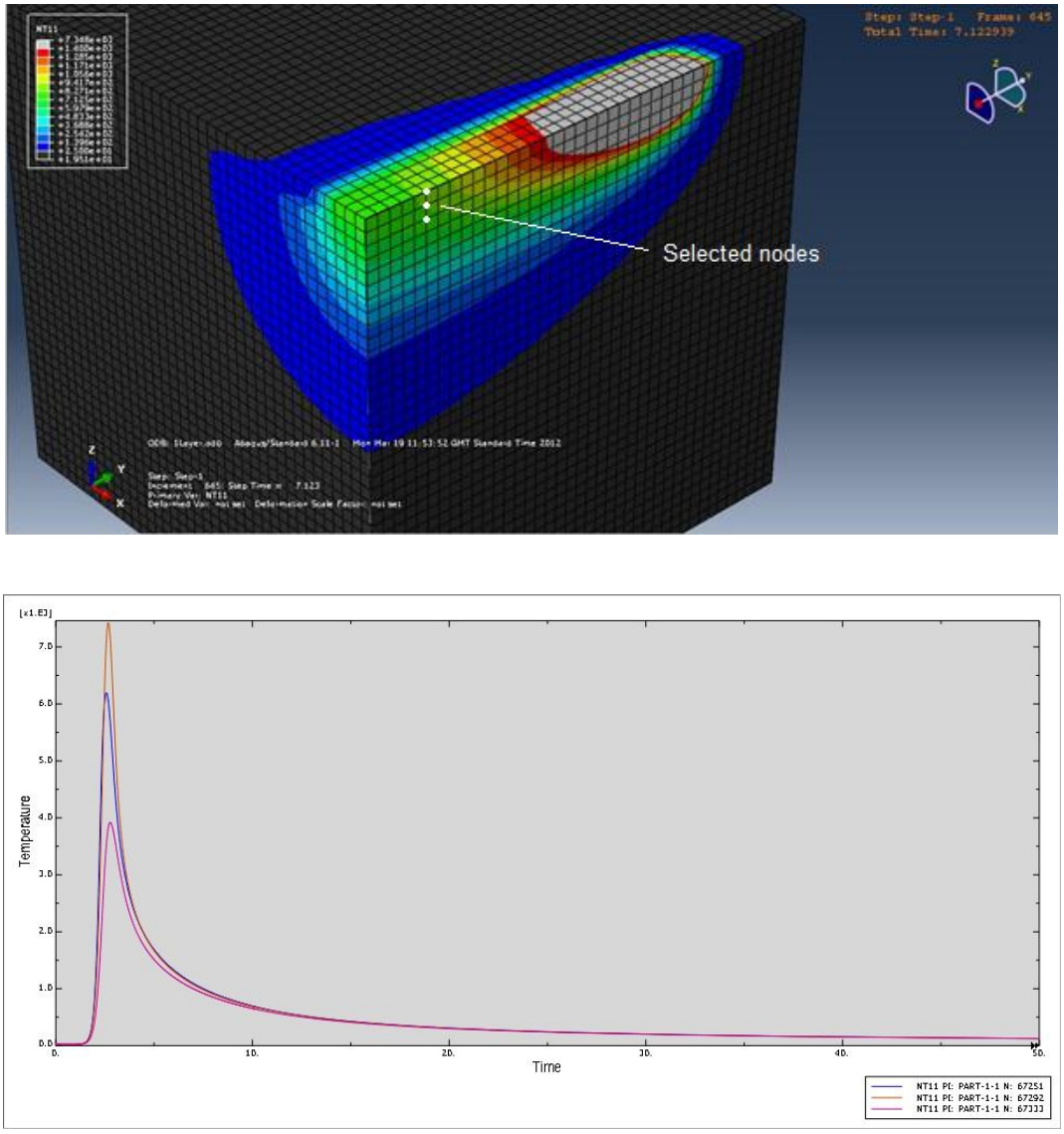

Figure 8-8 Temperature distribution result (top), temperature history for 3 selected nodes (bottom), layer 1

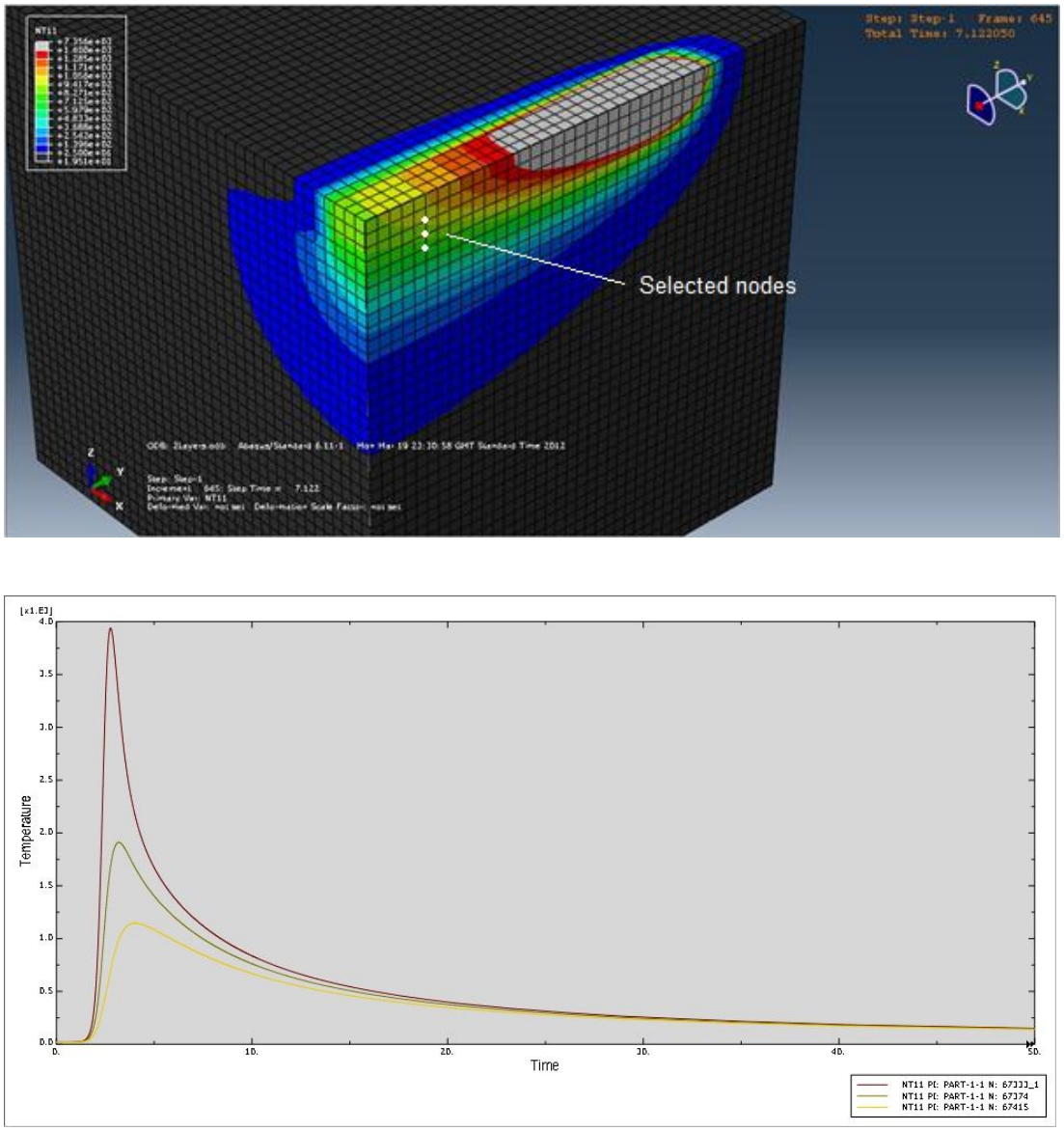

Figure 8-9 Temperature distribution result (top), temperature history for 3 selected nodes (bottom), layer 2

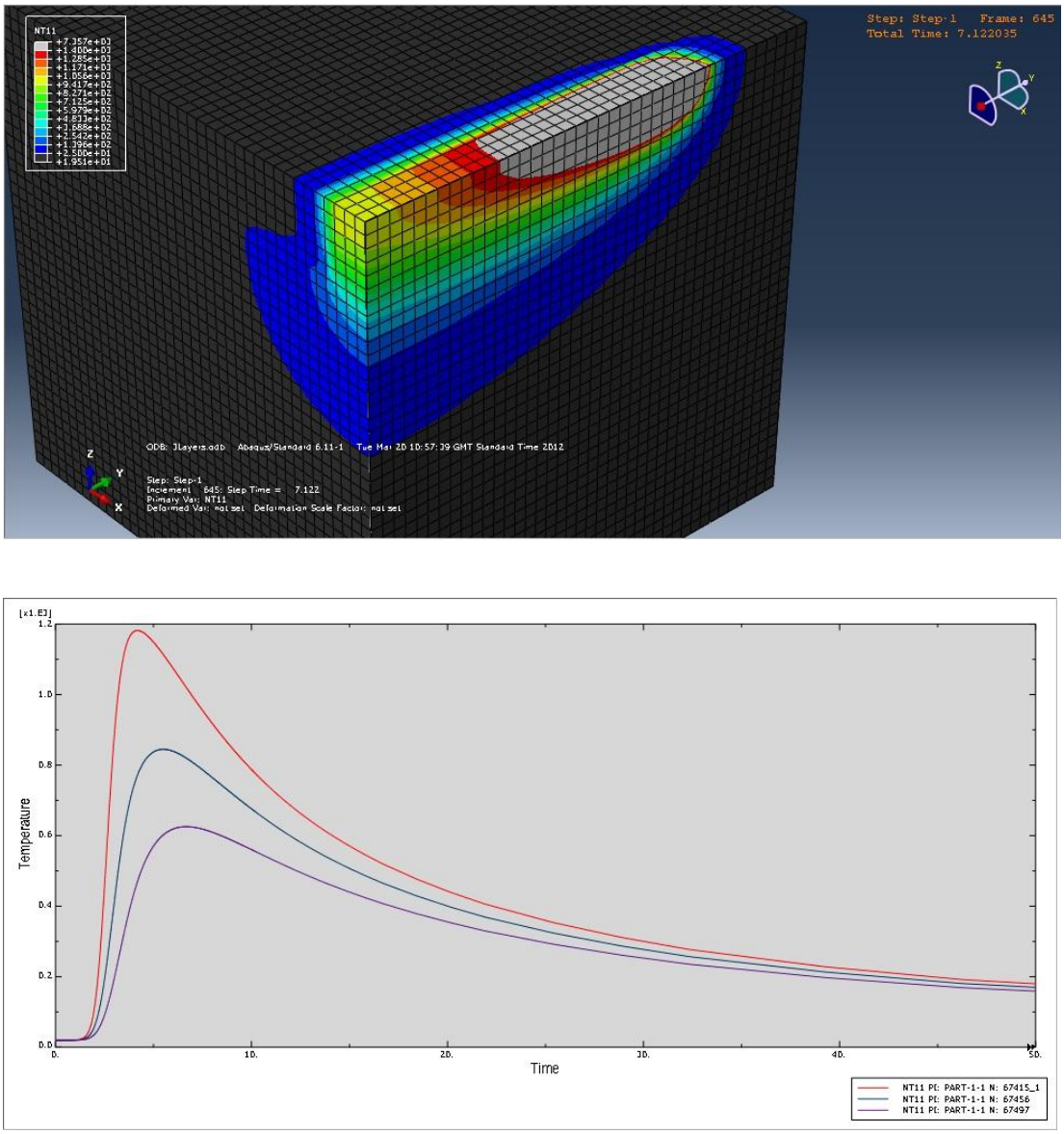

Figure 8-10 Temperature distribution result (top), temperature history for 3 selected nodes (bottom), layer 3

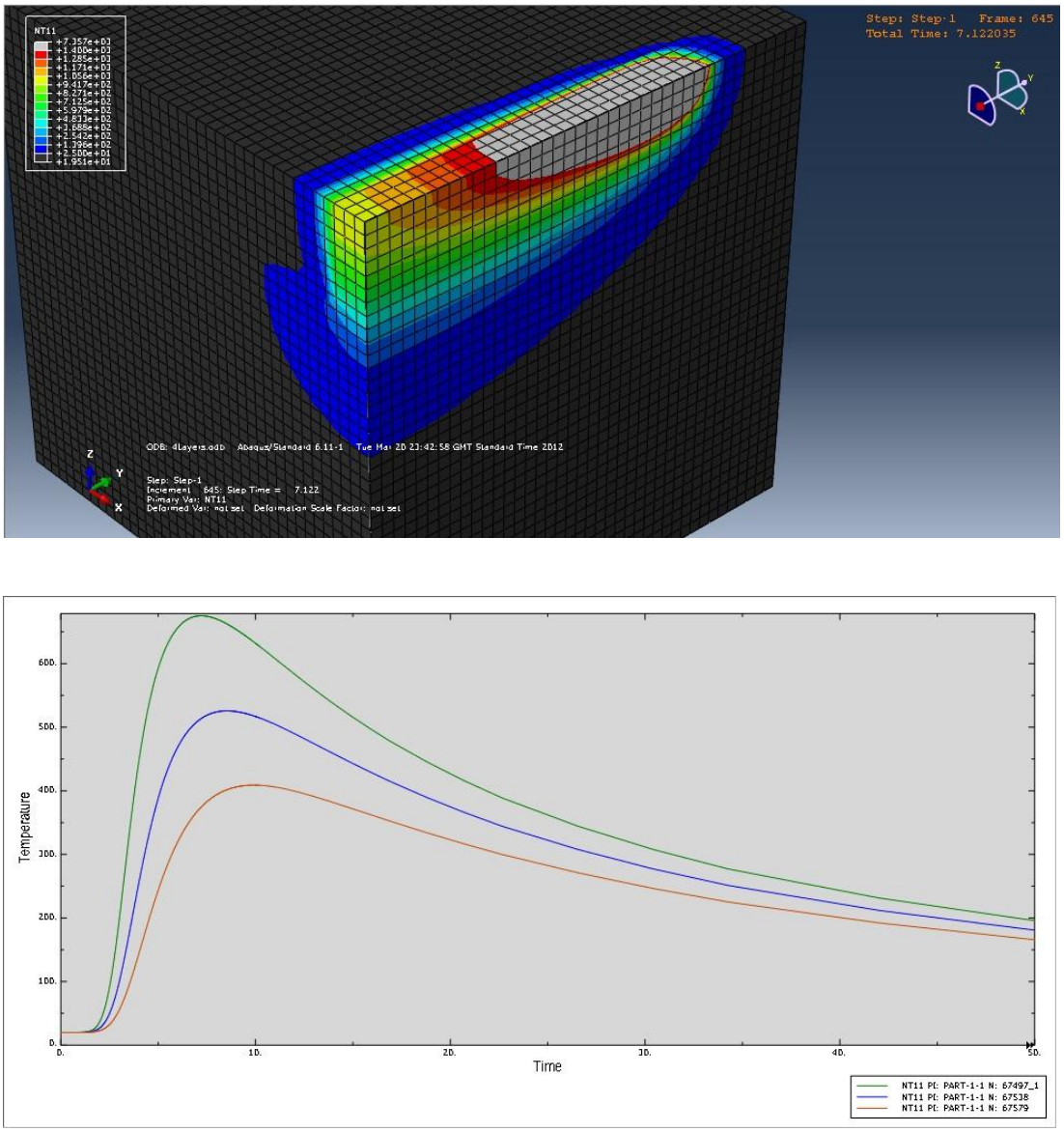

Figure 8-11 Temperature distribution result (top), temperature history for 3 selected nodes (bottom), layer 4

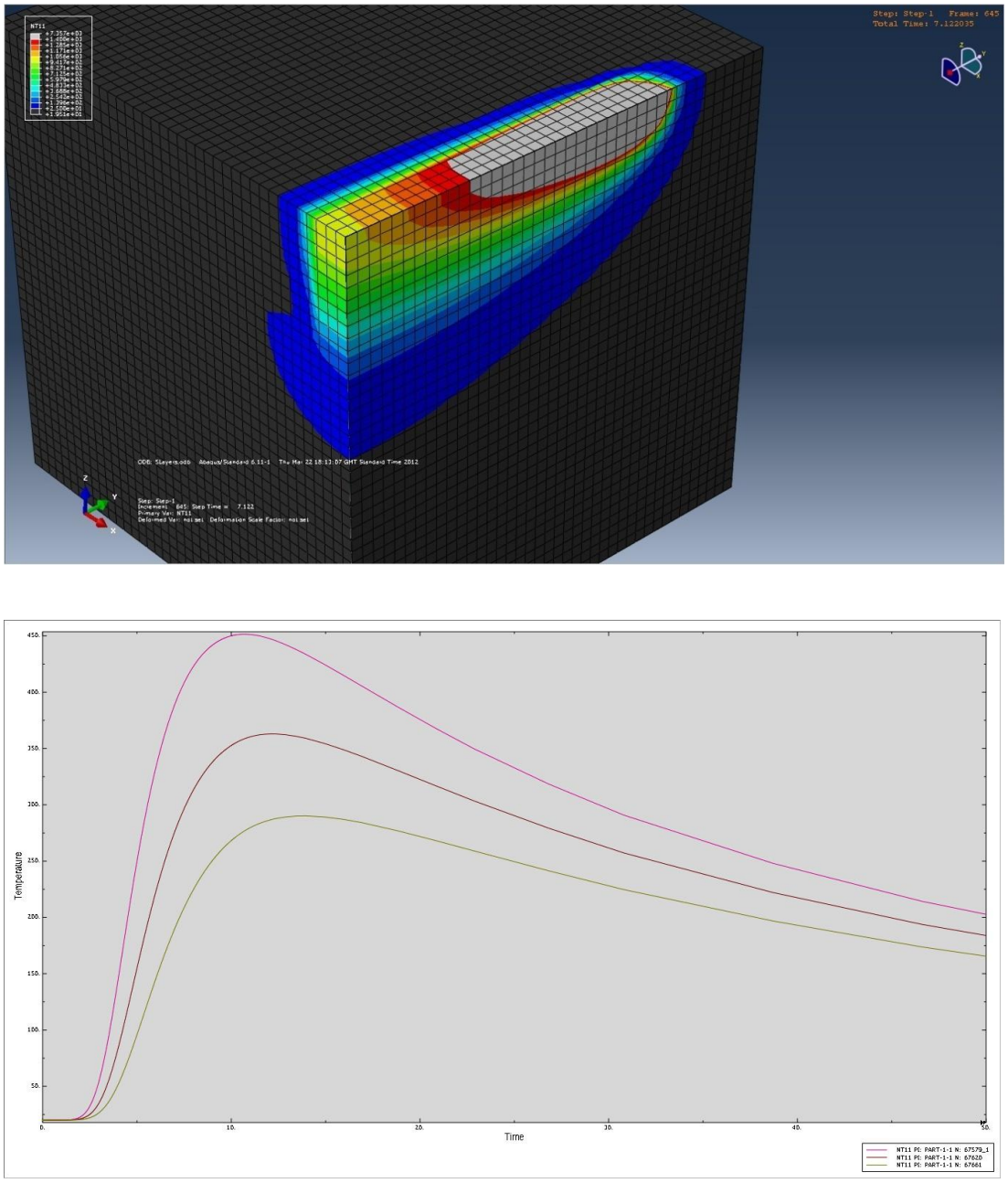

Figure 8-12 Temperature distribution result (top), temperature history for 3 selected nodes (bottom), layer 5

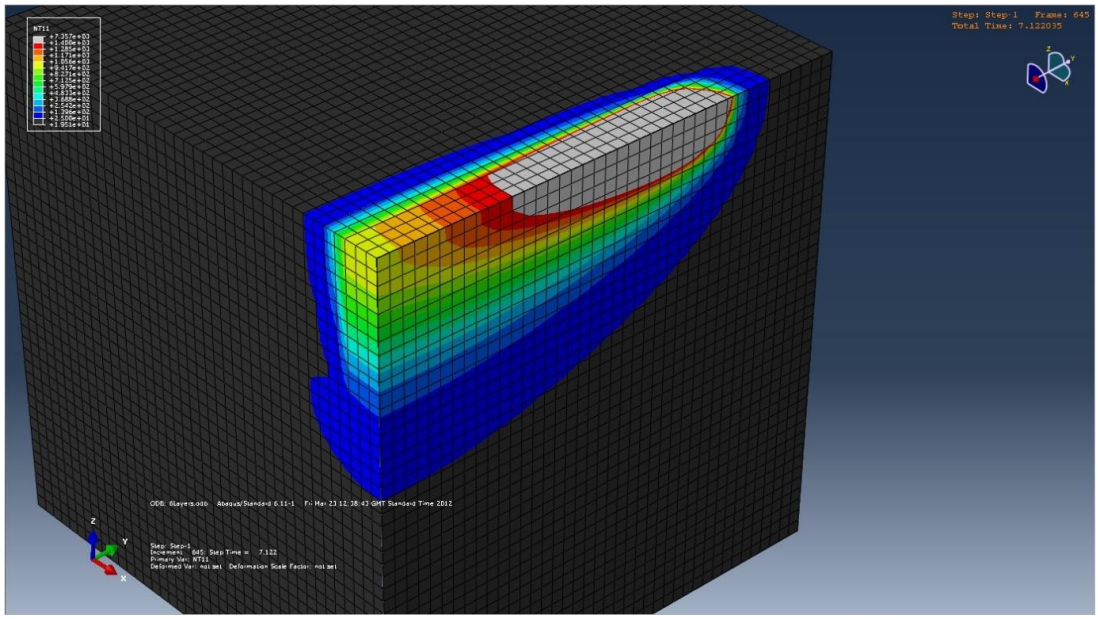

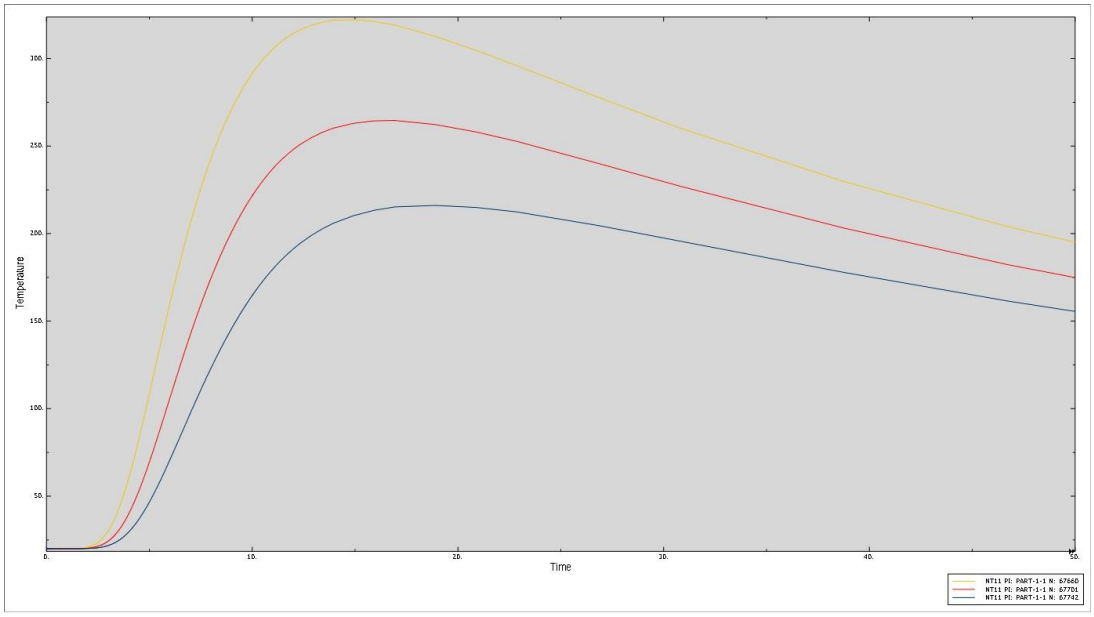

Figure 8-13 Temperature distribution result (top), temperature history for 3 selected nodes (bottom), layer 6

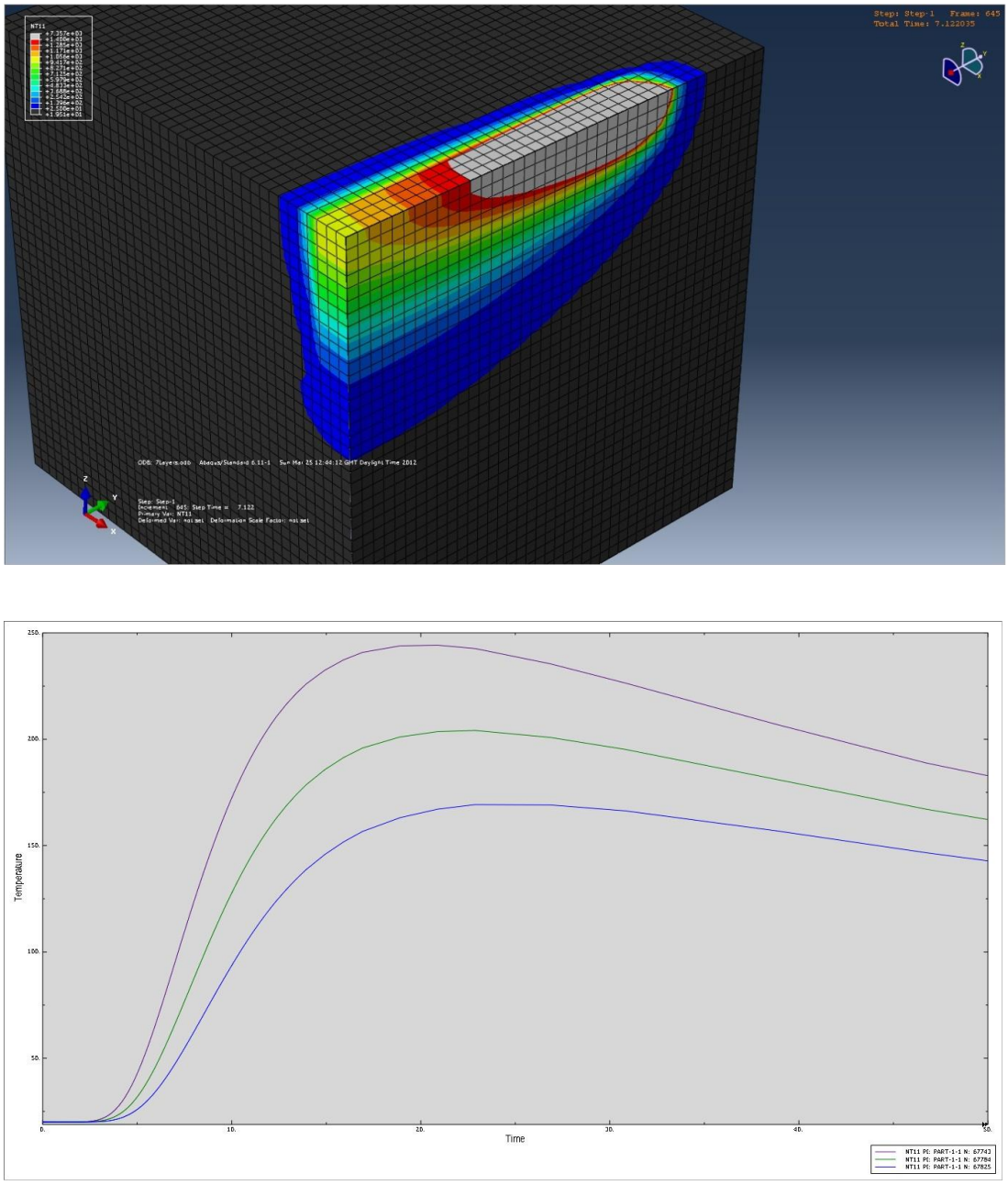

Figure 8-14 Temperature distribution result (top), temperature history for 3 selected nodes (bottom), layer 7

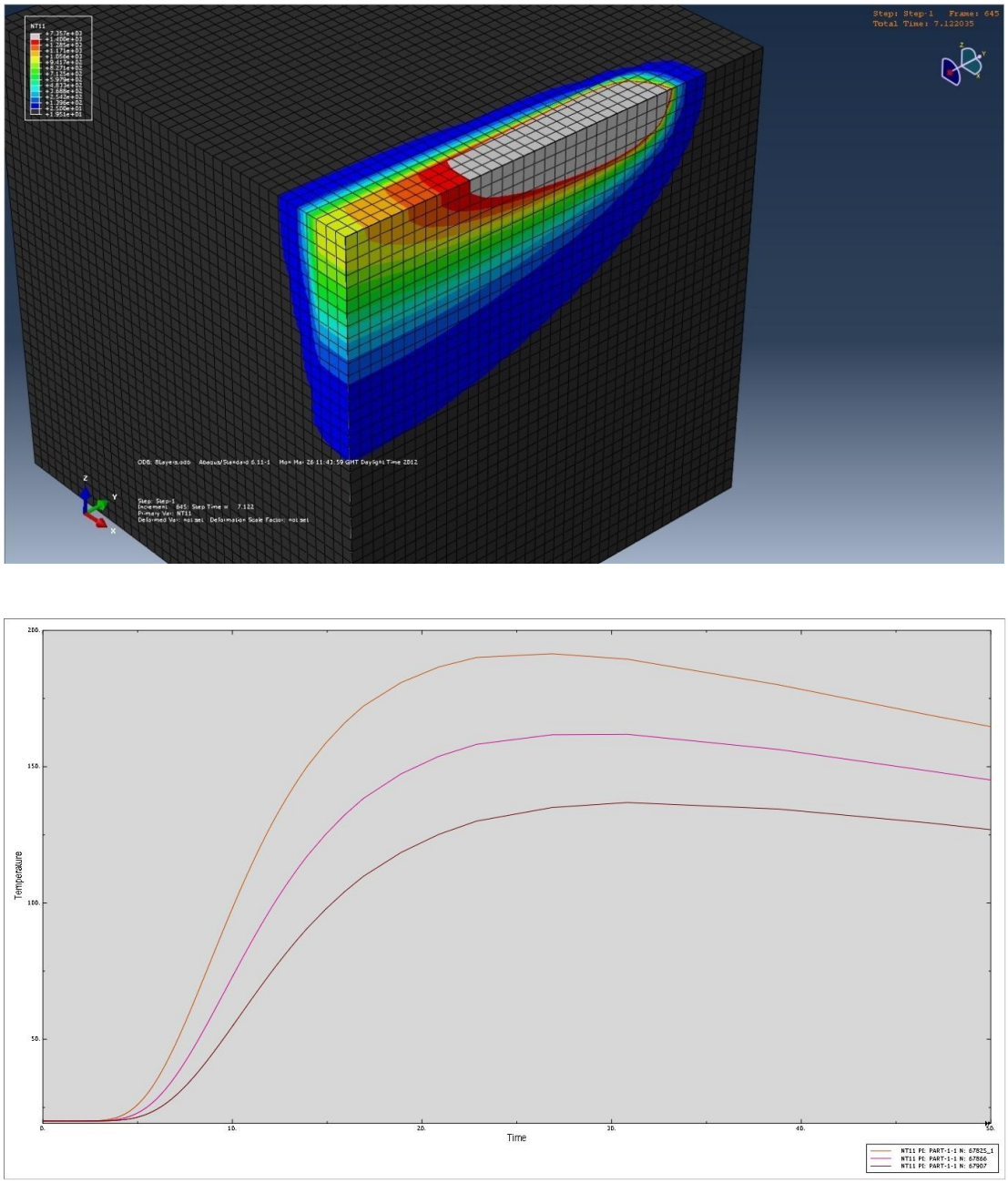

Figure 8-15 Temperature distribution result (top), temperature history for 3 selected nodes (bottom), layer 8

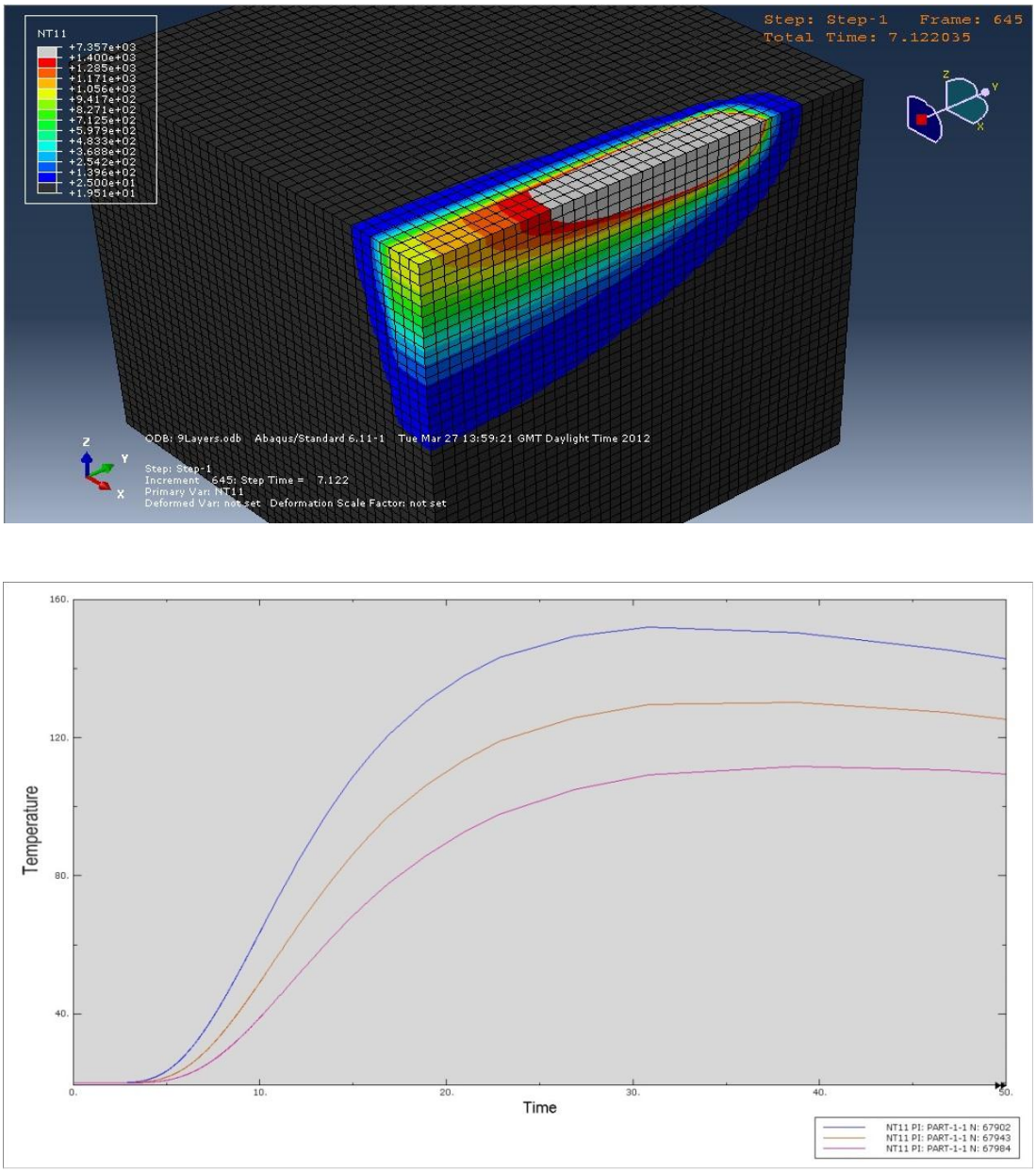

Figure 8-16 Temperature distribution result (top), temperature history for 3 selected nodes (bottom), layer 9

The temperature distributions in Figure 8-8 to Figure 8-16 show a trend that the heat affected zone became smaller and smaller from layer 1 to layer 9, while the melt pool became larger. This is because of the relatively low thermal conductivity of the powder bed compared to the solid material, so the heat had less freedom to be transferred further into the geometry when the powder layers build up. The shape of the heat affected zone was similar to

the one predicted in the solid material state when 1 layer of powder was applied, but close to the one predicted in the powder state when 9 layers of powder were applied. The maximum depth of heat affected zone reached 9 layers, indicating that after 9 layers build, the shape and size of the heat affected zone and the melting pool would be constant. So the multi-layers modelling ceased at 9 layers.

The selected three nodes' temperature history was recorded from layer 1 to layer 9 in heat moving step. Their peak temperatures as a function of the layers are plotted in Figure 8-17. The temperatures have big drops from layer 1 to layer 3, indicating the heat was concentrated in the top 2 layers, where the laser-material interaction happened and the melt pool formed. The depth of the melt pool is close to 2 layers and suggests a strong bonding between layers. Some nodes temperatures in layer 1 and 2 are higher than the boiling point for a few seconds, where evaporation can be predicted. From layer 3, all nodes' peak temperatures are below the melting point, indicates the elements there remain the solid state when re-heated.

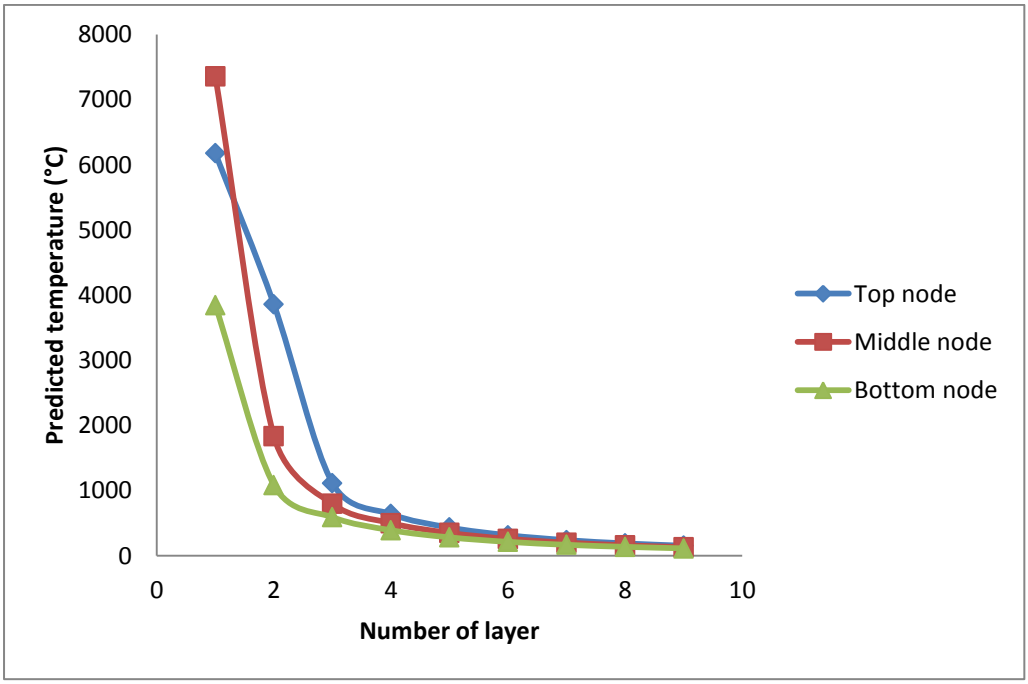

Figure 8-17 Selected nodes' peak temperatures in each layer

This multi-layers model predicted the temperature history for a moving laser with 50W power, 0.04mm beam diameter and 200mm/s scanning speed applied on a powder bed formed by LPW powder. Changing either the input energy intensity or the powder bed properties can result in a change of the prediction results. In the case of simulations with evaporation predicted, the material is assumed to evaporate and leave the model geometry; therefore the temperature in the heat affected zone should never be higher than the boiling temperature. Since this evaporation has not taken into account in this modelling work, the temperature of the melt pool is not bounded by the boiling temperature. This leads to a significant overheating of the liquid pool [196]. It should be noted that this over-heating is unphysical, and it is unlikely that the predicted temperature higher than the boiling point will actually occur without the evaporation of material.

This simulation work also contains limited assumptions in liquid material state behaviour and properties. It should be noted that the laser material interaction will change when the material states change, especially the energy absorption. The wetting behaviour of the molten material as a result of surface tension forces also affects the temperature distribution in the heat affected zone. Therefore, the modelling results can be improved if a solution to model these effects can be established; however, it has yet to be found [154].

A temperature history for the middle node from layer 1 to layer 9 was recorded, and is plotted in Figure 8-18. It presents a whole thermal history for a certain point (middle node of each layer) during the SLM process. The material at this point experienced a melting or vaporising, followed by the solidification; then re-melting and solidification again; was re-heated by the heat conduction a few times before not be affected by the laser energy any more. The temperature history can be used for microstructure prediction, and is discussed in the next chapter.

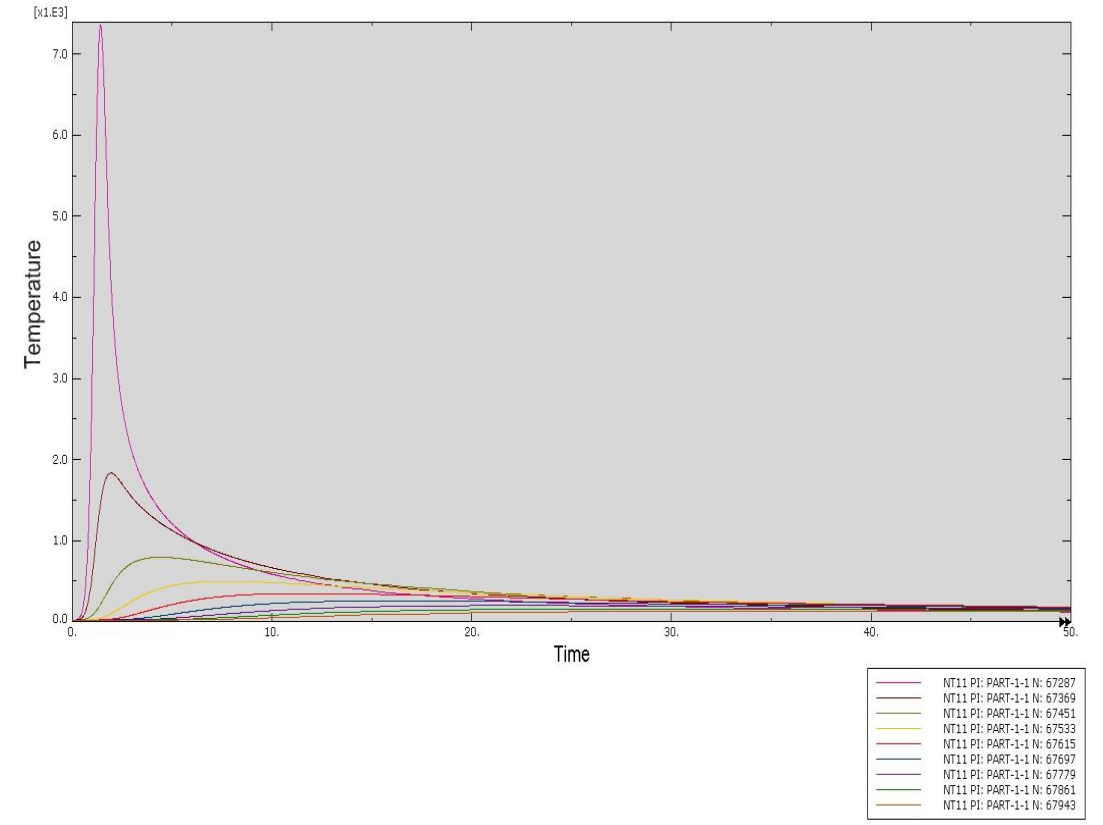

Figure 8-18 Temperature history for the middle node from layer 1 to layer 9

8.5 Summary

The results of the heat transfer modelling work were presented and analysed in this chapter. Three main steps on the heat transfer model establishment are presented.

When applying a moving heat source to a solid state medium, the melt pool shows a stable size with the width and length in equilibrium in the laser moving period. Decreasing the moving heat source speed leads to a larger melt pool generation, and helps to reduce the porosity in the part built by SLM. Improper low scanning speed results in some elements' temperatures going over the material's boiling temperature 2900°C and form material evaporation. The predicted modelling results show a good agreement with the experiment results.

Three FE models with a moving heat source applied to three different material states have results presenting that the sizes and shapes of both melt pool and the heat affected zone are different when the moving heat source is applied to different material states. Therefore it is important to use the state variable material properties in the simulation to obtain accurate temperature distribution.

Multi-layers modelling results presented a trend that the heat affected zone became smaller while the melt pool became larger when the layers build up. The maximum depth of heat affected zone reached 9 layers, where the modelling creased. The heat generated by the laser concentrated in the top 2 layers, where the laser-material interaction happened and the melt pool formed. A whole thermal history for the material at a certain point during the SLM process was presented, and can be used for the microstructure prediction in the next chapter.

9 Results & Discussions - Microstructure Prediction and Validation

9.1 Introduction

This chapter presents microstructural prediction based on the results obtained in the modelling work, as well as the results from the fourth part of the experiment – microstructure examination. The experimental examination of the microstructure is a validation process for the predictive heat transfer model developed in Chapter 8.

9.2 Microstructure prediction

Microstructural prediction was based on the temperature distribution history obtained from the heat transfer modelling work in chapter 8. The isothermal transformation diagram (time-temperature-transformation diagram) for rapid cooled austenite stainless steel was used for determining phase formation during the SLM process, shown in Figure 9-1. Considering the chemical composition of stainless steel 316L, three equilibrium phase diagrams – Fe-C (Iron-carbon), Fe-Cr (Iron-Chromium) and Fe-Ni (Iron-Nickel) were also referred to, figures can be found in section 2.3.9. Figure 8-18 gives a temperature history from layer 1 to layer 9, and the results are used in the prediction. The cooling rate changes during each cooling process, but a major effective cooling rate which describes the majority temperature change can be calculated.

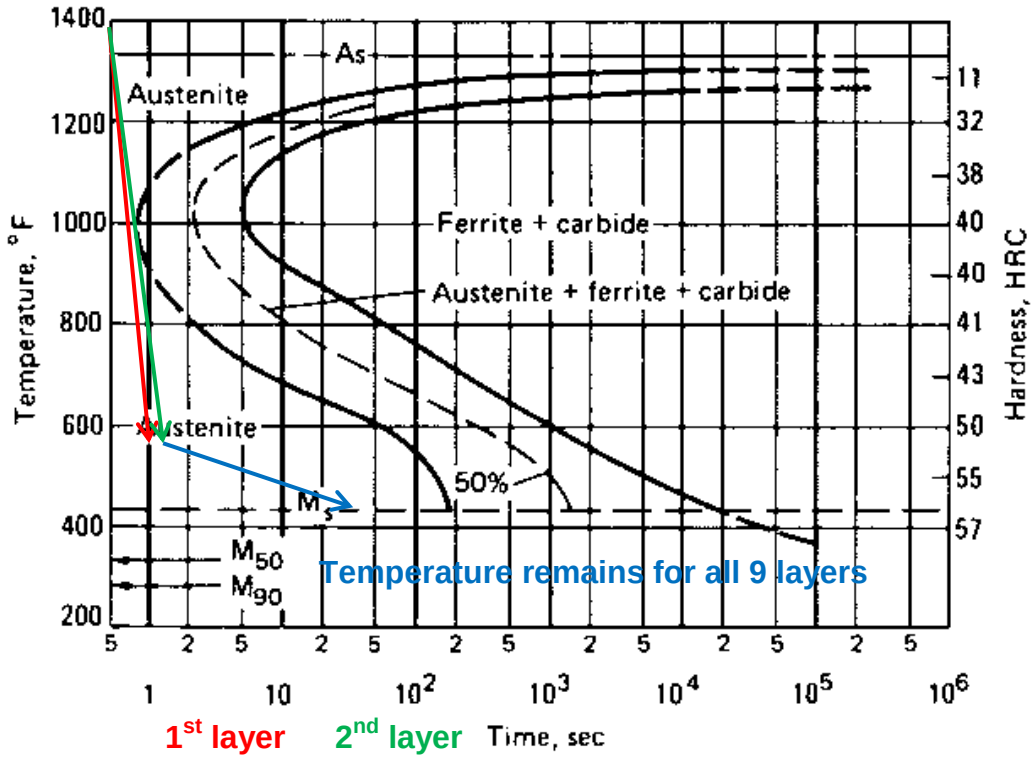

Figure 9-1 Isothermal transformation diagram for carbon steel [197]

In the multi-layer heat transfer model, elements in layer 1 (top layer) which were directly heated and melted by the moving source had an overall temperature over the boiling point and then were cooled down very fast, as shown in Figure 9-1. Due to this rapid heating and cooling process, massive γ-iron should be generated.

Elements in layer 2 (one layer underneath) were affected by the heat conduction, and part of them were re-melted. Most elements had the temperature increased to the melting point and then cooled down fast too, as shown in Figure 9-1. Due to very fast heating and cooling rate again, γ-iron should be re-generated.

Elements in layer 3 to layer 9 were also affected by the heat conduction, but remained in the solid material state since their maximum temperature did not reach the melting point. They experienced a fast heating rate and relative

fast cooling rate, but the temperature remains in the 400-600°C for about 30 seconds, as shown in Figure 8-18. This is also happened to the top 2 layers. Since this temperature maintaining still sits in the austenite area, the austenite phase generated before should remain the same.

In the Fe-C phase diagram, with carbon weight percentage less than 0.03%, austenite is expected in the temperature range from 912°C to 1394°C. In Fe-Cr phase diagram, with chromium weight percentage around 16.5%, the binary Fe-Cr alloys are nearly ferrite (α-iron) over the whole temperature range below melting point. In Fe-Ni phase diagram, with nickel weight percentage around 10.1%, austenite is expected when the temperature above 700°C.

In the iron-rich corner of the C-Cr-Ni-Fe system, α-iron usually does not form in a very fast cooling procedure [105]. Rapid cooling from the γ region should give a retained austenite structure.

9.3 Microstructure examination

Polished and etched (based on the practice standard ASTM E407) thin wall samples were examined under optical microscopy and SEM. Since SEM images could give more clear details than optically captured images, they were picked for microstructure examination and discussion. Figure 9-2 and Figure 9-3 show the SEM images of SLM part's microstructure on horizontal view, while Figure 9-7 and Figure 9-8 on vertical view. The horizontal view is parallel to the laser moving path, and the vertical view look at the layer building direction.

9.3.1 Horizontal view

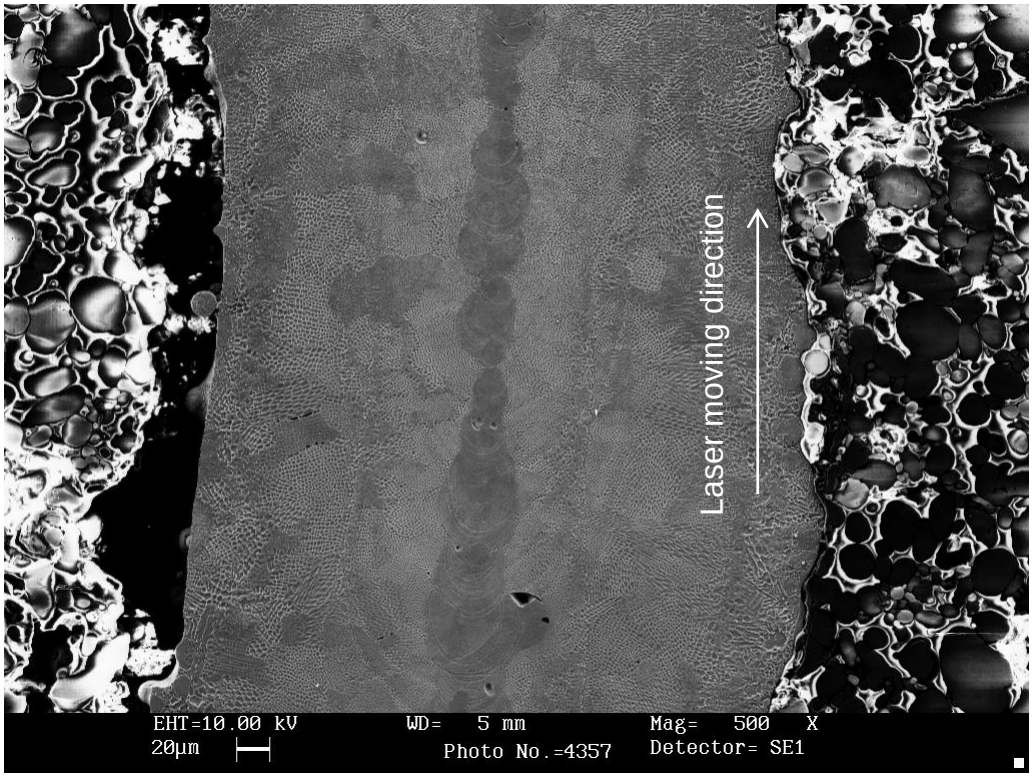

Figure 9-2 SLM stainless steel microstructure under SEM, mag=500, horizontal view

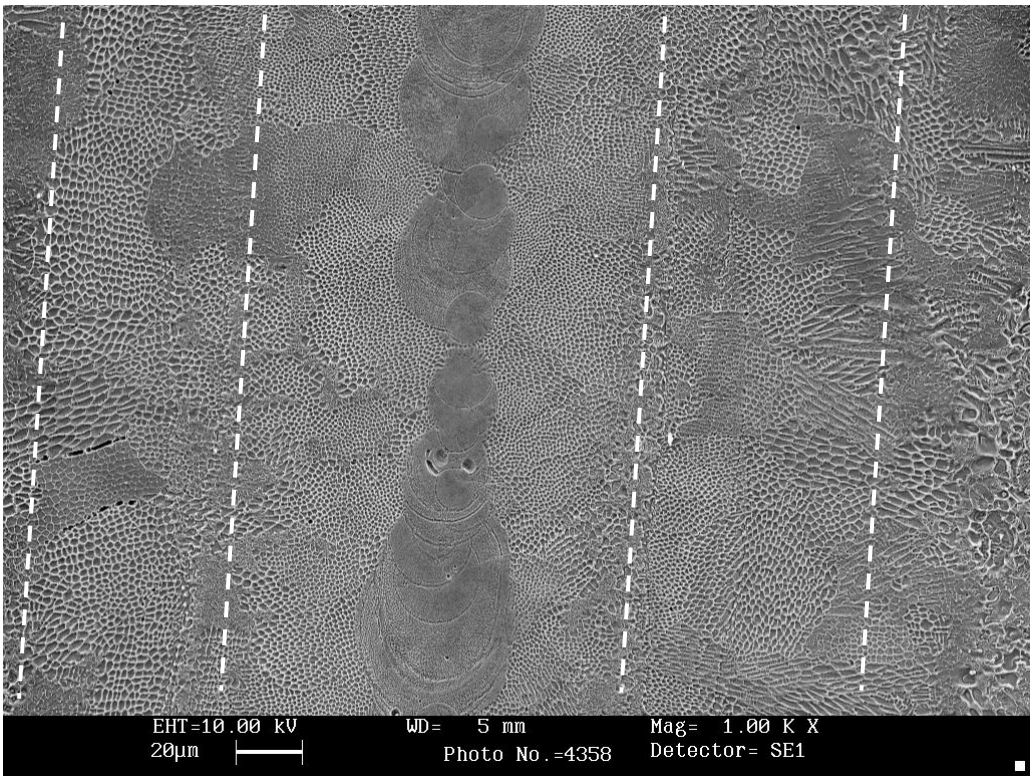

Figure 9-3 SLM stainless steel microstructure under SEM, mag=1000, horizontal view

Variable sizes of grains can be found in the horizontal view, and most sizes fit into the range of 30-45μm. It can be found that the grain size becomes smaller at the edges. There is no significant grain growth phenomenon along the laser moving track, indicating relative average temperature distribution change and cooling rate in the horizontal view during the laser movement.

In Figure 9-3, it can be seen that the whole horizontal view was divided into several areas by the lines parallel to the laser moving path. These lines are not grain boundaries, but were generated by the temperature changes inside the heat affected zone during laser movement, as shown in Figure 9-4. Five nodes were picked from the centre to the edge of the heat affect zone, and their temperature history was plotted in Figure 9-4. Nano indentation was done on each area to check if there is any property difference. The result is shown in Figure 9-5.

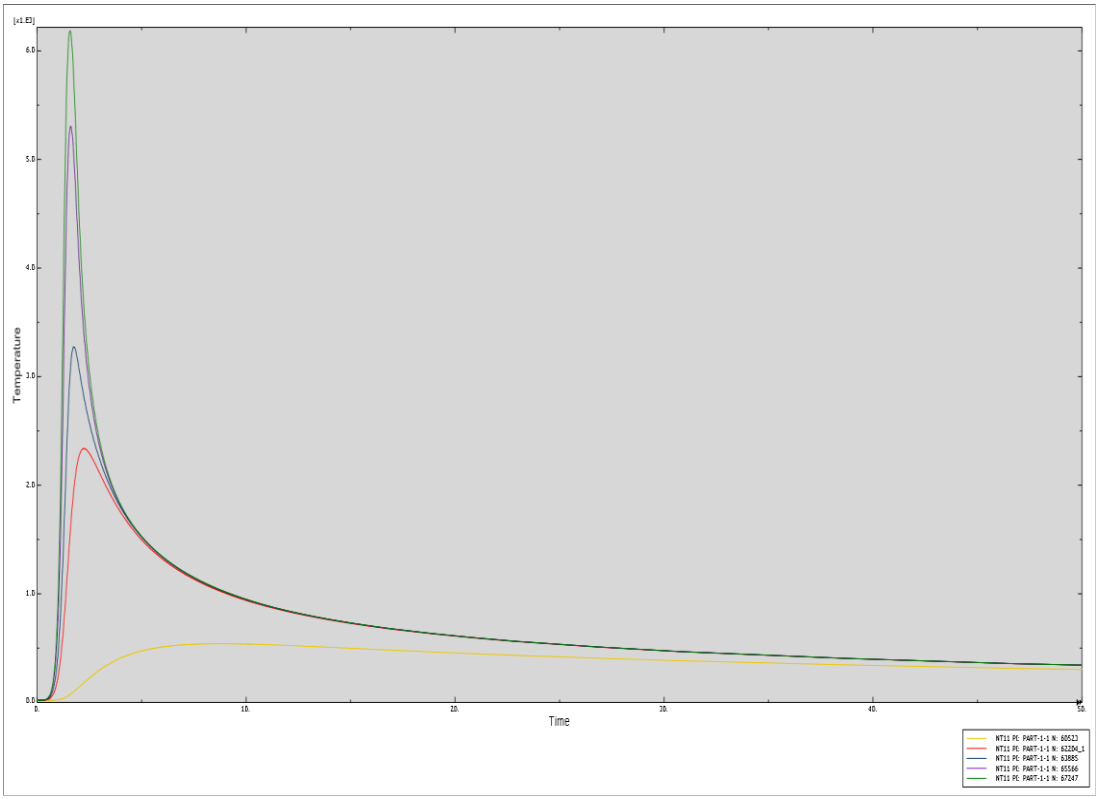

Figure 9-4 Temperature history of five nodes picked from the centre to the edge of the heat affected zone

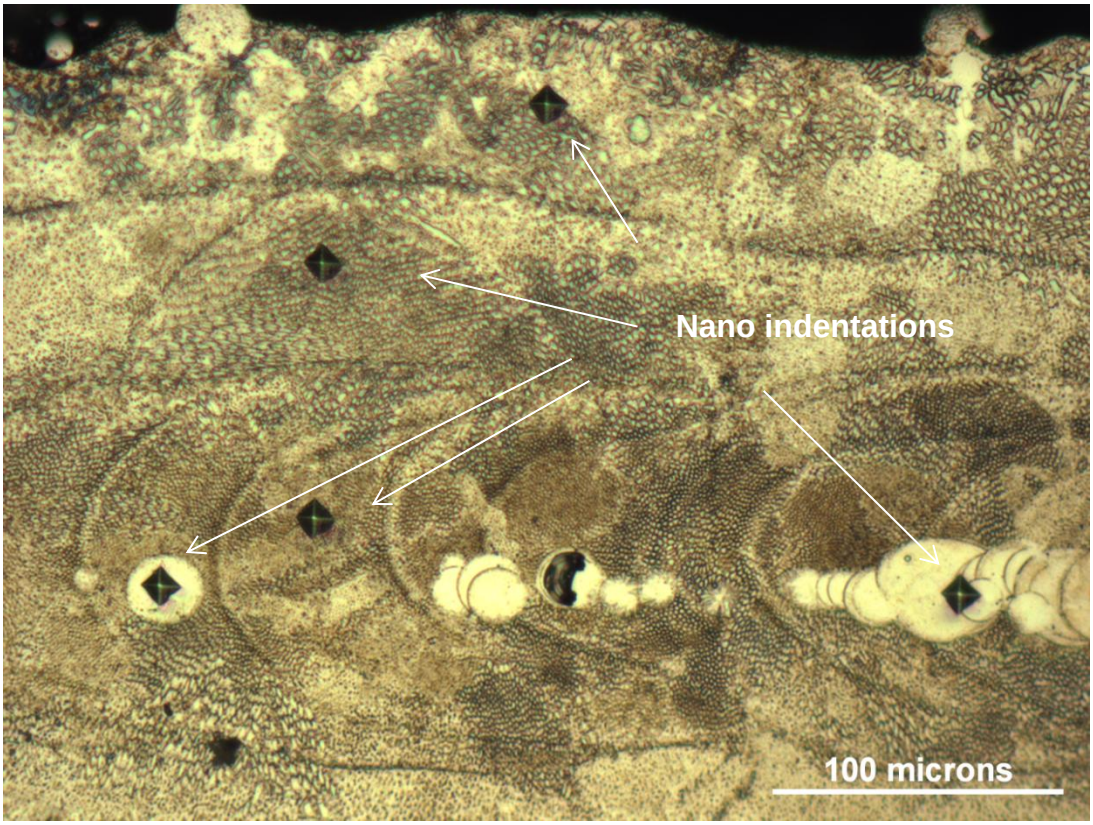

Figure 9-5 Nano indentations on polished SLM thin wall horizontal side

In Figure 9-5, the indentations in different areas had a similar shape and the indentation sizes within a range of 12.0μm - 13.6μm. It indicated that even the grains were located in different areas, they still had very close material properties, and they should be the same phase.

Another observable feature is located in the centre of the sample, where both grain boundaries and grain features are very difficult to see. Additional nano indentation testing was carried out on this special area and surrounded grains, the result is shown in Figure 9-6. The indentations in surrounded grains are smaller than the ones in the centre area, in an increment of 0.49μm, suggests a tiny increase in hardness. Since the difference could not be recognised as relative significant, it still indicated that the central area should be the same phase, and should have similar material properties.

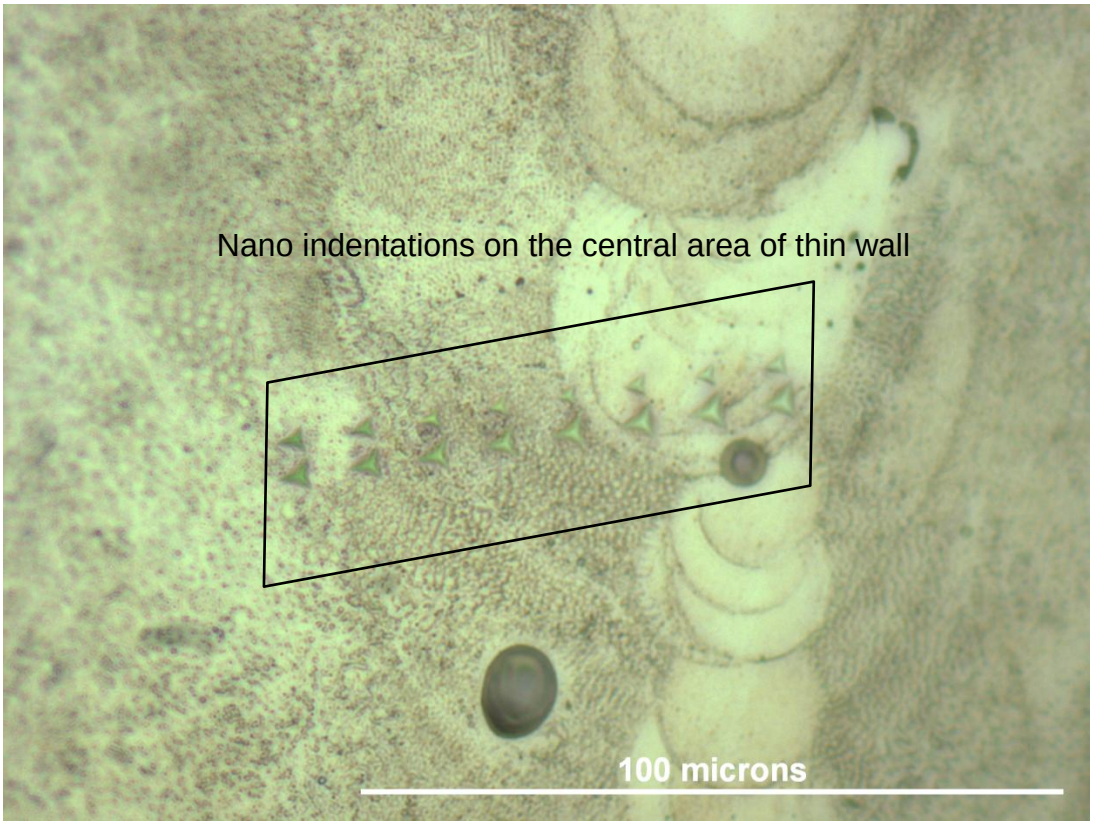

Figure 9-6 Nano indentations on the central area and surrounded grains

9.3.2 Vertical view

Variable sizes of grains can also be found in the vertical view (Figure 9-7 and 9-8), with the shape different from the horizontal view. Significant grain growth can be observed from the centre to the edges of the sample, through several layers, forming long narrow grains in the vertical view. The grain's size also becomes much smaller at the side edges.

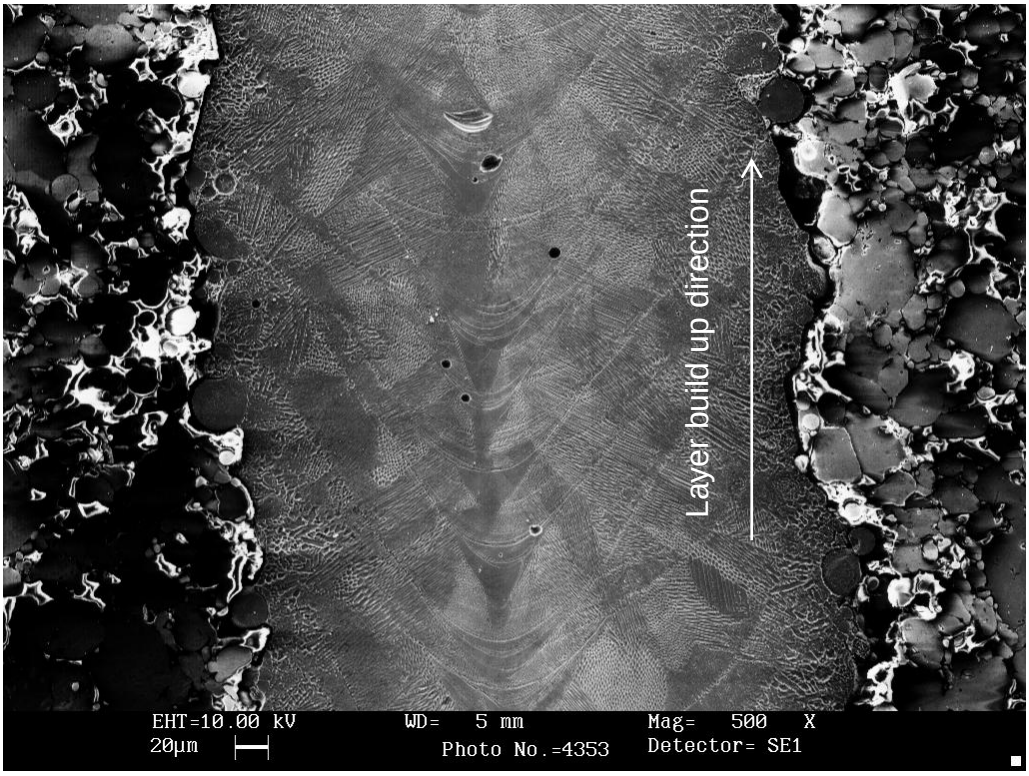

Figure 9-7 SLM stainless steel microstructure under SEM, mag=500, vertical view

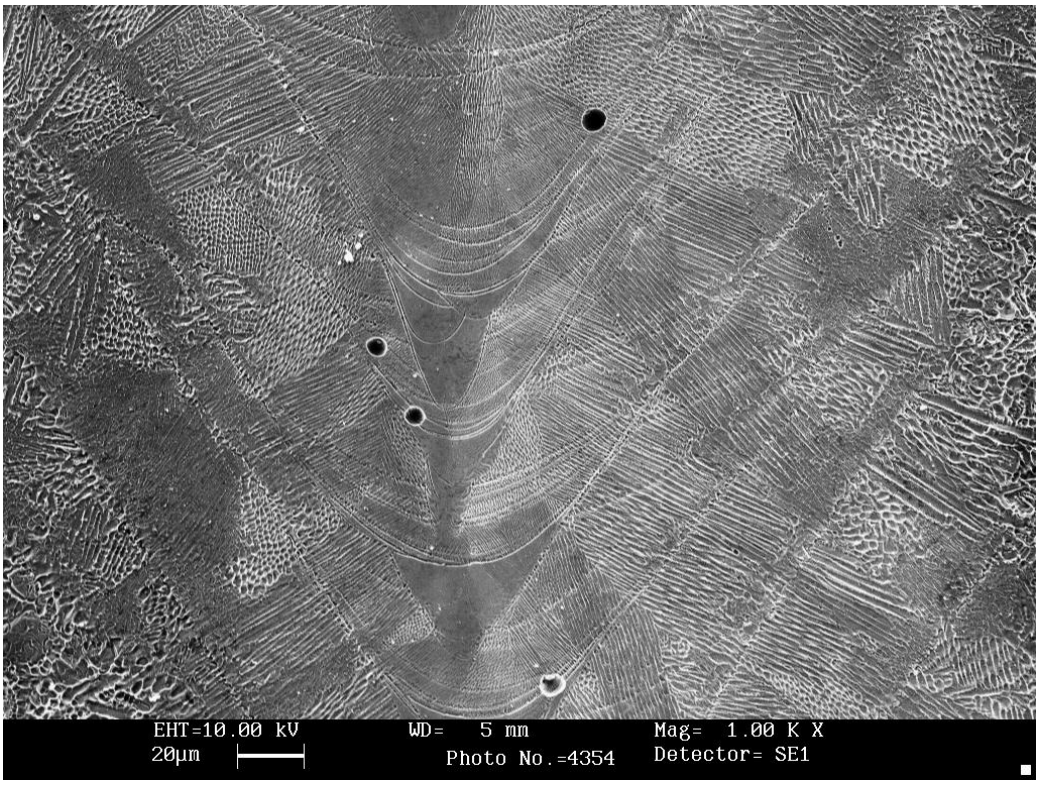

Figure 9-8 SLM stainless steel microstructure under SEM, mag=1000, vertical view

The SLM process can be considered as a rapid solidification process, as proved by the modelling results. Cellular microstructure in solidification of the alloys usually occurs under constitutional supercooling [111]. For a certain solute concentration profile, the highest temperature gradient corresponds to planar growth [83]. When the temperature gradient decreases, crystallisation mode changes from planar to cellular, then to cellular-dendritic, and finally to a dendritic solidification mode [83].

As a layer by layer built up process, the temperature gradient decreases from the top layer which has directly contact with the laser beam, to the underneath layer which has only been heat affected by the heat conduction. This results the grains with elongated shape appear in the vertical cross section of the sample, and grow with certain angle regarding the layer built up direction, as shown in Figure 9-8. These grains are crystallised in a cellular-dendritic mode, with a few of them in a dendritic mode.

In conventional directional solidification, crystals grow perpendicularly to the crystallisation front following the highest thermal gradient [111]. The grains formed at the central heat affected area can grow following the highest thermal gradient without divergence, as shown in Figure 9-8. This grow can continue over several layers before the crystallisation finished.

9.3.3 Phase identification

EBSD techniques were used on phase identification, as well as delivering clear details on grain sizes and boundaries. The grain sizes and directions present the same situation observed from SEM images. Crystalline orientation maps of the austenitic phase can be found in Figure 9-9 and Figure 9-10. Crystallographic orientation results showed that 99.7% of detected area was formed by γ-iron (Gamma ferrite), which is known as Austenite. This result proves the microstructure prediction in section 9.2 is the correct.

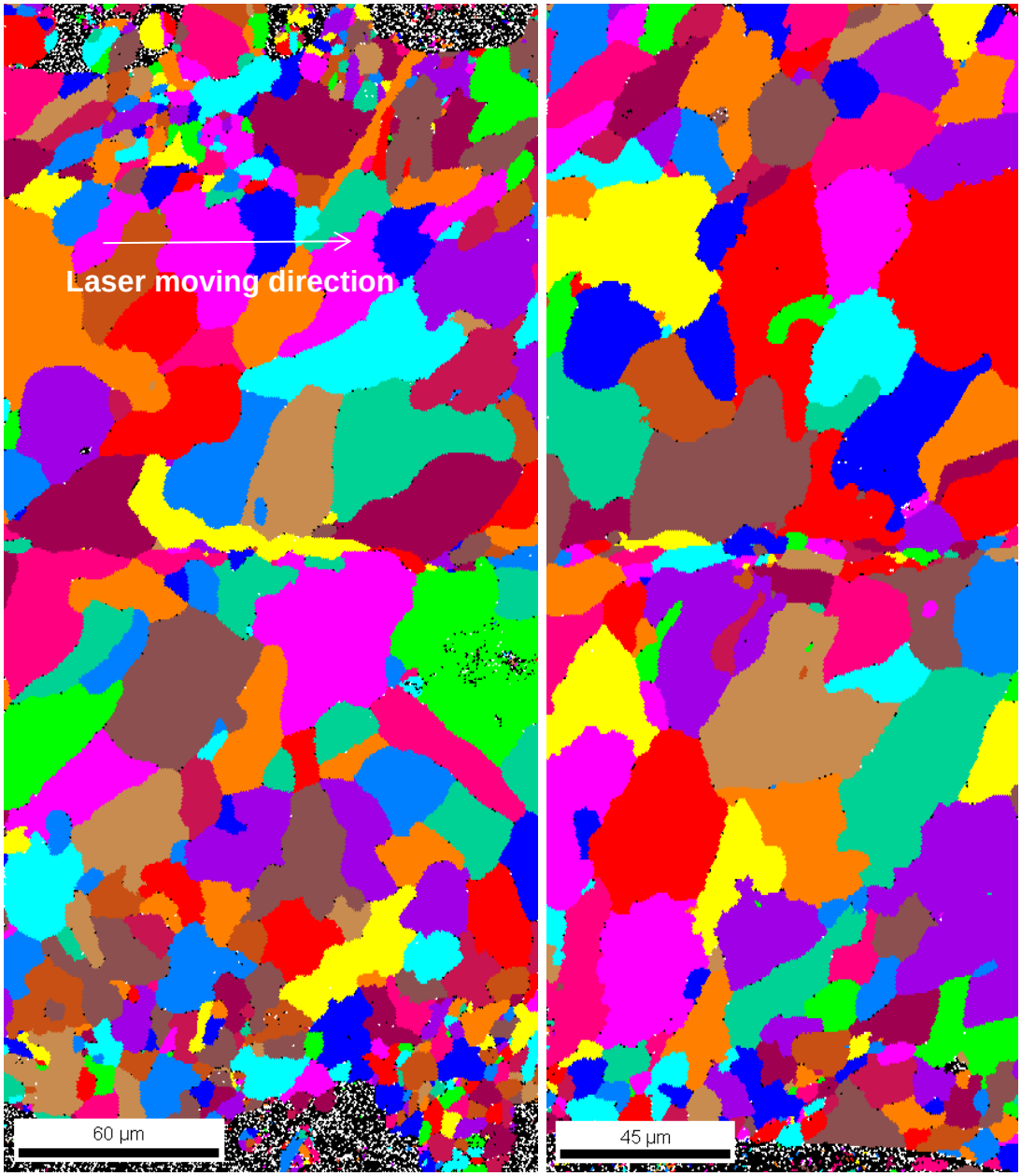

Figure 9-9 Crystalline orientation maps of SLM thin wall part, horizontal view

Figure 9-10 Crystalline orientation maps of SLM thin wall part, vertical view

The grains' size and grow direction in the Figure 9-9 and 9-10 show agreements with the microscopy images, and validate the previous analysis.

10 Discussions

10.1 Introduction

A discussion of the experimental results and the finite element modelling work is presented. The connection between all the works done in this research is discussed at the beginning, followed by the discussions of the results achieved. Energy input's effects on the SLM part's quality are discussed, along with the effect from the building conditions. Powder material's properties effects are analysed. Heat transfer modelling temperature distribution results, microstructure prediction and validation are discussed. The contribution of this thesis to the SLM research area is discussed at the end.

10.2 Connection between the works

Both experiment and modelling works have been carried out in this research, and their connection needs to be presented. The aim of this research is to assist the SLM process become more controllable and repeatable. This requires a good awareness and understanding on all possible effects which may influence the process and the final part's quality.

Experiments were carried out first to investigate the three leading factors in the SLM process - energy input, build conditions and raw material properties. The effect of these processing parameters can be studied by the experiment results directly. However, key factors which describe and determine the melting process such as the melting pool behaviour and thermal history are not easy to be measured and investigated from the experimental programme. Therefore, a modelling work is needed for further understanding the laser melting process.

Experiment results help to have an idea on which process parameter needs to be involved in the modelling work, and provide the correct model inputs for a reliable and accurate simulation. Chapter 5 and 6 presented the results from SLM process control parameters study. They give a basic knowledge on the SLM technique, with a further understanding in controlling it. The relationship between the input (laser energy, powder bed, build conditions, etc.) and the output (part's physical and mechanical properties) of the SLM technique has been presented and analysed, and it is the basis of the further modelling work. The results in these two chapters identify the effective process parameters which are converted to main model inputs in chapter 7, and provide the experimental explanations for the post-simulation analysis in chapter 8.

Chapter 7 presented the essential model inputs for the simulation work in chapter 8. The finite element model cannot be established without these inputs. Predictions from the modelling work in chapter 8 present further knowledge on the melting process and thermal history, and provide the explanations in a schematic way. The results agreements between the experiment and modelling prediction give a confidence in controlling the SLM process and built part's quality. Chapter 8 provides the temperature history in the SLM process for the microstructure prediction in Chapter 9.

Chapter 9 delivers the aim of this research. Microstructure prediction was carried out based on the results from chapter 8 and the knowledge obtained from previous four results and discussion chapters. A final microstructure examination is presented as a validation of the modelling work, as well as a useful complement of the process control study in chapter 5 and 6.

Experiment works in this research provide the model inputs and validate the modelling results, while the modelling work predict the melting process and explains some experiment results. Both of the works add the useful knowledge to the SLM technology for a better control.

10.3 Energy input and building conditions

Successful fabrication of SLM parts requires suitable energy input and proper build conditions. Energy input involves the processing parameters from both optical scanning system and process scanning strategy. Laser power, beam profile, scanning speed and hatch distance are four key factors which primarily affect the final parts quality.

Energy density definition in Equation (2.9) actually describes a liner solution along the laser moving direction. Due to the tiny width of the laser beam on the powder bed, the area formed using laser beam diameter multiply by the laser scanning speed can still be considered as 1D geometry. To expand this solution into 2D area, hatch distance can be added, shown in Equation (5.2).

High energy density input helps to achieve high density SLM part with relative high tensile strength and elongation. Keep increasing the laser energy density may introduce porosity to the SLM part since high energy can vaporise few powder material, and decrease the tensile strength and elongation. When improper high laser energy density is delivered to the powder bed, the vaporised particles and plasma formation above the powder bed decreases the laser energy absorption, and generates series sizes of sintered particles covering the top surface of the powder bed. These sintered particles absorb and disperses the laser energy, leaving the SLM part with high surface roughness, low density and low tensile strength.

With F-theta lens equipped inside the SLM optical system, a flat field at the image plane of scan is provided and the laser energy can be delivered uniformly to the powder bed. The parts built by the same energy density input can have the same physical and mechanical properties regardless their positions in the whole building area. Insert gas flow inside the chamber helps to cool down the heat affected zone and melting pool solidification, but it does not affect laser-powder interaction and SLM parts' quality. With Argon as protecting gas filled in the process chamber, oxidation can hardly happen and affect the part's quality.

Re-melting a solid layer can improve the surface finishing, and can be used not only on the finishing layer. Smooth surface allows uniform powder material delivery for each layer, and helps to generate uniform laser-powder interaction and heat distribution. The built part can have relative stable material properties through layers. Unlike re-melting process, pre-heating on the build substrate could not deliver enough heat to reduce the temperature gradient in the heating and cooling procedure, so it cannot generate significant improvement compared with non pre-heating process.

10.4 Powder material's properties effect

Powder, as raw material used in the SLM process, has particle shape and size distribution effect the laser-material interaction in the SLM process. Powder flowability can be affected by both the particle shape and size distribution. Spherical particles with narrow range size distribution usually contain high flowability.

Particle size distribution determines powder bed density. Due to different powder bed density, laser energy absorption and laser penetration varies, producing different temperature distribution and heat affected zone. Wider range of particle size provides higher powder bed density, which helps to generate higher density parts than lower powder bed density under the same laser energy density input (except in very high laser energy density region). There is no strict relevance between powder bed density and SLM parts' mechanical properties. Powder with narrow range of particle size generates parts with higher UTS and larger hardness, while powder with wide range of particle size generates smoother side surface finishing parts.

Powder sustainability study indicates powder degradation during long time SLM building and recycling procedure. Powder with wider range of particle size has its size distribution change more significant than narrower range one. This size distribution change affects the SLM parts' quality by increasing the top and side surface roughness and decreasing the tensile strength.

Obvious trends can be found when adding the processing time. The fine particles with the size below 10μm gradually disappear during the building and recycling procedure. They were sintered during the build by the laser to form a larger particle, or vaporised by the laser high energy intensity. They also disappear when unloading, sieving and loading as they are very easy to flow in the air.

Particles in the heat affected zone during the build can be affected by the high heating and cooling rate. It could be assumed that there is recrystallization happening and the grains inside the particles tend to become smaller. When two particles are sintered together, both strong necking with grains growing through and weak necking with grains still stay separately can be formed.

10.5 Temperature distribution history and microstructure prediction and validation

When the laser is delivered to the powder bed, powders on the top surface are melted very quickly to form a melting pool. The heat generated by the laser could not transfer a lot further due to the low conductivity of the non-continuous powder bed. The shape of the heat affected zone on the laser moving path tends to be a narrow width track. Melt particles have the solidification happens immediately after the laser moves away, leaving a solid path for easier heat conduction. This solidification helps to maintain stable melting pool shape and moving speed.

When layers are built up and gradually away from the solid substrate, the size of the heat affected zone and the melting pool may change according to the surrounding material's thermal properties. The depth of the heat affected zone can only reach certain layers, so the layers built up afterwards should have the same temperature distributions.

Due to the rapid heating and cooling process on stainless steel 316L powder in SLM build, massive γ-iron can be generated. When re-melting happens to the γ-iron phase with remained fast cooling rate, austenite is re-generated. Heat affection by the conduction which could not melt the stainless steel 316 L materials, rapid cooling in the γ-iron region should give a retained austenite structure.

Experimental microstructure examination proves the correct prediction from heat transfer modelling results, by showing 99.7% of EBSD detected area is austenite structure.

10.6 Linkage and contribution to SLM research area

In this research, the initial study on the process control parameters, especially the laser energy intensity investigation, was carried out based on the literature work. The results and analysis obtained show agreements with the previous work. Build direction and gas flow effect study fill in small gaps of the knowledge in the literature.

The powder bed studies on the particle size distribution effect on the SLM build quality, as well as the powder sustainability study, fill the gap in the literature. It has been reported that the metal powder can be recycled and reused [25, 71], but did not give effective powder life time. The powder's properties have been studied and reported, but powder bed properties are lack of investigation. This research has contribution to this area, as the powder bed can also affect the SLM process.

The heat transfer model was established based on the previous works. The major model input – moving heat source is a resource directly from Goldak [119, 134]. Other model inputs such as the state variable material properties have been developed based on the idea of the powder consolidation kinetics [142-145]. The initial modelling results also show agreements with the previous SLM modelling work.

The main contribution of this research is the establishment of a ‘layer by layer manner’ multi-layer heat transfer model. This model allows the temperature field prediction into a 3D system. It expands the boundary of the SLM models prediction, and gives the opportunities to do further study in the thermal behaviour investigations.

Another main contribution of this research is to use the thermal models on microstructure prediction. This helps to control the SLM process and final part quality. The microstructure prediction supplies extra explanations on the crystallisation and grains formation process, and will help to gain accurate and reliable expectations for the mechanical properties.

The knowledge gained in this research can always be transferred to another material in the SLM process, and the model established can be converted and developed for other materials too.

11 Conclusions and Future Works

11.1 Conclusions

The main conclusions of this research are presented as follows.

1. Successful fabrication of SLM parts requires a comprehensive understanding of laser energy input, raw material characterisation and building conditions.
2. Laser power, beam profile, scanning speed and hatch distance are four key factors which affect the final part's quality primarily.
3. Improper high energy density will generate vaporised particles or plasma during the building, results the built part with high porosity and low mechanical properties.
4. Re-melting the current solid layer helps to smooth the surface finishing.
5. Powder particles shape and size distributions affect the powder bed physical and thermal properties, and therefore affect the final SLM parts quality.
6. High powder bed density will help to build high density SLM parts.
7. Metal powder will degrade after long time processing.
8. Heat affected zone and melting pool sizes and shapes varies depending on surrounding material properties.
9. The depth of heat affected zone can only reach certain layers.
10. Due to high heating and cooling rate during SLM process on stainless steel 316L, the majority (and only) phase generated is austenite – γ-iron.

11.2 Future works

Research in selective laser melting has been developed with many works were presented in energy input study and processing parameters optimisation. Very few works looked at the laser-powder material interaction during the build. Since powder particles shape and size distributions determine the powder bed density and thermal properties, which will affect the laser energy absorption and penetration. An efficient way to measure the laser energy absorption for different powder bed formation needs to be developed. Experimental method will be more practical.

Powder sustainability study can be continued to study the effective metal powder life in the SLM process. This will help to maintain the controllability and repeatability of the SLM process.

Thermal modelling on the temperature distribution and microstructure prediction can be developed into a further step, which involves mechanical analysis such as residual stresses prediction. The thermal mechanics modelling work has wider application that may give accurate prediction on the curling issues happen during the SLM build.

To obtain more accurate predictions from the thermal modelling work, evaporation simulation should be involved in the model. Model geometry change by changing the elements active states can be used.

Melt pool dynamics simulation can also be developed for a better understanding on the melt pool behaviour. Efficient experimental measurement methods need to be developed to quantify the liquid state material properties, as well as the laser energy absorption. This will help the temperature history prediction more accurate and reliable.

In this research, a multi-layer model with one laser pass for each layer has been established. Multiple passes for each layer can be developed to gain more details in 3D sample structures.

The heat transfer model can also be applied onto different geometries, such as cylinder, lattice, etc. With a temperature distribution on the whole geometry of built part, it provides more information for a better understanding of the whole SLM process.

Reference

1. Vincent; Earls, Alan R. (February 2011), "Origins: A 3D Vision Spawns Stratasys, Inc. *Today's Machining World's* new feature "Origins" tells us the stories of how successful technologies, companies and people got their start. This month we interview a pioneer of rapid prototyping technology, Scott Crump, the founder and CEO of Stratasys Inc.",*Today's Machining World* (Oak Forest, Illinois, USA: Screw Machine World Inc) 7 (1): 24–25.
2. Albert, Mark [Editor in Chief] (2011-01-17), *"Subtractive plus additive equals more than (− + + = >): subtractive and additive processes can be combined to develop innovative manufacturing methods that are superior to conventional methods ['Mark: My Word' column—Editor's Commentary"*], *Modern Machine Shop* (Cincinnati, Ohio, USA: Gardner Publications Inc) 83 (9): 14.
3. J.J. Beaman, J.W. Barlow, D.L. Bourell, R.H. Crawford, H.L. Marcus, K.P. McAlea, Solid Freeform Fabrication: A New Direction in Manufacturing, Kluwer Academic Publishers, 1997.
4. L. Lu, J. Fuh, Y.S. Wong, Laser Induced Materials and Processes for Rapid Prototyping, Kluwer Academic Publishers, 2001, ISBN: 0792374002.
5. R.Hague, S. Mansour and N. Saleh, Material and design considerations for Rapid Manufacturing. International Journal of Production Research, 42(22), 2004, 4691.
6. RENISHAW / MTT, Selective laser melting and additive manufacturing, http://www.renishaw.com/en/additive-manufacturing--15239.
7. K. Osakada, M. Shiomi, Flexible manufacturing of metallic products by selective laser melting of powder, International Journal of Machine Tools and Manufacture, 46(11), 2006, pp.1188-1193.

8. M. Rombouts, J.P. Kruth, L. Froyen and P.Mercelis, Fundamentals of Selective Laser Melting of alloyed steel powders. *CIRP Annals – Manufacturing Technology*, 55(1), 2006, pp187-192.
9. C.K. Chua, K.F. Leong, Rapid Prototyping: Principles and Applications in Manufacturing, Wiley, New York, 1997.
10. M. Burns, Automated Fabrication: Improving Productivity in Manufacturing, PTR Prentice-Hall Inc., 1993.
11. O. Bjorke, How to make stereolithography into a practical tool for tool production, *Manufacturing Technology*, CIRP Annals, Vol.40, 1, 1991, pp.175-177.
12. M. Shellabear, J. Lenz, V. Junior, *E-manufacturing with laser sintering-to series production and beyond*, in: Proceedings of the Fourth Laser Assisted Net Shape Engineering, LANE 2004,Vol. 1, September, Erlangen, Germany, pp. 435–444.
13. J.P. Kruth, Material incress manufacturing by rapid prototyping techniques, *CIRP Annals*, 40/2, 1991, pp603-614.
14. J.P. Kruth, M.C. Leu, T. Nakagawa, Progress in additive manufacturing and rapid prototyping, *CIRP Annals*, 47/2, 1998, pp525-540.
15. T. Wohlers, State of the Industry Report – Executive Summary, Proc. Rapid Prototyping and Manufacturing'98 Conf. SME, 1998, pp951-962.
16. N. Hopkinson, R. Hague, P. Dickens, Rapid Manufacturing: An Industrial Revolution of the Digital Age, John Wiley & Sons Ltd, 2006, ISBN: 0470016132.
17. T. Wohlers, Wholers Report, *Rapid Prototyping and Tooling*, State of the Industry, Wohlers Associates, 2005.
18. Gebhart, A., *Rapid Prototyping*, Hanser Publishers, Munich, 2003.
19. Hu Y., Fadel G.M., Blouin V.Y. and White D.R., *Optimal design for additive manufacturing of heterogeneous objects using ultrasonic consolidation*, Virtual and Physical Prototyping, Vol. 1, 1, 2006, pp. 53-62.
20. Kong, C.Y., Soar, R.C. and Dickens, P.M., *Optimum process parameters for ultrasonic consolidation of 3003 aluminium*, Journal of Materials Processing Technology, Vol. 146, 2004, pp. 181-7.
21. M.L. Griffith, M.E. Schlienger, L.D. Harwell, M.S, Oliver, M.D. Baldwin, M.T. Ensz, J.E. Smugeresky, M. Essien, J. Brooks and C.V. Robino,

Thermal Behaviour in the LENS Process, in Proceedings from the Solid Freeform Fabrication (SFF) Syposium, Austin, Texas, 1998, pp89-96.

22. M.L. Griffith, T. Ensz, J.D. Puskar, C.V. Robnio, *Understanding the Microstructure and properties of components fabricated by laser engineered net shaping (LENS)*, Materials Research Society, Symposium Y Proceedings 625, 2000, pp. 9–20.
23. L. Sexton, S. Lavin, G. Byrne, A. Kennedy, Laser cladding of aerospace materials*, Journal of Materials Processing Technology*, 122(1), 2002, pp.63.
24. Brooks, J., Robino, C., Headley T., Goods S., Griffith M., *Microstructure and property optimization of LENSs deposited H13 tool steel*, Proceedings of the 10th Solid Freeform Fabrication Symposium, Austin, TX, 1999, pp. 375–382.
25. Levy, G. N., Schindel, R., Kruth, J.P., Rapid manufacturing and rapid tooling with layer manufacturing (LM) technologies, state of the art and future perspectives, Annals of the CIRP 52, 2, 2003, pp. 589–609.
26. F. Feenstra, B. Holmer, G. Pohl H., M.N. Tromans, B. Mieritz, RP, RT, RM Trends and Developments/Research Survey, 4th National Conference of Rapid & Virtual Prototyping and Applications, Buckinghamshire, UK, 2003, 95-138.
27. C.B. Williams, F. Mistree and D.W. Rosen, Towards the design of layer-based additive manufacturing process for the realization of metal parts of designed microstructure. Solid Freeform Fabrication Symposium, Austin, Tx, 217-230.
28. Deckard, C., Miller, D. *Process and Control issues in Selective Laser Sintering*, Proc ASME Conference. 1988.
29. Deckard, C., *Methods and apparatus for producing parts by selective laser sintering*, US Patent 4863538, filed October 17, 1986, published September 5, 1989.
30. Deckard, C., Miller, D. *Energy delivery for Selective Laser Sintering: Issues and directions – a review*, Proc 27th Int. SAMPE Tech Conf. 1995.
31. Tolochko, N., S. Mozzharov, T. Laoui, L. Froyen, *Selective laser sintering of Single- and two-component metal powders*, Rapid Prototyping Journal 9, 2, 2003, pp. 68–78.

32. Kruth, J. P., Wang, X., Laoui, T., Froyen, L., *Lasers and materials in selective laser sintering*, Proceedings of the Third Laser Assisted Net Shape Engineering, LANE 2001, August, Germany, pp. 3–24.
33. Larsson, M., Lindhe, U. and Harrysson, O., *Rapid manufacturing with electron beam melting (EBM)-a manufacturing revolution?*, 14th SFF Symposium, Texas 2003, pp. 433-8.
34. Arcam AB, http://www.arcam.com/, 2008
35. Mines, R. A. W., McKown, S., Cantwell, W., Tsopanos, S., Brooks, W. and Sutcliffe, C. J., *On the Characterisation of Foam and Micro-lattice Materials used in Sandwich Construction*, Strain 44 (1) pp. 71-83 (2007)
36. Shen, Y. , McKown S., Tsopanos S., Sutcliffe C.J., Mines R. and Cantwell W.J., *Structures based on high performance lattice structures*, SAMPE Europe Conference Paris, 2008.
37. Hauser C., Childs T.H.C. and Dalgarno K.W., *Atmospheric Control during Direct Selective Laser Sintering of Stainless Steel 314S*, Powder Proc Solid Freeform Fabrication Symposium, University of Texas at Austin, Vol. 10, 1999.
38. L. Xue, M.U. Islam, Freeform laser consolidation for producing metallurgically sound and functional components. Journal of Laser Applications, 12(4), 160-165.
39. D.L. Bourell, M. Wohlert, N. Harlan, S. Das and J.J. Beaman, Powder densification maps in selective laser sintering. Engineering Materials, 9(4), 663-669.
40. Patel, C. K. N. (1964). "Continuous-Wave Laser Action on Vibrational-Rotational Transitions of CO_2". *Physical Review* 136 (5A): A1187–A1193. doi:10.1103/PhysRev.136.A1187.
41. Walter Koechner, 1965, *Solid-state laser engineering*, Springer-Verlag, p. 507
42. Becker, P. C.; Olson, N. A.; Simpson, J. R. 1999. *Erbium-doped fiber amplifiers: fundamentals and theory*. Academic press.
43. Paschotta, Rüdiger. "Brillouin Scattering". *Encyclopedia of Laser Physics and Technology*. RP Photonics.

44. Saleh, Bahaa E. A. and Teich, Malvin Carl (1991). *Fundamentals of Photonics*. New York: John Wiley & Sons. ISBN 0-471-83965-5. Chapter 3, "Beam Optics," pp. 80–107.
45. K. Kanzler, How much energy are you throwing away? Photonics Spectra, 2006.
46. J.F. Ready, Effects of High-Power Laser Radiation, Academic Press, New York, London (1971) p. 433.
47. Siegman, A. E. (1986). *Lasers*. University Science Books. pp. 664–669. ISBN 0935702113.
48. Lumonics, JK701-702 Nd:YAG laser manual and programming,1995.
49. Rodolfo Hermans, Wikipedia, Gaussianbeam.png, 22 Feb 2009.
50. F. Pampaloni and J. Enderlein (2004). "Gaussian, Hermite-Gaussian, and Laguerre-Gaussian beams: A primer". *ArXiv:physics/0410021*.
51. C.E. Webb, J.D.C. Jones, Handbook of laser technology and applications, Taylor&Francis, ISBN 0750309660, 2004.
52. B.N. Chichkov, C. Momma, S. Nolte, Femtosecond, picoseconds and nanosecond laser ablation of solids. Appl Phys A (63), 109-115.
53. N.K. Tolochko, Y.V. Khlopkov, S.E. Mozzharov, M.B. Ignatiev, T. Laoui, V.I. Titov, Absorptance of the powder materials suitable for laser sintering, *Rapid Prototyping Journal*, 6, 3, 2000, pp.155-160.
54. William M. Steen, Laser material processing – 3rd Edition, Springer, 2003, ISBN: 1852336986.
55. M. Van Elsen, M. Baelmans, P. Mercelis, J.P. Kruth, Solutions for modelling moving heat sources in a semi-infinite medium and applications to laser material process, *International Journal of Heat and Mass Transfer*, 50, 2007, pp.4872-4882.
56. W.W. Duley, Laser processing and analysis of materials, Plenum Press, New York, 1983.
57. V.S. Kovalenko, A.D. Verhoturoy, P.Ph. Golovko, I.A. Podchemjaeva, Laser and electroerosive hardening of materials, Nauka Press, Moscow, 1986.
58. A.G. Grigoriantz, A.N. Saphonov, Bases of laser thermohardening of alloys, Vishava shkola Press, Moscow, 1988.

59. A.G. Grigoriantz, A.A. Sokolov, Laser processing of non-metal materials, Vishava shkola Press, Moscow, 1988.
60. J. Laeng, J.G. Stewart, F.W. Liou, Laser metal forming processes for rapid prototyping – a review. *International Journal of Production Research*, 38, 2000, pp.3973.
61. F. Fankhauser, S. Kwasniewska, Lasers in Ophthalmology: Basic, Diagnostic, and Surgical Aspects: A Review, Kugler Publications, 2003, ISBN: 9062991890.
62. X.C. Wang, J.P. Kruth, Energy absorption and penetration in selective laser sintering: A ray tracing model.
63. J.P. Kruth, G. Levy, F. Klocke, T.H.C. Childs, K.U. Leuven, Consolidation phenomena in laser and powder-bed based layered manufacturing, Annals of the CIRP, 56, 2007, 730-759.
64. Gusarov, A.V., 2003, Mechanisms of selective laser sintering and heat transfert in Ti powder, Rapid Prototyping J., 9/5: 314-326.
65. Van Der Schueren, B., 1996, Basic contributions to the development of the selective metal powder sintering process. PhD thesis, K.U.Leuven, Eng. Faculty, Belgium.
66. Aggarangsi, P., Beuth, J.L., 2006, Localized preheating approaches for reducing residual stress in additive manufacturing, Proc. SFF Symp., Austin: 709-720.
67. Mercelis, P., Kruth, J.-P., 2006, Residual stresses in selective laser sintering and selective laser melting, Rapid Prototyping J., 12/5: 254-265.
68. S. Tsopanos, Micro heat exchangers by SLM, PhD thesis, University of Liverpool, 2009.
69. K. Mumtaz, Selective Laser Melting of Inconel 625 using Pulse Shaping, PhD thesis, Loughborough University, 2008.
70. T.H.C. Childs, Raster scan selective laser melting of the surface layer of a tool steel powder bed. *Proc. IMechE*, 219(B), 2005, pp.109-115.
71. J.P. Kruth, P. Mercelis, J.V. Vaerenbergh, L. Froyen, M. Rombouts, Binding mechanisms in selective laser sintering and selective laser melting, *Rapid Prototyping Journal*, 11(1), 2005, pp.26-36.

72. R. Morgan, C.J. Sutcliffe, W. O'Neill, Density analysis of direct metal laser re-melted 316L stainless steel cubic primitives, *Journal of Materials Science*, 39(4), 2004, pp.1195-1205.
73. http://www.jenoptik-los.com/data/downloads/515/Prosp%20Ftheta_en.pdf
74. www.cvilaser.com/common/pdfs/FTL.pdf
75. P. Fischer, N. Karapatis, V. Romano, R. Glardon, H.P. Weber, A model for the interaction of near-infrared laser pulses with metal powders in selective laser sintering, *Applied Physics*, A 74, 2002, pp.467-474.
76. W. Meiners, K. Wissenbach, R. Poprawe, Direct selective laser sintering of steel powder, Proc. Laser Assisted Net Shape Engineering 2. Meisenbach Bamberg, 1997.
77. N.K. Tolochko, S.E. Mozzharov, N.V. Sobolenko, Yu.V. Khlopkov, I.A. Yadroitsev, V.B. Michailov, Main relationships governing laser sintering of loose single component metallic powders, *Journal of Advanced Materials*, Vol.2, 2, 1995, pp.151-157.
78. N.K. Tolochko, S.E. Mozzharov, I.A. Yadroitsev, T. Laoui, L. Froyen, V.I. Titov, M.B. Ignatiev, Balling processing during selective laser treatment of powders, *Rapid Prototyping Journal*, Vol.10, 2, 2004, pp.78-87.
79. P. Regenfuss, L. Hartwig, S. Klotzer, R. Ebert, Industrial freeform generation of microtools by laser micro sintering, *Rapid Prototyping Journal*, Vol.11, 1, 2005, pp.18-25.
80. S.O. Onuh, B. Hon, Application of the Taguchi method and new hatch styles for quality improvement in Stereolithography. *Journal of Engineering manufacture*, B6 (212), 1998, pp.461-472.
81. M.V. Elsen, Complexity of Selective Laser Melting: a new optimisation approach. PhD.
82. R.W. Messler, Principles of Welding, processes, physics, chemistry and metallurgy, Wiley-Interscience, ISBN 0-471-25376-6.1999.
83. S. Kou, Welding metallurgy, Wiley interscience, 2003.
84. K.G. Watkins, Achieving the potential of direct fabrication with lasers, proc 3rd international. *LANE* Erlangen, 2001, pp.25-38
85. H. Pohl, A. Simchi, M. Issa and H.C. Dias, Thermal stresses in direction metal laser sintering. Solid Freeform Fabrication Symposium, Austin, Texas, 2001, 366-372.

86. C. Over, Generative Fertigung von Bauteilen aus Werkzeugstahl X38CrMoV51 und Titan TiAl6V4 mit Selective Laser Melting, RWTH Aachen, Germany, PhD Thesis, 2003.
87. S. Das, J.J. Beaman, M. Wohlert, D.L. Bourell, Direct laser freeform fabrication of high performance metal components. *Rapid Prototyping Journal*, 4(3), 1998, pp.112-117.
88. F. Abe, K. Osakada, M. Shiomi, K. Uematsu, M Matsumoto, The manufacturing of hard tools from metallic powders by selective laser melting. Journal of Materials Processing Technology, 111(1), 2001, 210-213.
89. F. Abe, E.C. Santos, Y. Kitamura, K. Osakada, M. Shiomi, Influence of forming conditions on the titanium model in rapid prototyping with the selective laser melting process. Proceedings of the IMECH E part C Journal of Mechanical Engineering Science 217, 2003, 119-126.
90. W.N. Su, Layered Fabrication of Tool Steel and Functionall Graded Materal with a Nd:YAG Pulsed Laser. Rapid Manufactruing Research Group, Loughborough University, Phd, 2002.
91. J.P. Kruth, L. Froyen, J. Van Vaerenbergh, P. Mercelis, M. Rombouts and B. Lauwers. Selective laser melting of iron-based powder. Journal of Materials Processing Technology, 149(1-3), 2004, 616-622.
92. S. Pogson, P. Fox, W. O'Neill and C.J. Sutcliffe, The direct metal laser remelting of copper and tool steel powders. Materials Science and Engineering, A 386(1-2):453, 2004.
93. O. Rehme, C. Emmelmann, Reproducibility for properties of Selective Laser Melting products. *Proceedings of the Third International WLT-Conference on Lasers in Manufacturing*, Munich, 2005.
94. Randall M. German, Powder Metallurgy Science – 2nd Edition, Metal Powder Industries Federation, 1994, ISBN: 1878954423.
95. M.W. Khaing, J.Y.H. Fuh, L. Lu, Direct metal laser sintering for rapid tooling: processing and characterisation of EOS parts, *Journal of Materials Processing Technology*, 113(1-3), 2001, pp.269.
96. C. Hauser, C. Sutcliffe, M. Egan, P. Fox, Spiral Growth Manufacturing (SGM) – A continuous Additive Manufacturing Technology for Processing

Metal Powder by Selective Laser Melting. *Solid Freeform Fabrication Symposium*, Austin, Tx.1-12, 2005.

97. P. Carroll, Information on laser deposition at TWI, *AILU Technology Workshop*, Rotherham, UK, 2007.
98. J. Mazumder, D. Dutta, N. Kikuchi, A. Ghosh, Closed loop direct metal deposition: art to part. *Optics and Lasers in Engineering*, 34(4-6), 2000, pp.397.
99. A.J. Pinkerton, Matching the additive process and parameters to the purpose, *AILU Technology Workshop*, Rotherham, UK, 2007.
100. Michael F. Ashby and David R.H. Jones, Engineering materials 2 : an introduction to microstructures, processing and design, 3rd edition, Oxford : Butterworth-Heinemann, 2005.
101. N.P. Karapatis, A sub-process approach of selective laser sintering, Switzerland, Ecole Polytechnique Federal de Lausanne, Thesis no.2506, 2002.
102. A.M. Von, Laser-beam interactions with materials. Berlin, Springer-Verlag, 1987.
103. ASM Metals Handbook, Ninth Edition, v. 9, "Metallography and Microstructures," American Society for Metals, Metals Park, OH, 1985, p. 12.
104. R. E. Smallman, A. H. W. Ngan, Physical metallurgy and advanced materials, 7th edition, Amsterdam ; iOxford : Elsevier Butterworth-Heinemann, 2007.
105. D.R.F. West, Ternary Equilibrium Diagrams, Second Edition, 1982, Published by Chapman & Hall.
106. www.calphad.com
107. Serge V. Garnov ; Vitali I. Konov ; Alexander S. Silenok ; Olga G. Tsarkova ;Vladimir N. Tokarev ; Friedrich Dausinger Experimental study of temperature dependence of reflectivity and heat capacity of steels and alloys at continuous wave Nd:YAG laser heating SPIE Proceedings Vol. 3093. Nonresonant Laser-Matter Interaction (NLMI-9), Vitali I. Konov; Mikhail N. Libenson, Editors, pp.160-175
108. K. Dan, L. Shaw, 2002. Preheating effects on multiple materials laser densification. In: Bourell, D.L., Beaman, J.J., Crawford, R.H., Marcus,

H.L., Barlow, J.W. (Eds.), Proceedings of 13th Annual Solid Freeform Fabrication Symposium. The University of Texas at Austin, USA, pp. 392–399.

109. Kruth, J.-P., Badrossamay, M., Yasa, E., Deckers, J., Thijs, L., Van Humbeeck, J., 2010. Part and material properties in selective laser melting of metals. In: Proceedings of the 16th International Symposium on Electromachining (ISEM XVI), Shanghai, China.

110. K. Kempen, E. Yasa, L. Thijs, J. P. Kruth, J. Van Humbeeck, Microstructure and mechanical properties of Selective Laser Melted 18Ni-300 steel, Physics Procedia, 12 (2011) 255-263.

111. I. Yadroitsev, P. Krakhmalev, I. Yadroitsava, S. Johansson, I. Smurov, Energy input effect on morphology and microstructure of selective laser melting single track from metallic powder. Journal of Materials Processing Technology 213 (2013), 606– 613.

112. P. Fischer, V. Romano, H.P. Weber, N.P. Karapatis, E. Boillat and R. Glardon, Sintering of commercially pure titanium powder with a Nd:YAG laser source, Acta Materialia, 51(6), 2003, 1651-1662.

113. P. Howard, M.J. Koczak, How porosity and atmosphere effect the thermal conductivity of P/M parts. *International Journal of Powder Technology*, 17, 1981, pp.25-35.

114. Cary, Howard B. and Scott C. Helzer (2005). Modern Welding Technology. Upper Saddle River, New Jersey: Pearson Education. ISBN 0-13-113029-3.

115. P. J. Withers and H. K. D. H. Bhadeshia, Residual Stress Part 1 - Measurement Techniques, *Materials Science and Technology,* Vol. 17, 2001, 355-365.

116. P Mercelis, J P Kruth, Residual stresses in selective laser sintering and selective laser melting, Rapid Prototyping Journal (2006), Volume: 12 Issue: 5 Pages: 254-265

117. J.Y. Jeng, M.C. Lin, Mold fabrication and modification using hybrid processes of selective laser cladding and milling, Journal of Materials processing technology 1(110), 2003, 98-103.

118. W. Meiners, K. Wissenbach, R. Poprawe, Direct generation of metal parts and tools by Selective Laser Powder Re-melting (SLPR), Proc. ICALEO, 1998, Section E, Laser Institute of America.
119. J. Goldak, A. Chakravarti, M. Bibby, A double ellipsoid finite element model for welding heat sources, IIW Doc, No.212-603-85, International Institute for Welding, Strasbourg, France, 1985.
120. S. Kikuchi, Numerical analysis model for thermal conductivities of packed beds with high solid-to-gas conductivity ratio, Int. J. Heat Mass Transfer, 44 (2001) 247-251.
121. A.V. Luikov, Heat Mass Transfer, Handbook, Energia, Moscow, 1971.
122. Carnot, Sadi (1824). Réflexions sur la puissance motrice du feu et sur les machines propres à développer cette puissance. Paris: Bachelier.
123. J P Holman, *Heat Transfer* 9th Ed, McGraw Hill, 2002
124. D. Rosenthal, The theory of moving sources of heat and its application to metal treatments, Trans Amer Soc Mech Eng, 1946, 68.
125. M. Lax, Temperature rise induced by a laser beam. J Appl Phys, 1977, 48: 3919-3924.
126. Y.I. Nissim, A. Lietoila, R.B. Gold, J.F. Gibbons, Temperature distributions produced in semiconductors by a scanning elliptical or circular CW laser beam. J Appl Phys, 1980, 51: 274-279.
127. J.M. Dowden, R. Ducharme and P.D. Kapadia, Time dependent line and point sources: a simple model for time-dependent welding processes. *Lasers Eng* **7** (1998), pp. 215–228.
128. W.M. Steen, J. Dowden, M. Davis and P. Kapadia, A point and line source model of laser keyhole welding. *J Phys D* **21** (1988), pp. 1255–1260.
129. R. Akhter, M. Davis, J. Dowden, P. Kapadia, M. Ley and W.M. Steen, A method for calculating the fused zone profile of laser keyhole welds. *J Phys D* **21** (1989), pp. 23–28.
130. D. Rosenthal, Mathematical theory of heat distribution during welding and cutting, *Weld Journal*, 20(5), 1941, pp.220-234.
131. N. Rykalin, A. Uglov, A. Kokora, O. Glebov, Laser Machining and Welding, Mir Publishers, Moscow, 1978.
132. H. Carslaw, J. Jaeger, Conduction of Heat in Solids, Oxford, 1990.

133. T.W. Eagar, N.S. Tsai, Temperature fields produced by travelling distributed heat sources, *Weld Journal*, 62(12), 1983, pp.346-355.

134. J. Goldak, Chakravarti A and Bibby M. A new finite element model for welding heat sources model. *Metallurgical Transactions B*. 1984; 15B:299-305.

135. N.T. Nguyen, A. Otha, K. Matsuoka, N. Suzuki, Y. Maeda, Analytic solutions for transient temperature of semi-infinite body subjected to 3-D moving heat sources, *Weld. Res. Suppl*. 1999, pp.265-274.

136. N.T. Nguyen, Y.-W. Mai, S. Simpson, A. Otha, Analytical approximate solution for double ellipsoidal heat source in finite thick plate, *Weld. Res*. 2004, pp.82-93.

137. J.C. Maxwell. *A Treatise on Electricity and Magnetism* Oxford University Press, London (1891).

138. D.A. De Vries. *The Thermal Conductivity of Granular Materials* Inst. Int. Froid., Paris (1955).

139. J.C. Maxwell, A treatise on Electricity and Magnetism, Dover, New York, 1954.

140. S. Yagi, D. Kunii, Studies on effective thermal conductivities in packed beds, J. AIChE 2 (1957) 373-381.

141. E. L. Kitanin, M. S. Ramm, V. V. Ris and A. A. Schmidt, Heat transfer through source powder in sublimation growth of SiC crystal, Materials Science and Engineering B, Volume 55, Issue 3, 1998, Pages 174-183.

142. A.V. Gusarov, J.P. Kruth, Modelling of radiation transfer in metallic powders at laser treatment, International Journal of Heat and Mass Transfer, 2005, 48:3423-3434.

143. A.V. Gusarov, I. Smurov, Modeling the interaction of laser radiation with powder bed at selective laser melting, Physics Procedia, 5 (2010) 381-394.

144. Haseung Chung, Suman Das, Numerical modeling of scanning laser-induced melting, vaporization and resolidification in metals subjected to step heat flux input, International Journal of Heat and Mass Transfer 47 (2004) 4153-4164.

145. L. Dong, A. Makradi, S. Ahzi, Y. Remond, Three-dimensional transient finite element analysis of the selective laser sintering process. Journal of materials processing technology, 209 (2009) 700-706.
146. G.B.M. Cervera, G. Lombera, Numerical prediction of temperature and density distributions in selective laser sintering processes, Rapid Prototyping Journal 5 (1) (1999) 21–26.
147. S.S. Sih, J.W. Barlow, The prediction of the emissivity and thermal conductivity of powder beds, Particulate Science and Technology 22 (2004) 427–440.
148. I.A.Roberts, C.J.Wang, R.Esterlein, M.Stanford, D.J.Mynors, A three-dimensional finite element analysis of the temperature field during laser melting of metal powders in additive layer manufacturing, International Journal of Machine Tools & Manufacture 49 (2009) 916–923.
149. F. J. Gürtler, M. Karg, K. H. Leitz, M. Schmidt, Simulation of laser beam melting of steel powders using the three-dimensional volume of fluid method, Physics Procedia 41 (2013) 874-879.
150. A.V. Gusarov, I. Smurov, Two-dimensional numerical modelling of radiation transfer in powder beds at selective laser melting, Applied Surface Science 255 (2009) 5595–5599.
151. Evgeny Kharanzhevskiy, Sergey Kostenkov, Modeling of laser radiation transport in powder beds with high-dispersive metal particles, Journal of Alloys and Compounds, 2013.
152. Dharani Sowdari, Pradip Majumdar, Finite element analysis of laser irradiated metal heating and melting processes, Optics & Laser Technology 42 (2010) 855–865.
153. A.V. Gusarov, I. Yadroitsev, Ph. Bertrand, I. Smurov, Heat transfer modelling and stability analysis of selective laser melting, Applied Surface Science 254 (2007) 975–979.
154. F. Verhaeghe, T. Craeghs, J. Heulens, L. Pandelaers, A pragmatic model for selective laser melting with evaporation, Acta Materialia 57 (2009) 6006–6012.
155. M. Badrossamay, T.H.C. Childs, Further studies in selective laser melting of stainless and tool steel powders, International Journal of Machine Tools & Manufacture 47 (2007) 779–784.

156. Giovanni Strano, Liang Hao, Richard M. Everson, Kenneth E. Evans, Surface roughness analysis, modelling and prediction in selective laser melting, Journal of Materials Processing Technology 213 (2013) 589-597.
157. http://www.ipgphotonics.com/Collateral/Documents/English-US/YLM_Series.pdf
158. Operating Manual MCP SLM Realizer 100, MCP HEK Tooling GmbH, Release 10.2007.
159. http://www.3m.com/intl/kr/img/pdf/7847.pdf
160. Józef Iwaszko, Surface remelting treatment of plasma-sprayed Al2O3 + 13 wt.% TiO2 coatings Surface and Coatings Technology Volume 201, Issue 6, 4 December 2006, Pages 3443-3451.
161. http://www.azom.com/article.aspx?ArticleID=2382
162. ASTM A 387/ A387M – 06a Standard Specification for Pressure Vessel Plates, Alloy Steel, Chromium-Molybdenum.
163. Beddow, J. K. 1995. "Professor Dr. Henry H. Hausner, 1900–1995." Particle & Particle Systems Characterization 12: 213. doi:10.1002/ppsc.19950120411
164. M.J. O'Hara, I.B. Cutler, Sintering Kinetics of binary mixtures of alumina powders. Proceedings of the British Ceramic Society, 12, 1969, pp.145-154.
165. H.M. Lee, C.Y. Huang, C.J. Wang, Forming and sintering behaviours of commercial α-Al_2O_3 powders with different particle size distribution and agglomeration, Journal of materials processing technology, 209, 2009, pp.714-722.
166. Baoshan Li, Guorong Li, WangZhong Zhang, AiLi Ding, Influence of particle size on the sintering behaviour and high-power piezoelectric properties of PMnN-PZT ceramics, Materials science and engineering, B 121, 2005, pp.92-97.
167. Ken Darcovich, Floyd Toll, Pierre Hontanx, Virginie Roux, Kazunari, Shinagawa, An experimental and numerical study of particle size distribution effects on the sintering of porous ceramics, Materials science and engineering, A 348, 2003, pp.76-83.
168. J.S. Chappell, T.A. Ring, J.D. Birchall, Particle size distribution effects on sintering rates, Journal of Applied Physics, 60 (1) 1986, pp.383-391.

169. T.S. Yeh, M.D. Sacks, Low-temperature sintering of aluminium oxide, Journal of the American ceramic society, 71 (10) 1988, pp.841-844.
170. Neal K. Vail, Badrinarayan Balasubramanian, Joel W. Barlow, Harris L. Marcus, (1996),"A thermal model of polymer degradation during selective laser sintering of polymer coated ceramic powders", Rapid Prototyping Journal, Vol. 2 Iss: 3 pp. 24 – 40.
171. Katherine Plummer, Michael Vasquez, Candice Majewski and Neil Hopkinson, Study into the recyclability of a thermoplastic polyurethane powder for use in laser sintering, *Proceedings of the Institution of Mechanical Engineers, Part B: Journal of Engineering Manufacture,* 10 April 2012.
172. P5687 Thermal Conductivity Apparatus Instruction Manual, Cussons Technology Ltd, Issue 4b, July 2003.
173. J.B. Henderson, J.A. Wiebelt, M.R. Tant and G.R. Moore, A Method for the Determination of the Specific Heat and Heat of Decomposition of Composite Materials, *Thermochimica Acta*, 57 (1982) pp. 161-171.
174. http://www.engineeringtoolbox.com/convective-heat-transfer-d_430.html.
175. Harlan H. Bengtson, Convection Heat Transfer Coefficient Estimation, A SunCam online continuing education course
176. Lienhard, J. H. IV, Lienhard, J. H. V, A Heat Transfer Textbook, 4th Ed, Cambridge, MA, Phlogiston Press, 2011. (A Free Electronic Textbook).
177. ABAQUS/CAE v6.9 user manual.
178. http://www.coherent.com/downloads/Copy%20of%20UnderstandingLaserBeamParameters.pdf
179. https://www.cvimellesgriot.com/products/Documents/TechnicalGuide/Beam_Profiling_and_Beam_Measurement.pdf
180. https://www.cvimellesgriot.com/products/Documents/TechnicalGuide/Gaussian_Beam_Propagation.pdf
181. http://mccombe.physics.buffalo.edu/lab-manuals/MG-GaussianBeams.pdf
182. Dallal, Gerard E. (2012). The Little Handbook of Statistical Practice.
183. http://www.chem.arizona.edu/~salzmanr/480a/480ants/heat/heat.html

184. M. Shiomi, K. Osakada, K. Nakamura and T. Yamashida, Abe F(2004) Residual stress within metallic model made by Selective Laser Melting Process. CIRP Annals, 53(1):195-198.
185. E. Yasa, J. P. Kruth, J. Deckers, Manufacturing by combining Selective Laser Melting and Selective Laser Erosion/laser re-melting, CIRP Annals – Manufacturing Technology 60(2011), 263-266.
186. E. Yasa, and J. P. Kruth, Microstructural investigation of Selective Laser Melting 316L stainless steel parts exposed to laser re-melting, Procedia Engineering, 19 (2011), 389-395.
187. F. Wisselink, Use of the plume initiation time in laser milling, PhD Thesis, Universiteit Twente, 1996.
188. American Society for Metals, Metals Handbook Ninth Edition, Volume 3 – Properties and Selection: Stainless steels, Tool Materials and Special-Purpose Metals, 1980.
189. http://www.ohio.edu/mechanical/thermo/property_tables/air/air_Cp_Cv.html
190. http://www.engineeringtoolbox.com/air-properties-d_156.html
191. Shimadzu-dsc-60 user manual.
192. Material Properties Handbook, *UCLA*.
193. http://www.chem.arizona.edu/~salzmanr/480a/480ants/heat/heat.html.
194. http://encyclopedia.airliquide.com
195. E. W. Lemmon, R. T Jacobsen, Viscosity and Thermal Conductivity Equations for Nitrogen, Oxygen, Argon, and Air. *International Journal of Thermophysics*, Vol. 25, No. 1, January 2004, pp.21-69.
196. Gusarov AV, Yadroitsev I, Bertrand Ph, Smurov I. Model of radiation and heat transfer in laser–powder interaction zone at selective laser melting. J Heat Transf 2009;131:072101.
197. Atlas of Isothermal Transformation and Cooling Transformation Diagrams, American Society for Metals, 1977.